Nonlinear Dynamics in Chiral Torsional Metamaterials

A thesis submitted for the degree of

Doctor of Philosophy of

The Australian National University

Mingkai Liu

Nonlinear Physics Centre,
Research School of Physics and Engineering

June 2015

Australian National University

Declaration

This thesis is an account of research undertaken in the Nonlinear Physics Centre within the Research School of Physics and Engineering at the Australian National University between September 2011 and January 2015 while I was enrolled for the Doctor of Philosophy degree.

The research has been conducted under the supervision of Dr. David A. Powell, Dr. Ilya V. Shadrivov and Prof. Yuri S. Kivshar. However, unless specifically stated otherwise, the material presented within this thesis is my own original work.

None of the work presented here has ever been submitted for any degree at this or any other institution of learning.

Mingkai Liu

June 2015

To my mother, father and grandma

给我的妈妈、爸爸和奶奶

Publications

Journal Publications

Papers with results included in this thesis:

Mingkai Liu, David A. Powell, Ilya V. Shadrivov, Mikhail Lapine, and Yuri S. Kivshar, "Spontaneous chiral symmetry breaking in metamaterials", *Nature Commun.* **5**, p 4441-9 (2014).

Mingkai Liu, David A. Powell, Ilya V. Shadrivov, Mikhail Lapine, and Yuri S. Kivshar, "Self-oscillations in nonlinear torsional metamaterials", *New J. Phys.* **15**, p 073036-16 (2013).

Mingkai Liu, Yue Sun, David A. Powell, Ilya V. Shadrivov, Mikhail Lapine, Ross C. McPhedran, and Yuri. S. Kivshar, "Nonlinear response via intrinsic rotation in metamaterials ", *Phys. Rev. B* **87**, p 235126-6 (2013).

Mingkai Liu, David A. Powell, and Ilya V. Shadrivov, "Chiral meta-atoms rotated by light", *Appl. Phys. Lett.* **101**, p 031105-4 (2012).

Mingkai Liu, David A. Powell, Ilya V. Shadrivov, and Yuri S. Kivshar, "Optical activity and coupling in twisted dimer meta-atoms", *Appl. Phys. Lett.* **100**, p 111114-4 (2012).

Papers with results not included in this thesis:

Tatsunosuke Matsui, **Mingkai Liu**, David A. Powell, Ilya V. Shadrivov, and Yuri S. Kivshar, "Electromagnetic tuning of resonant transmission in magnetoelastic metamaterials", *Appl. Phys. Lett.* **104**, p 161117-4 (2014).

Mingkai Liu, Kebin Fan, Willie J. Padilla, David A. Powell, Ilya V. Shadrivov, "Meta liquid crystals", (in preparation)

Media Release

Mingkai Liu, David A. Powell, Ilya V. Shadrivov, Mikhail Lapine, and Yuri S. Kivshar, "Chiral torsional metamaterials", selected as **Optics in 2014** in the December issue of *Opt. Photon. News*, p 51, (2014).

Mingkai Liu, David A. Powell, Ilya V. Shadrivov, Mikhail Lapine, and Yuri S. Kivshar, "A new twist on nonlinear metamaterials", *AOS News*, **28**, p 27-29, (2014).

"New material puts a twist in light", *News, Australian National University, 21 July 2014*, http://www.anu.edu.au/news/all-news/new-material-puts-a-twist-in-light

The work of "spontaneous chiral symmetry breaking in metamaterials" was also reported by *phys.org, photonics.com, sciencedaily.com*, etc., and was selected as a research highlight in *Nature Materials*,
http://www.nature.com/nmat/journal/v13/n9/full/nmat4077.html.

Book Chapters

David A. Powell, **Mingkai Liu** and Mikhail Lapine, *Coupled Electromagnetic and Elastic Dynamics in Metamaterials*, Chapter 4 in *Nonlinear, Tunable and Active Metamaterials*, Springer (2015).

Conference Presentation

Mingkai Liu, David A. Powell, Ilya V. Shadrivov, Mikhail Lapine and Yuri S. Kivshar, "Nonlinear symmetry transitions in magneto-elastically coupled meta-molecules", *21th Congress of the Australian Institute of Physics – AIP 2014*, Canberra, Australia, Dec. 2014.

Mingkai Liu, David A. Powell, Ilya V. Shadrivov, Mikhail Lapine, and Yuri S. Kivshar, "Spontaneous chiral symmetry breaking in magnetoelastic metamaterials", *Progress in Electromagnetics Research Symposium – PIERS 2014*, Guangzhou, China, Aug. 2014.

Mingkai Liu, David A. Powell, Ilya V. Shadrivov, Mikhail Lapine, and Yuri S. Kivshar, "Self-oscillation in Torsional Metamaterials", *Australian and New Zealand Conference on Optics and Photonics – ANZCOP 2013*, Fremantle, Australia, Dec. 2013.

Mingkai Liu, David A. Powell, Ilya V. Shadrivov, Mikhail Lapine, and Yuri S. Kivshar, "Dynamic optical activity of self-oscillating torsional metamaterials", *7th International Congress on Advanced Electromagnetic Materials in Microwaves and Optics – Metamaterials 2013*, Bordeaux, France, Sep. 2013.

Mingkai Liu, Yue Sun, David A. Powell, Ilya V. Shadrivov, Mikhail Lapine, Ross C. McPhedran and Yuri S. Kivshar, "Giant Nonlinear Response via Twists and Turns of Metamaterials", *7th International Congress on Advanced Electromagnetic Materials in Microwaves and Optics – Metamaterials 2013*, Bordeaux, France, Sep. 2013.

Mingkai Liu, Yue Sun, David A. Powell, Ilya V. Shadrivov, Mikhail Lapine, Ross C. McPhedran and Yuri S. Kivshar,"Giant nonlinearity in torsional metamaterials", *4th International Topical Meeting on Nanophotonics and Metamaterials – Nanometa 2013*, Seefeld, Austria, Jan. 2013.

Mingkai Liu, Yue Sun, David A. Powell, Ilya V. Shadrivov, Mikhail Lapine, Ross C. McPhedran and Yuri S. Kivshar, "Light-driven Chiral Meta-atoms", *20th Congress of the Australian Institute of Physics – AIP 2012*, Sydney, Australia, Dec. 2012.

Acknowledgments

I still remember how happy I was about four years ago, when I was offered a PhD scholarship to pursue my degree in the prestigious group led by Prof. Yuri S. Kivshar. I am very grateful to Prof. Yuri S. Kivshar, Dr. David A. Powell and Dr. Ilya V. Shadrivov for giving me this opportunity to come to the wonderful continent of Australia, to study freely the topics I am interested in, and to be surrounded by lovely people, lovely animals and the lovely natural environment.

The interesting thing is, the reason I chose the Nonlinear Physics Centre was because I valued the importance of theory and wanted to be better trained before doing experiments; while the actual reason I was chosen, as I later noticed, was probably because of my nominal experience in experiments during my masters degree study in China, and experimentalists became more demanded in our group – anyway, physics is a subject based on experiments. Fortunately, my supervisors are very open-minded and agreed to my request – no lab experiments until I developed my own ideas.

Although being a self-motivated semi-theorist and semi-experimentalist turned out to be more demanding than I thought, I was very lucky since my supervisors David and Ilya were always around, offering inspiration, guidance and encouragement to my research, saving me from the swamp of equations and giving me help in the lab. I would like to thank my chief-supervisor David, for spending time on discussing about my crazy ideas and providing his critical thinking, and for his timely and careful corrections to my papers and thesis – even during Christmas holidays! Many thanks to my co-supervisor Ilya for giving me the opportunity to involve in the exciting projects of terahertz metamaterials, which allows me to fill the "THz gap" of my experience in metamaterials. I am also grateful to my advisor Yuri for sharing his valuable insight for my research, and believing in me that I can be an experimentalist even though I spent most of my time in front of the computer.

The works presented in this thesis would have been much more difficult to be accomplished without the help of my collaborators and the inspiration from my colleagues. Thanks to Dr. Mikhail Lapine, for his inspiration of bringing electromagnetics and mechanics together in metamaterials, for his very detailed correction to my papers and giving me a special lecture on how to write notations correctly. I would also like to thank my fellow student and co-author Yue Sun for her help on data import with Matlab and a lot of useful and inspiring discussion on optomechanics. Thanks to Guangyao Li for sharing his knowledge of the nonlinear physics in condensed matter systems.

I also want to thank my supervisors for supporting me to learn nano-fabrications, even though my project was based on microwave experiments. Although it's a pity that the fabrication process I tried to develop did not work as expected, I got some valuable experience and a lot of help from the experts in nano-fabrication. Many thanks to Dr. Manuel Decker, Dr. Isabelle Staude, Prof. Dragomir N. Neshev from our department, and Dr. Naeem Shahid, Dr. Kaushal Vora and Dr. Fouad Karouta from the Australian National Fabrication Facility (ANFF) for sharing their expertise and technical support.

I want to thank all my friends and fellow PhD students for all the nice time we had together, making my PhD journey full of joy. Special thanks to Allen Wu, Rui Guo, Wei Liu and Yue Sun for sharing their happiness and passion with me, for the endless conversations and inspiration, and the wonderful travels around Australia we had together will always be remembered. Thanks to the Centre for Ultrahigh bandwidth Devices for Optical Systems (CUDOS), its annual workshops and topical workshops are full of knowledge, passion, insight, great food and fun. Also I would like to thank the Optical Society of America (OSA) and the Society of Photo-Optical Instrumentation Engineers (SPIE) for their support of the student chapter at ANU; thanks to the student chapter committee Alexander S. Solntsev, Sergey S. Kruk, Diana A. Antonosyan, Katie Chong and Ben Hopkins for spending their time and energy on organizing the lovely events.

Most importantly, great thanks to my parents, grandma and all the relatives and friends for their understanding of my absence on the important festivals and the big moments in their lives, for their love, their patience and unconditional support.

Mingkai Liu

at Le Couteur Building,
the Australian National University,

January 2015

Abstract

The advent and rapid development of metamaterials introduced many revolutionary concepts for manipulating electromagnetic waves. As an important class of metamaterials, chiral metamaterials allow us to control the polarization of electromagnetic waves at the subwavelength scale. While much work has been done on using chiral metamaterials to control electromagnetic waves, the accompanying effects, such as the electromagnetic force and torque acting on the structures, as well as nonlinear optomechanical effects, are still largely unexplored.

The exploration of these areas could provide useful insight from both fundamental and practical points of view. In this thesis, we study new properties of chiral metamaterials, in particular the optomechanical properties and nonlinear effects that arise from the coupling between electromagnetic and elastic degrees of freedom. An accurate and efficient model based on the free-space Green's function under the eigenmode approximation is developed for the study.

In Chapter 1, we provide a comprehensive introduction to the basic concepts and history of metamaterials, followed by more focused reviews on chiral metamaterials, different paradigms of tunable metamaterials, the nontrivial electromagnetic force and torque, as well as the nonlinear optomechanical effect in different platforms. Finally, the motivation and the scope of the thesis are summarized.

To understand the optical activity in coupled structures, in Chapter 2, we employ the model developed to study the near-field coupling, far-field scattering and optical activity of chiral meta-molecules based on twisted coupled cut-wire pairs. The numerical results from our model agree well quantitatively with full-wave calculation. We also discuss the optimum twist angle of the structure.

After exploring the optical activity, in Chapter 3, we study the optomechanical properties of chiral meta-molecules based on a pair of twisted split-ring resonators. This structure can provide a strong and tunable torque, and can support different optomechanical dynamics, making it a good candidate for subwavelength light-driven actuators.

To achieve strong coupling between electromagnetic resonance and elastic deformation in metamaterials, in Chapter 4, we introduce chiral torsional meta-molecules based on twisted split-ring pairs. We predict a rich range of nonlinear stationary effects including self-tuning and bistability. Importantly, these nonlinear effects including bistability are successfully observed in experiment.

After understanding the nonlinear stationary responses of torsional meta-molecules, in Chapter 5, we study their nontrivial nonlinear dynamic effects. We introduce a simple structure based on three connected split-rings and find that this structure can support novel nonlinear dynamics such as chaos, damping-immune self-oscillations and dynamic nonlinear optical activity.

To understand how intermolecular interaction can change system dynamics, in Chapter 6, we study the nonlinear effects of ensembles of enantiomeric torsional meta-molecules. We find that spontaneous chiral symmetry breaking can exist due to intermolecular interaction. For the first time in metamaterials, both spontaneous chiral symmetry breaking and self-oscillations are successfully demonstrated exper-

imentally. Our study provides a new route to achieve artificial phase transitions in metamaterials without using naturally occurring phase change materials.

In Chapter 7, we summarize the work and discuss the future possible topics in related to the optomechanical effects in metamaterials.

Contents

Introduction

1.1 Thesis Statement

Novel methods of manipulating electromagnetic (EM) waves can have a strong impact or even cause a paradigm shift over a broad range of disciplines in science and technology. However, due to the limited properties of natural materials, most of the new materials in use today are artificially created, either on the *atomic or molecular level* through chemosynthesis, electronic energy band tailoring, or on the *meso-structural level* by controlling the refraction, reflection, scattering and interference effects via deliberately designed structures. Perhaps the most well-known examples of meso-structural tailoring are multilayer thin films, diffraction gratings and photonic crystals. In general, these devices have a characteristic scale around the operating wavelength, with their operation mechanism based on multiple scattering.

To develop novel devices that are ultra-compact and efficient, meso-structural tailoring needs to be explored at the subwavelength scale – this is what metamaterials can offer. Different from photonic crystals, metamaterials are meso-structures with characteristic scale smaller than the operating wavelength, and their novel effects are mostly based on the localized resonances of subwavelength units – meta-atoms.

This thesis aims to explore new functions of metamaterials from the level of single meta-atoms to large scale complex coupled systems. The study will focus on a specific type of metamaterial called *chiral metamaterials*. The scattering and polarization rotation effects of chiral metamaterials have been extensively studied, but the corresponding EM force and torque were largely unexplored until recently. Therefore, in this thesis, apart from the well-known polarization rotation effect, we will also discuss the novel optomechanical properties of chiral meta-molecules, and will highlight the nontrivial nonlinear effects when the internal EM torque is employed to achieve structural deformation and active tuning.

Based on this logic, a brief introduction to the history and basic concepts of metamaterials is first given in Sec.1.2; in Sec.1.3, a more focused review of the physics of chiral metamaterials is presented; in Sec. 1.4, different paradigms of tunable metamaterials are summarized; in Sec.1.5, the nontrivial EM force in metamaterials and the nonlinear optomechanical effects are covered; finally, the motivation and the scope of the thesis is summarized in Sec.1.6.

1.2 Introduction to Metamaterials

The field of metamaterials focuses on using subwavelength structured materials to control EM waves, and it experienced rapid development over the past 15 years. Many unconventional properties and paradigm shifting concepts have been introduced and verified experimentally, and they have revolutionized our traditional methodologies in controlling electromagnetic waves. This section will first provide a historical overview of the important milestones in this field, and then introduce the basic concepts and the physical origins of exotic electromagnetic parameters.

1.2.1 Historical Overview

Metamaterials are artificial meso-structures that exhibit exotic electromagnetic (EM) properties not found in nature [1–7]. Since the unit cells (meta-atoms or meta-molecules, see Sec. 1.2.2.1) of metamaterials are sub-wavelength in size, their EM properties can be described approximately by effective parameters based on homogenization procedures (as will be discussed below in Sec. 1.2.2.3) [8–11].

In fact, the history of artificial structured EM materials, in a broad sense, is much longer than the age of metamaterials – there had been some early examples of artificial EM structures before the concept of metamaterials was proposed, such as twisted bundles of jute [17] and the well known frequency selective surfaces [18,19]. But the vast development of this field started only in the late 1990s, when J. B. Pendry et al. predicted that conducting wire arrays can work as a low-frequency plasma [20] with a negative value of effective permittivity, while arrays of split-ring resonators (SRRs) can support strong magnetic resonances leading to a negative value of effective permeability [21]. By combining these two structures and overlapping the frequency bands of negative permittivity and permeability, D. R. Smith et al. demonstrated the first metamaterial with negative refractive index in 2000 [3] [see Fig. 1.1(a) and (b)]; in a negative index medium, the directions of wave vector and energy flux are opposite, which is also known as *backward waves*. These are important breakthroughs, since predictions of exotic behaviour for negative index materials by V. Veselago in 1968 [22], such as negative refraction [see Fig. 1.1 (a)], reversed Doppler effect and reversed Cherenkov radiation can be realized.

To push the concept of negative refractive index towards higher frequencies, new approaches such as coupled cut-wires [12], fishnet structures [31–33] [Fig. 1.1 (c)] and coaxial waveguide arrays [34], etc. have been introduced. On the other hand, the new potential application of metamaterials such as the superlens [Fig. 1.1 (d) and (e)] that can overcome the diffraction limit attracted great attention and further stimulated the development of this field [13, 14, 35–37]. The initial quest for negative refraction in anisotropic media brought in the concept of *indefinite media* and *hyperbolic dispersion* [6], now generally referred to *hyperbolic metamaterials* [Fig. 1.1 (g)] [15]. Such type of metamaterials can possess a giant photonic density of states, which would find application in a multitude of topics from super-resolution imaging [Fig. 1.1 (f)] [14,36,38], quantum photonics [16,39,40] [Fig. 1.1 (h)] to nonlinear optics [41] and bio-sensing [42].

With the rapid development of the field, it was soon realized that metamaterials possess much broader potential. In contrast to the Bragg resonances in photonic crystals [43], localized resonances of the composite units (meta-atoms) play a dominant role in the properties of metamaterials. This provides an opportunity to engineer the

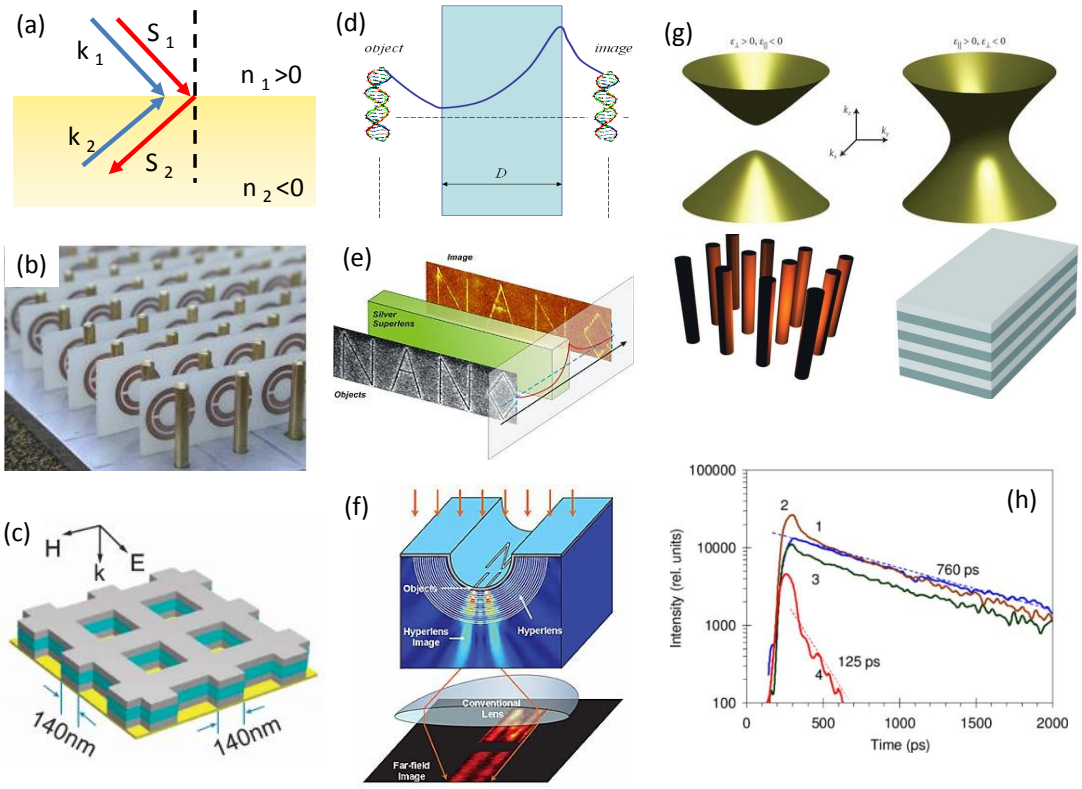

Figure 1.1: (a) Schematic of negative refraction; in negative index media, the directions of wave vector and energy flux are opposite, which is also known as *backward waves*. (b) The first demonstration of a negative index microwave metamaterial composed of split-ring resonators and cut-wires [3]. (c) Schematic of a double layered fishnet structure that can support negative index in infrared and optical frequencies [12]. (d) Principle of a superlens made of single negative materials, which can amplify the evanescent wave components and images, where sub-wavelength details can be reconstructed in the near-field. (e) Experimental demonstration of superlens effect with a thin slab of silver [13]. (f) A hyperlens based on metal-dielectric multilayers on a curved surface, with which a sub-wavelength image can be magnified so that it can be resolved with a conventional lens [14]. (g) Two types of hyperbolic metamaterials based on metallic wires and metal-dielectric multilayers, which exhibit different spatial dispersion [15]. (h) Emission kinetics of IR140/PMMA films deposited on different substrates. Curve 4 is for hyperbolic metamaterials based on silver-filled alumina membrane [16].

local electric and magnetic response of the structure, simply by modifying the geometry of each meta-atom. Based on such great flexibility, the new and fruitful research area of transformation optics has skyrocketed since 2006 [23, 44] [Fig. 1.2 (a)], which provides a powerful methodology for designing structures with unconventional EM behaviour [45], such as invisibility cloaks [24–26, 46–48][Fig. 1.2 (b) to (d)], exotic lenses [49, 50] and light harvesting structures [27, 51, 52] [Fig. 1.2 (e)]. Although early theoretical and experimental studies on metamaterials and transformation optics were conducted with EM waves, the concepts were soon extended to other fields, including the manipulation of various mechanical waves [28, 53–56] [Fig. 1.2 (f)], heat flows [29, 57–59] [Fig. 1.2 (g)], and even matter waves [Fig. 1.2 (h)] [30, 60, 61].

Due to the complexity of fabricating three dimensional metamaterials [69], many

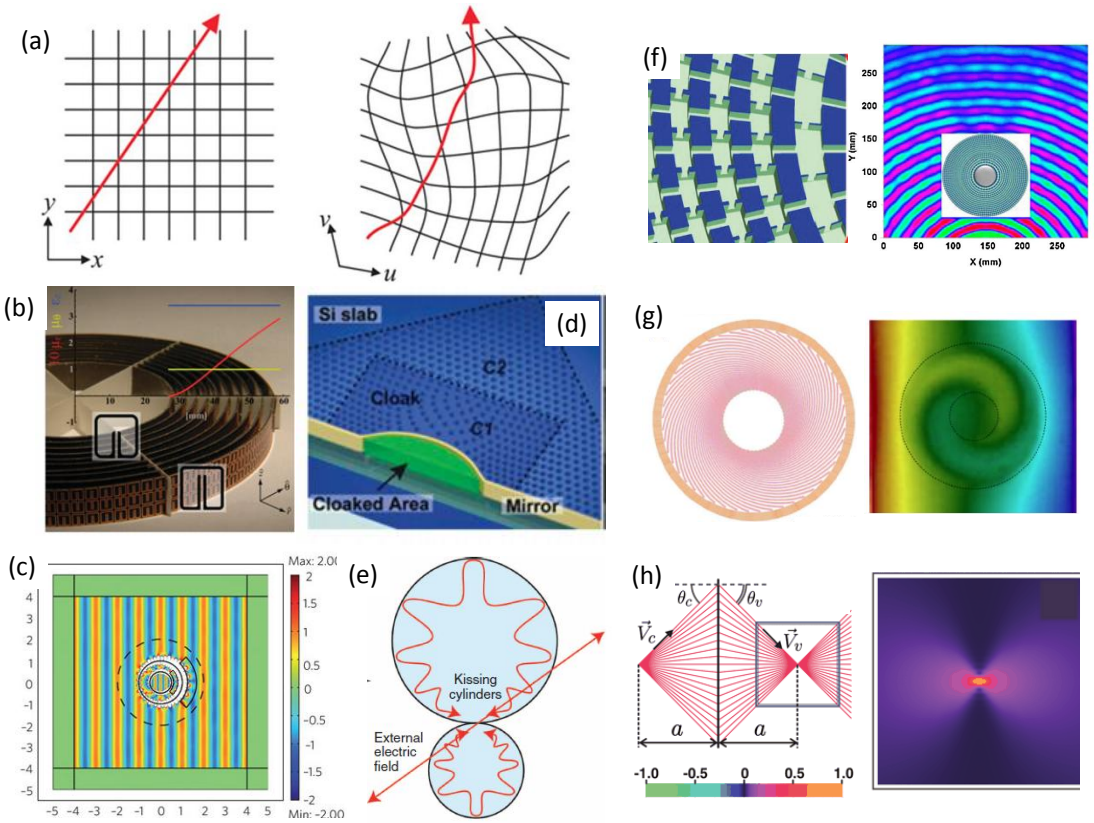

Figure 1.2: (a) Basic concept of transformation optics. Straight field line in Cartesian coordinates (left) and distorted field line in distorted coordinates (right); the distortion in space can be transformed into a change of local ϵ and μ [23]. (b) A cylindrical invisibility cloak at microwave frequencies [24]. (c) A carpet cloak working at optical frequencies [25].(d) An external cloak based on complementary media [26] (e) Plasmonic light trapping revisited with transformation optics [27]. (f) A cylindrical acoustic cloak for ultrasound waves in water [28]. (g) A thermal inverter made of a spiral arrangement of copper and polyurethane (left), the temperature profile shows inversion of the heat flux (right) [29]. (h) Focusing of electrons via negative refraction by a grapheme p-n junction (left); interference pattern at the focal spot (right) [30].

studies revisited the thin planar version of metamaterials, now generally dubbed meta-surfaces [62,70,71]. For homogenizable meta-surfaces (most studied thin metamaterials with periodic meta-atoms fall into this category), it is more meaningful to characterize the constitutive relation with surface susceptibility rather than effective permittivity and permeability for bulk materials [70]. The strong resonances of meta-atoms can exert abrupt phase changes in their scattered waves; on account of Huygens' principle, meta-surfaces with spatial phase gradient are able to mould the scattered wave-fronts arbitrarily [62,63,71] [Fig. 1.3 (a)]. Although, in terms of functionality, the design philosophy of gradient meta-surfaces is closely related to the well-established fields of phase array antennas, holography and diffractive optics, its underlying mechanism for generating abrupt phase change is totally different, and thus it provides much greater design flexibility in manipulating the phase, amplitude [Fig. 1.3 (b) to (d)] and polarization [Fig. 1.3 (f) to (g)]] by interacting with electric or magnetic component (or both, [see Fig. 1.3 (d)]) with optically thin devices from the subwavelength scale [64–66,72–74].

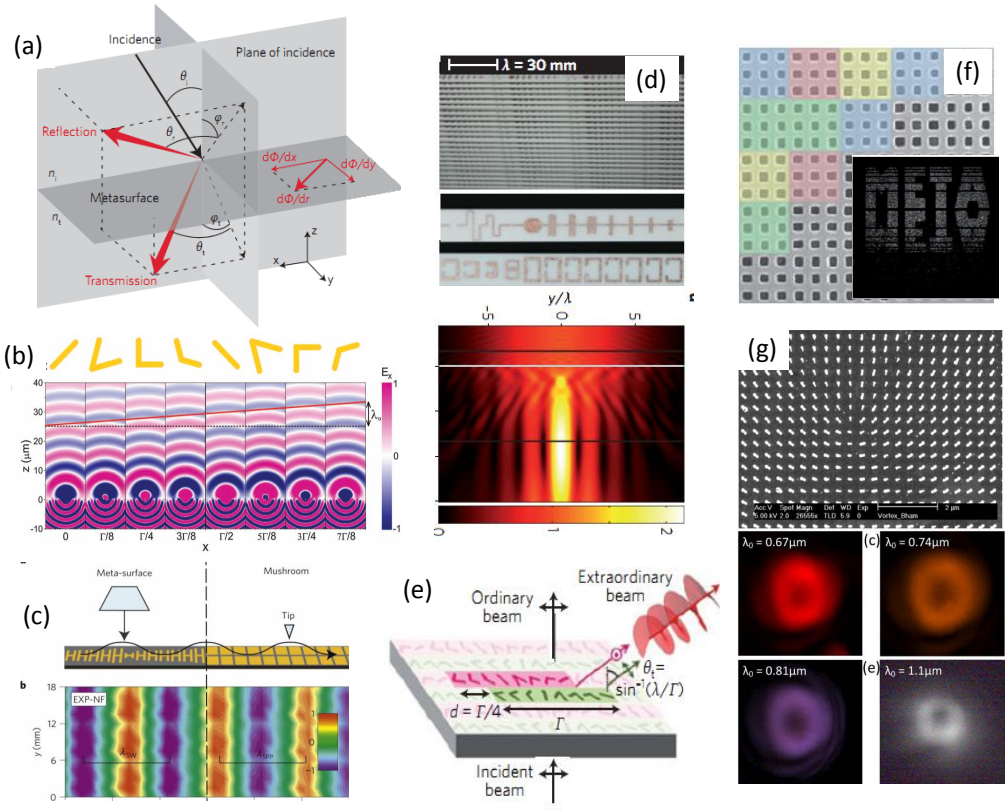

Figure 1.3: (a) Schematic of general laws of reflection and refraction in the presence of phase gradient at the interface [62]. (b) A meta-surface composed of V-shaped elements, where the phase of cross-polarization component can be controlled [63]. (c) A microwave meta-surface based on H-shaped meta-atoms on a ground plane, from which the plane wave can be coupled to the surface wave almost perfectly [64]. (d) A flat lens based on Huygens surface, where the impedance matching is optimized by exploiting both electric and magnetic resonances [65]. (e) A broadband background-free metasurface quarter-wave plate [66]. (f) A metasurface hologram made of aperture antennas. Different colours represent pixels with distinctive transmission coefficients. Inset is the image produced in the far-field [67]. (g) A metasurface composed of dipolar antenna array designed for generating an optical vortex beam by exploring the geometric phase (top); broadband vortex can be generated by circular polarization incidence (bottom) [68].

1.2.2 Basic Concepts

1.2.2.1 Meta-atom, meta-molecule and metamaterial

The properties of metamaterials rely on the proper design and fabrication of the building blocks – meta-atoms and meta-molecules. Although there is no exact definitions of "meta-atom" and "meta-molecule", in this thesis, we use an analogous concept in material science – "meta-atom" refers to the most basic functional elements in metamaterials that are "indecomposable", such as single cut-wires and split-rings, etc.; while "meta-molecule" refers to functional groups based on the strong EM coupling of two or more meta-atoms, such as a pair of coupled cut-wires. The coupling in meta-molecules can bring in much broader range of EM properties not available in single meta-atoms, just as synthesized molecules having properties beyond their

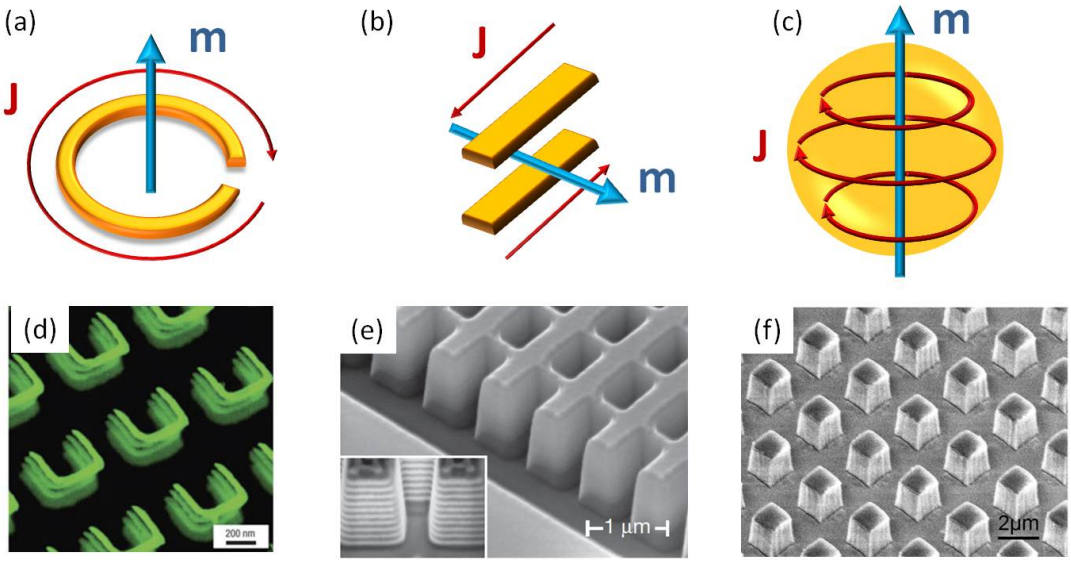

Figure 1.4: Three different designs for artificial magnetism: (a) split-ring resonators, (b) coupled metallic wires and (c) high index dielectric resonators. Their realization at infrared and optical frequencies: (d) multilayered split-ring resonators [79], (e) multilayered fishnet structures [80] and (f) matrix of silicon blocks [81].

constitutive atoms. When these building blocks are packed together to control the behaviour of EM waves on the macroscopic level, the system can be referred as a "metamaterial".

1.2.2.2 Artificial magnetism

Perhaps the most distinct effect of metamaterials is their ability to simultaneously interact with both the electric and magnetic components of EM waves, which subsequently leads to a variety of effective EM parameters that are not available in natural materials, for example, negative refractive index. To interact with both electric and magnetic components is not as straightforward as it sounds, since the EM properties of most natural materials is dominated by electric response, particularly at high frequencies, while magnetic response is usually available well below hundreds of GHz. The most prominent example of artificial magnetism is a split ring resonator [Fig. 1.4(a)], first introduced by W. N. Hardy and L. A. Whitehead in 1981 [75], and later revitalized by J. B. Pendry in 1999 [21]. It was predicted that when the split-rings are packed into a periodic array, the averaged macroscopic magnetic response can be described with *effective* permeability μ_{eff}, whose value can become negative near the resonance [21]. In this design, the oscillating loop of conduction current of the metallic split-rings gives rise to giant artificial magnetism, and the effect is scalable up to around 100 THz [76–79], when the metal can still be considered as a good conductor [Fig. 1.4(d)].

For higher frequency above 100 THz, saturation occurs due to the non-negligible kinetic energy of free electrons [82], and the strength of magnetic resonance decreases ($\mu_{\text{eff}} < 0$ disappears). A new design based on coupled cut-wire pairs was introduced by V. A. Podolskiy [83] and L. V. Panina [84] in 2002 [Fig. 1.4(b)] and was experimentally demonstrated by V. M. Shalaev and W. Cai et al. in 2005 [12]. In this design, a strong magnetic dipole moment arises from the near-field coupling

of cut-wire pairs, and displacement current takes up a larger proportion in the loop of oscillating current, which further pushes the magnetic resonance to the optical frequency band. This idea was further developed into the prominent double-layered fishnet structures that can support negative index in near infrared and optical frequency regime, and the idea was first demonstrated by S. Zhang et al. [31], followed with improved performance and higher operation frequencies [32, 33]. As the number of layers increases, the narrow band effect of negative index further evolves into a broadband phenomenon with improved figure of merit from infrared to visible frequencies, which was experimentally demonstrated by the group from X. Zhang [80] [Fig. 1.4(e)].

To overcome the unavoidable loss due to plasmonic resonances, there is a growing interest to revisit all-dielectric structures [81, 85–90], in which Mie resonances supported by high index dielectric resonators play a significant role in achieving artificial magnetic response [85, 86, 91, 92] [Fig. 1.4(c)]. In such a scenario, the circulating loop of current is contributed by the polarization current, and dissipative loss can be much smaller than in metallic resonators. Such an approach also provides a new tool box for optical nano-antennas [93–97] and low-loss meta-surfaces [81, 98–101] [Fig. 1.4(f)].

It has to be emphasized that the effective permeability with nonmagnetic resonators mentioned above is actually an effective description under homogenization approximation. When only nonmagnetic materials are employed to construct meta-atoms or meta-molecules, the magnetic response actually originates from the strong local curl of the electric field supported by some specific types of resonances, as is described by the Maxwell's equation,

$$\nabla \times \mathbf{E}(\mathbf{r}) = -\frac{\partial}{\partial t}\mathbf{B}(\mathbf{r}) = \mathrm{i}\omega\mu_0\mathbf{H}(\mathbf{r}). \tag{1.1}$$

A strong magnetic response can be obtained from a mode with a circulating loop of current (including polarization current and conduction current), leading to a strong magnetic dipole moment and non-trivial effective permeability ($\mu_{\text{eff}} \neq \mu_0$) when these unit elements are packed into a bulk metamaterial. Therefore, artificial magnetic responses in metamaterials are mostly resonance-based effects, and they are actually the manifestations of spatial dispersion (nonlocality) in these meso-structures, as will be further discussed below.

1.2.2.3 Spatial dispersion and constitutive relation of metamaterials

In natural materials, the scale of atoms, molecules and lattice constant is usually orders of magnitude smaller than the wavelength when the working frequency is well below visible light [102, 103], and thus the linear response of a natural material can usually be regarded as local, i.e. it is generally sufficient to describe the constitutive relation of the material with simple dyadic tensors $\overline{\overline{\boldsymbol{\epsilon}}}(\omega, \mathbf{r})$ and $\overline{\overline{\boldsymbol{\mu}}}(\omega, \mathbf{r})$.

In metamaterials, the situation becomes more complicated. Although on the *microscopic* level, one can describe the local response by using the $\overline{\overline{\boldsymbol{\epsilon}}}(\omega, \mathbf{r})$ and $\overline{\overline{\boldsymbol{\mu}}}(\omega, \mathbf{r})$ of the constitutive materials (strictly speaking, nonlocal effects on this level can come into play when the characteristic size of meta-atom is close to the diffusion length of electrons), on the *mesoscopic* level, it is generally preferable to use *effective* constitutive parameters to describe the averaged effect of wave interacting with these subwavelength meso-structures, if the detailed localized field distribution is not of

interest. The effective material responses, including the effective permeability mentioned above, are actually built on the *homogenization* of fields within a unit cell that is usually larger than $\lambda/10$. In such cases, spatial dispersion (nonlocal effects) becomes non-negligible, and such spatial dispersion is actually the physical origin of exotic electromagnetic parameters in metamaterials.

For a metamaterial composed of periodic nonmagnetic scatters, the nonlocal dielectric response can in general be described by a spatially dispersive permittivity tensor $\bar{\bar{\epsilon}}(\omega, \mathbf{r}, \mathbf{r}')$. In the Fourier domain, it can be written as $\bar{\bar{\epsilon}}(\omega, \mathbf{k})$, with $\mathbf{k}$ being the wave vector of the fundamental Bloch mode supported by the structure [10, 11]. It has been proved that if the spatial dispersion effect is weak and can be well approximated by the expansion of $\bar{\bar{\epsilon}}_{\text{eff}}(\omega, \mathbf{k})$ up to the second order of $\mathbf{k}$, then the nonlocal response can be reformed into a new set of "local" effective parameters [10], well known as the classic constitutive relation for bi-anisotropic materials [104],

$$\mathbf{D} = \bar{\bar{\epsilon}}\mathbf{E} + \bar{\bar{\xi}}\mathbf{H}, \tag{1.2}$$

$$\mathbf{B} = \bar{\bar{\zeta}}\mathbf{E} + \bar{\bar{\mu}}\mathbf{H}. \tag{1.3}$$

Note that the effective permeability here is actually a manifestation of the *second order* spatial dispersion of $\bar{\bar{\epsilon}}(\omega, \mathbf{k})$, and in general $\bar{\bar{\mu}} \neq \mu_0$. In this thesis, we only study reciprocal metamaterials, in such case

$$\bar{\bar{\epsilon}} = \bar{\bar{\epsilon}}^{\,T},\ \bar{\bar{\mu}} = \bar{\bar{\mu}}^{\,T},\ \bar{\bar{\xi}} = -\bar{\bar{\zeta}}^{\,T}, \tag{1.4}$$

"T" is the transpose operation [104].

The additional terms $\bar{\bar{\xi}}$ and $\bar{\bar{\zeta}}$ originate from the *first order* spatial dispersion, and they describe the magnetoelectric coupling effects [10, 104, 105]. This means unlike conventional isotropic or anisotropic materials, in a general bianisotropic material, electric and magnetic effects are mutually coupled – an electric (magnetic) field can induce not only electric (magnetic) polarization but also magnetic (electric) polarization, as can be told from Eq. (1.2) and Eq. (1.3).

The off-diagonal terms $\xi_{ij} = -\zeta_{ji}$ correspond to cross-polarized magnetoelectric coupling originated from the breaking of central symmetry, and they are usually called bi-anisotropic coefficients. A typical example is split-ring resonators, where the induced electric dipole and magnetic dipole moments are mutually coupled and oriented in perpendicular directions. The diagonal terms of $\xi_{ii} = -\zeta_{ii}$ require broken mirror symmetry of the system, which describes the co-polarized magnetoelectric coupling that leads to chiral effects (as will be further introduced in Sec. 1.3), and thus are called chiral coefficients. A typical example is spirals, where the induced electric and magnetic dipole moments are mutually coupled and parallel.

The chiral metamaterials studied in this thesis are characterized by the chiral coefficients. In the special case where the response becomes isotropic and the system is central symmetric (for example, in a metamaterials composed of randomly distributed helices), the off-diagonal terms of $\bar{\bar{\xi}} = -\bar{\bar{\zeta}}^{\,T}$ vanish and the diagonal terms become identical. The bi-anisotropic parameters can be rewritten in a simple scalar form, i.e. $\xi = -\zeta = -\mathrm{i}\kappa/c$. then Eq. (1.2) and Eq. (1.3) reduce to the relation for isotropic chiral materials

$$D = \epsilon E - \frac{\mathrm{i}\kappa}{c} H \tag{1.5}$$

$$B = \frac{\mathrm{i}\kappa}{c} E + \mu H \tag{1.6}$$

Apart from the macroscopic constitutive relation for bulk metamaterials, one can also use a similar form of microscopic model to describe the induced electric and magnetic dipole moments of a single bianisotropic meta-atom such as a split ring resonator [104].

$$\begin{pmatrix} \mathbf{p} \\ \mathbf{m} \end{pmatrix} = \begin{pmatrix} \bar{\bar{\boldsymbol{\alpha}}}^{\,\mathrm{ee}} & \bar{\bar{\boldsymbol{\alpha}}}^{\,\mathrm{em}} \\ \bar{\bar{\boldsymbol{\alpha}}}^{\,\mathrm{me}} & \bar{\bar{\boldsymbol{\alpha}}}^{\,\mathrm{mm}} \end{pmatrix} \begin{pmatrix} \mathbf{E} \\ \mathbf{H} \end{pmatrix} \tag{1.7}$$

This electric and magnetic dipole model is intuitive and would be particularly useful in understanding the nontrivial scattering properties of a single or an array of bianisotropic meta-atoms [106–108]. For reciprocal systems,

$$\bar{\bar{\boldsymbol{\alpha}}}^{\,\mathrm{ee}} = (\bar{\bar{\boldsymbol{\alpha}}}^{\,\mathrm{ee}})^T, \ \bar{\bar{\boldsymbol{\alpha}}}^{\,\mathrm{mm}} = (\bar{\bar{\boldsymbol{\alpha}}}^{\,\mathrm{mm}})^T, \ \bar{\bar{\boldsymbol{\alpha}}}^{\,\mathrm{em}} = -(\bar{\bar{\boldsymbol{\alpha}}}^{\,\mathrm{me}})^T. \tag{1.8}$$

1.3 Chiral Response in Metamaterials

The studies presented in this thesis focus on a particular type of metamaterials known as chiral metamaterials. In fact, the study of chiral materials has a much longer history than the field of metamaterials. This section will give a brief review of the pioneering works on chiral media for electromagnetic waves and then cover the recent development in chiral metamaterials.

1.3.1 Pioneering Works on Chiral Mediums

The term "chiral" was first used by Lord Kelvin in 1893:

"I call any geometrical figure, or group of points, 'chiral', and say that it has chirality if its image in a plane mirror, ideally realized, cannot be brought to coincide with itself". [109]

The electromagnetic (optical) properties associated with structural chirality are often referred as *chiral electromagnetic (optical) response* or *electromagnetic (optical) activity*. In nature, optical activity can be found in substances with nano/micro-structures that have broken mirror symmetry; in fact, most biomolecules are chiral in nature, but the underlying mechanism of homochirality (only one handedness dominates) is still a mystery [110,111]; these structures can show different responses to left-handed and right-handed circular polarizations, [see Fig. 1.5 (a) and (b) for examples] and are responsible for the polarization rotation of linearly polarized light.

Such effects can be phenomenologically understood from the effective refractive indexes for circular polarizations. For isotropic chiral materials described with

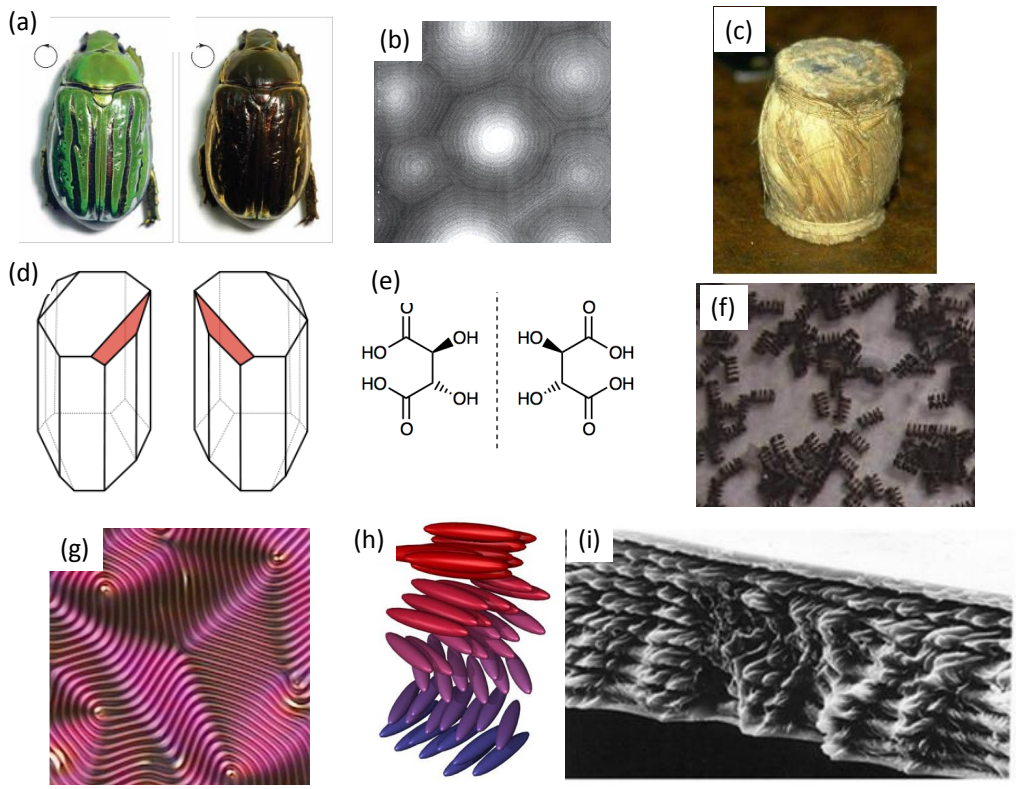

Figure 1.5: (a) Different colors shown by the beetle Chrysina gloriosa under left and right circular polarizers and (b) the micro chiral structure of its exoskeleton under scanning electron microscope [112]. (c) A twisted bundle of jute made by J. C. Bose that can rotate the polarization of EM waves [113]. (d) Two different forms of tarartic acid crystals [114] and (e) their molecular configurations [115]. (f) Chiral media composed of randomly oriented metallic helices (2 mm height and 1.2 mm outer diameter) that show strong circular dichroism [116]. (g) Fingerprint texture of chiral liquid crystals under heomeotropic boundary conditions (looking perpendicular to the helix axis) [117], (h) the schematic of chiral phase [118] and (i) the corresponding scanning electron microscope image of liquid crystal molecules in chiral phase. [119]

Eqs. 1.5 and 1.6, the indices for left and right circular polarizations can be expressed as

$$n_{L,R} = \sqrt{\epsilon\mu} \pm \kappa. \tag{1.9}$$

The difference in real parts of the refractive indexes leads to different phase delay and it is known as *circular birefringence*, while the difference in imaginary parts is responsible for the absorption difference known as *circular dichroism*.

The first demonstration of optical activity was in 1811 by François J. D. Arago with quartz crystals, in which he found the polarization rotation of linearly polarized light. Similar phenomena were also observed later by Sir John F. W. Herschel in quartz crystals with mirror-imaged crystalline structures, and by Jean Baptiste Biot in certain liquid and gases of organic substances, who also revealed the relation between the angle of rotation and wavelength [120]. But the relation between polarization rotation and structural chirality was still unclear until Louis Pasteur revealed the chiral

nature of tartaric acid molecules and deduced that such property could be associated with the opposite effects in crystal formation and polarization rotation – the crystals formed by chiral molecules of opposite handedness have mirror-symmetric structures, and the polarization rotation directions in crystals of opposite handedness are also mirror-symmetric [121] [see Fig. 1.5 (d) and (e)].

In 1898, Sir Jagadish. C. Bose demonstrated an experiment in millimeter waves to show the polarization rotation power of a twisted bundle of jute [17][Fig. 1.5 (c)]. This is the first experimental verification that three dimensional (3D) chiral structures can give rise to electromagnetic chiral effects. In a broad sense, the twisted bundle of jute made by Bose can also be considered as the first artificial electromagnetic material, although the term "metamaterials" widely used today was coined 100 years later in 1999 by Rodger Walser [122].

Later, artificial media composed of metallic helices were studied and found to exhibit strong polarization rotation due to large circular dichroism [123–125] [Fig. 1.5 (f)]. By the 1990s, classical artificial chiral media like helices and chiral liquid crystals [Fig. 1.5 (g) to (i)] were extensively studied due to the vast development in radio science, microwave technology and the display industry [126–130].

1.3.2 Chiral Metamaterials

1.3.2.1 Three dimensional (3D) chiral metamaterials

In 2000s, chiral media attracted substantial interest again due to new progress in metamaterials. Early methods of realizing negative index metamaterials generally require the overlapping of electric and magnetic resonances, while it was predicted independently by John B. Pendry and Sergei A. Tretyakov that artificial chiral media can provide an alternative way to achieve polarization-dependent negative refractive index, as long as the chirality κ is sufficiently strong [Fig. 1.6(a) and (b)] [131,137]. In fact, the possibility of negative refraction in chiral media was first identified in 1981 by B. Bokut' et al. [138] [as can be expected from Eq. (1.9)], but the practical route via chiral metamaterials was not discovered until two decades later.

The realization of negative index in chiral media was first reported by S. Zhang et al. with a 3D chiral metamaterial in THz [see Fig. 1.6(e) and (f)] [133], and in the same year by E. Plum et al. [139], J. Zhou et al [140] with bilayer designs, and by B. Wang et al. with 3D chiral structures [141] at microwave frequencies. The advantage of using bilayer designs is its ease of fabrication, but a direct extension to multilayered chiral structures does not necessarily bring in a bulk negative index material due to the complex inter-layer couplings. Later, C. Wu et al. analysed the photonic band structure of long metallic helix arrays and demonstrated negative refraction of a bulk chiral material at microwave frequencies [142] [see Fig. 1.6(i) and (j)]. In contrast to previous approaches based on localized resonances, negative refraction in long metallic helix arrays originates from the band-folding effect of propagating helical modes in a periodic helix, as has been shown in previous studies of helical tubes and helical waveguides [143–146].

In 3D chiral metamaterials, polarization rotation and circular dichroism near resonances are orders of magnitude stronger than conventional optically active materials [139,147,148]. For metamaterials based on multilayered structures [147,149–152], such enhancement benefits from the strong near-field interaction of meta-atoms that provides a giant co-polarized magnetoelectric coupling, and the effect can be controlled by changing the relative twist angles and displacement [79,149,152]. Recently,

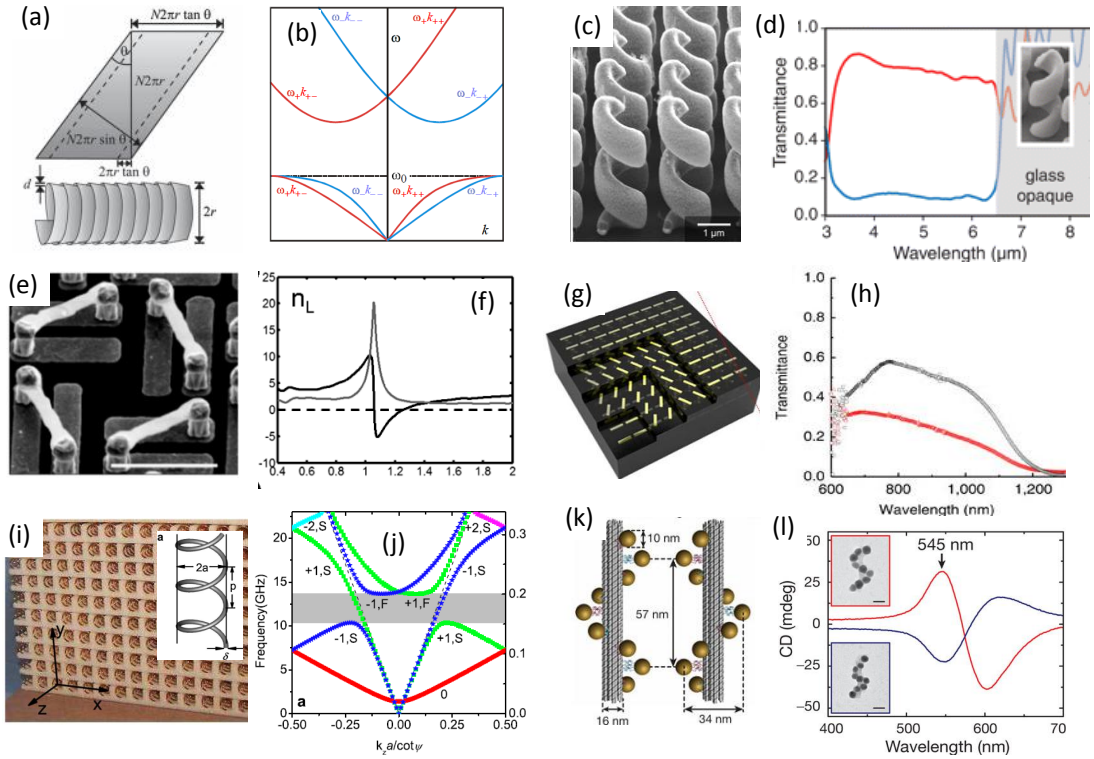

Figure 1.6: (a) Design for a chiral meta-atom by winding an insulated metallic strip into a helix, and (b) the band structure of a homogeneous isotropic chiral medium, showing the backward wave regime around the Brillouin zone centre [131]. (c) Metallic helices fabricated using direct laser writing; (d) the corresponding broadband circular dichroism at mid-infrared frequencies [132]. (e) The first chiral metamaterial with (f) negative index at THz frequencies [133]. (g) Chiral metamaterials based on multilayered twisted cut-wires, and (h) the corresponding optical spectrum of broadband circular dichroism [134]. (i) A microwave bulk chiral medium based on long metallic helices, and (j) the band diagram showing the backward wave regime around both the Brillouin zone centre and boundary [135]; the grey regime is the polarization gap leading to broadband circular dichroism. (k) DNA-based self-assembly of chiral plasmonic nanostructures with (l) tailored strong chiral response at visible light frequencies [136].

through deliberate design and fabrication, broadband wave plates [66,135], circular polarizers [132,134] and polarization rotators [153,154] were experimentally demonstrated with chiral metamaterials. The advances in nano fabrication, such as direct laser writing [Fig. 1.6(c), (d)] [132], multilayer electron-beam lithography [Fig. 1.6(g), (h)] [134,155] and DNA origami [Fig. 1.6(k), (l)] [136,156–158], offer new opportunities to realize three dimensional chiral structures with tens to hundreds of nanometers features, which further push the operation frequency of chiral metamaterials to near-infrared and visible light regime.

1.3.2.2 Planar metamaterials with chiral effects

Apart from the 3D chiral metamaterials mentioned above, there is another important class of chiral metamaterials based on planar structures. In contrast to 3D chiral

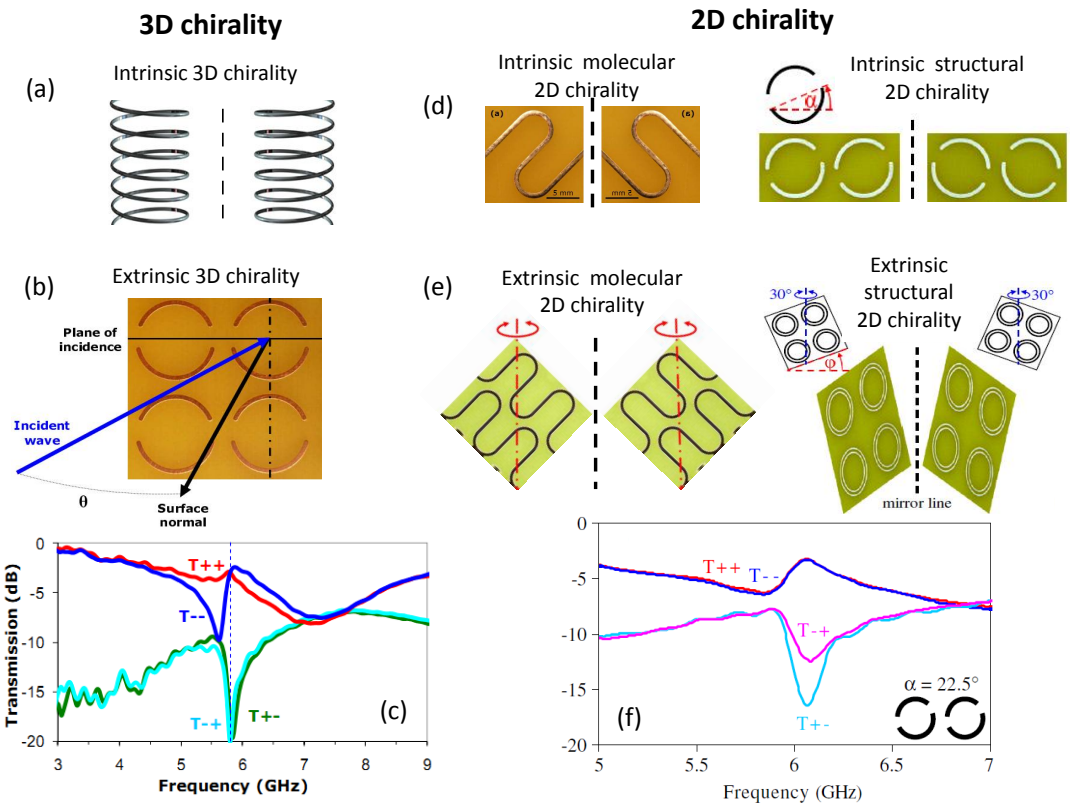

Figure 1.7: Schematic of (a) intrinsic 3D chirality in chiral structures, and (b) extrinsic 3D chirality for 2D planar structures under oblique incidence [161]; (c) typical 3D chirality is described by circular birefringence and dichroism $T_{++} \neq T_{--}$ [161]. (d) Intrinsic 2D chirality, where structures can show asymmetric transmision at normal incidence, while for (e) extrinsic 2D chirality, structures show the effect only at oblique incidence [164]. (f) Typical 2D chirality is described by circular conversion dichroism $T_{+-} \neq T_{-+}$ [164].

structures [Fig. 1.7 (a)], the handedness of planar chiral structures is reversed when observed from opposite sides. Therefore, planar structures are considered to be chiral only in a two dimensional (2D) sense, i.e. as long as they do not overlap with their mirror images in the two dimensional space, but it's no longer true if they can be lifted off and flipped over in the third dimension. Usually, planar chiral structures can not show circular birefringence or circular dichroism as 3D chiral structures do, unless the mirror symmetry in the third dimension is broken (such as adding a substrate) [159], or the wave is obliquely scattered away from to the planar surface [160]. For the latter situation, the structure even does not need to be chiral, e.g. a single split-ring resonator can already show optical activity at oblique scattering due to the inherent bianisotropy [107], and it is the underlying mechanism of "extrinsic 3D chirality" [161–163] [see Fig. 1.7 (b)]. For 3D chirality (both intrinsic and extrinsic), chiral response is featured by the different *co-polarization* transmission coefficients, i.e. circular birefringence and dichroism [see Fig. 1.7 (c)].

In 2006, a phenomenon called *circular conversion dichroism* was found in planar chiral structures [165] [so-called intrinsic 2D chirality, see Fig. 1.7 (d)]. Such an effect is general for a system with non-equal off-diagonal elements in the transmission matrix and can lead to reciprocal asymmetric transmission of polarized waves [164–

166]. Later, S. V. Zhukovsky pointed out that this effect can be interpreted as elliptical dichroism found in biaxial elliptically dichroic crystals, and the co-rotating elliptical eigen-polarization states found is an inherent property of such type of systems [167, 168]. Asymmetric transmission can also be achieved when the structural orientation of a non-chiral meta-surface becomes chiral with respect to the incident plane [so called extrinsic 2D chirality, see Fig. 1.7 (e)]. For 2D chirality (both intrinsic and extrinsic), chiral response is featured by the different *cross-polarization* transmission coefficients [see Fig. 1.7 (f)].

The reduced mirror symmetry in planar structures also enables in-plane directional scattering [169, 170] and the excitation of sharp trapped modes [171], which provides an elegant platform for strong light-matter interactions [172–174], and new functionality such as broadband slow light and ultra-sensitive spectroscopy can be realized [175, 176].

1.4 Active Tuning of Metamaterials

Although many exotic properties are still to be explored in passive metamaterial structures, for example the newly developed concept of meta-surfaces and photonic topological effects [177, 178], more and more studies are now focusing on functionalizing metamaterials and creating meta-devices [179]. This is driven by the fact that metamaterials offer extensive opportunities to manipulate light-matter interaction on the subwavelength scale, promising various ultra-compact and highly efficient meta-devices.

In particular, the ability to actively tune the responses of metamaterials is highly desirable. Since most metamaterials are resonant in nature, active tuning provides many advantages, such as overcoming the limit of narrow-band operation, creating various frequency-agile devices, enhancing the signal-to-noise ratio of detectors, and manipulating the phase and amplitude of wave actively on the subwavelength scale.

Various methods have been demonstrated to achieve tunability, including hybridizing functional (nonlinear, tunable or quantum) elements or media with passive metamaterials, modifying the configuration of meta-atoms or meta-molecules, and exploring the nonlinear effects within a metamaterial itself. Most of these methods can be characterized into two categories – tuning based on the local change of EM environment and structural change of metamaterials. The main part of the work presented in this thesis is closely related to this theme. An overall review of the representative works are summarized below.

1.4.1 Tuning based on Local Change of Electromagnetic Environment

A straightforward way to achieve tunability is to introduce a local change of electromagnetic environment. Many different methods have been proposed and demonstrated, such as tuning based on nonlinear effects, hybridizing passive metamaterial with tunable mediums, and carrier injection in semiconductors, etc.

1.4.1.1 Tuning with nonlinear self-actions

The local field within metamaterials can be orders of magnitude stronger than the incident field and it provide a promising platform for enhancing nonlinear effects – for example, in J. B. Pendry's seminal work on negative permeability, he already forecast the nonlinear enhancement via highly localized electric field within the gaps of split ring resonators [21].

Indeed, the first breakthrough in tunable metamaterials was made in *nonlinear metamaterials* [180, 181]. In 2003, the novel concept and various peculiar effects of nonlinear metamaterials were introduced by A. A. Zharov et al. [182], and M. Lapine et al. who proposed a practical route of electronic diode insertion to create nonlinear microwave metamaterials [183]. The hybridization of diodes with linear electric or magnetic meta-atoms gives rise to nonlinear electric or magnetic response, which was later demonstrated by I. V. Shadrivov et al. [Fig. 1.8 (a)] [184, 185] and D. A. Powell et al. [186, 187].

The basic mechanism is that the effective conductivity and capacitance of electronic diodes are strong nonlinear functions of the applied voltage [183, 186, 194]. Thus when the diode is connected to a meta-atom, the effective impedance of the coupled system becomes power-dependent, and the corresponding microscopic electric or magnetic response becomes nonlinear. When a high power signal is applied, the *resonant frequency* can be shifted due to the nonlinear capacitance, while the *resonance strength* can be tuned with a nonlinear conductivity. So far, a variety of nonlinear self-action effects, such as self-tuning [184, 185, 187] and bistability [195] have been demonstrated based on this concept. In fact, this concept is very general and can be applied to any type of nonlinear inclusion. For example, the hybridization with photosensitive diodes provides a novel route for metamaterials controlled by light [196–198], and an extension to quantum inclusions, such as quantum dots and Josephson junctions, can introduce metamaterials with tunable quantum effects [199–201].

While insertion of nonlinear elements is mostly employed in microwave metamaterials, hybridizing nonlinear host media with metamaterials is more suitable for high frequencies. The recent development in high-field THz sources enables the realization of nonlinear THz metamaterials via direct THz pulse pumping. Such nonlinear response arises from the nontrivial THz electric field-induced carrier dynamics that increases or decreases (depending on field strength) the conductivity of the doped and semi-insulating GaAs substrates [202]. For frequencies up to infrared and visible light, metallic nano-structures exhibit plasmonic field enhancement that might improve the nonlinear response of adjacent nonlinear layers. Successful demonstration was first made in optical fishnet metamaterials via plasmonic enhanced optical carrier injection in α-Si layers [Fig. 1.8 (b)] [188, 203]. A more compact approach is to enhance the nonlinear response in ultra-thin capping layers based on carbon nanotubes or graphene [Fig. 1.8 (c)] [173, 204]. Yet the most straightforward way is to explore the nonlinearity in nano-structured metal itself. Ultrafast nonlinear responses based on the nonlocality-enhanced interband transition in metallic nanorod metamaterials [41], and localized plasmon-enhanced two-photon absorption in planar metamaterials have been demonstrated [205].

When nonlinear elements are hybridized with chiral metamaterials, novel effects such as giant nonlinear optical activity that are seven orders of magnitude stronger than the one available in natural materials, and nonreciprocal directional transmis-

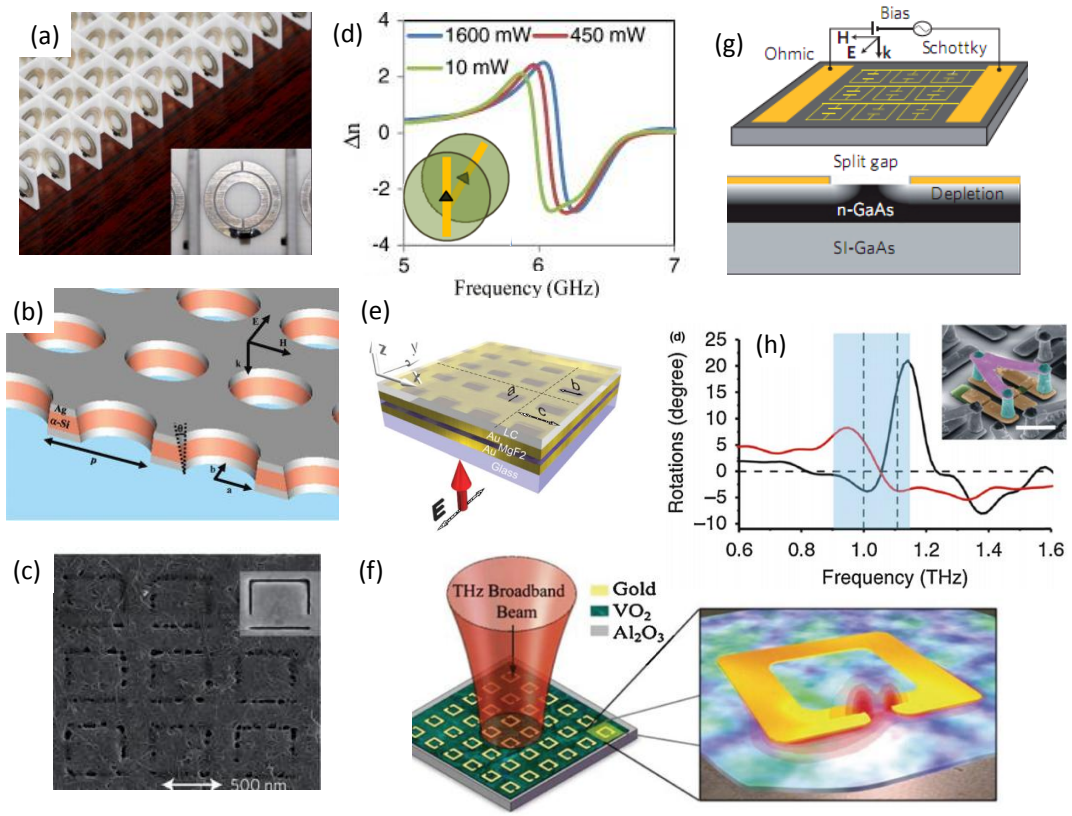

Figure 1.8: (a) A nonlinear microwave magnetic metamaterial with varactor diode insertions [185]. (b) A fishnet optical metamaterial supporting sub-picosecond response by exploiting the ultrafast carrier dynamics in the α-Si spacing layer [188]. (c) A plasmonic metamaterial coated with carbon nanotubes can show sub-picosecond nonlinear response via strong exciton–plasmon coupling at the near-infrared frequencies [173]. (d) Power-dependent optical activity in a nonlinear chiral metamaterial [189]. (e) A fishnet optical metamaterial infiltrated with nematic liquid crystals shows tunable response under electric or optical control [190]. (f) (Left) schematic of a THz metamaterial with SRRs fabricated on a VO_2 thin film grown on a sapphine substrate; (right) the electric field distribution during the phase transition, where the green islands indicate growing metallic puddles within an insulating host (blue) [191]. (g) Schematic of a THz metamaterial modulator fabricated on a doped GaAs substrate; voltage can be applied between an Ohmic contact and a Schottky gate to control the injection and depletion of carriers [192]. (h) The spectra of polarization rotation before (black) and after (red) photoexcitation in a THz chiral metamaterial (inset) show a switching of handedness [193].

sion have been demonstrated at microwave frequencies [189, 206] [Fig. 1.8 (d)]. Enhanced nonlinearity in a patterned metallic film has also been used to demonstrate strong nonlinear polarization rotation in planar optical metamaterials under oblique incidence ("extrinsic chirality") [207].

1.4.1.2 Tuning with external material change

Tunability can also be achieved by directly combining passive metamaterials with tunable materials, whose properties can be changed with external electric, magnetic, optical or thermal stimuli.

Liquid crystals can provide reasonably strong birefringence over a broad frequency band and have been widely applied to achieve tunable metamaterials from microwave to optical frequencies. A successful demonstration was first made at microwave frequencies with electric and magnetic tuning methods [208–211], and recently in THz with electric [212–214] and thermal tuning methods [215]. Although the early theoretical proposal was made based on optical metamaterials [216], it turns out to be far more complicated in practice due to the local inhomogeneous distribution and surface anchoring effect of liquid crystal molecules, significantly reducing the practical tuning performance. Successful tuning of double layered fishnet structures [Fig. 1.8 (e)] and split-ring resonators have been demonstrated recently via thermal [217], optical [190, 218] and electrical controls [190, 219, 220].

Integration with phase change materials is another approach. One important type of phase-change metamaterials is based on vanadium dioxide (VO_2) thin films that can show an insulator-to-metal transition when the temperature reaches percolation threshold around 342 K [191,221]. This mechanism allows the meta-atoms hybridized with the thin film to be short-circuited when the film becomes highly conductive, and the resonance is modified significantly [Fig. 1.8 (f)] [191, 222, 223]; moreover, memory effects were also demonstrated due to the temperature hysteresis of VO_2 [222, 224, 225]. Another successful solution is the combination of metallic frameworks and the temperature induced amorphous-crystalline phase transition in GST chalcogenide glass, which have been widely applied in optical data storage. Both electrical and optical methods have been used to achieve the different temperatures required for the melting and recrystallisation processes, and non-volatile switching was shown to be feasible for infrared metamaterials [226–228].

Direct integration of electrically tunable elements such as diode and more complex circuits with individual meta-atoms was widely used in RF and microwave metamaterials, enabling various types of tunable transmission line, smart antennas and filters [229, 230]. In higher frequency ranges, carrier injection or depletion in semiconductors proved to be a promising approach for achieving spatial tuning of meta-atoms. In 2006, H. Chen and et al. demonstrated the first electrically tunable THz metamaterials with doped GaAs substrate [Fig. 1.8 (g)] [192]. A similar concept can also be realized via photogenerated carrier injection [196, 231]. By tuning the concentration of carriers via electrical bias or illumination flux, the properties of GaAs can be changed between insulator and conductor, and the combination of active regime and meta-atoms can provide tunability in resonant depth or resonant frequency [232–234]. A distinct advantage of photoexcitation control is its possibility of ultrafast modulation (1∼10 ps) due to the short recombination time of carriers [188, 203, 235].

This concept can also be applied to chiral metamaterials, where reversible handedness and giant tunable optical activity were demonstrated [Fig. 1.8 (h)] [193, 236, 237]. A more straightforward and flexible all-optical approach demonstrated active control of THz optical activity via chiral patterned photoexcitation in a semiconductor with a spatial light modulator [238], which in principle allows arbitrary pattern generation.

Recently, a more compact approach based on gate-controlled carrier injection in single-layered graphene was demonstrated in THz and infrared metamaterials [239]; compared with semiconductor substrates, graphene provides lower insertion loss, moderate modulation range and even memory effect [240, 241]. M. Tamagnone et al. recently revealed with an equivalent scattering matrix model that the modulation

performance is ultimately limited by the conductivity of the 2D materials [242].

1.4.2 Tuning based on Structural Change

Structural change is another important class of mechanisms to realize tunability in metamaterials. This is based on the fact that the response of a metamaterial depends not only on the resonance of individual meta-atoms, but can also be modified significantly when the mutual interaction of meta-atoms is changed. Therefore, such change can be introduced by a direct geometry change of meta-atoms, or a relative position shift of meta-atoms that changes the mutual interaction [243, 244]. Compared with mechanisms based on local EM environment change shown above, structural tuning could be slower in speed, but has the advantages in other aspects, such as very "clean" modulation, i.e. no additional loss or local inhomogeneity introduced, large modulation contrast (can be close to 100%), and the ability to control the response of individual meta-atoms.

1.4.2.1 Tuning with MEMS and NEMS

One of the most successful paradigm of structural tuning is the combination of micro-electro-mechanical systems (MEMS) with metamaterials. The first MEMS metamaterial devices was realized at microwave frequencies via mounting an RF switch over the gap of a split-ring resonator to turn on/off the resonance [252]. This idea was soon extended to THz metamaterial, where deformation is achieved via thermal activation of the bimaterial cantilever within each unit cell [Fig. 1.9 (a)] [245], and the change of tilt angle alters the coupling between magnetic meta-atoms and the incident wave. More sophisticated designs were performed on comb-drive electrostatic actuators [Fig. 1.9 (b)], in which one part of coupled meta-atoms is fixed on an isolated anchor while the other part is on a moving frame driven by actuators [246, 253, 254]. By tuning the relative displacement of the two parts, the resonance changes significantly due to the change of mutual interaction. The idea of MEMS tuning was recently extended to chiral metamaterials [247], where the originally planar spiral pattern can be transformed into 3D chiral structure by electric actuation and thus allows the electromagnetic activity to be tuned [Fig. 1.9 (c)].

Although the early demonstration of MEMS metamaterials were mostly at microwave and THz frequencies, recent development in this area further pushed the operation frequency to mid/near-infrared. One example is to hybridize many infrared meta-atoms on a single unit of MEMS membrane [Fig. 1.9 (d)], which can be actuated under electrostatic force [248]. The back electrode of the MEMS unit simultaneously functions as the ground plane of infrared perfect absorbers. By tuning the distance between the membrane and the back electrode, the resonant frequencies and the absorption strength change [248]. More intriguing designs has been demonstrated recently by J. Ou et al., in which infrared meta-atoms are hybridized with parallel nano-beams that can be deformed under thermal [255] or electrical actuation [Fig. 1.9 (g)] [251]. The electrically tuned example possess megahertz bandwidth, paving the way towards fast tunable optical metamaterials based on nano-electro-mechanical systems (NEMS).

Apart from the active tuning shown above, structural deformation of microstructures also provides a novel route to change the local response of a metamaterial through a mechanical reaction to the environment. An elegant design of "smart

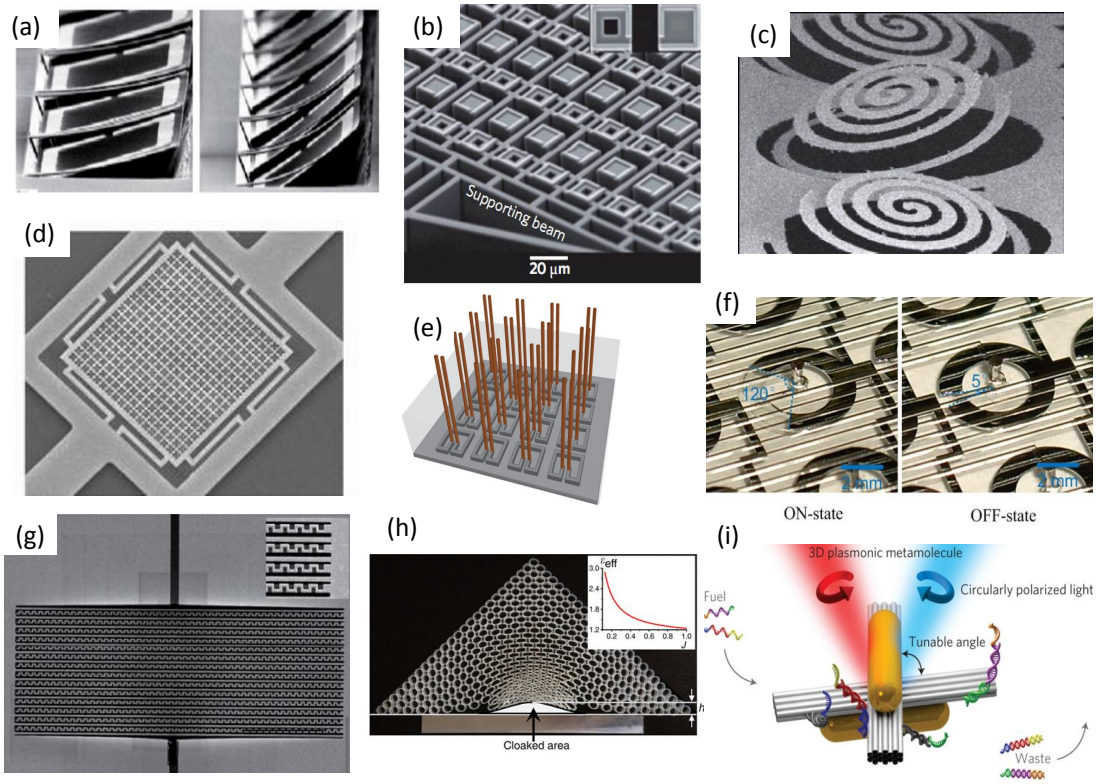

Figure 1.9: (a) An array of THz meta-atoms with tunable tilt angles based on thermal activation of bimaterial cantilevers [245]. (b) A tunable THz metamaterial manufactured on a comb-drive silicon MEMS platform [246]. (c) A chiral THz metamaterials shows tunable EM activity based on spirals with height controlled by electric actuation [247]. (d) A tunable infrared metamaterial perfect absorber achieved by hybridizing with a membrane that can be actuated under electrostatic force [248]. (e) Schematic of a microwave metamaterial with switchable properties based on liquid metal injection [249]. (f) A metamaterial controlled with a micro-channel pneumatic array and a ternary valve multiplexer. The air pressure from the pneumatic valve pushes mercury away from the cavity void forming tunable air gap size [250]. (g) A plasmonic metamaterials manufactured on dielectric silicon nitride nano-beams allows electrostatic modulation up to megahertz frequencies [251]. (h) Experimental sample of a self-adjustable smart metamaterial cloak. The inset is the effective permittivity curve versus Jacobian values. (i) Schematic of a reconfigurable plasmonic chiral molecules based on DNA origami template with two connected bundles, the relative angle between the gold nanorods can be actively controlled by two DNA locks from the sides of the DNA origami bundles [158].

elasto-electromagnetic metamaterials" was demonstrated recently [Fig. 1.9 (h)] [256, 257]. By properly designing the auxetic materials with an effective negative poison ratio, the gradient-index profile required for a quasi-conformal transformation can be achieved naturally from a boundary load. With this type of self-adjustable metamaterials, devices based on transformation optics can maintain their performance within a much larger range of deformation.

1.4.2.2 Tuning with fluids

Micro-fluidics provide an alternative approach for reconfigurable metamaterials. The basic idea is to control the injection of conductive liquids into the liquid channels so as to tune the shape of an individual meta-atom. The first demonstration was made at microwave frequencies [Fig. 1.9 (e)], where a significant spectral change was observed after liquid mercury was injected into split-ring shaped capillaries [249]. The decrease in channel size down to the micrometer scale and the use of eutectic gallium indium as conductive liquids can further push the operation frequency to THz [258, 259], but further scaling down would become very challenging due to the much stronger viscosity and surface tension. A more complex design of a matrix network of liquid metal meta-atoms, controlled with pneumatic micro-channel arrays and a ternary valve multiplexer was demonstrated recently [250]. In this design, *each individual meta-atom* can be randomly accessed and reshaped [Fig. 1.9 (f)], allowing arbitrary control of their scattering amplitude and phase, which is an important milestone of fully spatial controlled meta-devices.

Another related tuning mechanism is based on fluid-solid interactions, in which flexible metamaterials can deform in response to the change of fluidic environment. Although this interaction has not been reported for electromagnetic metamaterials, it has already be demonstrated with acoustic metamaterials, where the resonant frequency of an array of airfoil resonators was self-tuned in response to the change of the incident airflow [260]. We note that optomechanical interaction such as Brilloin scattering has already been studied in fluidic environment [261], the exploration of this interaction in electromagnetic metamaterials is expected to be promising.

1.4.2.3 Tuning with DNA origami

Recent advances in DNA origami technique allows preparation of various complicated structures via "programming" from the molecular level [262–264]. The combination of this powerful technique with plasmonics provides a bottom-up approach to create meta-molecules with designed fine geometries below the capability of top-down fabrication approaches [136, 265–268]. Recently, efforts have been made into creating plasmonic chiral meta-molecules, where the handedness of meta-molecules can be controlled by the sequence of DNA strands employed [136, 157, 269, 270].

The first attempt to dynamically tune the chiral response of plasmonic chiral meta-molecules is by functionalizing one end of the DNA origami bundles with biotin groups so that the helices can be attached ("standing up") to a BSA-biotin-neutravidin-coated substrate. The orientation of helices can be changed from "standing up" to "lying down" when the buffer liquid is dried, and the directional circular dichroism changes sign [271]. Recently, A. Kuzyk et al. demonstrated a more elegant approach by changing the twist angle of a pair of gold nanorods hosted on switchable DNA origami bundles [Fig. 1.9 (i)]. The two DNA bundles are connected in the middle and their relative twist angle can be controlled by two DNA locks extended from the sides of the origami. By mixing specifically designed DNA strands into the solution, the plasmonic molecules can be driven to desired states via toehold-mediated strand displacement reactions [158].

1.5 Exploiting Electromagnetic Force with Artificial Structures

So far, the studies introduced above can be interpreted as manipulating the energy, momentum and angular momentum of EM waves with metamaterials, as well as various methods to change the response of metamaterials and achieve active tuning via external stimuli.

We recall that when EM waves interact with a material, this process is usually accompanied with the interchange of linear or angular momentum, and thus the material experiences EM forces or EM torque. This principle has been employed to create various tools and devices. In optics, well-known examples include optical tweezers that employ gradient optical forces to trap tiny objects in a stable position [272, 273], optical wrenches that can apply and directly measure torque on microscopic birefringent particles using spin momentum transfer [274, 275], and optical motors that can transfer the angular momentum of light into continuous mechanical rotation to drive machines or liquids in micrometer scales [276, 277].

In the field of metamaterials, much effort has been made into using metamaterials to control EM waves, while the accompanying effects – the EM forces and torques acting on metamaterials, as well as the nonlinear properties due to optomechanical coupling are still largely unexplored until recently.

To increase our understanding and provide useful insight of this largely unexplored area, this section will summarize some previous related works on EM forces and optomechanics. Particularly, it will focus on the nontrivial EM force and torque in metamaterials, the giant nearfield EM force enhancement and its application in trapping and conveying subwavelength particles, and finally a very brief review of the nonlinear effects due to optomechanical coupling.

1.5.1 Nontrivial Electromagnetic Force and Torque of Metamaterials

Intuitively, a particle in a homogeneous environment should always be "pushed" away by the incident wave due to the exchange of momentum [278]. However, the scattering force experienced by a particle could become counter-intuitive in the presence of metamaterials. Indeed, the quest for a nontrivial EM force can date back to the seminal paper by V. Veselago on negative index materials [22]. It has been pointed out that the scattering force inside a negative index metamaterial could become attractive (opposite to the launching direction of wave) due to the reversed direction of wave momentum [see Fig. 1.10 (a)] [279–282], but controversy still remains due to the disagreement on the definition of momentum and force density [283, 284].

Recent studies of the optical pulling force achieved in different scenarios further deepen our understanding of the complex relation between the direction of the EM force and the properties of the electromagnetic field, the environment as well as the particles themselves [285]. For example, it is recently shown that magnetoelectric particles with multiple scattering channels (i.e. supporting multiple resonances) can experience an optical pulling force in a Bessel beam due to the enhanced directional forward scattering [286]. On the contrary, if a particle is covered with an invisibility cloak, the total scattering force will be significantly reduced and should be exactly zero with a perfect cloak, but the internal stress becomes higher due to the squeezed electromagnetic space [287, 288].

The interaction between spin angular momentum and linear momentum in particles with strong chiral effect provides an alternative route to realizing a chirality-

dependent optical pulling force [289]; a transverse force with direction perpendicular to the incident wave exists in the present of a substrate [290]. Apart from EM force, the scattering EM torque experienced by chiral meta-molecules could also be nontrivial. By employing the resonant-enhanced light-matter interaction and the scattering of linear polarization into higher orders of *orbital* angular momentum modes, M. Liu et al. demonstrated a light-driven nano-motor based on planar plasmonic chiral structure, with rotary power two orders of magnitude stronger than its dielectric counterpart [291].

Another novel EM force effect available with metamaterials is levitation. Y. Urzhumov et al. proposed that macroscopic objects with negative permeability ($\mu < 0$) metamaterials may experience resonant-enhanced magnetic levitation in a low frequency magnetic field [292]. On the other hand, it is well know that perfect diamagnetism ($\mu = 0$) can achieve levitation of magnets via field repulsion; an analogous concept was introduced recently by using ϵ-near-zero metamaterial substrates [see Fig. 1.10 (b)]; this approach is more robust to losses and material dispersion compared to the approach based on $\epsilon < 0$ substrates, and thus it allows the levitation of electric sources over a broader bandwidth [293]. Unlike levitation based on the Casimir effect [294, 295], the approaches based on EM force require sources and the effects can be actively switched on and off.

1.5.2 Giant Electromagnetic Force in the Near Field

We recall that metamaterials are composed of resonating elements; in fact, the strongest EM force is produced in the near-field regime, where gradient forces dominate. The EM force between plasmonic cut-wire pairs in a metamaterial was studied by R. Zhao et al. [297], it was found that for isolated cut-wire pairs, the anti-symmetric mode (magnetic dipole) generally leads to mutual attraction while the symmetric mode (electric dipole) gives mutual repulsion. However, in a periodic array, the attractive force can turn into a repulsive one as the distance between neighbouring unit cells becomes smaller. This is mainly due to the change of relative strength of Coulomb force (contributed by charges) and Laplace force (contributed by currents) [see Fig. 1.10 (d)]. Similar negative pressure was also reported by H. Liu et al. in a nano-cavity composed of two gold patches, where such an attractive force can be attributed to the internal inductance and the kinetic energy of conduction electrons [300]. Interestingly, when the plasmonic gold is replaced by perfect electric conductors (PEC), the negative pressure changes to positive [300, 301]; but if the surface of the PEC patches is roughened or corrugated, negative pressure exists again due to the enlarged contribution of the Coulomb force [301]. The strong mutual attraction also exists in a dielectric metamaterial supporting a subradiant trapped mode, and the EM force between meta-atoms can be even larger than its plasmonic counterpart due to the higher Q-factor of the resonance [302].

On the macroscopic level, such near-field EM force enhancement also exists. J. Zhang et al. predicted a light-controlled attraction effect between a layer of metamaterial and a substrate [303]. Y. He et al. demonstrated that the nanoscale optical field enhancement and localization in slot waveguides of hyperbolic metamaterials can give rise to giant transverse optical forces, more than two orders of magnitude stronger than the force created in conventional silicon slot waveguides [304]. Interestingly, V. Ginis et al. introduced the idea of transformation optics for optical forces and showed that a thin layer of double-negative or single-negative metamaterial can

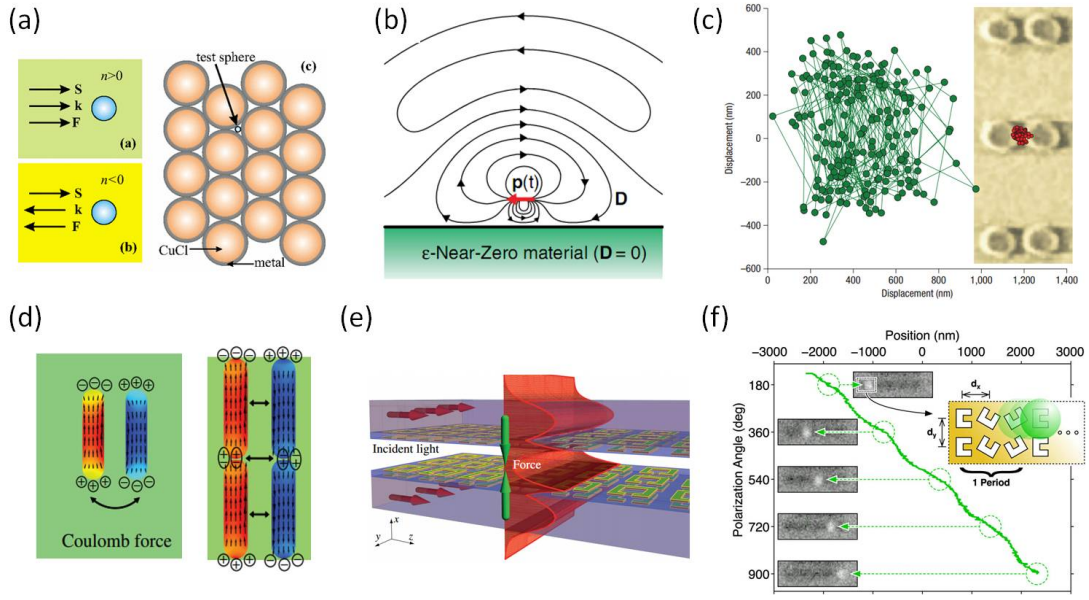

Figure 1.10: (a) Schematic of backward wave and negative force in a negative index metamaterial composed of metal-coated CuCl nanoparticles [280]. (b) Levitation of an electric source near an ϵ-near-zero metamaterial substrate [293]. (c) Gap mode formed by two adjacent gold nano-discs can assist conventional optical tweezers to reduce the spatial confinement of 200 nm polystyrene beads down to subwavelength dimensions [296]. (d) EM force between coupled plasmonic nano-rod pairs that support antisymmetric mode. When the separation of neighbouring pairs is large (left), Coulomb force dominates and leads to mutual attraction; when the separation becomes smaller (right), Laplace force dominates and results in mutual repulsion [297]. (e) EM force enhancement between two dielectric waveguides with thin layers of single-negative metamaterials [298]. (f) Nano-optical conveyor belts consists of resonant C-shaped engravings. By rotating the polarization, subwavelength particles can be conveyed over a long distance [299].

shrink the interwaveguide distance perceived by light, resulting in a more than tenfold enhancement [298] [see Fig. 1.10 (e)].

1.5.3 Trapping and Conveying with Subwavelength Precision

Optical trapping is an important technique widely applied in different fields from bio-science to atomic physics [272, 305]. The traditional trapping method based on propagating beams is very powerful in manipulating specimens of micrometer-size, but faces fundamental limitations when dealing with nanometre-sized specimens due to the diffraction limit [306, 307]. To achieve stable trapping of nanometer scale objects, the field gradient and field strength need to be much stronger than that for micrometer-sized specimens, since the trapping force acting on the specimens follows an R^3 law (R is the nominal radius of the specimen) [306].

The strong localized field in specifically designed nano-structures can offer a novel route for trapping with subwavelength precision. Early studies demonstrated trapping of μm-sized dielectric beads with arrays of plasmonic discs [308], but a further down-scaling has been shown to be difficult for stable trapping due to the limited intensity and symmetry in the optical near field, as well as heating from strong ohmic loss [309]. Recently, K. Wang et al. solved the problem and demonstrated trapping

and rotation of dielectric nanoparticles as small as 110 nm using a template-stripped plasmonic nanopillar incorporating a heat sink, which significantly reduced the local heat generation [310].

A much higher trapping ability requires more deliberate design of the near field profile. The first successful demonstration of sub-wavelength trapping was made by Grigorenko et al. [296] by employing the well-known plasmonic dimer structure that can support a strong electric field enhancement in the gap [see Fig. 1.10 (c)]. Later, parallel trapping [311] and *in vivo* detection of trapped 10 nm-scale specimens were demonstrated by exploiting the ultra-high environmental sensitivity of the gap plasmonic mode [312]. Another design is based on plasmonic nano-apertures that allows trapping of particles below 50 nm size [313–315]. It turns out that by properly engineering the plasmonic mode such that the local intensity within the apertures is maximized when the object is present, self-induced back-action could be achieved, greatly enhancing the trapping ability [316].

Recent advances in metasurfaces provide new ingredients for manipulating sub-wavelength particles over long distances. P. Hansen et al. recently proposed the idea of nano-optical conveyor belts, and it was demonstrated by Y. Zheng et al. [see Fig. 1.10 (f)] [299, 317]. This design consists of a spatial distribution of three distinct plasmonic traps based on C-shaped structures, with each element separately addressable by its resonant wavelength or polarization; by varying the wavelength or polarization continuously, a transport of subwavelength polystyrene spheres over 4.5 μm distance was successfully demonstrated [299].

1.5.4 Active Tuning with Intrinsic Electromagnetic Forces

As has been discussed in Section. 1.4, structural deformation has its unique advantages in tuning the performance of metamaterials; it is natural to ask whether the strong near-field enhancement of the EM force mentioned above can also be employed directly to achieve active deformational tuning of metamaterials.

In fact, the idea of using resonant EM force to control the EM response of a system dates back to the early attempts of laser interferometric detection of gravitational waves with Fabry-Perot cavities, where a suspended end-mirror that supports harmonic oscillation is employed for acoustic isolation [325] [see schematic in Fig. 1.11 (a)]. Such systems turned out to be the fountain of various novel optomechanical effects discovered later. The most simple situation is *static* optomechanical coupling, where the EM resonance has a much shorter life time than the mechanical oscillation period; in such cases, the EM force can be considered as instantaneous and displacement-dependent [319]. The mechanical potential of the system changes with input power due to the contribution of the conservative EM force, and the induced bistability have been demonstrated in both optical cavities [326, 327] and microwave cavities [328].

More intriguing effects arise when the EM resonance and mechanical deformation are *dynamically* coupled [see Fig. 1.11 (b)]; in such cases, the life time of the EM resonance needs to be comparable to or longer than the mechanical oscillation period such that the EM field and mechanical oscillation have sufficient time for interaction [319]. In the weak coupling regime, where the coupling coefficient is smaller than the linewidth of EM resonance and mechanical resonance, the EM resonant force mainly changes the effective damping and stiffness of mechanical oscillation, giving rise to novel phenomena such as optical spring effects (changed effective me-

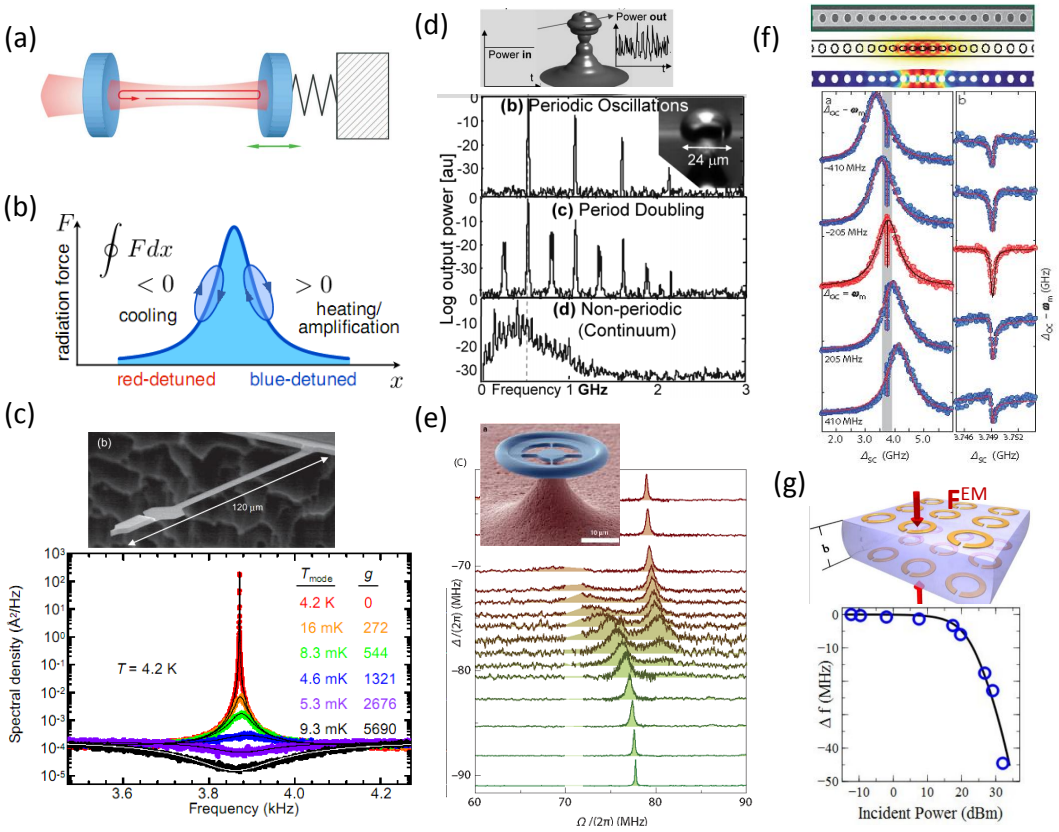

Figure 1.11: (a) Schematic of optomechanical coupling in a cavity with a movable mirror [318]. (b) Schematic diagram depicting the work done by the retarded radiation force during one oscillation cycle, the sign of the work depends on the detuning of the pump [319]. (c) Spectral density of mechanical oscillation shows optomechanical active feedback cooling of a cantilever as it is cooled from a base temperature 4.2 K. Feedback gain g is related to the intensity of incident light [320]. (d) Transition from periodic self-oscillations towards chaotic motion in a microcavity with continuous pumping [321]. (e) Experimental observation of the coherent coupling between the mechanical oscillation and optical mode in a micro-toroidal optical cavity [322] . (f) Optomechanically induced transparency in an optomechanical crystal nanocavity where optical and mechanical modes are co-localized [323]. (g) A schematic of magnetoelastic metamaterials, where the elastic substrate can be deformed by the EM force between meta-atoms, leading to nonlinear self-tuning [324]

chanical stiffness of the cavity) [329,330], self-cooling (enlarged effective mechanical damping) [see Fig. 1.11 (c)] [331–335] and self-oscillation (negative effective mechanical damping, i.e. mechanical "lasing"; see Fig. 1.11 (d)) [321,336–338]; meanwhile, the mechanical oscillation modulates the EM signal and the generated sidebands (Stokes and anti-Stokes signals) can be resolved if the EM resonance linewidth is much smaller than the mechanical oscillation frequency [339–342].

In the strong coupling regime, where the coupling coefficient is much larger than the linewidth of EM resonance and mechanical resonance, EM resonance and mechanical resonance are hybridized to form two new modes [319, 339], leading to normal mode splitting [see Fig. 1.11 (e)] [322, 342–344], optomechanically induced transparency [see Fig. 1.11 (f)] [323,345,346], absorption and amplification of probe signals, etc. This strong coupling regime is particularly interesting for studying quan-

tum optomechanical effects [319, 347, 348], since quantum states can be transferred between the EM field and the mechanical oscillator, allowing the mechanical oscillator state to be controlled using a wide range of available quantum optical techniques, and novel quantum entanglement effects (such as "Schrödinger cat") to be observed in macroscopic systems.

While previous studies of optomechanical effects are mostly performed in optically large systems, it is still an open question how the effects would change when the interaction happens in subwavelength scale systems, such as metamaterials. The first prototype of this idea was called magnetoelastic metamaterials proposed by M. Lapine et al. in 2012 [Fig. 1.11 (g)]. In this design, meta-atoms are embedded in an elastic medium; when the structure is illuminated with a frequency close to the resonance, the EM force between meta-atoms can compress the elastic substrate such that the meta-atoms reach a new stable equilibrium when the EM force and the elastic feedback from the substrate are balanced. Due to the resonant nature of the EM force, the feedback mechanism leads to nonlinear self-actions, and the self-tuning effect was demonstrated experimentally [324].

The idea of magnetoelastic metamaterials is quite general and was later extended to other designs, where strong self-tuning was observed in helical metamaterials [349, 350]. Due to the scalability of the principle, it is expected that similar effects could also be attained in optical metamaterials hybridized with optomechanical designs that are more favourable to nano-fabrication, such as nano-beam arrays [351]. Recent experimental progress already demonstrated a small transmission modulation effect due to the optical force in a reconfigurable metamaterial consisting of gold plasmonic resonators supported by free-standing silicon nitride bridges [352]. Compared to the approach based on MEMS or NEMS, using EM force for active tuning is also applicable to all-dielectric metamaterial structures and could provide much richer nonlinear effects in additional to simple modulation.

1.6 Motivation and Thesis Outline

More and more studies of metamaterials now focus on finding potential applications. On one hand, several important issues need to be addressed in order to promote the wide application of metamaterials, such as high loss, narrow bandwidth, and strong spatial dispersion; on the other hand, many novel physical phenomena, new functions and applications of metamaterials are still to be explored, especially when they are hybridized with other functional elements and become devices, or when multiphysics couplings – the interaction between electromagnetic waves and other types of physical effects, such as mechanical (acoustic), thermal, electric, magnetic and fluidic effects, etc., come into play and lead to qualitatively different phenomena.

This PhD thesis explores new properties of chiral metamaterials. Although much effort has been made on using chiral metamaterials to control the polarization of EM waves, the EM force, torque and the nonlinear optomechanical properties in such type of systems are still largely unexplored. The study of these unknown effects is of interest from both fundamental and practical points of view. In order to study these properties more efficiently, we develop a semi-analytical model based on the free-space Green's function under eigenmode approximation. This method allows us

to efficiently and accurately determine the electric and magnetic interaction energy, the EM near-field and far-field responses, as well as the EM force and torque acting on each meta-atom in the coupled system. The studies presented in this thesis cover several closely related topics, highlighting the optomechanical properties and the nonlinear effects that arise from EM-elastic coupling in chiral metamaterials. This thesis gives answers to the following problems:

(1) How can we accurately model chiral meta-molecules in the full-wave regime?

Chiral meta-molecules exhibit giant optical activity near the resonances. Accurate modeling of these complicated structures generally relies on full-wave calculations, which is accurate but lack physical insight. In Chapter 2, we employ the near-field interaction model to study the near-field coupling, far-field scattering and optical activity of chiral meta-molecules based on twisted coupled cut-wire pairs. Excellent agreement is found between our semi-analytical model and full wave simulation. We explicitly show the relation between spatial dispersion, resonant enhancement and strong chiral optical effects. It is found that the optimum twist angle, defined by the strongest polarization rotation, varies with frequency, and near resonance is substantially lower than 45 degrees, which is "counter-intuitive" from simple geometry considerations; the underlying reasons of such variation are discussed in details.

(2) Is it possible to use a chiral meta-molecule as an efficient subwavelength optical motor?

The scattering properties of chiral meta-molecules have been extensively studied, and it is well known that chiral meta-molecules can show giant optical activity near their resonances. From the view point of angular momentum conservation, chiral meta-molecules themselves should also experience strong scattering torque, indicating that chiral meta-molecules might find new application in nano-fluidics and nano-robotics as nano light-driven actuators. In Chapter 3, we study the optomechanical properties of chiral meta-molecules based on a pair of twisted split-ring resonators. The condition for achieving continuous rotation, and the roles played by chirality and anisotropy are revealed with a simple analytical model. Moreover, this coupled structure can provide a strong and tunable torque, and can support different optomechanical dynamics under different frequencies of incident waves. By comparing with the full wave calculation, we confirm that this structure can be used as a general prototype of subwavelength light-driven actuators over a wide range of frequencies.

(3) Is there anyway to extend the concept of magnetoelastic metamaterials to chiral meta-molecules and achieve strong nonlinear self-action?

As has been introduced in Sec. 1.5.4, nonlinear self-action using EM force has been demonstrated in many optically large systems, and this idea was recently introduced in subwavelength systems – magnetoelastic metamaterials. However, the original design based on collinear force balancing shows a limited self-tuning effect, mainly due to the limited power density available in practical applications. To enlarge the optomechanical effect, we introduce a different degree of freedom in Chapter 4 – the internal torsional rotation driven by the EM torque within structural elements. We introduce a prototype called torsional chiral meta-molecules based on coupled pairs

of twisted split-ring resonators connected with elastic thin wires. The new design has much higher sensitivity to EM power, and the elastic and EM properties can be independently designed to optimize the response. A rich range of nonlinear phenomena including self-tuning and bistability are predicted with the near-field interaction model, and are demonstrated experimentally at the microwave frequencies, showing that torsional chiral meta-molecules provide an ideal platform for studying various slow nonlinear effects.

(4) Torsional chiral meta-molecules can show giant stationary nonlinear response, how about the dynamical nonlinear response?

Previous studies in cavity-optomechanics already showed that the coupling between mechanical oscillation and retarded EM force from high Q modes can lead to a rich range of dynamic nonlinear effects, such as self-oscillations and chaos. Yet, in most metamaterial systems, the Q factors for EM resonances are usually less than 100, mainly due to their strong scattering loss. This means that the retardation of EM force and torque becomes negligibly small, and the effect can be considered as instantaneous and displacement-dependent. In such cases, torsional meta-molecules with only one degree of mechanical freedom can show only damped oscillation due to the conservative nature of the EM torque involved. In Chapter 5, we introduce a simple structure to achieve nonlinear self-oscillations. The structure extends the torsional double split-rings presented in Chapter 4 by connecting an additional split-ring resonator. The additional degree of freedom introduced allows the system to accumulate EM energy to compensate the damping loss and to achieve self-oscillations. Contrary to many previously studied optomechanical systems, self-oscillations of torsional meta-molecules can be extremely robust against mechanical damping. The chiral nature of the oscillating structure leads to dynamic nonlinear optical activity, which can be actively controlled by a range of parameters such as the field strength and polarization of the incident wave. Note that the optical activity effects in natural chiral molecules and previously studied chiral metamaterials are static and dominated by the linear response, thus this is an effect hardly found in previously studied system.

(5) How does the intermolecular interaction influence the nonlinear behaviour in ensembles of chiral torsional meta-molecules?

Studies of torsional meta-molecules in Chapter 4 and Chapter 5 concentrate on the nonlinear behaviour of single meta-molecules. In practice, these nonlinear meta-molecules can be assembled to control the behaviour of EM waves at the macroscopic level, and the intermolecular EM interaction could bring in qualitatively new effects. In Chapter 6, we study a nonlinear system composed of two or more coupled enantiomeric torsional meta-molecules, i.e. torsional chiral meta-molecules with opposite handedness. It is found that intermolecular EM coupling can change the system stability and lead to spontaneous chiral symmetry breaking. Importantly, such chiral symmetry breaking can be found in both the dynamic and stationary responses of the system, and the effects are successfully demonstrated in a microwave pump-probe experiment. Such symmetry breaking can lead to a giant nonlinear polarization change, energy localization and mode splitting, which provides a new possibility for creating an *artificial phase transition* in metamaterials, analogous to that in ferrimagnetic

domains.

Optical Activity and Coupling in Chiral Meta-molecules

2.1 Introduction

Subwavelength metallic structures can exhibit exotic electromagnetic properties at resonance. These resonant elements are widely studied as functional devices [353, 354] or as the building blocks of metamaterials – meta-atoms [12, 355]. When the separation between meta-atoms is much smaller than the operation wavelength, such interaction is in the near-field regime and is thus called *near-field interaction*. This is usually the case when two or more meta-atoms are closely packed and function as a meta-molecule. When two or more elements are assembled to form a hybrid structure, its resonant frequencies and far-field scattering properties can be tuned externally by modifying the spatial arrangement of elements. Recently, such hybrid structures have been extensively studied, including coupled wires [356], coupled split-ring resonators (SRRs) [150, 357], plasmonic oligomers [358], etc. Many interesting spectral features arise in these strongly coupled systems, including mode splitting, Fano lineshapes [359, 360], crossing or avoided crossing [361] and strong polarization rotation [151, 362]. Since the spectral features of these hybrid structures are strongly affected by the inter-particle separation, a deliberate study of the spatial dependence of the inter-particle interaction can provide useful insight for optimizing the device performance.

Twisted dimers are a particularly interesting class of coupled metamaterials, since their reduced symmetry makes them chiral, causing them to rotate the plane of polarisation of an incident wave. Examples include gammadions [362, 364], crosses [140, 151, 365] and SRRs [149, 150, 152, 366] [see Fig. 2.1]. The simplest of such structures is a pair of wires, which have been analytically studied in the low frequency limit [363], but the strongest optical activity occurs around the resonance, which is not within this limit. Such structures are also suitable for adding nonlinear inclusions, leading to strong nonlinear optical activity [189].

In this Chapter, we study the optical activity of a twisted cut-wire dimer, showing that the resonant lineshapes can be easily predicted semi-analytically. This enables accurate modeling of the far-field scattering, clearly showing the polarization rotation in all regimes, including at resonance where the effect is the strongest. The semi-analytical model is based on the free-space Green's function under the eigenmode approximation (see Appendix A for details), using coefficients derived from the numerically obtained charge and current distributions [244], and a multipole expansion of far-field radiation. In contrast to point-dipole based models [106], our approach is applicable to the close spacing typically used in twisted dimers. We explicitly show

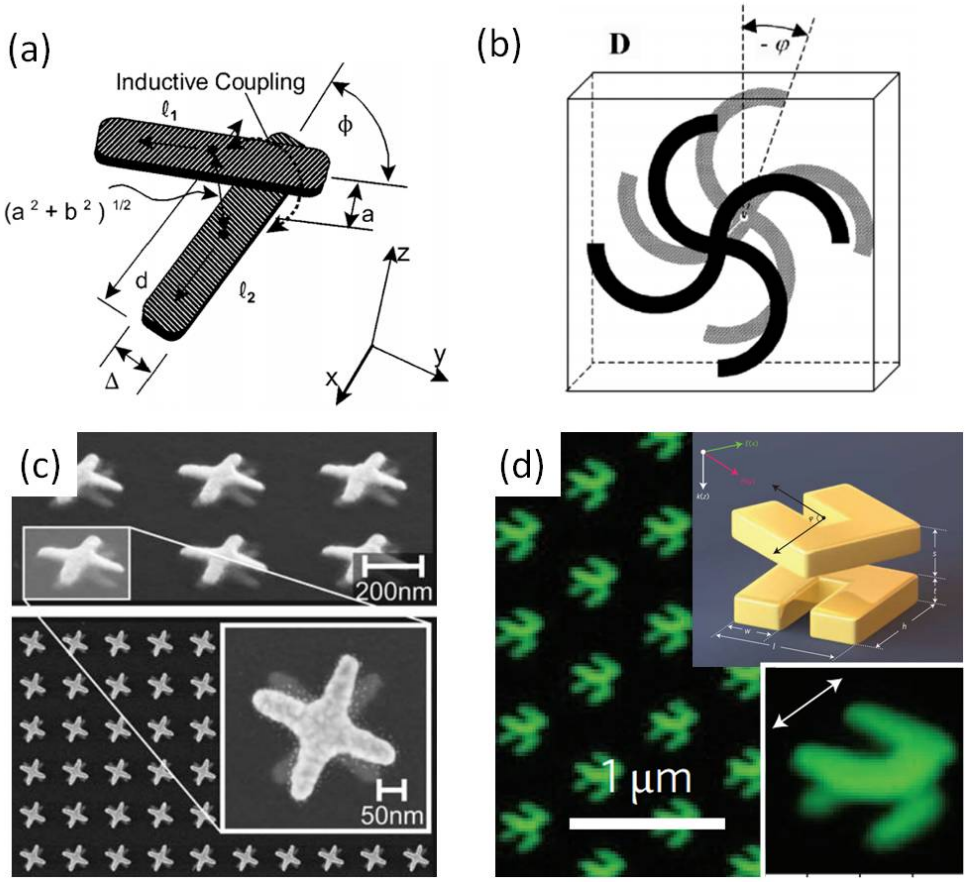

Figure 2.1: Chiral meta-molecules based on twisted coupled meta-atoms. (a) Twisted cut-wire pairs [363], (b) twisted gammadions [362], (c) twisted crosses [148], and (d) twisted split-ring pairs [150].

the relation between spatial dispersion, resonant enhancement and strong chiral effect. It is found that the optimum twist angle, defined by the strongest polarization rotation, varies with frequency, and near resonance is substantially lower than 45 degrees, which is "counter-intuitive" from simple geometry considerations; the underlying reasons of such variation are discussed in detail.

2.2 Chiral Meta-molecules based on Twisted Cut-wire Pairs

The twisted cut-wire pair being studied is illustrated in Fig. 2.2. The first cut-wire (denoted as "1") is located in the plane $z = -s/2$, oriented along the y direction, and the second cut-wire (denoted as "2") is in the plane $z = s/2$, rotated about the z axis by an angle θ. To model the coupling effect, we develop a semi-analytical model based on the free-space Green's function (see details in Appendix A). Under the eigenmode approximation, the frequency dependence of the spatial mode profile of a meta-atom can be considered as negligible around the frequency of the eigenmode (see Sec. A.1.2); in this case, we can numerically find the charge $\rho(\omega, \mathbf{r})$ and current distribution $\mathbf{J}(\omega, \mathbf{r})$ for a *single* cut-wire, and separate them into a frequency-

dependent mode amplitude $Q(\omega)$ and spatially-dependent charge density $\mathrm{q}(\mathbf{r})$ and current density $\mathbf{j}(\mathbf{r})$, i.e.

$$\begin{aligned} \rho(\omega,\mathbf{r}) &= Q(\omega)\mathrm{q}(\mathbf{r}), && (2.1)\\ \mathbf{J}(\omega,\mathbf{r}) &= -\mathrm{i}\omega Q(\omega)\mathbf{j}(\mathbf{r}), && (2.2)\\ \mathrm{q}(\mathbf{r}) &= -\nabla\cdot\mathbf{j}(\mathbf{r}). && (2.3) \end{aligned}$$

The normalized mode profile $\mathrm{q}(\mathbf{r})$ and $\mathbf{j}(\mathbf{r})$ can be used to calculate the effective impedance of the coupled system (see Sec. A.1.2), which allows us to determine the mode amplitude $Q_m(\omega)$ of each meta-atom in the coupled system. The lowest order eigenmode of a metallic cut-wire is electric dipole, which has a sinusoidal-like current distribution.

For the dimer system studied here, the sets of coupled equations can be written explicitly as

$$\begin{aligned} -\mathrm{i}\omega(Z_\mathrm{s}Q_1 + Z_\mathrm{m}Q_2) &= \mathcal{E}_1 && (2.4)\\ -\mathrm{i}\omega(Z_\mathrm{m}Q_1 + Z_\mathrm{s}Q_2) &= \mathcal{E}_2. && (2.5) \end{aligned}$$

$\mathcal{E}_m$ is the electromotive force acting on meta-atom m, determined by the overlap of the incident wave and the spatial mode profile [see Eq. (A.10)]; $Z_\mathrm{s} = Z_{1,1} = Z_{2,2}$, $Z_\mathrm{m} = Z_{1,2} = Z_{2,1}$ are the effective self impedance and mutual impedance, respectively. The impedance between meta-atom m and n has the following form:

$$Z_{m,n} = \mathrm{i}\omega L_{m,n} + \frac{1}{\mathrm{i}\omega}\left(\frac{1}{C_{m,n}} + \delta_{m,n}P_m - \mathrm{i}\delta_{m,n}R_m\right), \tag{2.6}$$

$\delta_{m,n}$ is the delta function. $L_{m,n}$ and $1/C_{m,n}$ are the effective inductance and elastance (inverse of capacitance), respectively, and they are directly related to the magnetic and electric interaction energy between meta-atoms m and n ($m = n$ corresponds to self interaction). $P_{m,m}$ and $R_{m,m}$ are the "local" terms related to the power stored and dissipated by the meta-atom, respectively. All the parameters above can be calculated from the normalized current $\mathbf{j}$ and charge q. Therefore, the coefficients are physically meaningful and no fitted parameters are required (for more details, see Sec. A.1.1 and Sec. A.1.2). The mode amplitude $Q_m(\omega)$ on each meta-atom can be found directly by solving the coupled equations.

To simplify the discussion, we assume the cut-wires are made from perfect electric conductors such that only scattering loss is taken into account; in this case, $P_{m,m}$ and $R_{m,m}$ vanish. We write the mode amplitudes in analytical forms

$$\begin{aligned} Q_1 &= \frac{Z_\mathrm{s}\mathcal{E}_1 - Z_\mathrm{m}\mathcal{E}_2}{-\mathrm{i}\omega(Z_\mathrm{s}^2 - Z_\mathrm{m}^2)}\\ &= \frac{\omega^2(\mathcal{E}_1 - \kappa_\mathrm{M}\mathcal{E}_2) - \omega_0^2(\mathcal{E}_1 - \kappa_\mathrm{E}\mathcal{E}_2)}{[\omega^2(1+\kappa_\mathrm{M}) - \omega_0^2(1+\kappa_\mathrm{E})][\omega^2(1-\kappa_\mathrm{M}) - \omega_0^2(1-\kappa_\mathrm{E})]}, && (2.7)\\ Q_2 &= \frac{Z_\mathrm{s}\mathcal{E}_2 - Z_\mathrm{m}\mathcal{E}_1}{-\mathrm{i}\omega(Z_\mathrm{s}^2 - Z_\mathrm{m}^2)}\\ &= \frac{\omega^2(\mathcal{E}_2 - \kappa_\mathrm{M}\mathcal{E}_1) - \omega_0^2(\mathcal{E}_2 - \kappa_\mathrm{E}\mathcal{E}_1)}{[\omega^2(1+\kappa_\mathrm{M}) - \omega_0^2(1+\kappa_\mathrm{E})][\omega^2(1-\kappa_\mathrm{M}) - \omega_0^2(1-\kappa_\mathrm{E})]}, && (2.8) \end{aligned}$$

where $\omega_0^2 = 1/(L_\mathrm{s}C_\mathrm{s})$ is the resonant frequency of a single cut-wire; $\kappa_\mathrm{E} = C_\mathrm{s}/C_\mathrm{m}$, $\kappa_\mathrm{M} =$

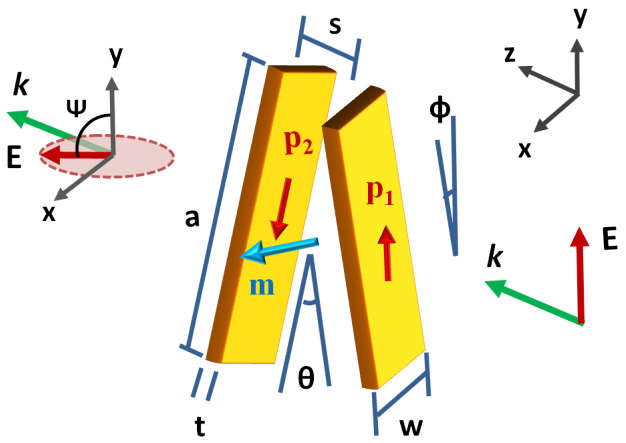

Figure 2.2: Schematic layout of the twisted cut-wire pair. The two cut-wires locate in the planes $z = -s/2$ and $z = s/2$, respectively, with a twist angle θ between them. We set their central points lying on the z axis. The impinging wave propagates in the z direction and polarized in y direction. Φ is the angle between cut-wire 1 and y axis.

L_m/L_s are the electric and magnetic mutual interaction coefficients, respectively. It is clear that two new hybrid resonances exist due to mutual coupling, whose frequencies are determined by the zero points of the denominator of Q, i.e.

$$\omega_1 = \omega_0\sqrt{(1+\kappa_E)/(1+\kappa_M)}, \tag{2.9}$$

$$\omega_2 = \omega_0\sqrt{(1-\kappa_E)/(1-\kappa_M)}. \tag{2.10}$$

ω_1, ω_2 correspond to the frequencies for symmetric ($Q_1(\omega_1) = Q_2(\omega_1)$) and antisymmetric ($Q_1(\omega_2) = -Q_2(\omega_2)$) modes, respectively. Note that the radiative damping is automatically included in the calculation of L and $1/C$ via the retardation term $\exp(\mathrm{i}k|\mathbf{r}-\mathbf{r}'|)$ in the Green's function [see Eq. (A.8) and Eq. (A.9) in Appendix A], thus the coupled modes have finite linewidths and overlap. Since the denominator achieves a nonzero minimum at resonance, it is generally difficult to excite pure symmetric or anti-symmetric modes unless the two cut-wires are excited intentionally with in-phase ($\mathcal{E}_1 = \mathcal{E}_2$) or out-of-phase ($\mathcal{E}_1 = -\mathcal{E}_2$) sources. For any source with different excitation on the cut-wires ($\mathcal{E}_1 \neq \pm\mathcal{E}_2$), both symmetric and anti-symmetric modes can be excited. Specifically, for the plane wave excitation used here,

$$\mathcal{E}_m = -\int \mathbf{j}_m \cdot \mathbf{E}^{\mathrm{i}}(\mathbf{r}_m)\mathrm{d}\mathbf{r}^3 = -\mathbf{l}_m \cdot \mathbf{E}^{\mathrm{i}}_m, \tag{2.11}$$

where $\mathbf{l}_m$ is the normalized dipole moment.

Having determined the mode amplitudes Q_1 and Q_2, we use them to investigate the scattering properties. Undoubtedly, a rigorous calculation of the vector potential by making a volume integral of the current density can give us the field information from near-field to far-field region. But in the far-field zone, a multipole expansion of the chiral meta-molecule can already give us a good approximation. Here we only take into account the three dominant terms: electric dipole $\overline{\mathcal{P}}$, electric quadrupole $\overline{\overline{\mathcal{Q}}}$ and magnetic dipole $\overline{\mathcal{M}}$; we use different calligraphic symbols for the multipole moments of *meta-molecules* to distinguish them from those of meta-atoms used in Ap-

pendix A. The radiated electric field at the far-field point $\mathbf{R}$ can be written explicitly as

$$\mathbf{E}(\mathbf{R}) \approx \frac{\exp(\mathrm{i}k_0 R)}{4\pi\epsilon_0 c^2 R}\left\{\frac{-\omega^2\mathbf{R}\times(\mathbf{R}\times\overline{\mathcal{P}})}{R^2}+\frac{i\omega^3\mathbf{R}\times[\mathbf{R}\times(\mathbf{R}\cdot\overline{\overline{\mathcal{Q}}})]}{2cR^3}-\frac{\omega^2\mathbf{R}\times\overline{\mathcal{M}}}{cR}\right\}. \tag{2.12}$$

From the symmetry of the charge and the current distributions, we can express the electric dipole, quadrupole and magnetic dipole moments of the chiral meta-molecule in terms of the electric dipoles of the cut-wires:

$$\begin{aligned}\overline{\mathcal{P}} &= \int \rho\mathbf{r}\mathrm{d}\mathbf{r}^3\\ &= Q_1\int \mathrm{q}_1\mathbf{r}_1\mathrm{d}\mathbf{r}_1^3+Q_2\int \mathrm{q}_2\mathbf{r}_2\mathrm{d}\mathbf{r}_2^3\\ &= l_\mathrm{e}[Q_1\sin\Phi+Q_2\sin(\Phi-\theta)]\cdot\mathbf{x}+[Q_1\cos\Phi+Q_2\cos(\Phi-\theta)]\cdot\mathbf{y},\end{aligned} \tag{2.13}$$

$$\begin{aligned}\overline{\mathcal{M}} &= \frac{1}{2}\int \mathbf{J}\times\mathbf{r}\mathrm{d}\mathbf{r}^3\\ &= \frac{-\mathrm{i}\omega}{2}\left(Q_1\int \mathbf{j}_1\times\mathbf{r}_1\mathrm{d}\mathbf{r}_1^3+Q_2\int \mathbf{j}_2\times\mathbf{r}_2\mathrm{d}\mathbf{r}_2^3\right)\\ &= \frac{\mathrm{i}\omega l_\mathrm{e}s}{4}\Big\{[Q_2\cos(\Phi-\theta)-Q_1\cos\Phi]\cdot\mathbf{x}-[Q_2\sin(\Phi-\theta)-Q_1\sin\Phi]\cdot\mathbf{y}\Big\},\end{aligned} \tag{2.14}$$

$$\begin{aligned}\overline{\overline{\mathcal{Q}}} &= \int \rho\mathbf{r}\mathbf{r}\mathrm{d}\mathbf{r}^3\\ &= Q_1\int \mathrm{q}_1\mathbf{r}_1\mathbf{r}_1\mathrm{d}\mathbf{r}_1^3+Q_2\int \mathrm{q}_2\mathbf{r}_2\mathbf{r}_2\mathrm{d}\mathbf{r}_2^3\\ &= \frac{l_\mathrm{e}s}{2}[Q_2\cos(\Phi-\theta)-Q_1\cos\Phi](\mathbf{yz}+\mathbf{zy})\\ &\quad+[Q_2\sin(\Phi-\theta)-Q_1\sin\Phi](\mathbf{xz}+\mathbf{zx}).\end{aligned} \tag{2.15}$$

$l_\mathrm{e}=|\mathbf{l}_1|=|\mathbf{l}_2|$ is the amplitude of the normalized dipole moment, s is the separation between two cut-wires. By substituting these expressions into Eq. (2.12), we can readily calculate the far-field radiation patterns and analyse the contribution of each term. From the above expressions for the electric and magnetic dipole moments of the chiral meta-molecule, we can also derive the effective magnetic polarizability $\overline{\overline{\boldsymbol{\alpha}}}^{\,\mathrm{mm}}$ and the magnetoelectric coupling constant $\overline{\overline{\boldsymbol{\alpha}}}^{\,\mathrm{em}}$ [see Eq. (1.7) in Chapter 1]. We neglect the effect of the quadrupole moment here first, since it leads to additional spatial dispersion. Recall that in Chapter 1, we discussed the relation between artificial magnetic response and nonlocal effects at the macroscopic scale; in fact, twisted cut-wire pairs provide a straight-forward insight of such relation at the microscopic scale [105]. The magnetic field $\mathbf{H}$ is related to the local curl of the electric field $\mathbf{E}$ [Eq. (1.1)]. Since the separation between cut-wires $s \ll \lambda$, the incident magnetic field in between the pairs can be approximated by

$$H_{\mathrm{i},x}=\frac{\mathrm{i}}{\omega\mu_0}\left(\frac{\partial}{\partial z}E_{\mathrm{i},y}\right)\approx\frac{\mathrm{i}}{\omega\mu_0 s}\left[E_{\mathrm{i},y}^{(2)}-E_{\mathrm{i},y}^{(1)}\right] \tag{2.16}$$

The effective magnetic polarizability and chiral coefficient can be calculated directly from the ratio of the dipole moments $\overline{\mathcal{P}}, \overline{\mathcal{M}}$ and the corresponding field components.

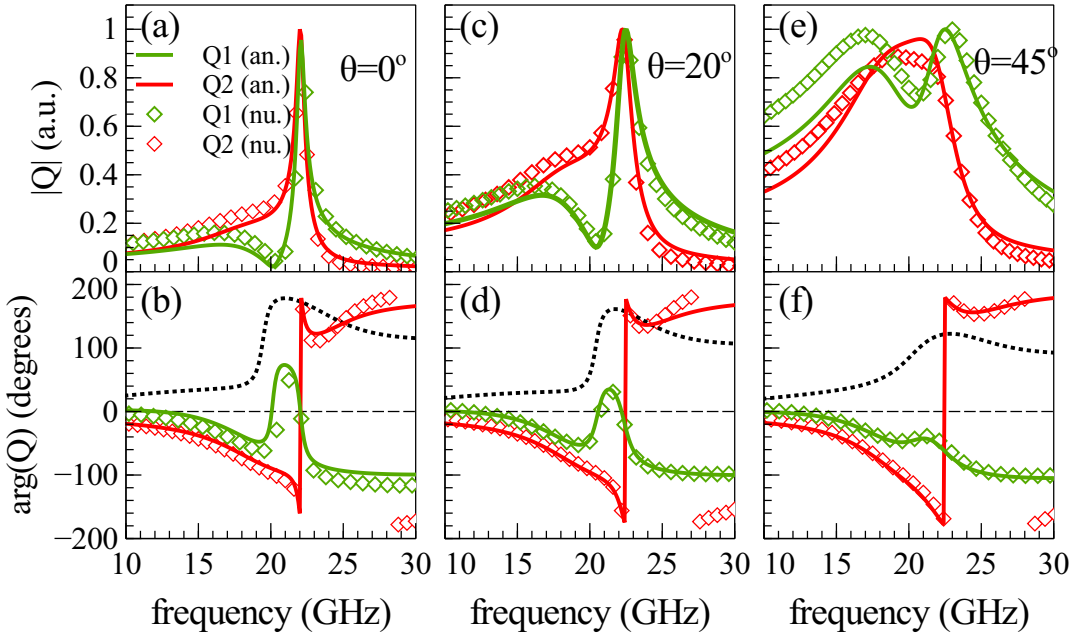

Figure 2.3: Normalized amplitudes and phases of Q_1 and Q_2 under $\Phi = 0°$ and different twist angles θ. (a,b) $\theta = 0°$, (c,d) $\theta = 20°$, (e,f) $\theta = 45°$. The results from our analytical model (an.) and numerical simulation (nu.) are plotted in (—) and (⋄), respectively. The black dotted lines are the phase differences between Q_1 and Q_2 calculated with the analytical model.

To take the xx components as an example,

$$\alpha_{xx}^{\mathrm{mm}} = \frac{\mathcal{M}_x}{H_{\mathrm{i},x}} = \frac{\omega^2 s^2 l_{\mathrm{e}}}{4c^2\epsilon_0} \frac{Q_2\cos(\Phi-\theta) - Q_1\cos\Phi}{E_{\mathrm{i},y}^{(2)} - E_{\mathrm{i},y}^{(1)}} \propto (k_0 s)^2, \tag{2.17}$$

$$\alpha_{xx}^{\mathrm{em}} = \frac{\mathcal{P}_x}{H_{\mathrm{i},x}} = \frac{-\mathrm{i}\omega s l_{\mathrm{e}}}{c}\sqrt{\frac{\mu_0}{\epsilon_0}} \frac{[Q_1\sin\Phi + Q_2\sin(\Phi-\theta)]}{E_{\mathrm{i},y}^{(2)} - E_{\mathrm{i},y}^{(1)}} \propto k_0 s. \tag{2.18}$$

This explicitly shows that artificial magnetic response and chiral response are actually manifestation of the second order and first order spatial dispersion, respectively [105].

2.3 Near-field and Far-field Responses

To test our model, we compare it with the results of full wave simulation from CST Microwave Studio (see Sec. A.4 for more details). In the calculation, we take a=6 mm, t=0.1 mm, w=1 mm and s=1 mm. The incident plane wave is polarized in the y direction, parallel to cut-wire 1 ($\Phi = 0°$); open boundaries are employed in all directions. To probe the resonant spectral features, two near-field probes are positioned 0.1 mm away from the ends of the cut-wires; a far-field probe is used to detect the forward scattered wave in the positive z direction.

Fig. 2.3 compares the results of Q_1 and Q_2 calculated using our model and the near-field spectra from CST-MWS. Both the normalized amplitudes and the phases from the model have an overall good agreement with CST-MWS. Since the near-field spectrum from a probe is position-dependent, it is inevitable that some difference

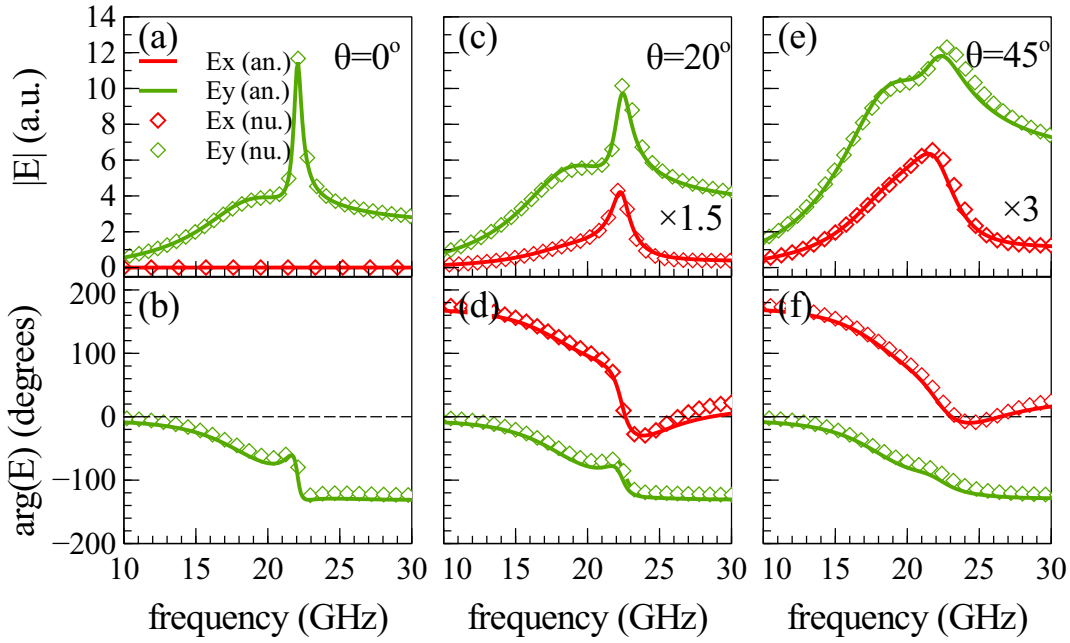

Figure 2.4: Amplitudes and phases of the electric field of forward scattered wave at (0,0,z), under $\Phi = 0°$ and different twist angle. (a,b) $\theta = 0°$, (c,d) $\theta = 20°$, (e,f) $\theta = 45°$. The results from analytical model (an.) and numerical simulation (nu.) are plotted in (—) and (⋄), respectively.

shows up. The sharp resonance at around 22 GHz corresponds to the antisymmetric mode, as can be confirmed by the phase difference between Q_1 and Q_2 (black dotted line). The amplitude spectra show typical Fano lineshapes due to the interference between the broad super-radiant symmetric mode and the narrow sub-radiant anti-symmetric mode. We note that using only the real parts of the self and mutual impedances correctly predicts the resonant frequencies, but gives erroneous lineshapes; therefore it is important to include all the imaginary terms from the retardation such that it can predict correct lineshapes.

Next, we compare the forward far-field radiation spectra, as shown in Fig. 2.4. The results have been normalized by the distance-dependent factor $\exp(ik_0z)/z$. The sharp peak around the antisymmetric mode in Fig. 2.4 is actually an effect related to the directive "super-scattering", when multiple channels (modes) of scattering interfere constructively in one direction [367–369]. This mechanism can be considered as a generalization of the well-known theory for directive RF antennas. Figure 2.5 demonstrate the three dimensional scattering patterns of $|E|$ calculated from our model and CST-MWS, very nice agreement is shown. Our model also allows us to characterize the contribution of each multipole component.

When cut-wire 2 is twisted by an angle θ, a cross component E_x is observed in the radiated wave. For clarity, the electric field amplitudes of radiation are multiplied by 1.5 and 3 in Fig. 2.4 (c) and (e), respectively. The excellent agreement between our method and numerical simulation is evident. Under a certain twist angle, the strongest cross polarization conversion occurs near the antisymmetric resonance, when Q_2 becomes maximum. This is consistent with Eq. (2.12): when $\mathbf{R} = (0,0,z), \Phi = 0$, $E_x(\omega, R) = -\omega^2 Q_2 l_e \sin\theta\,[1 - i\omega s/(2c)] \exp(ik_0z) \,/\, (4\pi\epsilon_0 c^2 z)$.

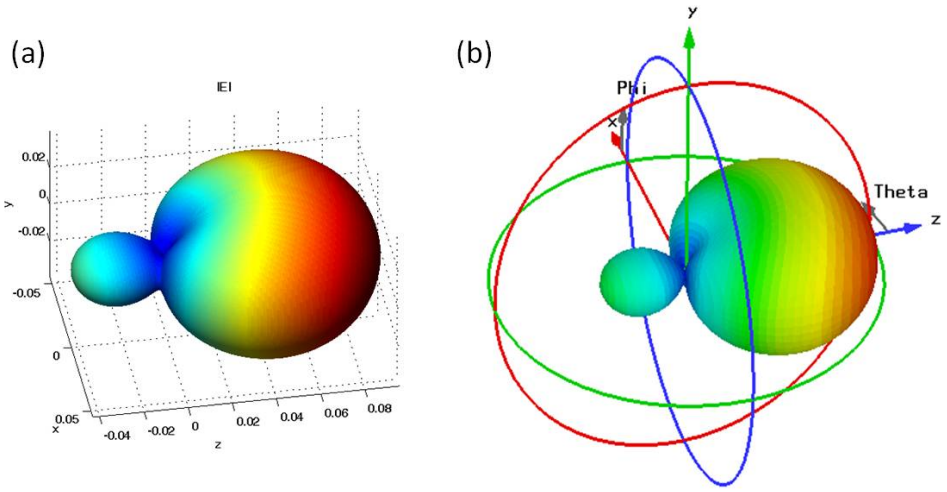

Figure 2.5: Directive scattering patterns at the antisymmetric mode with $\Phi = 0°, \theta = 0°$, calculated with (a) semi-analytical model, and (b) full-wave simulation (CST Microwave Studio).

2.4 Optimum Twist Angle

The dependence of the output polarization state on the twist angle and other parameters is of interest in the study of chiral structures. To show the efficiency of this model, we calculate the whole map of polarization states, when θ changes from $0°$ to $90°$ with a step of $1°$, as shown in Fig. 2.6(a). It is found that the optimum twist angle (magenta dots) varies with frequency, which is different from the result ($\theta = 45°$) predicted from simple geometrical considerations [370].

From the view point of symmetry, it is true that 45 degrees is half way between the symmetric configurations at $\theta = 0°$ and $\theta = 90°$, and hence would be expected to be the least symmetric configuration. As has been predicted [363, 370], such asymmetry can be characterized by the chirality index $\Xi = \frac{1}{2} s a^2 \sin 2\theta$ [363], which shows a maximum value at 45 degrees; for the transmission of a randomly-oriented assembly, if the spatial distribution of current and the interaction between neighbouring cut-wire pairs are not taken into account, the optimum twist angle, at which the polarization rotation effect becomes the strongest, will also occur at 45 degrees in the long-wavelength limit (far from resonance) [363]. This indicates that only when the wires are infinitely thin and the structure is in the long-wavelength limit, will the optimum angle be 45 degrees.

For the case of our resonant structures, the optimum twist angle with maximum polarization rotation is determined by several factors. The first one is the intrinsic anisotropy of the cut-wire pair. The polarization rotation depicted in Fig. 2.6 (a) has contributions from both the chirality and the anisotropy of the structure. To exclude the influence of anisotropy, we calculate the scattered wave from the twisted cut-wire pair with its orientation rotated by 90 degrees (i.e., cut-wire 1 becomes oriented in x direction), and combine with the original scattered wave when cut-wire 1 is oriented in y direction. The polarization rotation angle of the averaged scattered wave is shown in Fig. 2.6 (b), and the optimum angle for each frequency is determined by the maximum absolute value of the polarization rotation angle. It can be seen that far from resonance, the polarization rotation angle is very small since the effect of

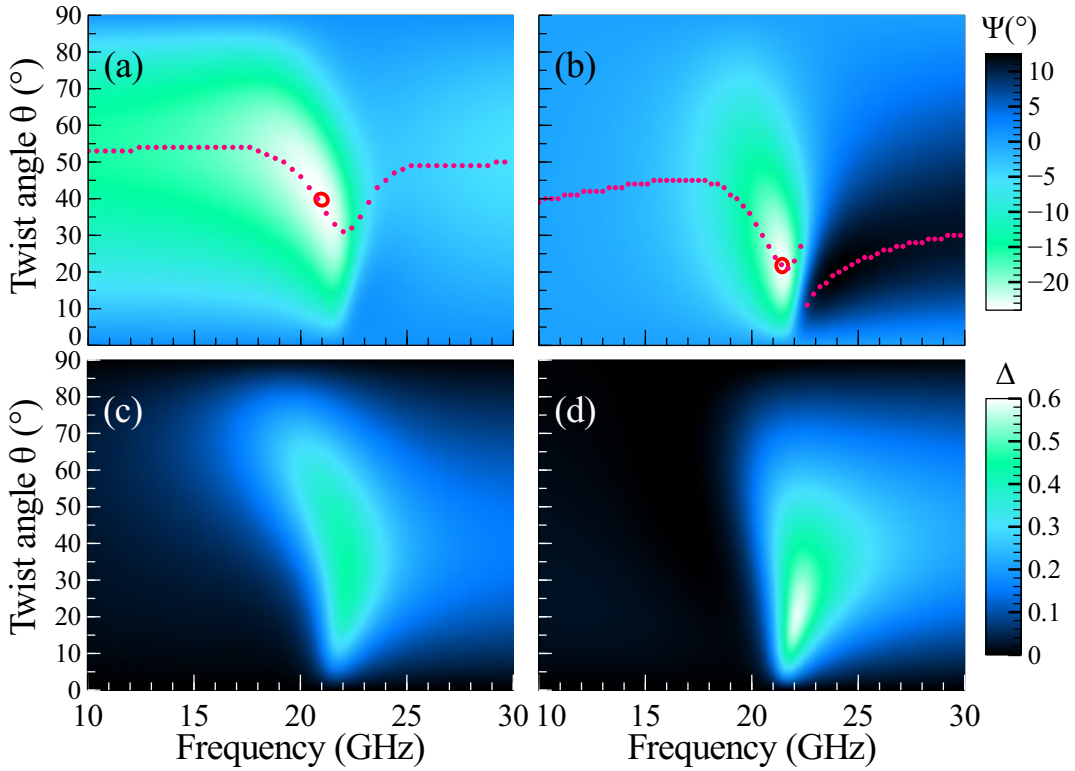

Figure 2.6: (a), (b) Polarization rotation angle Ψ and (c), (d) ellipticity Δ of the forward scattered wave as a function of frequency and twist angle θ. (a) and (c) For the scattered wave when cut-wire 1 is oriented along y direction ($\Phi = 0°$); (b) and (d) for the averaged scattered wave when cut-wire 1 is oriented along x ($\Phi = 90°$) and y directions ($\Phi = 0°$). The optimum twist angles for different frequencies are shown by the magenta dots, and the red circle denotes the position with maximum polarization rotation.

anisotropy is excluded. This result is consistent with previous predictions [363]: if the two cut-wires are twisted about their central points, the polarization rotation effect of a randomly-oriented assembly will disappear in the long-wavelength limit. However, the rotation effect remains strong near the antisymmetric mode, and the optimum angles are still strongly frequency dependent. Such behaviour is due to the second factor: large phase variation due to strong coupling. The phase difference between the two resonators cannot be described approximately by $\exp(ik_0|\mathbf{r} - \mathbf{r}'|)$ near the antisymmetric mode (which otherwise would be a straight line with respect to the frequency), as shown in Fig. 2.3. Some approximations used in the quasi-static limit become invalid and it will cause a significant variation from the results obtained [363], and the optimum points change drastically. The third factor is the finite width of the wire. The current distribution in such finitely-wide cut-wires can no longer be considered as line-current, and this can lead to different result in optimum angle even in the long wavelength limit. One extreme case is when $w = a$, the lowest symmetry point should locate at 22.5 degrees. Thus the lowest symmetry point for the case $w < a$ is expected to be between 22.5 and 45 degrees.

2.5 Summary

To conclude, in this chapter, we studied the coupling and optical activity of meta-molecules based on twisted cut-wire pairs. We developed a semi-analytical method based on the free-space Green's function under the eigenmode approximation and employed it to study the resonant and scattering properties of chiral meta-molecules. In this method, all the parameters can be obtained deterministically by considering the near-field interaction and the retardation effect. A twisted cut-wire pair was studied to test the model; both the near-field spectra and far-field scattering show good agreement with full-wave simulation, even in the regime where quasi-static theories fail. We provided a microscopic insight into the artificial magnetic and chiral responses, showing their relation with the spatial dispersion. With this model, we analyzed how the optimum twist angle changes with frequency and revealed that the difference from the simple geometry consideration is mainly due to the strong phase variation near the resonance and the finite width of the cut-wires.

This method can be further extended as an efficient tool for exploring other chiral and hybrid structures. The approach can also be extended to include the complex coupling in an array as well as the optomechanical properties of the system. In fact, the introduction of optomechanical coupling can greatly extend the functionality of chiral meta-molecules. For example, the study in this chapter and previous studies of chiral materials all showed that optical activity effects are *static* in time, but actually optical activity can also become *nonlinear and dynamic* when we introduce optomechanical coupling into chiral meta-molecules. These novel effects will be further discussed in the following chapters.

Statement

This chapter was written based on the work published in the journal paper:
Mingkai Liu, David A. Powell, Ilya V. Shadrivov, and Yuri S. Kivshar, "Optical activity and coupling in twisted dimer meta-atoms", *Appl. Phys. Lett.* **100**, p 111114-4 (2012).
In this work, I developed the theory and performed the simulation, with support from D. A. Powell and I. V. Shadrivov., and discussion with Y. S. Kivshar.

Chiral Meta-molecules Rotated by Light

3.1 Introduction

Using light to manipulate objects or even to drive a machine is a fascinating field of study. It is well known that the interaction between light and matter is usually accompanied by the transfer of linear or angular momentum [371]. Many tools and devices based on this principle have been developed, such as optical tweezers [272, 273], optical wrenches [274, 275] and optical motors [276, 277]. These light-driven tools provide novel ways to manipulate tiny objects and are widely employed in fields such as micro-fluidics [372] and biophysics [373].

Basically, there are two ways to generate optical torque. One is to introduce the angular momentum directly from the illuminating wave by manipulating its polarization state or phase front, for example, by using circularly polarized light or vortex beams [272, 274, 371, 374, 375] [Fig. 3.1 (a), (c) and (d)]. The other one is to use chiral structures [Fig. 3.1 (b)], which scatter light into different angular momentum modes with unequal intensity [376, 377]. Due to the conservation of angular momentum, chiral structures can generate torques even though the impinging wave has zero angular momentum (for example, a linearly polarized plane wave). However, due to the small dielectric constant (which also means a weak light-matter interaction) in most dielectric materials, early studies of optical torque often required birefringent or chiral structures that are of the order of (or even orders of magnitude larger than) the working wavelength to generate a sufficiently large torque [378]. Recently, it was demonstrated that by taking advantage of the plasmonic resonance, a strong radiation torque can be generated with a 100 nm-scale plasmonic nanomotor based on a planar chiral geometry [Fig. 3.1 (e)] [291] .

Generating strong torque with a sub-wavelength actuator is the key step towards highly integrated light-driven systems. The advent of metamaterials and plasmonic structures paves the way to achieve strong light-matter interaction at a sub-wavelength scale, and the coupled structures further offer us the chance to tune their performance through near-field interaction [360, 379]. As has been introduced in Chapter 2, twisted dimers, such as twisted split-ring resonators and cut-wire pairs, are a particularly interesting class of coupled chiral meta-molecules that can exhibit strong linear or even nonlinear optical activity near the resonances. Although much work has been done on their electromagnetic properties, their optomechanical properties are still largely unexplored.

Due to angular momentum conservation, it is expected that a chiral meta-molecule

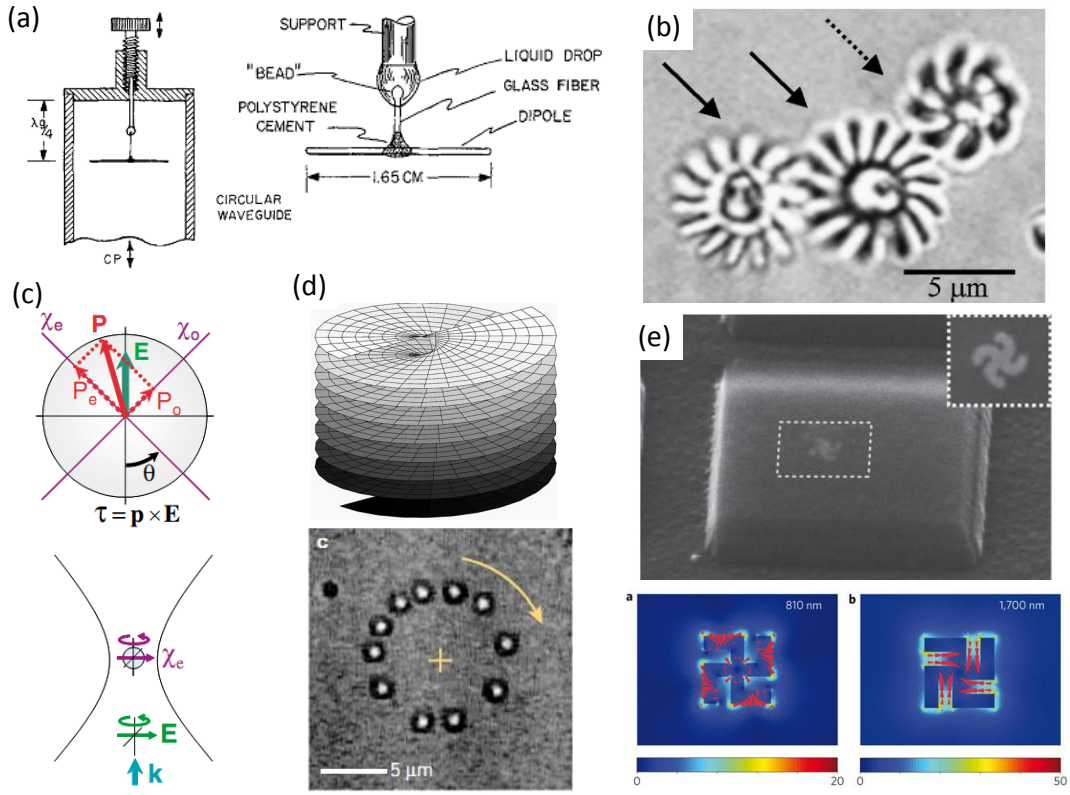

Figure 3.1: (a) Setup in an early study of electromagnetic torque. The liquid-drop-suspended electric dipole can be driven to rotate by a circularly polarized wave at microwave frequencies [371] . (b) Complex micromachine built by the two-photon polymerization technique. The two engaged cogwheels (pointed by solid arrows) are rotated by a light-driven chiral motor (pointed by dashed arrows) [276]. (c) (top) Schematic of polarization vector P induced in an anisotropic particle by an external electric field E. Torque is generated when P is not aligned with the field; (bottom) a particle being trapped can be rotated by rotating the incident polarization and works as an optical wrench [274]. (d) (top) Schematic of the wave front of a Laguerre-Gauss beam with LG_{02} mode [380]; (bottom)) Time-lapse image of a single colloidal sphere traveling around the optical vortex [381]. (e) (top) A silica microdisk rotated by the embeded light-driven plasmonic nanomotor (100 nm by 100 nm). (bottom) The electric field amplitudes and Poynting vectors of the two plasmonic modes that generate torques in opposite directions [291] .

should also generate strong torque. In this chapter, we provide an approach to achieving strong and tunable torque with a subwavelength chiral meta-molecule. We study the radiation torque generated in a twisted split-ring resonator pair when illuminated by linearly polarized plane waves. With the semi-analytical model based on near-field interaction, we explicitly show the mechanism and found that such structures can offer two rotational frequency bands (RFBs), in which the direction of the torque does not change as the structure rotates. The prediction from this simple model shows good overall agreement with full-wave calculations based on the Maxwell stress tensor. Moreover, we study the dynamics of this structure under the influence of friction and show that such a simple coupled structure can offer rich opto-mechanical modes, which enables the chiral meta-molecule to function as an optical motor or an optical

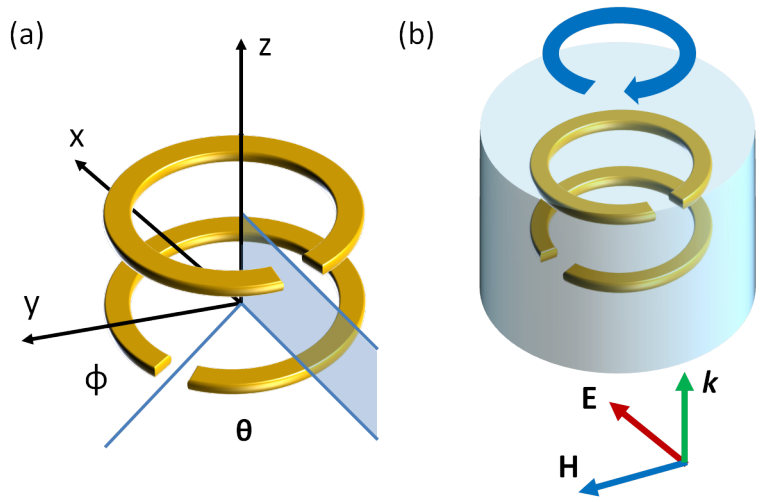

Figure 3.2: (a) Schematic layout of the twisted SRR pair. The centre-to-centre distance between the two coaxial SRRs is s, and the mutual twist angle is θ. A linearly polarized plane wave propagates along the z direction and the SRR pair rotates about the z axis, with the rotation angle denoted as Φ. (b) In practice, the SRR pair can be fixed inside a cylinder, so that their mutual twist angle does not change when the whole structure rotates.

wrench at different frequencies. Compared to the plasmonic nanomotor studied in Ref. [291], the twisted split-ring pair can generate strong and tunable torques with opposite directions within a much narrower bandwidth; the intrinsic anisotropy also allows the motion to be detected directly from the scattered wave, which further facilitate its implementation and application from microwave to optical frequency regimes.

3.2 Mechanism of Light-driven Actuators Based on Twisted SRR Pairs

The twisted SRR pair studied is illustrated in Fig. 3.2. The two identical SRRs (denoted as "1" and "2") are offset by a distance s in the z direction, and the twist angle between them is fixed at θ during rotation. The incident plane wave propagates along the z axis, with a linear polarization in the x direction. Since the structure is chiral, it may experience a radiation torque even under illumination by linearly polarized waves, and the rotation angle is denoted as Φ. To understand the optomechanical properties of the structure, we first need to find its electromagnetic response, then we use its frequency-dependent charge and current distributions to calculate the radiation torque for different rotation angles, and finally we can solve the dynamic equations of the system. As has been shown in Chapter 2, under the eigenmode approximation, we can separate the current and charge of a single SRR into a frequency-dependent mode amplitude $Q_m(\omega)$ ($m = 1, 2$) and spatial distributions $\mathbf{j}(\mathbf{r})$ and $\mathrm{q}(\mathbf{r})$. To simplify the calculation while retaining insight into the underlying physics, we treat each SRR as an infinitely thin current line with a spatially variant current distribution along the azimuthal direction. We find that compared to the full-wave calculated current distribution in a thin SRR, a sinusoidal function is a good

approximation for the lowest order mode (magnetic dipole mode):

$$\mathbf{j}(\alpha) = \begin{cases} 0, & \alpha \in [-\frac{\alpha_0}{2}, \frac{\alpha_0}{2}] \\ \hat{\mathbf{e}}_\alpha \cdot \sin[\frac{(\alpha-\alpha_0/2)\pi}{2\pi-\alpha_0}], & \alpha \notin [-\frac{\alpha_0}{2}, \frac{\alpha_0}{2}] \end{cases} \tag{3.1}$$

α is the azimuthal angle and α_0 is the angle of the gap; the charge spatial distribution can be obtained from

$$\mathrm{q}(\alpha) = -\nabla \cdot \mathbf{j}(\alpha) = -\frac{1}{a}\frac{\partial}{\partial \alpha} j(\alpha) \tag{3.2}$$

with a being the radius of the SRR. The effective self and mutual impedance, as well as the mode amplitudes can be worked out following the procedure introduced in Chapter 2.

$$Q_1 = \frac{Z_\mathrm{s}\mathcal{E}_1 - Z_\mathrm{m}\mathcal{E}_2}{-\mathrm{i}\omega(Z_\mathrm{s}^2 - Z_\mathrm{m}^2)}, \; Q_2 = \frac{Z_\mathrm{s}\mathcal{E}_2 - Z_\mathrm{m}\mathcal{E}_1}{-\mathrm{i}\omega(Z_\mathrm{s}^2 - Z_\mathrm{m}^2)} \tag{3.3}$$

with

$$\mathcal{E}_1 = -\mathbf{E}^\mathrm{i} \cdot \mathbf{l}_1 = |E^\mathrm{i}| l_\mathrm{e} \cos\Phi, \tag{3.4}$$

$$\mathcal{E}_2 = -\mathbf{E}^\mathrm{i} \cdot \mathbf{l}_2 = |E^\mathrm{i}| l_\mathrm{e} \cos(\Phi + \theta) \exp(\mathrm{i}\varphi). \tag{3.5}$$

$\varphi = k_0 s$ is the difference in excitation phase of the two SRRs due to retardation. Once we get the frequency-dependent current and charge distributions $\mathbf{J}(\mathbf{r}, \omega) = -\mathrm{i}\omega Q(\omega)\mathrm{q}(\mathbf{r})$ and $\rho(\mathbf{r}, \omega) = Q(\omega)\mathrm{q}(\mathbf{r})$, we can calculate the torque experienced by each of the SRRs, and their sum is the net external torque. The torque induced by the external field is

$$\mathbf{M}^\mathrm{ext} = \int_V \mathbf{r} \times [\rho(\mathbf{r})\mathbf{E}^\mathrm{i} + \mathbf{J}(\mathbf{r}) \times \mathbf{B}^\mathrm{i}] \mathrm{d}^3\mathbf{r} \tag{3.6}$$

We assume that the structure is only allowed to rotate about the z axis. Due to the structural symmetry, the magnetic part does not contribute to the EM torque about the z axis. The time averaged torque exerted on SRR 1 and SRR 2 can then be written in a very concise form when we only consider the dominant contribution from electric dipole moments:

$$\mathbf{M}_1^\mathrm{ext} = -\frac{1}{2}\mathrm{Re}[Q_1^*(\omega, \Phi)] l_\mathrm{e} |E^\mathrm{i}| \sin\Phi \cdot \hat{\mathbf{z}} \tag{3.7}$$

$$\mathbf{M}_2^\mathrm{ext} = -\frac{1}{2}\mathrm{Re}[Q_2^*(\omega, \Phi) \exp(\mathrm{i}\varphi)] l_\mathrm{e} |E^\mathrm{i}| \sin(\Phi + \theta) \cdot \hat{\mathbf{z}} \tag{3.8}$$

By substituting Eq. (3.3) and (3.4) into Eq. (3.7) and (3.8), we finally arrive at the total external torque, which we then decompose into two components $\mathbf{M}^\mathrm{o}$ and $\mathbf{M}^\mathrm{r}$

$$\mathbf{M}^\mathrm{ext} = \mathbf{M}_1^\mathrm{ext} + \mathbf{M}_2^\mathrm{ext} = \mathbf{M}^\mathrm{o} + \mathbf{M}^\mathrm{r} \tag{3.9}$$

where

$$\mathbf{M}^\mathrm{o} = \frac{l_\mathrm{e}^2 |E^\mathrm{i}|^2}{2} \mathrm{Re}(A^* \cos\theta - B^* \cos\varphi) \sin(2\Phi + \theta) \cdot \hat{\mathbf{z}} \tag{3.10}$$

$$\mathbf{M}^\mathrm{r} = \frac{l_\mathrm{e}^2 |E^\mathrm{i}|^2}{2} \mathrm{Im}(B^*) \sin\theta \sin\varphi \cdot \hat{\mathbf{z}} \tag{3.11}$$

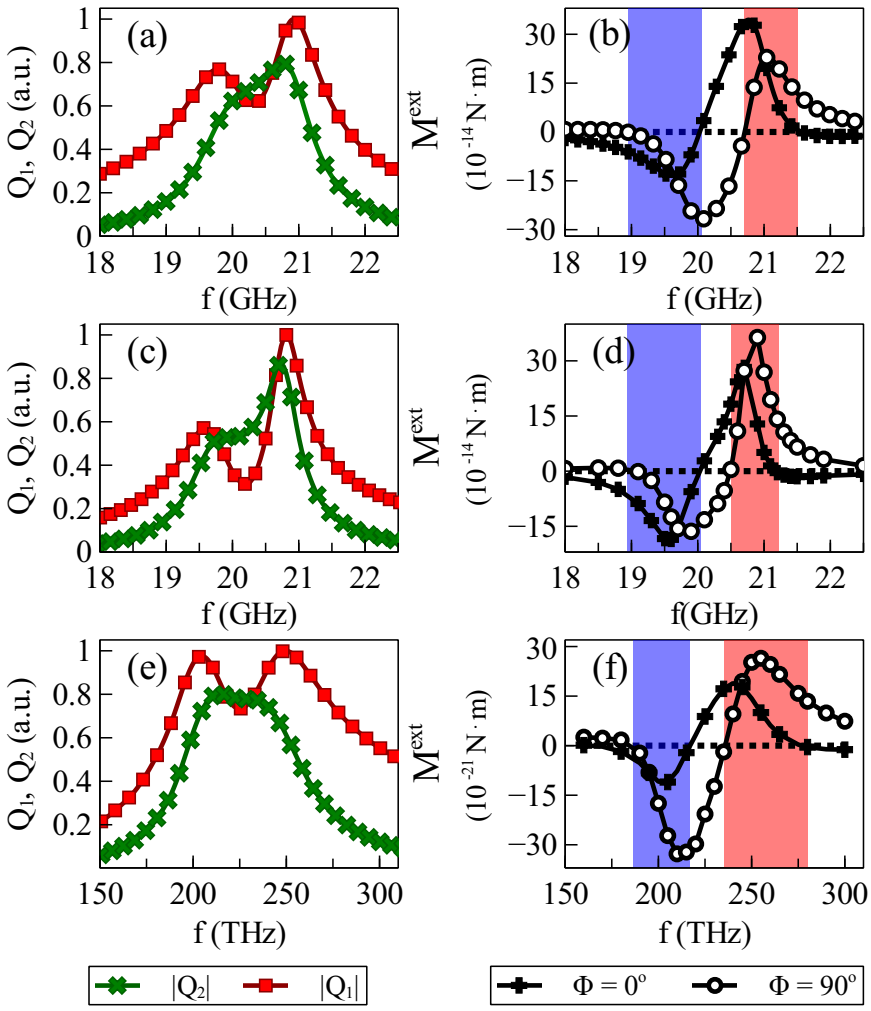

Figure 3.3: Normalized mode amplitudes Q_1, Q_2 and the radiation torque M^{ext} of the chiral meta-molecule with mutual twist angle $\theta = 90°$, where (a) and (b) are calculated from the analytical model, (c) and (d) are the full wave calculations of the microwave sample, and (e) and (f) are the full wave calculations of the optical sample. For the analytical model, a=1.16 mm, $\alpha_0 = 11°$; for the microwave sample, a=1.2 mm, metal thickness t=0.03 mm, width w=0.24 mm, gap size g=0.2 mm and separation between SRRs s=2 mm; for the optical sample, a=80 nm, t=30 nm, w=30 nm, g=30 nm and s=80 nm. The blue and red shadings in the torque diagrams denote the rotational frequency bands.

with $A = Z_s/[-i\omega(Z_s^2 - Z_m^2)]$ and $B = Z_m/[-i\omega(Z_s^2 - Z_m^2)]$. Note that A and B are independent of the rotation angle Φ. Therefore, $\mathbf{M}^{\text{o}}(\Phi)$ is a rotation angle-dependent torque, whose sign is periodically changing as the structure rotates, and thus it leads to the oscillatory dynamics. The component $\mathbf{M}^{\text{r}}$ does not depend on Φ and it contributes to the continuous rotation. We further note that $\mathbf{M}^{\text{r}}$ vanishes when any of the following three go to zero: the mutual interaction Z_m, the retardation φ or the twist angle θ, which verifies its relation with the structural chirality. It can be expected that there will be a rotational frequency band when $\Delta M = |\mathbf{M}^{\text{r}}| - \max(|\mathbf{M}^{\text{o}}|) > 0$, in which the chiral meta-molecule will be driven to rotate continuously in one direction.

3.3 A General Prototype of Sub-wavelength Light-driven Actuator

To verify our prediction, we compare our model with the results from full wave simulation using CST Microwave Studio (see Sec. A.4 for more details). In the analytical model, we choose a=1.16 mm and $\alpha_0 = 11^\circ$. In the full wave simulation, we calculate the structures that work at microwave and optical frequencies, respectively. For the microwave sample, the metal is chosen as copper ($\sigma = 5.8 \times 10^7 \mathrm{S/m}$) and the background is vacuum; while for the optical sample, the metal is gold described by the Drude model ($\epsilon_\infty = 1$, $\omega_p = 1.37 \times 10^{16} \mathrm{rad/s}$, $\Gamma = 1.2 \times 10^{14} \mathrm{Hz}$) and the background is set as SiO_2 ($\epsilon_r = 2.13$). The external torque is calculated via the Maxwell stress tensor [382] (see Sec. A.2). Since any linear-polarization can be decomposed into two orthogonal components, we calculate the torques under $\Phi = 0^\circ$ and 90° to confirm the position of the rotational frequency bands.

For the microwave sample, both the trends of the normalized mode amplitudes and the torques show good overall agreement with our simple model, as shown in Fig. 3.3 (a) to (d). The difference mainly arises from the actual geometries of the structures and some perturbation of the charge and current distributions due to strong near-field interaction. For the optical sample [Fig. 3.3 (e) and (f)], the simple model (not shown) gives only qualitative agreement due to the omission of the metal dispersion. However, the numerical results confirm that the physics is the same for the microwave and optical regimes.

The values in Fig. 3.3 (b) and (d) are normalized to an input power density of $1\mathrm{mW/mm^2}$; in Fig. 3.3 (f), the values are normalized to a power density of $1\mathrm{mW}/\mu\mathrm{m}^2$. The two resonances around 19.6 GHz (205 THz) and 20.8 GHz (250 THz) correspond to the symmetric mode and antisymmetric mode, respectively. We note from Fig. 3.3 (b), (d) and (f) that there are two rotational frequency bands around the resonances, which are denoted by the blue and red shadings: in the blue area (the lower frequency bands), $\mathbf{M}^{\mathrm{ext}}$ is always negative; while in the red area (the higher frequency bands), $\mathbf{M}^{\mathrm{ext}}$ is always positive. Such agreement demonstrates that the simple analytical model of the twisted SRR pair can be used for calculating and designing subwavelength light-driven actuators over a wide range of frequencies. Moreover, it is quite inspiring that the torque calculated from the unoptimized subwavelength ($\approx \lambda^3/500$) optical sample is of the order of $2 \times 10^{-20} \mathrm{N{\cdot}m}$, which is comparable to that shown in previous works which use much larger dielectric chiral structures ($> 25\lambda^3$) and higher power trapping beams [378].

In contrast to the optical motor based on a single resonator, the chiral meta-molecule enables us to tune its resonant properties and optomechanical behaviour, by changing the geometry of the resonators. To capture insight into the evolution of the rotational frequency bands as the twist angle θ and the separation s change, we plot $\Delta M > 0$ as a function of frequency and θ in Fig. 3.4 (a) and (b) by fixing s=1 mm and s=2 mm; in Fig. 3.4(c) and (d), s varies from 0.5 mm to 3.5 mm, while θ is fixed at 45° and 90°, respectively. The regimes with $\Delta M > 0$ correspond to the rotational frequency bands. Through the tuning, we can change the bandwidths, spectral distance and the strength of the two bands.

When carefully examining the evolution of the rotational frequency bands, one feature attracts our attention: although the rotational frequency bands centre around the two branches of resonances, the variation of their bandwidths and the rotating power does not coincide with the change of the resonances. For the twisted SRR pair

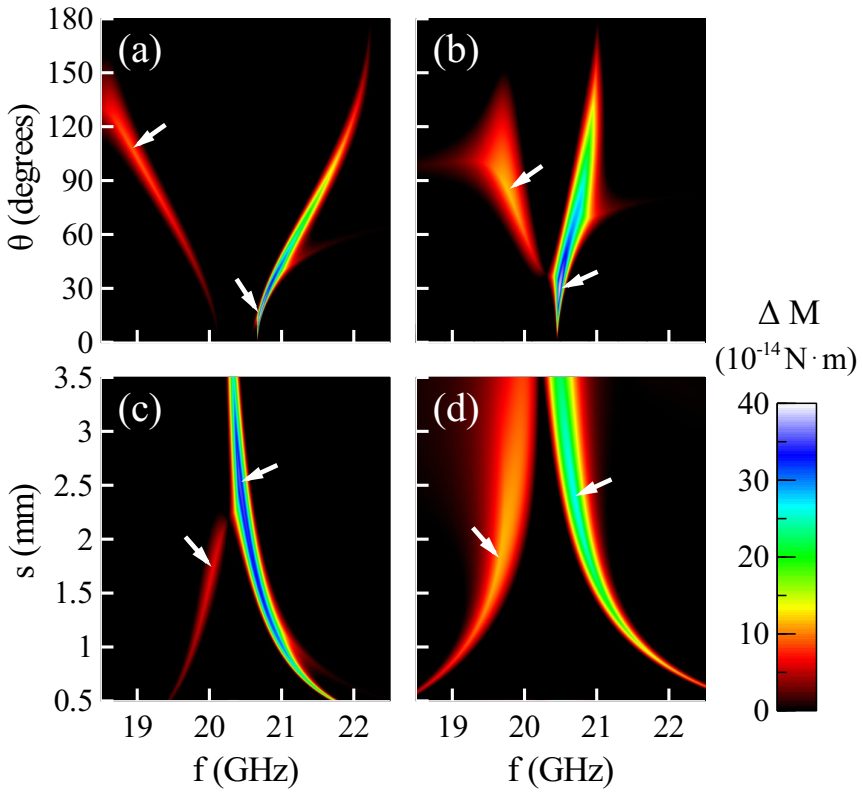

Figure 3.4: The frequency bands of continuous rotation as a function of mutual twist angle θ and mutual separation s. The frequency bands are determined from the condition $\Delta M = |\mathbf{M}^{\mathrm{r}}| - \max(|\mathbf{M}^{\mathrm{o}}|) > 0$. (a) s=1 mm, (b) s=2 mm, (c) $\theta = 45^\circ$ and (d) $\theta = 90^\circ$. The white arrows indicate the optimum points.

studied, the bandwidth of the symmetric mode exhibits a monotonic decrease as the twist angle or separation increases, while a reversed trend can be observed for the antisymmetric mode [152]. However, the bandwidths of rotational frequency bands show a more complicated non-monotonic behaviour since they are affected by several factors. For a given twist angle or separation, there is an optimum configuration in which we can get the strongest rotational power, as shown by the white arrows in Fig. 3.4. Qualitatively, we can understand this behaviour from Eq. (3.11): the strength of $\mathbf{M}^{\mathrm{r}}$ is simultaneously affected by the mutual interaction Z_{m}, the retardation φ and the twist angle θ. To take the antisymmetric mode as an example, decreasing the separation or twist angle usually gives a stronger resonance, however, this comes at the expense of smaller values of $\sin\theta$ and $\sin\Phi$, thus the optimum configuration should be a balance of the resonance strength, the degree of asymmetry and the retardation.

3.4 Rotational Dynamics

Using the analytical expression for the torque, we study the dynamics of the structure also taking into account friction in the system, which can be caused by the medium in which the meta-molecule is placed. Here, we suppose the chiral meta-molecule is fixed in a polystyrene (with relative permittivity of approximately 1) disk with radius R=2 mm, and the whole structure is suspended in air. The angular speed $\Omega = \mathrm{d}\Phi/\mathrm{d}t$ of the chiral meta-molecule can be found from the dynamic equation

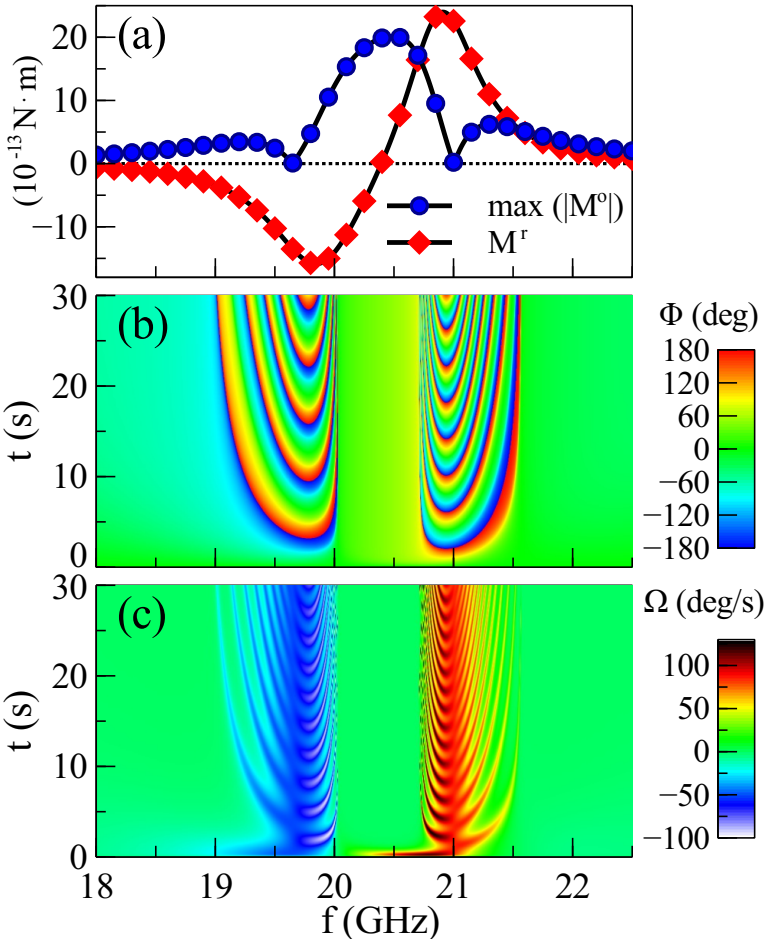

Figure 3.5: Dynamics of the twisted SRR pairs with air friction, under an illumination power density of 10 mW/mm^2. The structural parameters are the same as the ones used in Fig. 3.3 (a) and (b). (a) Torque components $\mathbf{M}^{\mathrm{r}}$ that contributes to continuous rotation, and max ($|\mathbf{M}^{\mathrm{o}}|$) that leads to periodic oscillation. (b) Rotation angle Φ and (c) angular speed Ω as a function of pump frequency and time. In the frequency bands of $|\mathbf{M}^{\mathrm{r}}| >$max($|\mathbf{M}^{\mathrm{o}}|$), the chiral meta-molecule can function as an optical motor.

using, e.g., numerical Runge-Kutta method

$$I\frac{\mathrm{d}^2\Phi}{\mathrm{d}t}+\gamma\frac{\mathrm{d}\Phi}{\mathrm{d}t}=M^{\mathrm{ext}}(\Phi) \tag{3.12}$$

where I is the moment of inertia of the structure, $\gamma=\pi R^2\eta(4R/3+2s)$ is the damping coefficient, and η=17.8$\times10^{-6}$Pa·s is the viscosity of air. The introduction of additional friction may change the rotational velocity, but will not change the overall dynamic characteristics. Fig. 3.5 depicts the torque components $\mathbf{M}^{\mathrm{r}}$ and max($|\mathbf{M}^{\mathrm{o}}|$) as well as the rotational dynamics of the chiral meta-molecule with parameters corresponding to Fig. 3.3 (a) and (b), and an incident power density of 10 mW/mm^2. As expected, two frequency bands with opposite rotation directions appear near the symmetric and antisymmetric resonances, with their regimes determined by $|\mathbf{M}^{\mathrm{r}}| >$max($|\mathbf{M}^{\mathrm{o}}|$), as predicted in Fig. 3.3 (b).

The twisted SRR pairs will experience a continuous rotation when driven by a fre-

quency within the rotational frequency bands, and thus it can act as a subwavelength motor; while outside the rotational frequency bands, the rotation angle becomes stable after a relaxation process, and the structure behaves as an anisotropic scatterer and can function as an optical wrench. The scattered wave amplitude also changes periodically as the structure rotates, and thus it provides the possibility of detecting its motion and the torque. In contrast to chiral structures with a high degree of rotational symmetry or simple anisotropic structures, the twisted SRR pairs can offer a variety of optomechanical modes: (1) rotation with constant angular speed, which can be obtained around the frequency point of $\max(|\mathbf{M}^o|) \to 0$; (2) rotation with time-varying angular speed, where the structure accelerates and decelerates repeatedly, with its variation period determined by the frequency; (3) damped oscillations, in which one can control the equilibrium position by changing the input polarization angle or the frequency. Such a multifunctional subwavelength light-driven actuator can potentially find a variety of applications in nano-fluidics and nano-robotics.

3.5 Summary

To conclude, in this chapter, we proposed the use of a pair of twisted SRRs as an efficient subwavelength optical actuator. By using a simple analytical model, we explicitly revealed the underlying mechanism and the condition for continuous rotation. Comparison with full wave calculation showed that this structure can be used as a general design prototype in a wide frequency range from microwaves to optics. Such a coupled structure provides strong rotational power comparable to that achieved by other dielectric structures, which are much larger in size and require more power. Moreover, due to the combined effect of chirality and anisotropy, the structure can support multiple optomechanical modes, and can function as an optical motor and an optical wrench at different frequencies. The proposed structure is expected to find application in a variety of fields.

Statement

This chapter was written based on the work published in the journal paper:
Mingkai Liu, David A. Powell, and Ilya V. Shadrivov, "Chiral meta-atoms rotated by light",
In this work, I developed the theory and performed the simulation, with support from D. A. Powell and I. V. Shadrivov.

Nonlinear Response via Intrinsic Rotation in Metamaterials

4.1 Introduction

As has been introduced in Section 1.5.4, nonlinear bistability due to the interplay between mechanical deformation and optical resonance was identified 30 years ago by A. Dorsel et al., in a Fabry-Perot cavity with a suspended mirror [326]. A similar effect was later observed in an analogue cavity system at microwave frequencies [328]. The basic principle can be explained by an effective potential [see Fig. 4.1 (a)]. The range of effects available in this way becomes much broader when dynamic couplings are taken into account, now known as the prominent field of cavity-optomechanics [319, 383, 384].

While many studies in optomechanics have been performed in optically large systems, it would be instructive to study such coupling in subwavelength systems such as metamaterials, particularly when considering the great design flexibility and the intriguing effective EM parameters provided by metamaterials might lead to new effects. Recently, M. Lapine et al. initiated the first step and pointed out that introducing a mechanical degree of freedom into electromagnetic metamaterials could lead to an interesting range of nonlinear effects, giving rise to a new class of *magnetoelastic metamaterials* [324] [see Fig. 4.1 (b)] and to wide-band operation [385]. At the same time, the implementation of magnetoelastic metamaterials [324] remains challenging. Although nonlinear self-tuning has already been demonstrated experimentally, first in the original prototype based on ring resonators [324] [see Fig. 4.1 (b)], and later in metamaterials based on flexible helices [349, 350] [see Fig. 4.1 (c)], the demonstration of strong nonlinear self-actions such as bistability is still challenging. In addition, designs applicable for microwave frequencies, such as the conformational nonlinearity in resonant spirals, remains inaccessible for optics, and new designs that are more suitable for micro/nano-fabrication are required [see Fig. 4.1 (d)]. The reason for this is that the electromagnetic forces employed in the initial designs are relatively weak, and it requires either high power or extremely small elastic restoring forces to achieve large deformation and giant nonlinearity, which poses a considerable manufacturing challenge.

We recall that earlier studies on structurally tunable metamaterials [152, 243, 244, 357] as well as our studies in Chapter 2 and Chapter 3, showed that near-field interaction can significantly improve the tunability range. Therefore, we expect that the most efficient approach to implementing strong coupling between electromagnetic and mechanical effects should rely on near-field interactions. In particular, changing the mutual orientation between the neighboring elements can have a profound effect

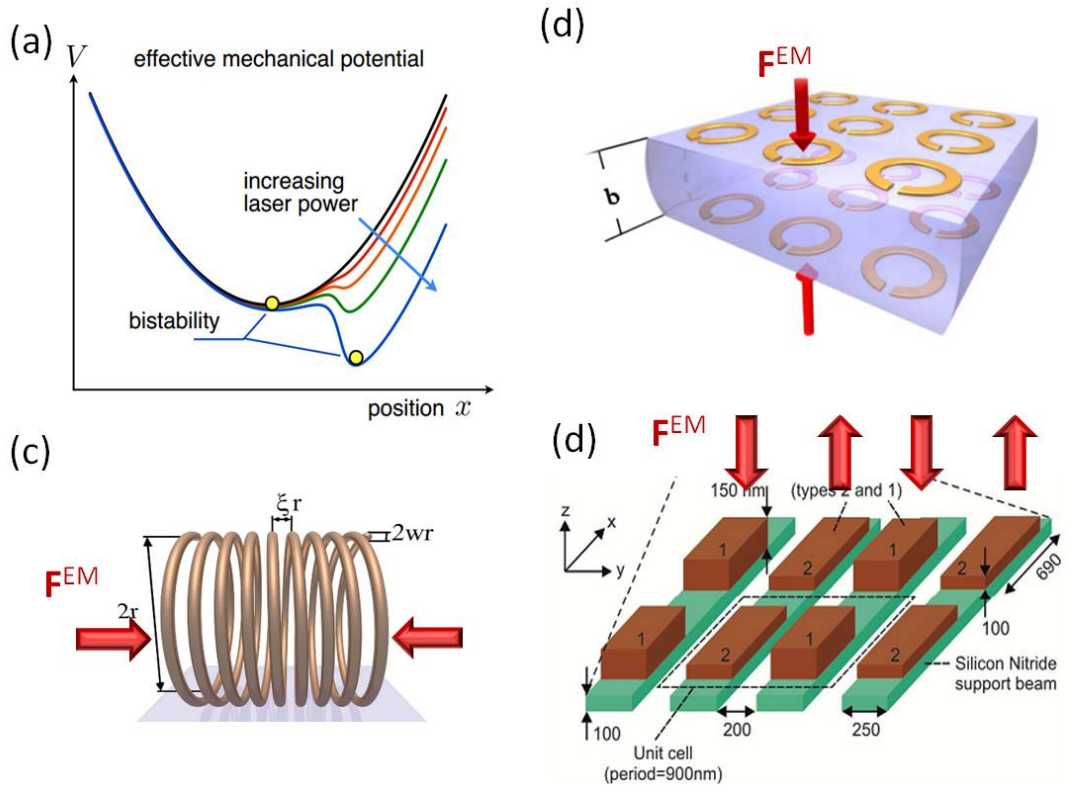

Figure 4.1: (a) Basic principle of optical force induced bistability explained by effective potential [319]. (b) to (d) Exploiting optomechanical effects with subwavelength sized structures. (b) Magnetoelastic metamaterials [324] and (c) helical chiral metamaterials showing conformational nonlinearity [350]. (d) Design of a dielectric infrared metamaterial hybridized with flexible nano-beams. Optomechanical nonlinear effects such as bistability and unidirectional nonlinear transmission were shown numerically [351]. The red arrows indicate the directions of the EM force experienced by the structure.

on the resonator coupling and the structure of the coupled modes. Instead of a considerable displacement of an entire array of meta-atoms, it is sufficient to move the crucial *parts* within the meta-molecules — for example, the gaps of the two coupled split-ring resonators of a chiral meta-molecule, as has been shown in Chapter 3.

4.2 General Concept of Chiral Torsional Metamaterials

Let us now introduce our concept: *nonlinear chiral metamaterials with intrinsic torsional rotation*. As a building element of the structure (see Fig. 4.2), we consider two coaxial split ring resonators (SRRs) with elastic feedback between them. The rings are allowed to rotate about the common axis, while the elastic feedback is provided by connecting a thin elastic wire. Indeed, the use of elastic wires has a prominent history in physics, for example, the milestone achievement of the experimental demonstration of light pressure by P. N. Lebedev [278]. Here, we employ the electromagnetic (EM) torque to construct a "light-driven" chiral meta-molecule, which enables us to modulate the resonant frequencies by twisting the rotatable element *directly* with EM waves. The component of the EM forces which twists the rings with respect to each

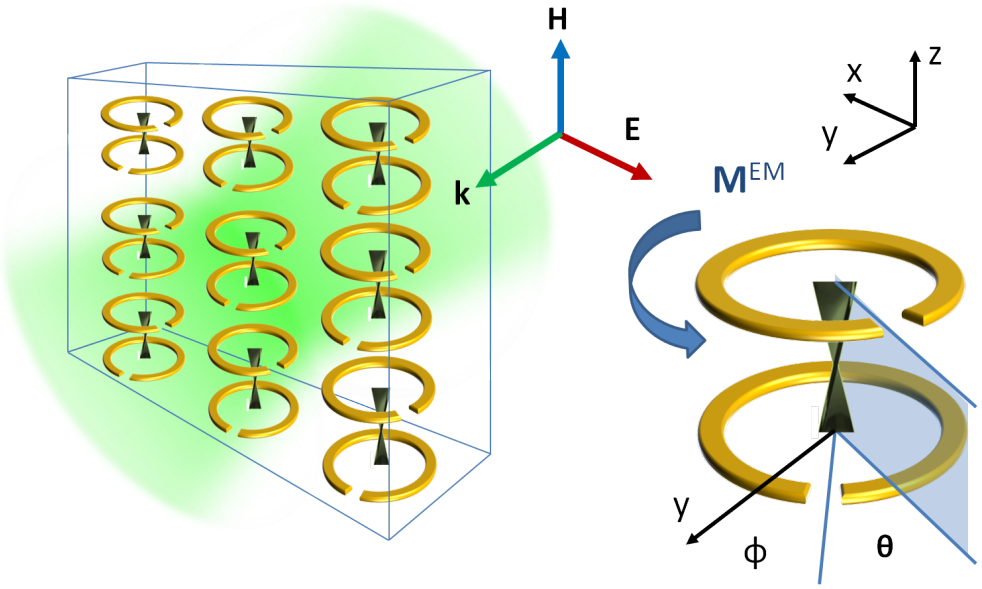

Figure 4.2: Conceptual layout of a torsional metamaterial and its rotational meta-molecule. Incident wave propagates along y direction, having a linear polarization with the electric field along x and magnetic field along z. The induced electromagnetic torque between the resonators changes the mutual twist angle θ between the rings, connected by an elastic wire.

other is normally not the strongest among the forces involved, but the prominent advantage of using EM torque instead of collinear EM force to drive a meta-atom, is that the effective lever arm of the azimuthal EM force can be much larger than that of the azimuthal restoring force from a thin wire; this can effectively magnify the deformation in the azimuthal direction by orders of magnitude.

Technically, there are a number of ways to implement this general scheme. In our design, one of the rings is fixed to a substrate and the other one is suspended on a long wire. One can attach additional short wires to the suspended ring to provide stability against tilt in other directions (see Fig. 4.4 for example). In this design, therefore, the only favorable movement is the rotation of the suspended ring with respect to the fixed ring over the common axis, and all other mechanical degrees of freedom can be neglected.

Suppose the initial position is such that the ring slits have a certain angle θ between them with respect to the common axis (Fig. 4.2). An EM wave then induces a certain distribution of charges and currents in the two resonators, and the resonance of the system is determined by their mutual orientation. These charges and currents also result in EM torque between the two rings, which drives the suspended ring to rotate until the EM torque is balanced by the elasticity of the twisted wire. Meanwhile, the entire pattern of charges and currents gets modified and the torque also changes, so the final stable equilibrium is only achieved via a complex nonlinear feedback. The twisted wire provides a restoring torque to balance the EM torque, so that we can control the twist angle (and thus the resonance) by changing the external field signal.

An additional feature of the proposed design is that the nonlinear dynamics of the rotatable meta-molecule not only depend on the parameters of the wire, but also on the EM mode initially excited in the resonators, which is determined by the starting

angle between the gaps. The latter can be made arbitrary, and an implementation has the possibility to deliberately adjust it, introducing tunability to the system.

The above design, therefore, offers *a tunable resonant nonlinear system with elastic feedback* and, as we show below, yields a rich pattern of nonlinear response including self-tuning and nonlinear bistability, which are much stronger than those provided by using nonlinear semiconductor components. Below, we first present a detailed theoretical analysis of rotational meta-atoms. We then proceed to the experimental results obtained with a fabricated prototype of the torsional meta-molecule placed in a rectangular waveguide, and confirm all important features predicted by theory. Finally, we perform full-wave numerical simulations of an array of meta-molecules (i.e. a metamaterial), and demonstrate that all the nonlinear effects observed for the single torsional meta-molecule in the waveguide are qualitatively the same in a dilute array.

4.3 Theoretical Analysis

4.3.1 Semi-analytical Model

To start with, we use the semi-analytical model introduced in Chapter 2 (see Appendix A for details) to study the dynamics of an isolated torsional meta-molecule in free space. It will subsequently be demonstrated that this model explains all qualitative features of an array. As shown in Fig. 4.2, the two coaxial identical SRRs are offset by a distance s in the z direction, and the twist angle between them is θ. The incident wave propagates along the y direction, with its magnetic field in the z direction and electric field in the x direction. The orientation of the gaps with respect to the incident electric field polarization is described by the angle Φ between the azimuth of the gap of the bottom ring as seen from the ring axis, and y axis. It should be noted that, the choice of this incident direction is to be consistent with the experimental condition; the effects predicted would be qualitatively the same for other incident directions.

To study the nonlinear behaviour of the torsional meta-molecule, we utilize the model to predict the EM response as well as the optomechanical properties of the structures. The mode amplitudes $Q_{1,2}$ can be obtained after solving the coupled equations:

$$Q_1 = \frac{Z_s\mathcal{E}_1 - Z_m\mathcal{E}_2}{-i\omega(Z_s^2 - Z_m^2)}, Q_2 = \frac{Z_s\mathcal{E}_2 - Z_m\mathcal{E}_1}{-i\omega(Z_s^2 - Z_m^2)}, \tag{4.1}$$

where $\mathcal{E}_1$ and $\mathcal{E}_2$ correspond to the effective electromotive force applied to the bottom (index 1) and top (index 2) SRRs by the incident fields $\mathbf{E}^i$ and $\mathbf{B}^i$:

$$\mathcal{E}_1 = -\mathbf{E}^i \cdot \mathbf{l}_1 \cdot e^{ik_0 a_E \cos\Phi} + i\omega\mathbf{B}^i \cdot \mathbf{u}_1 \cdot e^{ik_0 a_M \cos\Phi}, \tag{4.2}$$

$$\mathcal{E}_2 = -\mathbf{E}^i \cdot \mathbf{l}_2 \cdot e^{ik_0 a_E \cos(\Phi+\theta)} + i\omega\mathbf{B}^i \cdot \mathbf{u}_2 \cdot e^{ik_0 a_M \cos(\Phi+\theta)}, \tag{4.3}$$

where $\mathbf{l}_m(\theta,\Phi) = \int_{V_m} q(\mathbf{r}_m)\mathbf{r}_m d\mathbf{r}_m^3$ is the normalised electric dipole moment of the lowest order mode supported by a single SRR, and $\mathbf{u}_m(\theta,\Phi) = \frac{1}{2}\int_{V_m} \mathbf{r}_m \times \mathbf{j}(\mathbf{r}_m) d\mathbf{r}_m^3$ is the corresponding normalised magnetic dipole moment.

We define the effective central positions of the electric and magnetic dipoles

$$a_{\mathrm{E}} = \frac{\int_{V_1}[\mathrm{q}(\mathbf{r}_1)\mathbf{r}_1\cdot\hat{\mathbf{x}}](\mathbf{r}_1\cdot\hat{\mathbf{y}})\mathrm{d}\mathbf{r}_1^3}{\left|\int_{V_1} q(\mathbf{r}_1)\mathbf{r}_1\mathrm{d}\mathbf{r}_1^3\right|}, \tag{4.4}$$

$$a_{\mathrm{M}} = \frac{\int_{V_1}[\mathbf{r}_1\times\mathbf{j}(\mathbf{r}_1)\cdot\hat{\mathbf{z}}](\mathbf{r}_1\cdot\hat{\mathbf{y}})\mathrm{d}\mathbf{r}_1^3}{\left|\int_{V_1}\mathbf{r}_1\times\mathbf{j}(\mathbf{r}_1)\mathrm{d}\mathbf{r}_1^3\right|}, \tag{4.5}$$

similar to the definition of centre of mass, and they are calculated based on the charge and current distributions of the lower SRR when $\Phi = 0$. The phase terms of the effective voltages describe the phase retardation experienced by the SRRs in the direction of wave propagation.

Once the frequency-dependent mode amplitudes are known, we can calculate the EM torque experienced by the SRRs. Here, we are particularly interested in the torque on the top rotating ring: $\mathbf{M}^{\mathrm{EM}} = \int_{V_2}\rho(\mathbf{r}_2)\mathbf{r}_2\times\mathbf{E}+\mathbf{r}_2\times[\mathbf{J}(\mathbf{r}_2)\times\mathbf{B}]\mathrm{d}\mathbf{r}_2^3$, where the integration is performed over the volume V_2 of the top SRR. We can decompose the total torque into two parts: the external torque $\mathbf{M}^{\mathrm{ext}}$ contributed by the external incident fields, and the internal torque $\mathbf{M}^{\mathrm{int}}$ due to the near-field interaction between the two SRRs, i.e. $\mathbf{M}^{\mathrm{EM}} = \mathbf{M}^{\mathrm{ext}} + \mathbf{M}^{\mathrm{int}}$. We assume that the lower SRR is fixed while the top SRR is only allowed to rotate about the z axis. The full expressions of the EM torque have been given from Eq. (A.32) to Eq. (A.36) in Sec. A.2.2. Here, we further assume that the center of rotation coincides with the circular center of the SRR, such that the magnetic part of the torque does not contribute to the z component. The explicit expressions for the external and internal torque are reduced to the following forms:

$$\begin{aligned}\mathbf{M}^{\mathrm{ext}} &= \frac{1}{2}\mathrm{Re}\left[\int_{\mathbf{V}_2}\rho^*(\mathbf{r}_2)\mathbf{r}_2\times\mathbf{E}^{\mathrm{i}}\mathrm{d}\mathbf{r}_2^3\right]\cdot\hat{\mathbf{z}}\\ &= -\frac{1}{2}\mathrm{Re}\left[Q_2^*(\omega,\Phi)e^{\mathrm{i}k_0 a_{\mathrm{E}}\cos(\Phi+\theta)}\right]\mathbf{E}^{\mathrm{i}}\cdot\mathbf{l}_{\mathrm{e}}\sin(\Phi+\theta)\cdot\hat{\mathbf{z}},\end{aligned} \tag{4.6}$$

while the internal torque can be expressed as

$$\begin{aligned}\mathbf{M}^{\mathrm{int}} &= \frac{1}{2}\mathrm{Re}\left[\int_{V_2}\rho^*(\mathbf{r}_2)\mathbf{r}_2\times\mathbf{E}^{\mathrm{int}}(\mathbf{r}_2)\mathrm{d}\mathbf{r}_2^3\right]\cdot\hat{\mathbf{z}}\\ &= \frac{1}{2}\mathrm{Re}\Bigg\{\frac{Q_1(\omega)Q_2^*(\omega)}{4\pi\epsilon_0}\int\int\frac{\mathrm{q}(\mathbf{r}_2)e^{\mathrm{i}k_0|\mathbf{r}_1-\mathbf{r}_2|}}{|\mathbf{r}_1-\mathbf{r}_2|}\left[\frac{1-\mathrm{i}k_0|\mathbf{r}_1-\mathbf{r}_2|}{|\mathbf{r}_1-\mathbf{r}_2|^2}\right.\\ &\quad\left.\cdot\mathrm{q}(\mathbf{r}_1)\mathbf{r}_1\times\mathbf{r}_2+k_0^2\mathbf{r}_2\times\mathbf{j}(\mathbf{r}_1)\right]\mathrm{d}\mathbf{r}_1^3\mathrm{d}\mathbf{r}_2^3\Bigg\}\cdot\hat{\mathbf{z}}.\end{aligned} \tag{4.7}$$

For a cylindrical wire that can be used to suspend the rotatable SRR, the restoring torque can be estimated as

$$M^{\mathrm{R}} = -\pi a^4 G(\theta-\theta_0)/(2d), \tag{4.8}$$

where a and d are the radius and the length of the wire, respectively. G is the shear

modulus and θ_0 is the initial twist angle of the structure. A series of equilibrium twist angles can be found by solving the nonlinear equation

$$M^{\mathrm{EM}}(\theta, P_{\mathrm{I}}) + M^{\mathrm{R}}(\theta, \theta_0) = 0. \tag{4.9}$$

4.3.2 Numerical Example

We model a pair of twisted SRRs, with radius $r = 6\,\mathrm{mm}$ and vertical spacing $s = 2\,\mathrm{mm}$. The size of the slit in each ring can be characterised by the angle subtended by the gap from the ring centre, $\alpha_0 = 10^\circ$. The elastic coupling is provided with a wire of radius $a = 50\,\mu\mathrm{m}$ and of length d=100 mm, made from rubber with a shear modulus of $G = 0.6\,\mathrm{MPa}$.

Figures 4.3(a) and 4.3(b) depict the mode amplitude Q_2 and the total EM torque $\mathbf{M}^{\mathrm{EM}} = \mathbf{M}^{\mathrm{ext}} + \mathbf{M}^{\mathrm{int}}$ experienced by the top SRR as functions of frequency and twist angle θ. In our dimer meta-molecule, changing Φ generally leads to some difference in the coupling efficiency between the input plane wave and the eigenmodes, but does not cause any substantial qualitative difference such as the direction of EM torque, since it is a property governed by the symmetry of the mode profiles. Without loss of generality, we have assumed $\Phi = 0$ for the calculations. Since radiation losses are taken into account in the model, we are able to accurately describe the evolution of the mode amplitudes, phases and lineshapes of the resonances. As has been shown in Chapter 3, this chiral meta-metamolecule supports two hybrid resonances, which can be characterized as symmetric (lower frequency branch) and antisymmetric (higher frequency branch) modes, according to the symmetry of the H_z component [149, 150, 152].

The directions of the EM torque at these two resonances are also opposite. For the symmetric mode, $\theta = 0^\circ$ corresponds to the configuration of the highest potential energy (unstable point), and thus the two SRRs repel each other once $\theta > 0^\circ$, until they come to the stable state at $\theta = 180^\circ$ if there is no mechanical feedback, while the reverse is true for the antisymmetric mode. The evaluated external torque is about one order of magnitude smaller than the internal torque, and the total torque is of the order of $10^{-10}\,\mathrm{N{\cdot}m}$ when the structure is pumped with a power density P_{I}=1 $\mathrm{mW/mm^2}$. This is confirmed by the full-wave simulation (CST Microwave Studio) followed by calculation based on the Maxwell stress tensor, which yields the EM torque through a surface integral of the field components around the object [382] (see Sec. A.2).

The overall mechanism of achieving a nonlinear effect is presented in Figs. 4.3 (c, d). As an example, we choose a pump frequency (3.5 GHz) at the symmetric mode [regime denoted by the black dashed line in Fig. 4.3 (b)]. It can be seen that $\mathbf{M}^{\mathrm{EM}}$ is a Lorentz-like function of the twist angle, while the restoring torques $\mathbf{M}^{\mathrm{R}}$ under different initial twist angles θ_0 are approximated by linear functions (Hooke's law). The intersections of these two functions, $\mathbf{M}^{\mathrm{EM}}(\theta_e, P_{\mathrm{I}}) + \mathbf{M}^{\mathrm{R}}(\theta_e) = 0$, correspond to the equilibrium angles θ_e. However, only the angles with $\frac{\partial}{\partial\theta}\left[\mathbf{M}^{\mathrm{EM}}(\theta_e) + \mathbf{M}^{\mathrm{R}}(\theta_e)\right] < 0$ are stable. As the pump power P_{I} increases from zero to maximum and then reduces, the stable angles also change accordingly. With this method, we can numerically find a sequence of stable angles under different pump power P_{I}.

Since the EM torque is a nonlinear function of twist angle, it naturally leads to nonlinear solutions. As shown in Fig. 4.3 (d), the power-dependent twist angles under different initial angles demonstrate the evolution from smooth nonlinear self-

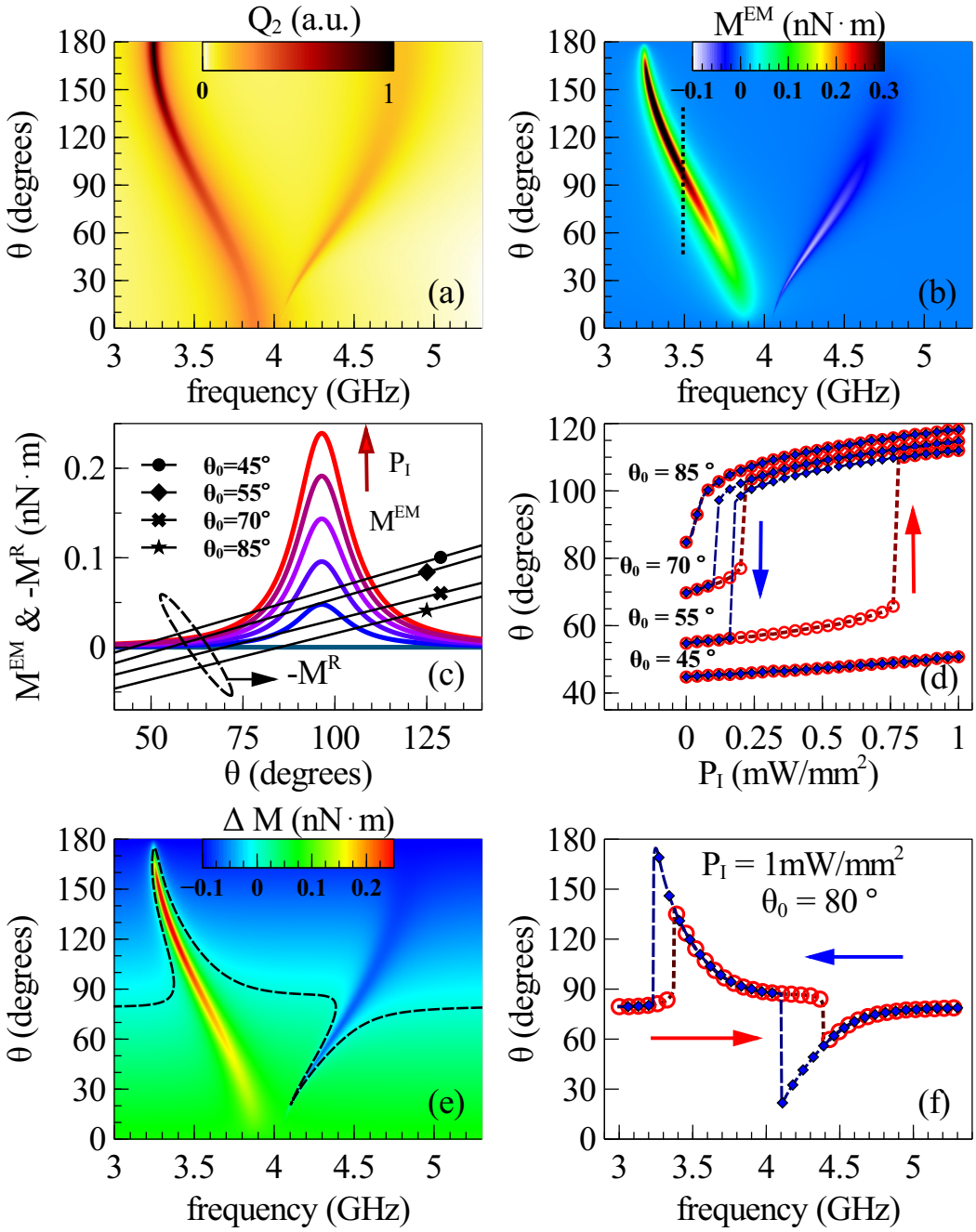

Figure 4.3: The principle of nonlinear response in chiral torsional meta-molecules. (a) The mode amplitude Q_2 and (b) the EM torque $\mathbf{M}^{\mathrm{EM}}$ of the top rotatable SRR. (c) The EM torque at 3.5 GHz for different pump powers from 0 to 1 $\mathrm{mW/mm^2}$ in 0.2 $\mathrm{mW/mm^2}$ steps, and the restoring torque for different initial twist angle θ_0; (d) the corresponding paths of power-dependent twist angles under different θ_0. (e) Spectrum of $\Delta M = M^{\mathrm{EM}} + M^{\mathrm{R}}$, with P_{I}=1mW/mm^2 and $\theta_0 = 80°$; (f) the corresponding frequency-dependent bistable path.

tuning to bistable response as θ_0 departs from the angle of maximum EM torque. In principle, as θ_0 moves further away from the resonance, more noticeable rotation and hysteresis effects are expected, but higher pump power is required (see the case for $\theta_0 = 45°$, in which the system can not show bistability within the limited power). Such evolution of the power-dependent nonlinear response can also be ob-

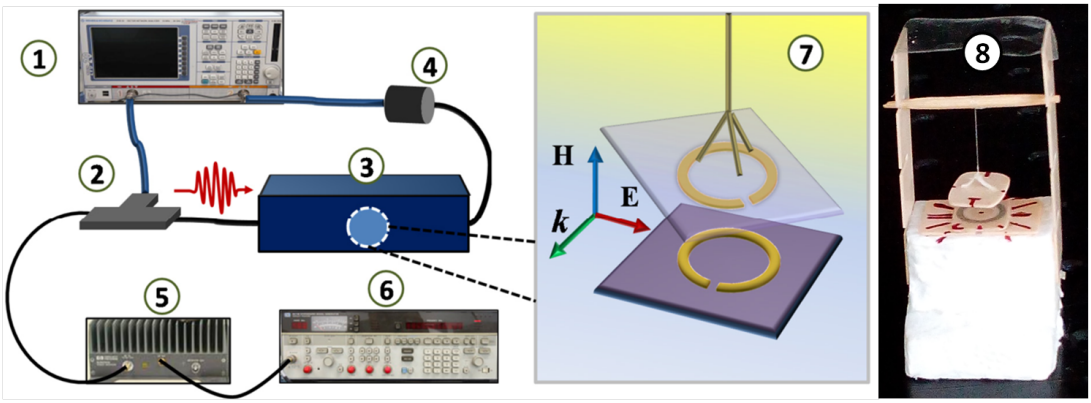

Figure 4.4: Schematic of the experimental set-up. The pump and probe signals are combined by a 3 dB combiner. The sample is positioned in the centre of the waveguide. 1: vector network analyser; 2: 3 dB combiner; 3: rectangular waveguide; 4: 20 dB attenuator; 5: power amplifier; 6: signal generator; 7: sample; 8: photograph of the sample.

served by fixing the initial twist angle but changing the pump frequency, as will be demonstrated in the experiment below. An alternative way to realize the nonlinear or bistable tuning is to change the pump frequency continuously while keeping the pump power fixed. As shown in Fig. 4.3 (e), the black dashed curve corresponds to the equilibrium points. As the pump frequency increases from lower frequency to higher frequency and regresses, a bistable path can be observed [see Fig. 4.3 (f)].

4.4 Experimental Verification

4.4.1 Experimental Setup and Measurement

To confirm the feasibility of the proposed nonlinear torsional meta-molecules, we carry out *a pump-probe microwave experiment*. To experimentally realise a strong nonlinear or even bistable effect, the restoring torque from the wire has to be sufficiently small so that the structure can be twisted by a large enough angle within the maximum available power. We found that rubber is a good candidate, since the shear modulus of rubber is of the order of 0.2 MPa – 2.4 MPa [386], which is at least three orders of magnitude smaller than it is for other polymers.

Schematic and a photograph of the experimental setup are shown in Fig. 4.4. We have used two separated copper SRRs (inner radius $r = 3.2$ mm, track width 1 mm, copper thickness 0.035 μm and slit width $g = 0.2$ mm) printed on Rogers R4003 substrates ($\epsilon_r = 3.5$, loss tangent 0.0027, substrate thickness 0.5 mm). The lower SRR is fixed and positioned at the centre of a WR229 rectangular waveguide [2.29 inches ($\sim$ 58.2 mm) $\times$ 1.145 inches ($\sim$ 29.1 mm)] with $\Phi = 0°$, and the top SRR is suspended with a thin rubber wire (radius $a = 50\mu$m, length $d = 20$ mm), so that it can rotate about the common axis. The two SRRs are aligned coaxially, with a face to face distance of 0.75 mm, separated by air. The horizontal positions of the SRRs are carefully adjusted and the initial twist angle θ_0 is set at around 70°. The mass of the suspended sample is 101 mg, which leads to a 6.1% elongation of the wire. The Young's modulus is thus estimated as 2.06 MPa, and the shear modulus follows as $G \approx 0.69$ MPa.

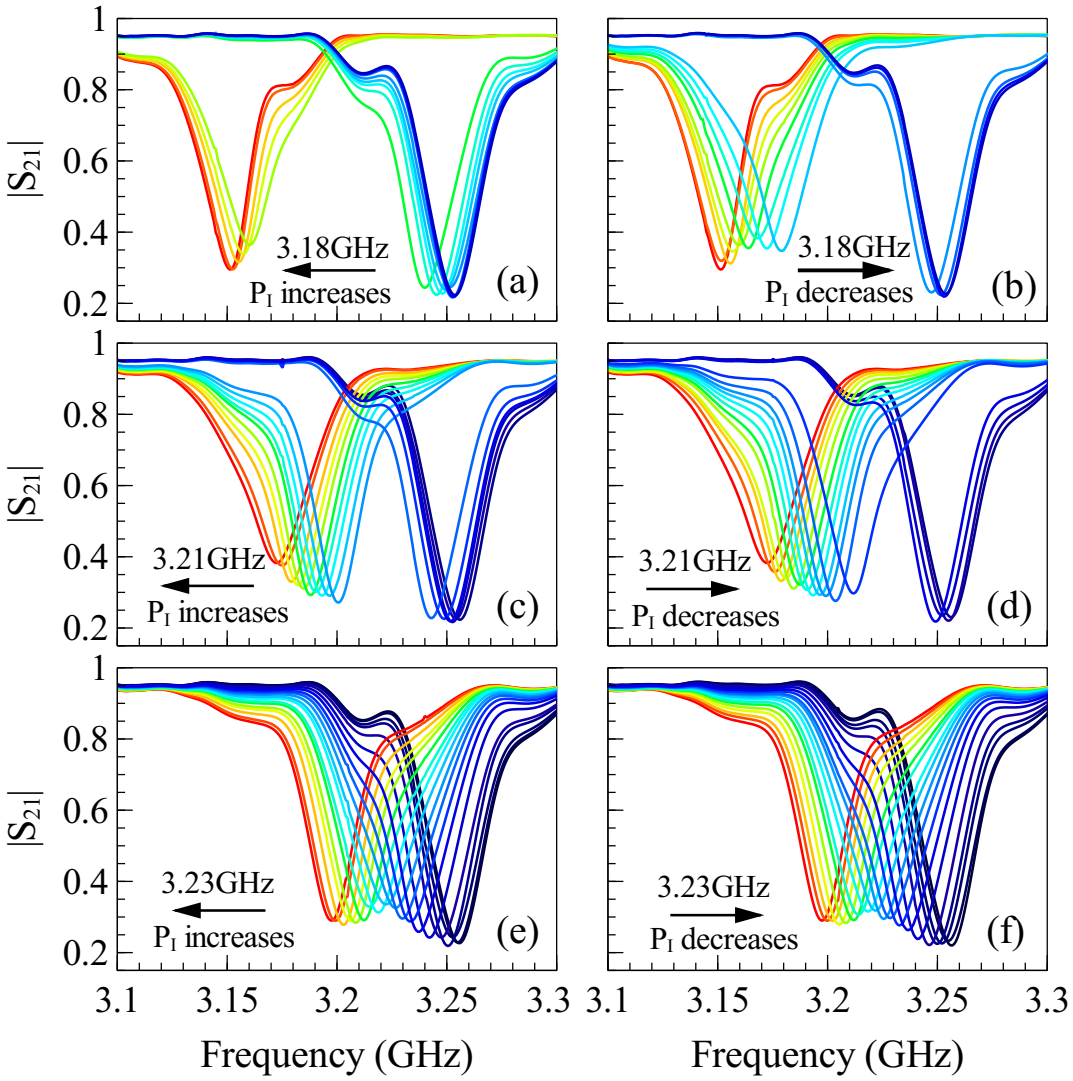

Figure 4.5: Experimental transmission coefficients $|S_{21}|$ for different detuned pump frequencies when the power (as is indicated by the color of curves) increases from minimum to maximum [for (a), (c) and (e)], then regresses from maximum to minimum [for (b), (d) and (f)]. The initial resonance locates around 3.256 GHz and the pump power is swept in 1 dB steps. (a) and (b) pump at 3.18 GHz, power changes from 15.2 dBm to 27.2 dBm; (c) and (d) pump at 3.21 GHz, power changes from 12.2 dBm to 27.2 dBm; (d) and (e) pump at 3.23 GHz, power changes from 15.2 dBm to 27.2 dBm. For large detuning [(a) and (b)], giant bistability can be obtained; as detuning decreases, the range of bistability decreases [(c) and (d)], and eventually reduces to monotonic self-tuning [(e) and (f)].

Since the mechanism of the nonlinear response is the dynamic feedback between electromagnetic and elastic properties, the experimental setup exhibits the same physics as the conceptual schematic in Fig. 4.2. The calculated torque is a Lorentz-like function and the maximum is around 0.8 nN·m. The maximum attractive force between the two SRRs is around 2 μN, which leads to a negligible elongation of the wire (0.012%); while the force in the lateral direction is around 0.1 μN, about 1000 times smaller than the gravitational force exerted on the sample, and thus it only gives rise to a tiny swing angle (0.056°).

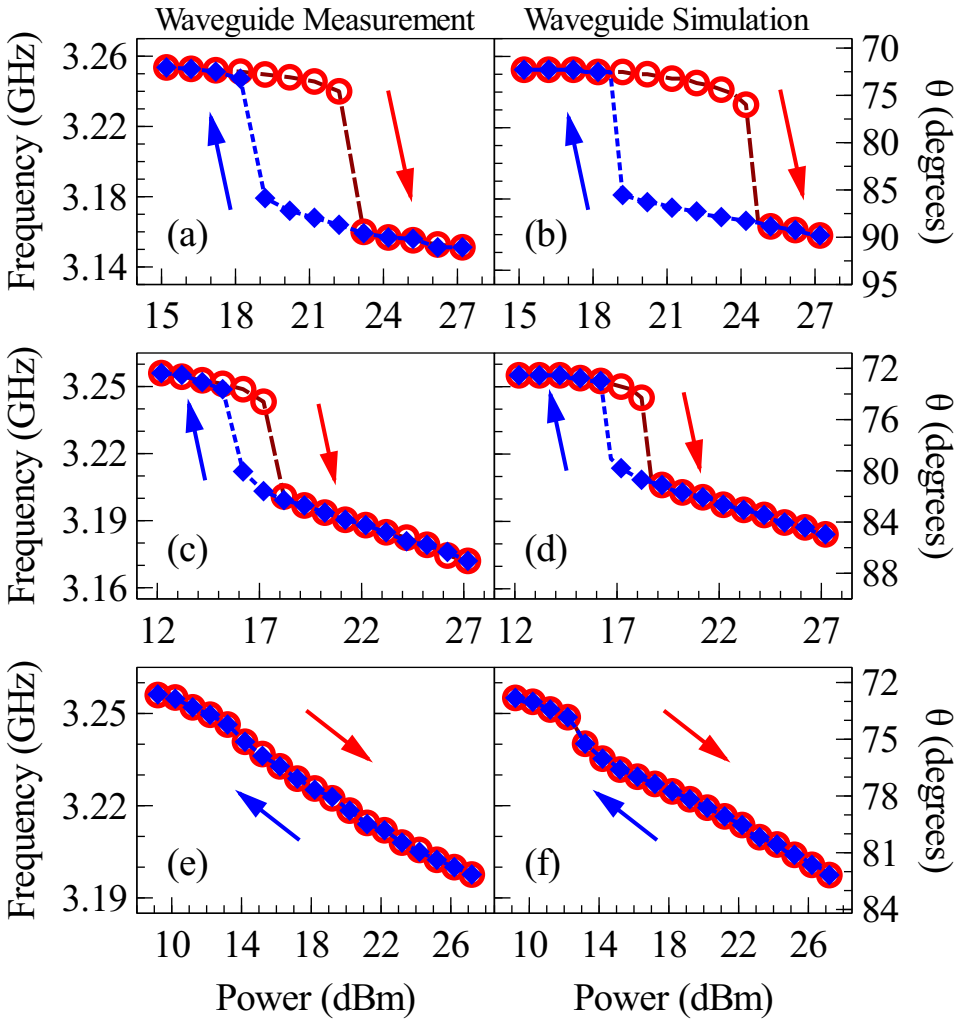

Figure 4.6: Comparison of experimentally (a), (c), (e) and numerically (b), (d), (f) calculated resonant frequency sweeps. The corresponding stable twist angles are shown on the right axes. (a) and (b) pump at 3.18 GHz; (c) and (d) pump at 3.21 GHz; (e) and (f) pump at 3.23 GHz.

The transmission spectrum measurements are performed by a vector network analyser (Rohde and Schwarz ZVB-20). The CW pump signal is generated by a signal generator (HP 8673B) and is further amplified by a power amplifier (HP 83020A) before being sent into the waveguide. Three pump frequencies (3.18, 3.21 and 3.23 GHz) are chosen in order to capture the evolution of the nonlinear response with different detuning from the initial resonance. The pump power is increased in 1 dB steps; for each step, the sample reaches steady state after 30 seconds. The mechanical rotation is quite significant and can be visually observed in the experiment, thus ruling out other possible nonlinear mechanisms such as heating.

The experimentally observed transmission spectra are shown in Fig. 4.5, and the corresponding resonant frequencies are depicted in Fig. 4.6 (a), (c) and (e), where the predicted evolution from bistability to smooth nonlinearity is clearly shown. The initial resonance (symmetric mode) without pump is located around 3.256 GHz, and it red-shifts as the pump power increases, which indicates that the twist angle is increased. When the pump frequency is at the red tail of the resonance, a large spectral

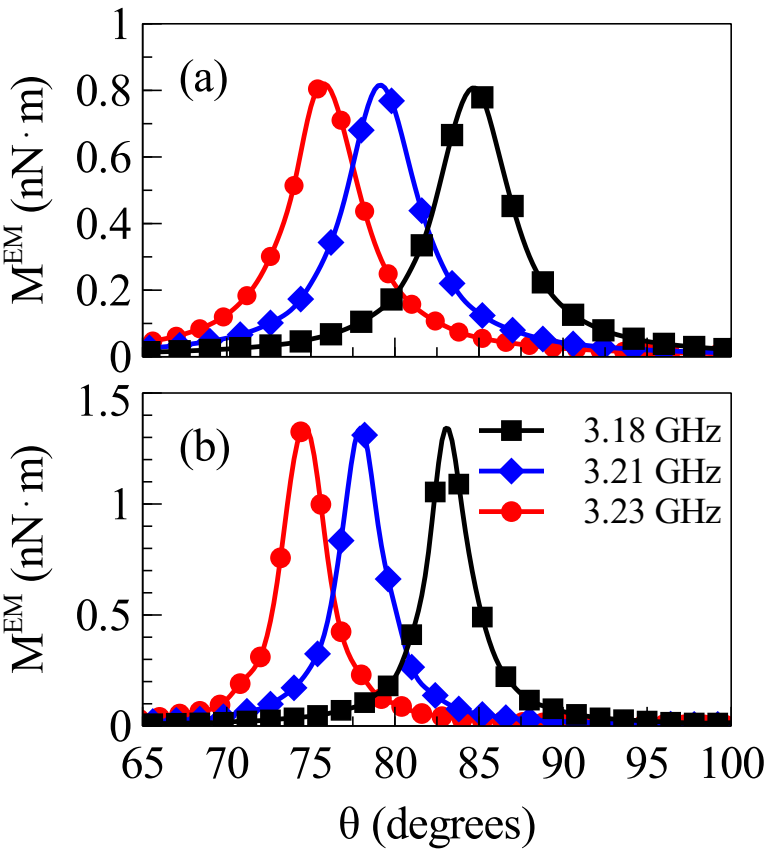

Figure 4.7: Mutual EM torque as a function of twist angle at different pump frequencies. (a) A single chiral torsional meta-molecule in a rectangular waveguide, and (b) a dilute periodic array of chiral torsional meta-molecules, with periodicity 45 mm in the lateral directions and one layer in the propagating direction of EM wave. The EM torques shown correspond to a 1W power pumped into the waveguide or one unit cell. The markers are included only to delineate the plots.

"jump" (about three times of the resonance linewidth) can be observed when the pump power passes a certain threshold value [Fig. 4.6 (a)]. The thresholds are different for increasing and decreasing pump powers. As the pump frequency approaches to the initial resonance, the spectral "jump" becomes smaller [Fig. 4.6 (c)] and finally disappears [Fig. 4.6 (e)]. We also observed similar effects (not shown) when the pump frequency is at the red tail of the antisymmetric mode, in which case the two resonances approach each other due to the opposite direction of the EM torque.

4.4.2 Comparison with Simulation and Discussion

To further validate the observed effect, we numerically simulated the exact experimental geometry by taking into account the effect of the waveguide using CST Microwave Studio. A pair of split-ring resonators are modeled in a rectangular waveguide, and the system is excited with the lowest order waveguide mode (see Sec. A.4 for more details). The transmission and reflection spectra, and the field distribution under different twist angles are calculated numerically. The EM torque exerted on the top SRR is calculated with the Maxwell stress tensor, as shown in Fig. 4.7 (a). Once the twist angle-dependent torque is known, the power-dependent twist angle

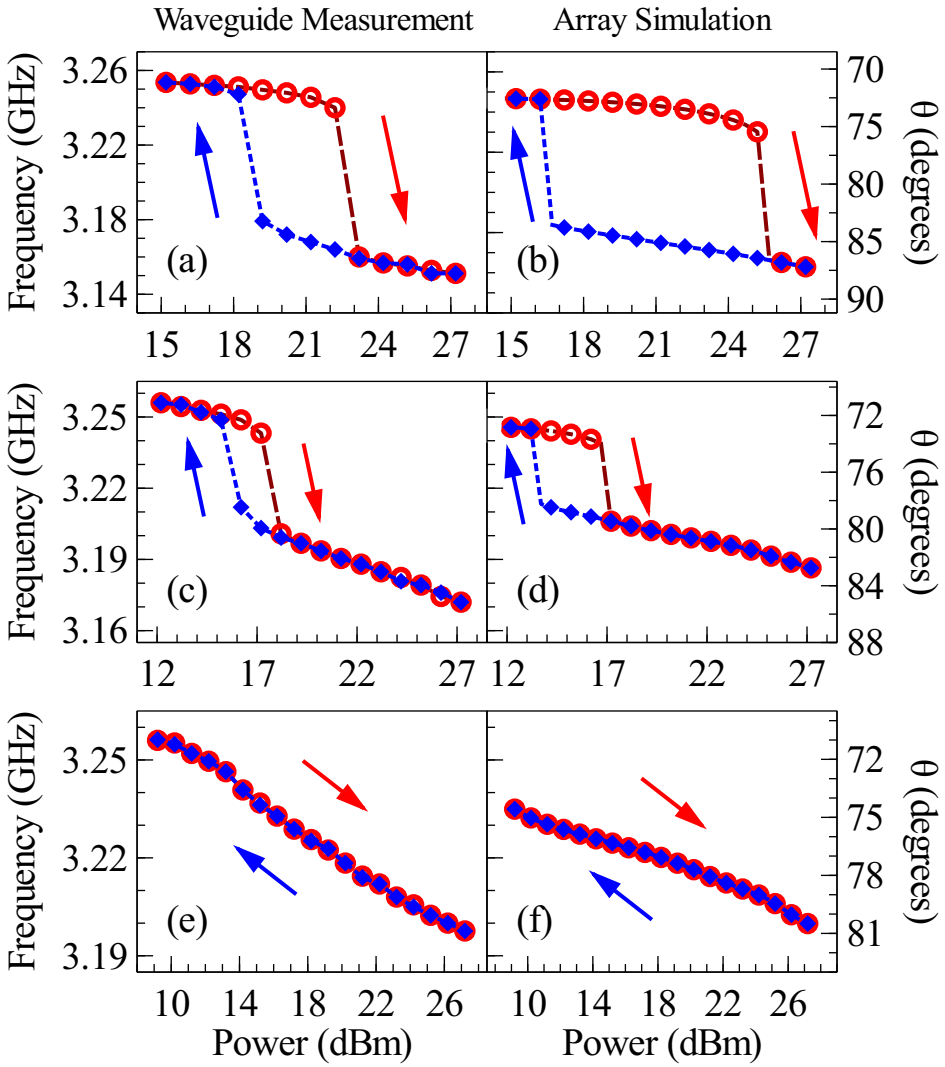

Figure 4.8: Comparisons of resonant frequencies demonstrated in a waveguide experiment and numerically calculated for an array with periodicity of 45 mm in the lateral direction and one layer in the propagating direction. (a) and (b) pump at 3.18 GHz; (c) and (d) pump at 3.21 GHz; (e) and (f) pump at 3.23 GHz. The stable twist angles for the array system are shown on the right axes. The power in the array is the power incident on each unit cell.

can be found by solving the nonlinear equation (4.9). The estimated optimum initial twist angle is around 72.5°, and the maximum twist angles obtained for the three pump frequencies (3.18 GHz, 3.21 GHz and 3.23 GHz) are around 90°, 85° and 82°, respectively. Finally we remap these angles back to the corresponding resonant frequencies according to the simulation spectra. We found very nice agreement between the measurement and simulation [see Fig. 4.6 (b), (d) and (f)], thus confirming that our numerical model has reproduced the experimental configuration with acceptable accuracy.

Due to the formation of image currents within the waveguide walls, a single meta-molecule within a waveguide has virtual neighbours. Just as in an array, there will be near-field interaction with these virtual neighbours, with some alteration due to the mirror reflections. This suggests that the waveguide system is analogous to an array, at least for relatively dilute lattice spacing. Indeed, when the neighbouring

interaction is weak, the nonlinearity mainly arises from individual meta-molecules; in this case, the behaviour in an array will not show qualitative difference from a single meta-molecule. The detailed study on the influence of neighbouring interaction will be present in Chapter 6. Here, we use full numerical simulation to model a dilute array with thickness of a single cell and periodicity of 45 mm in the transverse directions, arranged as in Fig. 4.2. The parameters of the meta-atoms used in the simulation are the same as in the experiment. The array and the waveguide experiment show quite good qualitative agreement (see Fig. 4.7 for the EM torque and Fig. 4.8 (b), (d) and (f) for the power-dependent resonance).

4.5 Summary

In this chapter, we proposed and verified experimentally a new concept for achieving strong nonlinear coupling between the electromagnetic and elastic properties in meta-molecules. The novel nonlinear meta-molecule described in this work proved to possess sensitive elastic feedback, bringing nonlinearity to the interaction of EM modes of the resonators. The resulting self-tuning and bistability of the response were successfully observed in experiments and it turns out that these results can be accurately predicted with theoretical modeling. We also note that this structure is chiral (except in the high symmetry cases of 0° and 180° angle between the rings), it should also exhibit nonlinear optical activity, an effect which is relatively weak in natural media [387], but can be quite strong in metamaterials [189]. This will be further discussed in the next chapter.

Although the experimental demonstration in this work was performed in the microwave frequency range, we expect that the general principle of operation is valid at any frequency where a resonant response can be excited in such or similar metamaterials elements, e.g. in the recently developed plasmonic chiral molecules based on DNA origami [136,157,158,269,270], and the way to analyse the same phenomena in THz or optical range is conceptually the same. Our study indicates that chiral torsional meta-molecule is an ideal platform for studying slow nonlinear effects in metamaterials.

Statement

This chapter was written based on the work published in the journal paper:
Mingkai Liu, Yue Sun, David A. Powell, Ilya V. Shadrivov, Mikhail Lapine, Ross C. McPhedran, and Yuri. S. Kivshar, "Nonlinear response via intrinsic rotation in metamaterials ", *Phys. Rev. B* **87**, p 235126-6 (2013).
In this work, M. Lapine, D. A. Powell, Y. Sun and I discussed and conceived the idea. I developed the theory, performed the simulation and experiment. Y. Sun helped with the numerical simulation; D. A. Powell and I. V. Shadrivov helped with the experiment.

Self-oscillations in Nonlinear Torsional Meta-molecules

5.1 Introduction

In Chapter 4, chiral torsional metamaterials were studied, and their *nonlinear stationary* properties were experimentally demonstrated. However, we expect that their *nonlinear dynamic* behaviour should also be nontrivial, introducing a new bridge between the spectral domain and time domain properties. We recall that nonlinear dynamic phenomena, such as self-oscillations and chaos, have been widely observed in different types of nonlinear systems [388–390] [see Fig. 5.1 (a) and (b) for example]. Recent research in optomechanics also demonstrated exotic dynamic coupling effects between optical resonance and mechanical vibration [318, 323, 332, 383] (for a more detailed introduction, see Section 1.5.4).

In optomechanical systems, the dynamic coupling between optical resonance and mechanical oscillation requires a phase lag ϕ between the optical force F and mechanical vibration x [see Fig. 5.1 (c) and (d)]. For a small amplitude oscillation, this effect can be explained approximately as

$$x = x_0 + A\cos(\Omega t), \tag{5.1}$$

$$F(t) \propto \int_{-\infty}^{t} I(t')e^{-(t-t')/\tau}\mathrm{d}t' \propto F_0\cos(\Omega t - \phi), \tag{5.2}$$

where I is the optical field intensity and τ is the time lag between the optical field and mechanical motion. The time lag is responsible for the phase lag ϕ and directly leads to nonzero work done by the optical force in each oscillation cycle

$$W = \int_0^T F(t)\dot{x}(t)\mathrm{d}t \propto F_0 A\sin\phi. \tag{5.3}$$

Depending on the detuning of the pump with respect to the resonance [Fig. 5.1 (c)], such nonzero work can be positive or negative and would be responsible for self-oscillations [336, 337] or self-cooling [320, 333] effects, respectively. The phase lag can be introduced by either retarded radiation pressure or bolometric force [337, 393, 394]; the former mechanism requires the spectral linewidth of the optical resonance to be comparable with the mechanical oscillation frequency, i.e. the quality factor of optical resonance need to be sufficiently high; while the latter arises from the photothermal effect, with a typical response time at the sub-millisecond scale, which can be significant for micro/nano mechanical oscillators [337, 395].

However, the condition to realize self-oscillations in previous optomechanical sys-

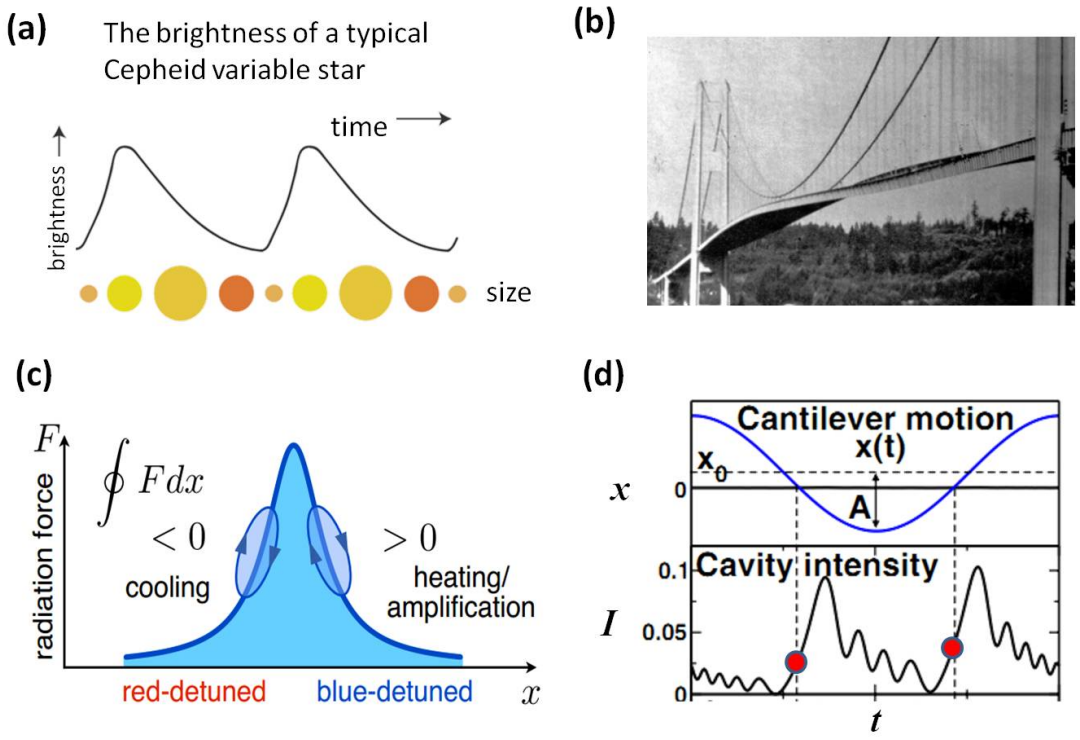

Figure 5.1: (a) Self-induced periodic brightness and size changes of a typical Cepheid variable star [391]. (b) The first suspension bridge over the Tacoma Narrows collapsed due to self-oscillations in response to winds [392]. (c) Detuning of pump frequency can lead to self-cooling or self-amplification in optomechanical systems [319]. (d) Dynamics of the cantilever motion and the retarded optical field intensity in a cavity; as can be seen from the red-circles, the intensity not only depends on the cantilever displacement but also on the direction and speed of the motion [336].

tems can not be satisfied by the dimer torsional meta-molecule we studied in Chapter 4, since the Q factors of EM resonances in meta-molecules are very low, which means the lifetime of EM resonance is much shorter than the mechanical oscillation period. In such cases, the phase lag (and thus the work done by EM torque) is negligible, with damped oscillations being the only type of dynamics observable in a system with a single degree of freedom.

In this chapter, we present a theoretical study of the nonlinear dynamical properties of torsional meta-molecules and demonstrate how to realise and actively control novel effects such as self-oscillations and dynamic nonlinear optical activity – an effect rarely found in natural chiral molecules. Contrary to most previously studied optomechanical systems, our structure can support self-oscillations in a highly damped environment (e.g. in a very viscous liquid), and its behaviour can be sensitively manipulated by the polarization of EM waves.

5.2 Torsional Trimer Chiral Meta-molecules

The torsional meta-molecules studied are shown in Fig. 5.2 (a). Each meta-molecule consists of three coaxial split-ring resonators (SRRs) connected by elastic wires; the twist angles with respect to the y axis are θ_m, $m \in [1,2,3]$. We assume that the first ring is fixed at $\theta_1 = 0^\circ$ to prevent the whole structure from rotating (as we showed

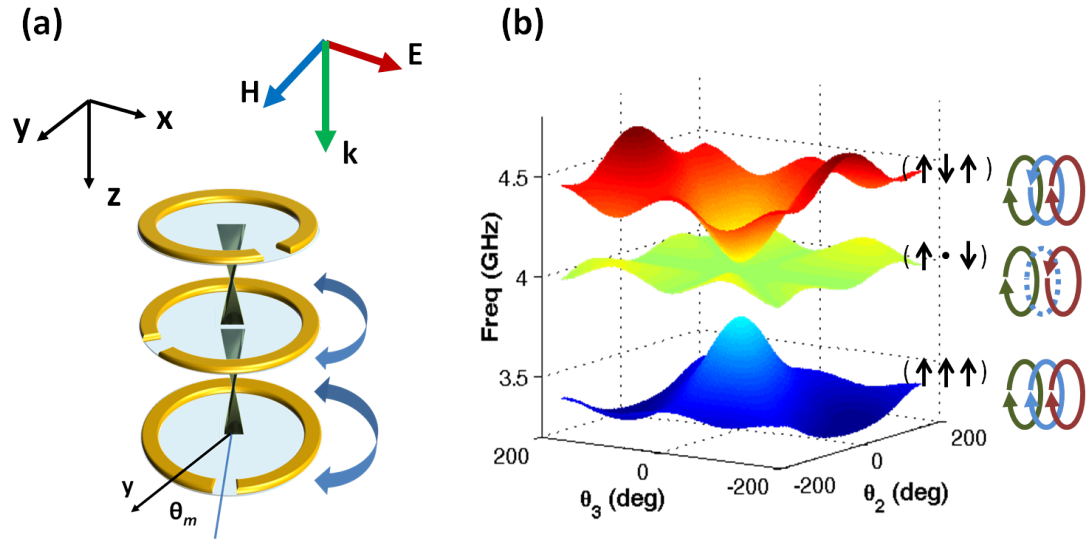

Figure 5.2: (a) Schematic of the torsional trimer meta-molecule and (b) the three eigen-frequencies it supports. The meta-molecule consists of three coaxial split-ring resonators connected elastically. The first ring is fixed, while the second and the third rings are free to rotate about the common axis z. The twist angles θ strongly modify the eigenfrequencies and are defined as the angle between the slit and the y axis.

in Chapter. 3), while the second and third rings are free to rotate about the common axis z.

When the meta-molecule is illuminated with a linearly polarized plane wave propagating in the z direction, three hybrid resonances with different mode symmetries can be excited due to near-field interaction, as shown in Fig. 5.2 (b). The eigenmodes in Fig. 5.2 (b) are calculated with our semi-analytical model by finding the singularities of the effective impedance of the system [Eq. (A.15)], which shows the change of resonances with respect to the two twist angles θ_2 and θ_3. We choose the radii of thin SRRs as 6 mm, slit width 1 mm, and inter-ring distance 3 mm in the calculation, and we will use the same parameters for SRRs and inter-ring distance in all the calculation shown below.

The charges and currents induced in the SRRs produce EM forces acting on each SRR. We restrict the allowed movement in our design to azimuthal rotation, where movement in the lateral and axial directions is usually negligible in comparison, and may be explicitly suppressed by the design if required, as was discussed in Chapter 4. For simplicity, we use a perfect electric conductor as the material for the SRRs in the simulation, so only the radiative component of the EM force is taken into account.

The mechanical response time of our design (of the order of 1s) is much slower than the lifetime of the low Q EM resonances (of the order of 10^{-7}s $\sim 10^{-8}$s), thus the resonant EM torques experienced by the rings can be considered as instantaneous and are determined by the twist angles. This approximation allows us to calculate the EM torque from the stationary response of the system. For the double ring systems with only one degree of freedom considered in Chapter 4, such "displacement-determined" torque means that the net work done in each oscillation cycle is zero, and the system will become stable after undergoing damped oscillation. However, in our current system where two degrees of freedom are involved, it becomes possible to achieve self-oscillations when there is a time delay between the movements of the

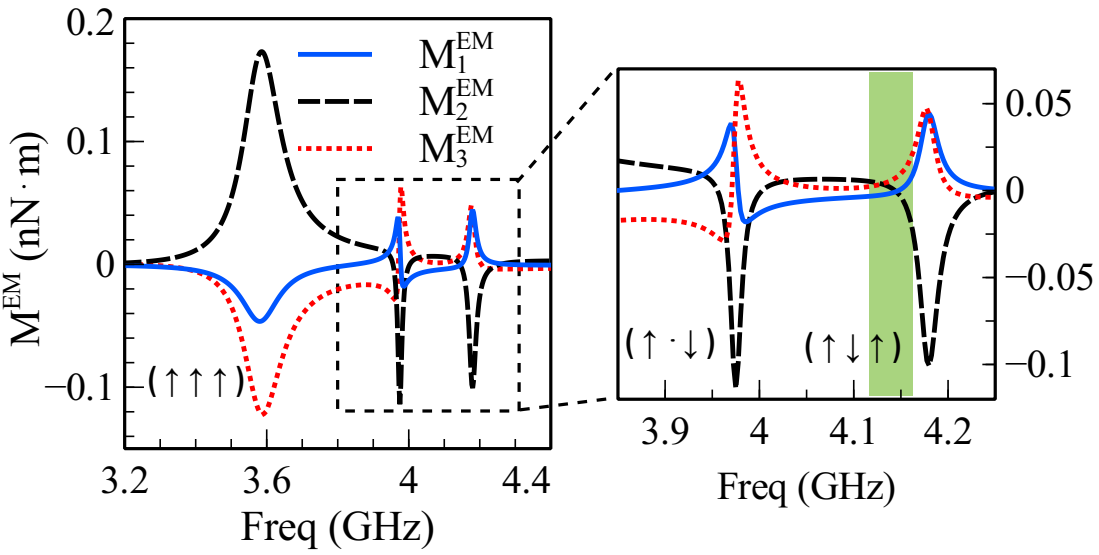

Figure 5.3: Electromagnetic torques M^{EM} experienced by the three rings with configuration $(\theta_1, \theta_2, \theta_3) = (0°, 30°, -30°)$. The incident wave propagates along the z direction, with its electric field component in the x direction ($\Phi = 0°$). The torques are normalised to a power density of $1\,mW/mm^2$. Inset on the right magnifies the details within the dashed rectangle, and the green shading shows the regime where self-oscillations can exist.

two rotatable rings. Such a delay produces loop trajectories in the phase diagram (as will be further showed in the follow sections), introducing non-zero work done by the EM torques to compensate the mechanical damping.

To provide a quantitative evaluation of the EM torques M^{EM} experienced by the torsional meta-molecules, we employ the semi-analytical model used in Chapter. 4 and take into account the contribution from the first three eigenmodes (See Fig. A.1 in Appendix A for reference). In the frequency regime of interest, the spectral response is dominated by the interaction of the first order eigenmodes (magnetic dipole modes), while higher order modes (electric dipole and electric quadrupole modes) provide minor corrections and enable more accurate evaluation. Since we have three SRRs and three eigenmodes involved, the coefficients of the effective impedance $Z_{m,n}^{(p,q)}$ can then be written in a 9×9 impedance matrix, and the spectral response of mode amplitude $Q(\omega)$ and the electromagnetic torque M^{EM} can be solved numerically. The full expressions of these terms are given in Sec. A.1.2 and Sec. A.2.2.

In our design, the SRRs are connected with cylindrical thin elastic wires, and the restoring torques are approximated by Hooke's law: $M_2^R = -\kappa\Big[2(\theta_2 - \theta_{0,2}) - (\theta_3 - \theta_{0,3})\Big]$, $M_3^R = -\kappa\Big[(\theta_3 - \theta_{0,3}) - (\theta_2 - \theta_{0,2})\Big]$, with $\kappa = \pi a^4 G/(2d)$; a and d are the radius and the length of the wires, respectively; G is the shear modulus and θ_0 is the initial twist angle. The coupled dynamic equations of the system can then be written as

$$-i\omega \sum_{q,n} Z_{m,n}^{(p,q)} Q_n^{(q)} = \mathcal{E}_m^{(p)}, \tag{5.4}$$

$$\ddot{\theta}_m + \Gamma\dot{\theta}_m = \frac{1}{I} M_m. \tag{5.5}$$

The upper scripts denote the p-th and q-th eigenmodes and the lower scripts denote the m-th and n-th SRRs. I is the moment of inertia and Γ is the damping coefficient. $M_m = (\mathbf{M}_m^{\mathrm{EM}} + \mathbf{M}_m^{\mathrm{R}}) \cdot \hat{\mathbf{z}}$ is the total torque experienced by the m-th SRR.

As an example, we model the EM torque experienced by a torsional meta-molecule, with twist angles $(\theta_1, \theta_2, \theta_3) = (0^\circ, 30^\circ, -30^\circ)$ (see Fig. 5.3). As our previous analysis of dimer meta-molecules showed, the EM torques experienced by a dimer chiral meta-molecule are dominated by the internal part M^{int}, whose directions are determined by the mode symmetry. However, in trimer or oligomer meta-molecules, the situation is more complicated. Since the EM torque experienced by an SRR is the sum of the effect from all other rings, its direction depends not only on the mode symmetry but the relative amplitude of resonance on each ring as well. Therefore, the direction of EM torque on the red side and blue side of a resonance can become opposite due to the change of relative amplitude, showing highly asymmetric Fano lineshapes, as can be seen from the inset of Fig. 5.3.

5.3 Self-oscillations and Stability Analysis

Our model provides a powerful tool to study the dynamics of meta-molecules with multiple degrees of freedom. By solving the coupled equations, we can study the dynamics of the system under different pump frequencies and power densities $(f_{\mathrm{P}}, P_{\mathrm{I}})$. In the calculation, we further assumed that each SRR is encapsulated within a thin polyurethane foam disk (permittivity $\epsilon \approx 1$). The moment of inertia of each encapsulated SRR is estimated as $I \approx 3.755 \times 10^{-10}\,\mathrm{kg \cdot m^2}$. The radius and shear modulus of elastic wires are chosen to be $50\,\mu$m and 1 MPa, respectively, similar to the ones used in Chapter 4 (where we used 0.6 MPa for shear modulus). For each pump frequency, the power density is increased from zero to the maximum ($60\,\mathrm{mW/mm^2}$) and then decreased back to zero, with $1\,\mathrm{mW/mm^2}$ steps.

The mutual twist angles θ_2 and θ_3 change under the effect of EM torques. Generally, the structure can become stable after undergoing damped oscillation, and strong nonlinear stationary responses such as self-tuning, bistability or even tristability can be found near the resonances. However, a distinct feature of the trimer meta-molecules as compared with dimer meta-molecules, is that *the trimer system can become unstable and exhibit self-oscillations*.

As a typical example, Fig. 5.4 (a) and (b) depict the nonlinear response of a meta-molecule for different values of mechanical damping. The initial twist angles are the same as in Fig. 5.3. The regime and amplitude of self-oscillations are denoted with the colour scale. This regime is located on the red side of the hybrid resonance $(\uparrow\downarrow\uparrow)$ (see green shading in Fig. 5.3), which shows a strong dependency on both pump frequency and power density. As the mechanical damping is increased, self-oscillations quench quickly in the frequency range from 4.12 GHz to 4.14 GHz, and they finally reduce to a purely stationary bistable response, with the threshold power densities of bistable hopping shown by orange circles. On the contrary, the regime of self-oscillations observed between 4.14 GHz and 4.16 GHz shows only a small decrease even when the mechanical damping is considerable (note that the mechanical damping $\Gamma = 1.42$ Hz used in Fig. 5.4 (b) is calculated based on the viscosity of water). For lower damping environment, periodic self-oscillations will evolve into aperiodic oscillations or even chaotic effects [see Fig. 5.4 (c)]. In the following discussion, we focus on periodic self-oscillations.

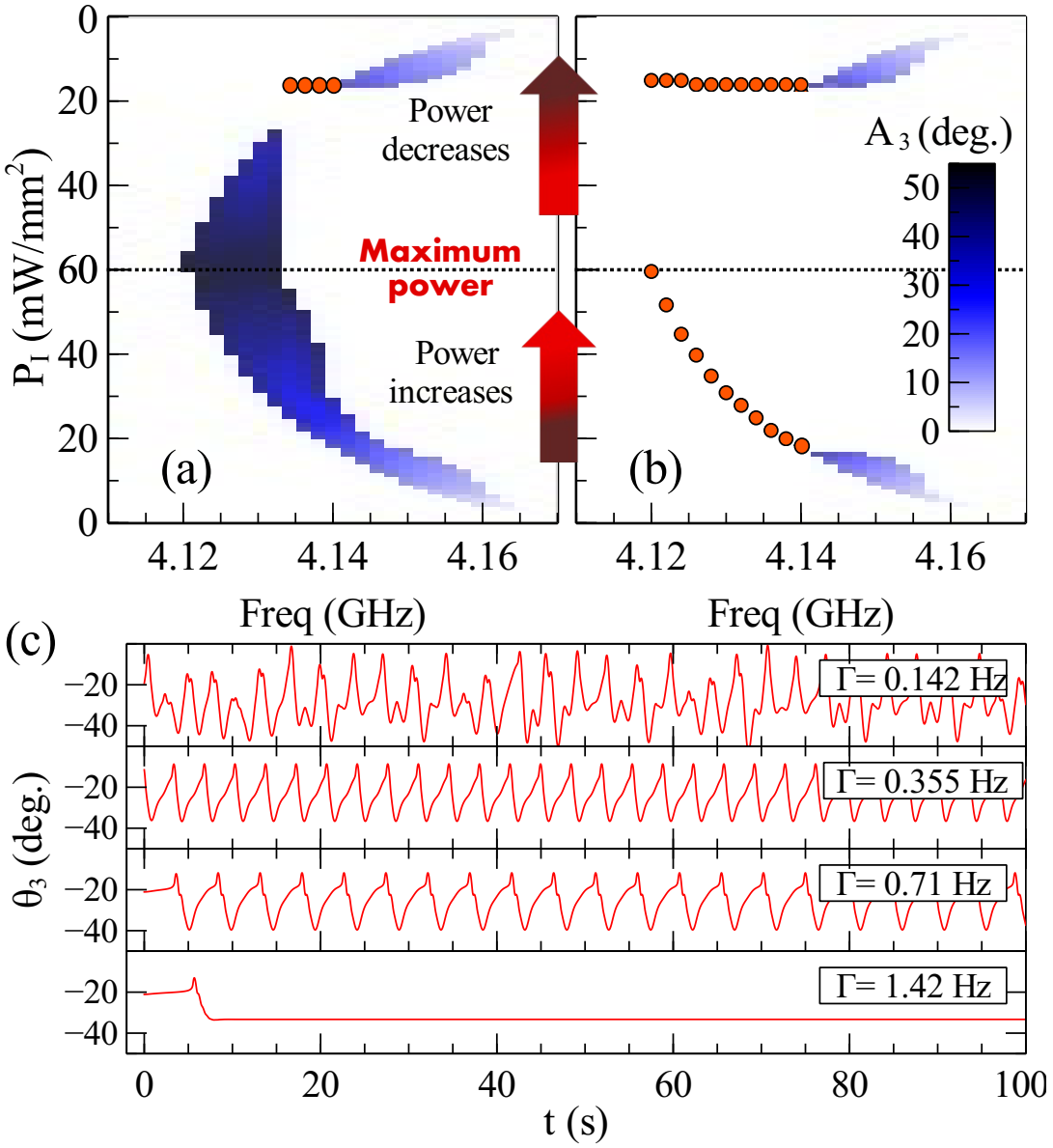

Figure 5.4: Nonlinear behaviour as a function of pump frequency and power density, under different damping coefficients. (a) and (b) The regime and amplitude of self-oscillations are denoted with colour scale. A_3 is defined as the peak amplitude of the oscillations of θ_3. The arrows denote the direction of power change, which increases from zero to 60 mW/mm^2 and then decreases back to zero. The orange circles show the threshold power densities of bistable hopping. Results with different damping coefficients are compared, (a) $\Gamma = 0.71$ Hz and (b) $\Gamma = 1.42$ Hz. (c) Nonlinear dynamics at frequency 4.134 GHz and threshold pump power 25 mW/mm^2; as damping increases, it evolves from aperiodic oscillation to periodic oscillation, and finally to a stable state after a damping process.

To better understand these intriguing phenomena, we analyse the local stability around the equilibria. Since the torque experienced by SRR m $(m = 2, 3)$ is simultaneously determined by θ_2 and θ_3, the equilibrium positions of the trimer meta-molecule are the crossovers of two curves: $M_2(\theta_2, \theta_3, f_P, P_I) = 0$ and $M_3(\theta_2, \theta_3, f_P, P_I)$=0. With the semi-analytical model, we can calculate the torque M_m for a given pump frequency as a function of the two twist angles, and study the evolution of equilibria

with respect to the power density P_{I}. Accordingly, the phase diagram of the system $(\theta_2, \theta_3, \dot{\theta}_2, \dot{\theta}_3)$ can be projected on the (θ_2, θ_3) plane to show the dynamic trajectory.

The local stability of a system can be estimated by analysing the eigenvalues of its linear variational dynamic equations [389]; in our case the coefficients can be written in a compact matrix form:

$$\begin{bmatrix} \frac{\partial F_2}{\partial \theta_2} & \frac{\partial F_2}{\partial \Omega_2} & \frac{\partial F_2}{\partial \theta_3} & \frac{\partial F_2}{\partial \Omega_3} \\ \frac{\partial G_2}{\partial \theta_2} & \frac{\partial G_2}{\partial \Omega_2} & \frac{\partial G_2}{\partial \theta_3} & \frac{\partial G_2}{\partial \Omega_3} \\ \frac{\partial F_3}{\partial \theta_2} & \frac{\partial F_3}{\partial \Omega_2} & \frac{\partial F_3}{\partial \theta_3} & \frac{\partial F_3}{\partial \Omega_3} \\ \frac{\partial G_3}{\partial \theta_2} & \frac{\partial G_3}{\partial \Omega_2} & \frac{\partial G_3}{\partial \theta_3} & \frac{\partial G_3}{\partial \Omega_3} \end{bmatrix} = \begin{bmatrix} 0 & 1 & 0 & 0 \\ C_1 & -\Gamma & C_2 & 0 \\ 0 & 0 & 0 & 1 \\ C_3 & 0 & C_4 & -\Gamma \end{bmatrix}, \tag{5.6}$$

with $F_{2(3)} = \Omega_{2(3)} = \dot{\theta}_{2(3)}$, and $G_{2(3)} = \dot{\Omega}_{2(3)} = \ddot{\theta}_{2(3)} = M_{2(3)}/I - \Gamma\Omega_{2(3)}$. The eigenvalues of the matrix have explicit expressions

$$\begin{aligned} \lambda_{1,2} &= \frac{-\Gamma}{2} \pm \left\{ \frac{(C_1 + C_4)}{2} + \frac{\Gamma^2}{4} + \frac{1}{2}\left[(C_1 - C_4)^2 + 4C_2C_3\right]^{1/2} \right\}^{1/2}, \\ \lambda_{3,4} &= \frac{-\Gamma}{2} \pm \left\{ \frac{(C_1 + C_4)}{2} + \frac{\Gamma^2}{4} - \frac{1}{2}\left[(C_1 - C_4)^2 + 4C_2C_3\right]^{1/2} \right\}^{1/2}. \end{aligned} \tag{5.7}$$

According to our calculation, as long as mechanical damping exists, all four eigenvalues have non-zero real parts, i.e. the equilibria are *hyperbolic* and thus the linear variational equations can correctly represent our nonlinear system locally [389]. When all four eigenvalues have negative real parts, the equilibrium point is locally stable; otherwise, the equilibrium is unstable.

By analysing the evolution of the equilibria, we found that the distinct behaviour of self-oscillations shown above corresponds to two different mechanisms. To better demonstrate them, we depict the nonlinear regimes for two different frequencies 4.134 GHz and 4.15 GHz in Fig. 5.5 (a) and (b), respectively. For clarity, we only show the evolution of θ_3. Red and blue colours represent increasing and decreasing power density, respectively. The red solid circles and blue empty circles denote the stable positions of the system, while the dashed and dotted lines show the boundaries of self-oscillations when the damping coefficient $\Gamma = 0.71$ Hz.

5.3.1 Self-oscillations Resulting from Limited Local Stability

For the case of 4.134 GHz, self-oscillations occur due to the limited local stability of the equilibria. As shown in Fig. 5.5 (a), when the power density increases and surpasses the threshold value around P_{I}=25 mW/mm^2, the first branch of stable equilibria ends. The system then starts to "wander" until it reaches a new state. We notice that there exists another branch of locally stable equilibria nearby, which the system could reach after damped oscillation. This is exactly what we found in Fig. 5.5 (b), where the system shows only a stationary bistable response at this frequency. This process is further shown with the dashed trajectory in Fig. 5.5 (c), where the stable equilibria S_{A} and S_{B} correspond to the ones shown in Fig. 5.5 (a).

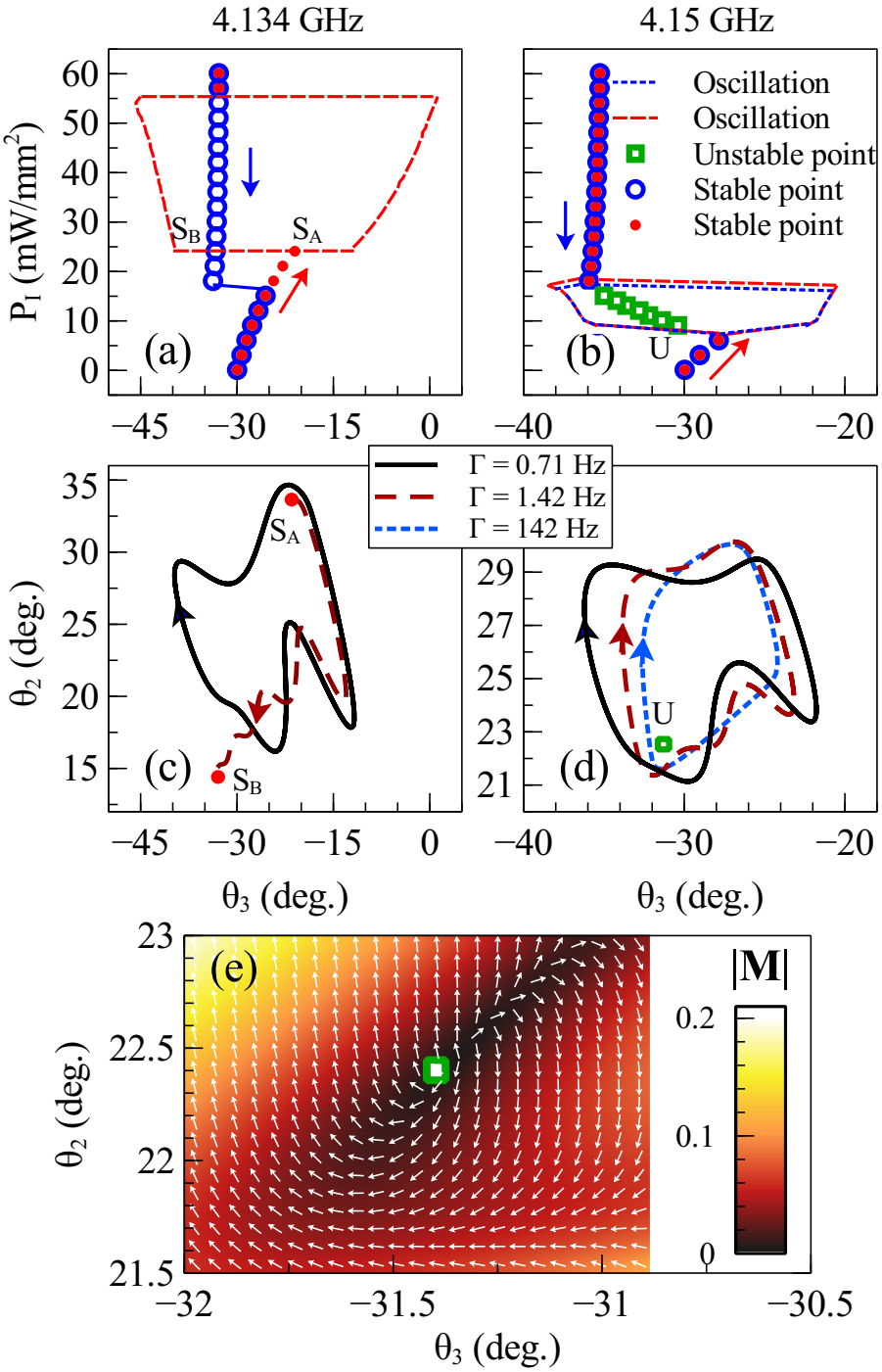

Figure 5.5: Evolution of the system at two different pump frequencies: (a) 4.134 GHz and (b) 4.15 GHz. The red solid circles and blue empty circles denote the stable equilibria during the process of increasing and decreasing power density, respectively. Green squares are the unstable equilibria. The red dashed curves and blue dotted curves show the boundaries of self-oscillation under the damping factor $\Gamma = 0.71$ Hz. The trajectories at the threshold power density of transition: (c) 4.134 GHz, P_I =25 mW/mm^2 and (d) 4.15 GHz, P_I =9 mW/mm^2. Damping factor $\Gamma = 1.42$ Hz is calculated based on the viscosity of water. S_A, S_B and U correspond to the equilibria denoted in (a) and (b). (e) The diagram of torque $\mathbf{M} = M_2\hat{\mathbf{e}}_{\theta 2} + M_3\hat{\mathbf{e}}_{\theta 3}$ near the equilibrium U shown in (d). The vectors show the direction of $\mathbf{M}$.

However, for smaller damping, the trajectory does not end at stable equilibrium S_B but develops into a limit cycle, as denoted by the black curve in Fig. 5.5 (c). This is because the equilibria are only locally stable. For smaller damping, the system can accumulate enough kinetic energy during the transition process to escape from the attraction of the stable equilibria. A limit cycle finally forms when the net work done by the EM torque over an oscillation period is balanced by the mechanical damping. The self-oscillations end as power further increases to such an extent that the equilibria have enough attraction power. Then the trajectory falls into the second branch of stable equilibria. As the power decreases from maximum to minimum, the system shows only a stationary nonlinear response since it does not posses enough kinetic energy to excite self-oscillations. The trajectory then follows the second branch of stable equilibria, until it reaches the bistable hopping threshold (the end of the second brand of stable equilibria) around P_I=18 mW/mm^2 and jumps back to the first branch of stable equilibria, as shown by the blue empty circles. This explains the asymmetric feature shown in Fig. 5.4.

5.3.2 Self-oscillations due to Local Instability

In the situation of 4.15 GHz, there are also two branches of stable equilibria, directly corresponding to the stationary nonlinear response of the system. But the mechanism of self-oscillations is very different. As shown in Fig. 5.5 (b), when the first branch of stable equilibria ends at around P_I =9 mW/mm^2, the system falls into a nearby branch of equilibria which is locally *unstable*, as denoted by the green squares. The system develops limit cycles until the second branch of stable equilibria is reached at around P_I =17 mW/mm^2. In this case, since the excitation of self-oscillations is due to local instability and does not require any initial kinetic energy, it *reoccurs* within the same range when power decreases from maximum to minimum.

One important feature of this mechanism is that the local instability is extremely robust against damping. Both local stability analysis and dynamic calculations show that self-oscillations remain even when the mechanical damping is further increased by orders of magnitude, as shown in Fig. 5.5 (d), dotted line. We found that the projected trajectories gradually converge to the blue-dotted one (Γ = 142 Hz) as Γ increases, even though the frequency of oscillation decreases significantly. This intriguing property can be visualized by plotting the torques M_2 and M_3 in a two dimensional vector form: $\mathbf{M} = M_2\hat{\mathbf{e}}_{\theta 2} + M_3\hat{\mathbf{e}}_{\theta 3}$, where $\hat{\mathbf{e}}_{\theta 2}$ and $\hat{\mathbf{e}}_{\theta 3}$ denote the unit vectors in the directions of θ_2 and θ_3, respectively. This two dimensional distribution around the unstable equilibrium [marked as U in Fig. 5.5 (d)] is shown in Fig. 5.5 (e). The spiral-like outward flow of vectors indicates that the system will *always* be driven away from the equilibrium point and develops a limit cycle around it as long as there is no additional stable equilibrium. This feature is distinct from many previously studied optomechanical systems, in which self-oscillations can not survive strong damping.

Although the regime of self-oscillations varies when the configuration changes, the two mechanisms shown above are general. For meta-molecules with more than three rings, self-oscillations can also be observed.

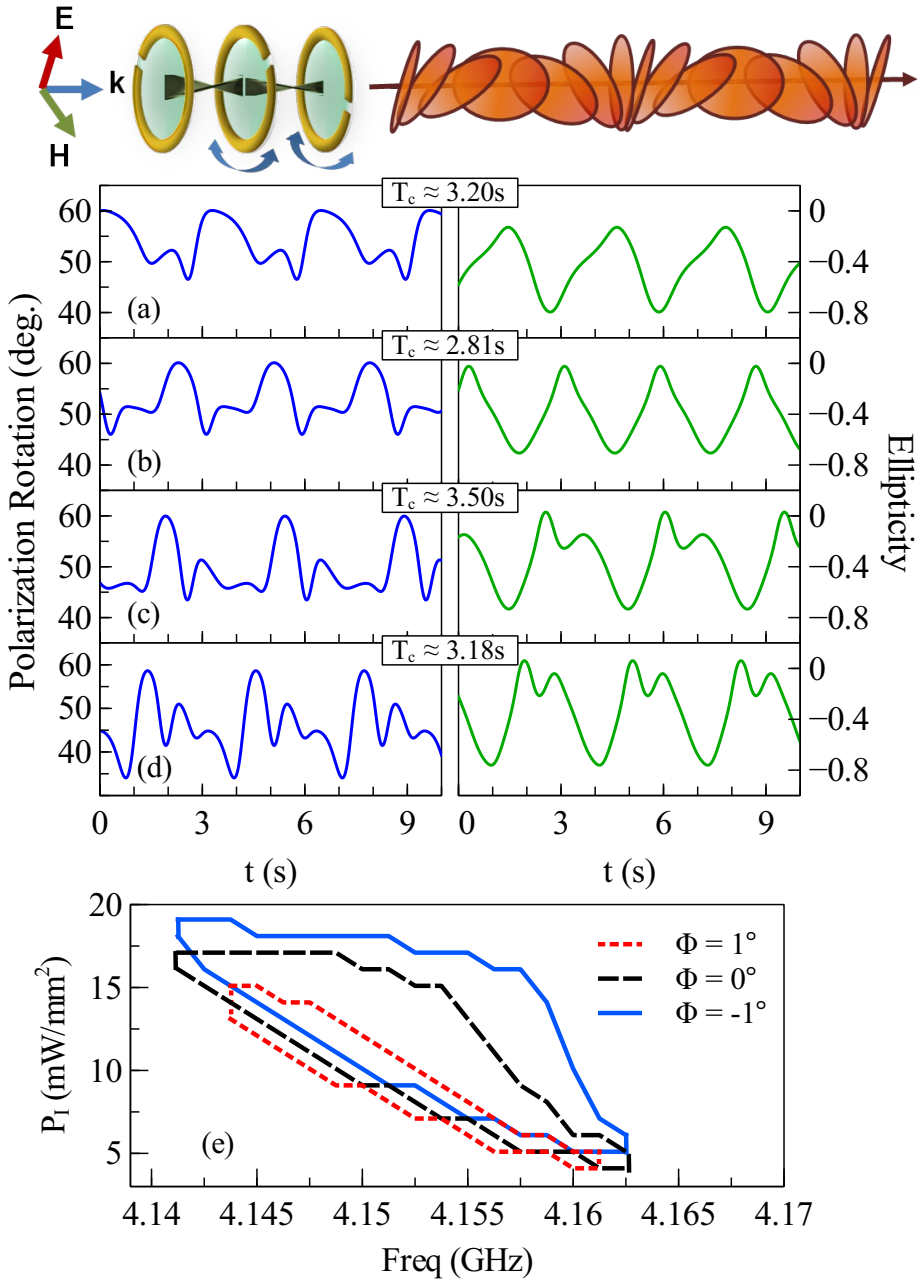

Figure 5.6: (a) to (d) Dynamic nonlinear optical activity at 4.16 GHz, with (a) P_I =4 mW/mm^2, (b) P_I =5 mW/mm^2, (c) P_I =6 mW/mm^2, (d) P_I =7 mW/mm^2. T_c is the period of self-oscillation. (e) Regimes of self-oscillations under different input polarization angles Φ, with Γ = 1.42 Hz. The top inset is a general schematic of how the polarization evolves dynamically in time.

5.4 Dynamic Nonlinear Optical Activity

Except for a few high-symmetry configurations, the three SRRs which are twisted with respect to each other form a chiral object. Chiral materials cause polarization rotation of transmitted electromagnetic waves, exhibiting optical activity. In nonlinear chiral metamaterials, optical activity also shows nonlinear features, which can be orders of magnitude stronger than the effect in natural chiral molecules [189, 207]. Therefore, it is particularly interesting to study the optical rotation effect of our meta-

molecules.

We calculate the multipole moments of each meta-atom, taking into account the contribution from all three eigenmodes, and model the far-field scattering with Eq. (2.12). The results show excellent agreement with full wave simulation (the accuracy was already verified in Chapter. 2), validating our calculation of polarization states. As expected, in the regime of strong stationary nonlinear response, giant nonlinear optical activity can be found.

The self-oscillations of chiral meta-molecules consequently leads to *dynamic nonlinear optical activity*. We recall that in natural chiral materials and previously studied chiral metamaterials, optical activity is domintated by the *stationary linear* response. Our study extends the concept of optical activity from the stationary linear regime to the dynamic nonlinear regime.

For a given pump power density, a slight change in the pump frequency or the initial twist angles can lead to a very different dynamic response. Similarly, for a given configuration of meta-molecules, the dynamic optical activity is also strongly dependent on the pump frequency and power density. Fig. 5.6 depicts the dynamic nonlinear optical activity with pump frequency 4.16 GHz, under different power levels. For clarity, we only show the polarization rotation angle and ellipticity of the scattered wave in the $+z$ direction. The time evolution of optical activity is sensitive to the change of power density, demonstrating the oscillation of polarization rotation angle with a non-monotonic variation of the period of oscillation, denoted by T_c in Fig. 5.6.

The dynamic nonlinear optical activity is also dramatically sensitive to a change in the input polarization angle Φ. We found that even with a slight variation of the input polarization angle, say $\Phi = \pm 1^\circ$, the regime of self-oscillation can be modified dramatically [see Fig. 5.6(e)]. Thus, for a given pump frequency and power density, the dynamic optical activity can be switched on and off with a small change in polarization. Such ultra-high polarization sensitivity appears to be unique for nonlinear torsional meta-molecules.

The above features connect the time domain response and the spectral domain nonlinear properties, and thus provide new possibilities for active control and detection based on time-resolved nonlinear spectroscopy of torsional meta-molecules.

5.5 The Effect in an Array

The above sections demonstrated the rich nonlinear dynamic properties of a single torsional meta-molecule. In metamaterials, however, mutual interaction is known to strongly affect the macroscopic properties in the bulk [396–400], and has even more dramatic consequences in arrays of finite size [401]. Below, we briefly assess the influence of mutual interaction when such meta-molecules are assembled into a two dimensional array.

In the ideal situation of a periodic infinite array, the EM torque experienced by the meta-molecule shows no qualitative difference as long as the distance between neighbouring units is sufficiently larger than the inter-ring separation within a meta-molecule. This is confirmed with full-wave simulation based on the Maxwell stress tensor, and the example of an infinite array with 30 mm lattice constant is shown in Fig. 5.7 (a).

In practice, an array always has a finite size, which can lead to stronger array

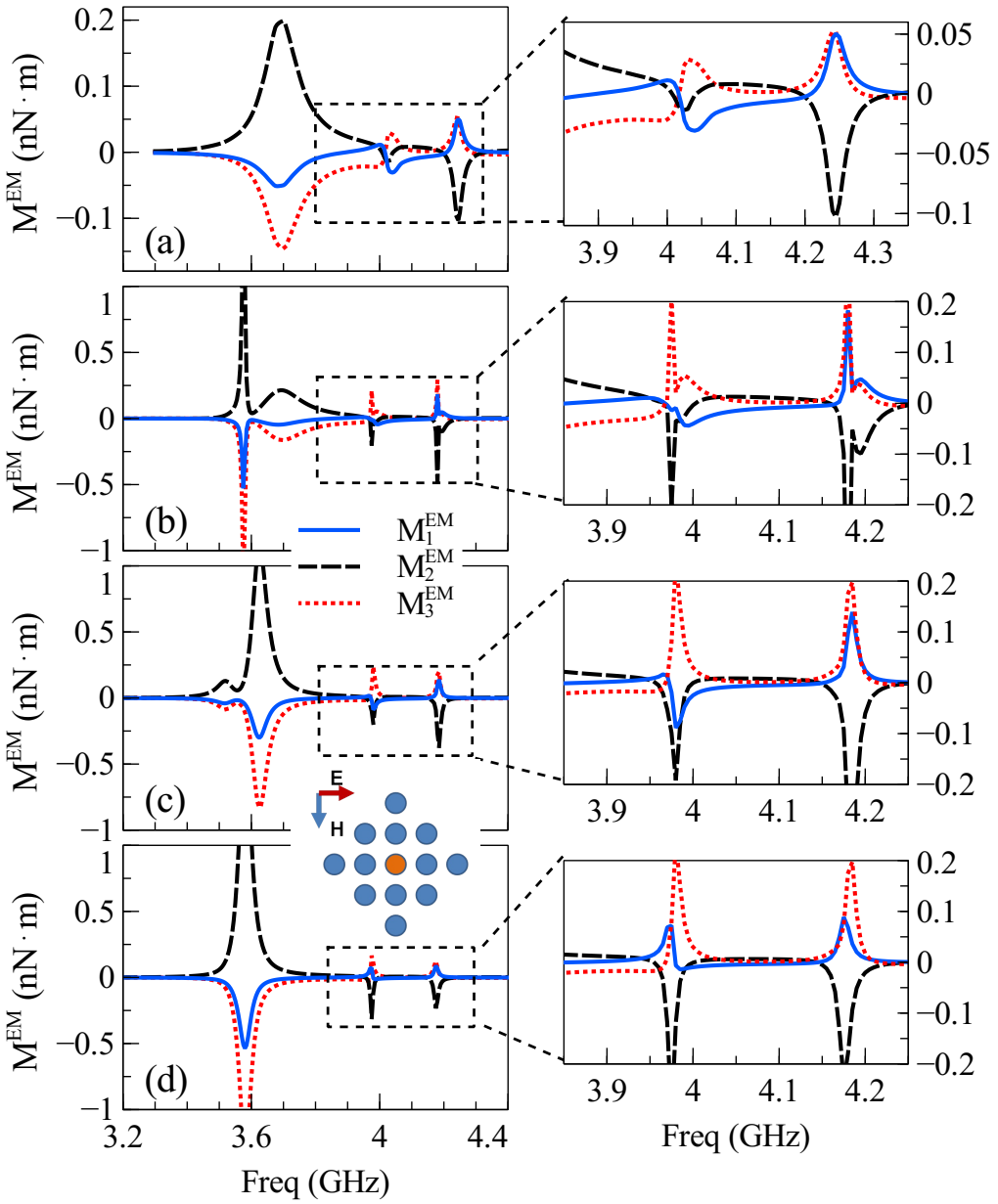

Figure 5.7: (a) EM torque experienced by the meta-molecule in an infinite square array with 30 mm lattice constant. (b), (c) and (d) Torque experienced by the meta-molecule at the centre of a finite square array. The meta-molecule at the centre is surrounded by 12 neighbouring identical meta-molecules, as denoted by the orange circle in the inset. Lattice constant (b) 30 mm, (c) 45 mm, (d) 60 mm. Insets on the right magnify the details within dashed rectangles. The EM torques are normalized to the power density of 1 mW/mm^2.

effects due to the excitation of multiple collective resonances. To check these effects, we calculate the torque experienced by the meta-molecule positioned at the centre of a finite square array. As an example, we depict the situation in which 12 nearest neighbours are taken into account, as shown from Fig. 5.7 (b) to (d), where the circles in the inset show the lattice structure.

Due to the interaction of all units, the initial three hybrid modes further split when the lattice constant is relatively small, as shown in Fig. 5.7 (b). Such split-

ting will dramatically influence the dynamic properties of the system and introduce much more complicated oscillation behaviour. Nevertheless, the directions of torques are still the same, because the mode symmetry within each meta-molecule remains unchanged.

Such splitting gradually disappears as the lattice constant further increases to more than half of the resonant wavelength [see Fig. 5.7 (c) and (d)], and the lineshapes of resonant torques become qualitatively the same as those of a single meta-molecule shown in Fig. 5.3. The resonant torques exhibit noticeable enhancement, accompanied by narrowing of the resonant linewidth, which shows the collective nature of the enhancement. Such enhancement can be made more prominent by increasing the number of neighbouring units. Interestingly, the enhancement factor of the symmetric mode (↑↑↑) is much larger than the other two hybrid modes. This difference could be attributed to the radiative nature of this mode, in which neighbouring units interact more strongly.

When the lattice constant increases further beyond the metamaterial limit to more than one resonant wavelength, the interaction becomes weak and the line-shapes of the resonant torques revert to the case of single meta-molecule shown in Fig. 5.3. We therefore expect that the effects, reported for a single meta-molecule, will be qualitatively similar to those observable when torsional meta-molecules form a dilute array.

5.6 Summary

In this chapter, we have studied the nonlinear dynamic properties of torsional meta-molecules. By employing a semi-analytical model based on near-field interaction, we are able to evaluate the internal electromagnetic torque experienced by the meta-molecule efficiently and accurately. This enables us to model the complicated dynamical behaviour of meta-molecules with two (or more) degrees of freedom.

We found that the torsional meta-molecules support self-oscillations. By analysing the local stability of the system, we revealed two different mechanisms leading to such an effect. The first mechanism relies on the limited local stability of equilibria: self-oscillations based on this mechanism can be triggered during bistable hopping but is quenched quickly as the mechanical damping increases. The second mechanism is due to the local instability of equilibria: in this case, self-oscillations do not rely on initial kinetic energy and are extremely robust against mechanical damping. The mechanism of self-oscillations studied here is quite general and can be found in other systems with more than one degrees of freedom; for example, in Chapter 6, we will show self-oscillations experimentally in a coupled system with multiple dimer torsional meta-molecules.

A direct consequence of self-oscillations in torsional meta-molecules is the dynamic nonlinear optical activity. The dynamic evolution of the optical rotation is sensitive to the change in a range of parameters including power density and incident polarization, which offers new possibilities for active control and detection.

Our design therefore provides an unusual and novel system with intriguing physics, and similar or even more complicated effects could also be found in coupled structures working at higher frequencies, such as chiral plasmonic molecules synthesized based on DNA templates [136, 268]. When the neighbour interaction among meta-moleculars becomes sufficiently strong, it could significantly change the EM torque,

the stability and the nonlinear dynamics of the system; these will be highlighted in Chapter 6.

Statement

This chapter was written based on the work published in the journal paper:
Mingkai Liu, David A. Powell, Ilya V. Shadrivov, Mikhail Lapine, and Yuri S. Kivshar, "Self-oscillations in nonlinear torsional metamaterials", *New J. Phys.* **15**, p 073036-16 (2013).
In this work, Y. S. Kivshar and I discussed and conceived the idea. I developed the theory, performed the simulation. D. A. Powell, I. V. Shadrivov and M. Lapine and Y. S. Kivshar contributed to the discussion of the results and the writing of the manuscript.

Spontaneous Chiral Symmetry Breaking in Metamaterials

6.1 Introduction

The studies in Chapter 4 and Chapter 5 focused on the nonlinear behaviour of a single torsional chiral meta-molecule. We recall that the overall response of a metamaterial depends not only on the property of the constitutive meta-molecules, but also on how the meta-molecules are arranged and coupled, in which the symmetry of the system plays a significant role. Therefore, it is particularly interesting to study the behaviour of a system composed of multiple torsional chiral meta-molecules, and to explore the interplay of nonlinearity, intermolecular interaction and system symmetry.

As an important concept in modern physics, symmetry describes the invariance of geometries or laws under specified transformations. Despite the beauty of symmetry, broken symmetry has been shown to play a significant role in the existence of new phenomena in various systems. In general, symmetry breaking can be divided into two types: *explicit* symmetry breaking and *spontaneous* symmetry breaking. The former indicates that the dynamic equations of a system are not invariant under the specified symmetry group; this can be achieved by introducing additional terms that manifestly break the original symmetry. The latter effect, in contrast, is a spontaneous process, during which a system in an initially symmetric state ends up in an asymmetric state, even though the underlying dynamic equations are still invariant under a symmetry transformation [402, 403].

Spontaneous symmetry breaking is an underlying mechanism of many fundamental phenomena [see Fig. 6.1 for examples]. Well-known examples include spontaneous magnetization [404] [Fig. 6.1 (c) and (d)], the symmetry breaking in strong interaction that is responsible for the bulk of mass of nucleons [405, 406], the recently discovered Higgs boson [407–411] [Fig. 6.1 (a)], and the breaking of chiral symmetry in biochemistry that is crucially important for the homochirality of biomolecules [412–414] [Fig. 6.1 (e) and (f)]. Recent studies of spontaneous symmetry breaking in nonlinear optical systems [415–417] and Bose-Einstein condensates [418, 419] [Fig. 6.1 (d)] further underline its ubiquity.

In the field of metamaterials, the introduction of structural asymmetry provides additional degrees of freedom in controlling light-matter interaction. A variety of phenomena including Fano resonances [359, 360] and directive in-plane scattering [169, 170, 420–422] can be obtained via the reduced mirror symmetry of a system. Complete breaking of mirror symmetry can result in optical activity [148, 149, 362], circular dichroism [132, 147] and asymmetric transmission [165, 423], which have

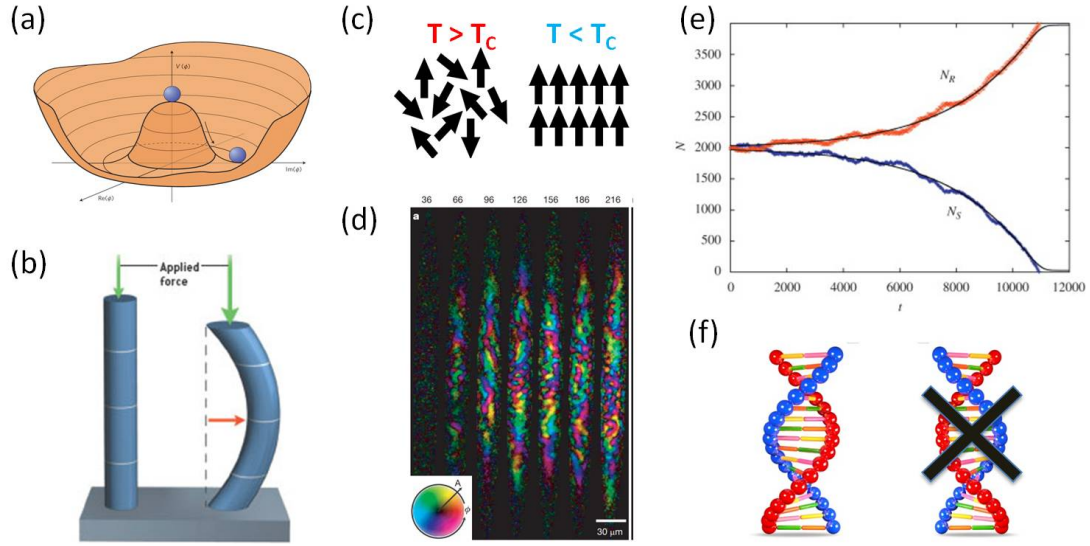

Figure 6.1: (a) An effective potential in the form of a "Mexican hat" leads to spontaneous symmetry breaking. In particle physics, the lowest energy around the bottom of the hat is vacuum. Depending on the symmetry represented, such broken symmetry can correspond to different fundamental particles such as Nambu-Goldstone boson or Higgs boson [424]. (b) Example of spontaneous symmetry breaking in a classical system. The cylindrical symmetry of the elastic stick breaks when the vertically applied force is sufficiently strong [425]. (c) Schematic of spontaneous magnetization; when the temperature reduces to below the Curie temperature T_c, the randomly oriented magnetic moments align to a specific direction. (d) *In situ* images of ferromagnetic domains and domain walls in a quenched ferromagnetic spinor Bose–Einstein condensate. The orientation of transverse magnetization is shown by the color and the magnitude is shown by the brightness [418]. (e) Dynamic simulation of the number of enantiomeric molecules R and S during a crystallization process under grinding. The originally small difference induced by spontaneous chiral symmetry breaking is amplified and finally leads to homochirality [426] – an effect widely found in bio-molecules such as (f) DNA (DNA molecules are dominated by right-handed helices).

been extensively studied in the context of chiral metamaterials, as was introduced in Sec. 1.3.2. These scenarios can all be classified as *explicit* symmetry breaking, since asymmetry is artificially introduced into the Hamiltonian by modifying the configuration of the system.

On the other hand, nonlinear metamaterials [182, 427] provide a unique platform for the study of *spontaneous* symmetry breaking. Apart from the nonlinear self-action effects mentioned in Sec. 1.4.1.1, various nonlinear localization effects such as solitons [428–430] and domain walls [431, 432] have also been studied theoretically. Most studies were performed in the context of metamaterials based on varactor diodes [183], and a direct observation of these effects is still challenging. The introduction of magnetoelastic metamaterials provides new opportunities to study these effects. As has been introduced in previous chapters, the nonlinear response in these structures originates from the coupling between electromagnetic (EM) resonances and elastic deformation of the structure. We extended this idea to chiral torsional metamaterials; in Chapter 4, we already predicted and demonstrated experimentally a rich variety of nonlinear stationary responses such as large self-tuning and bista-

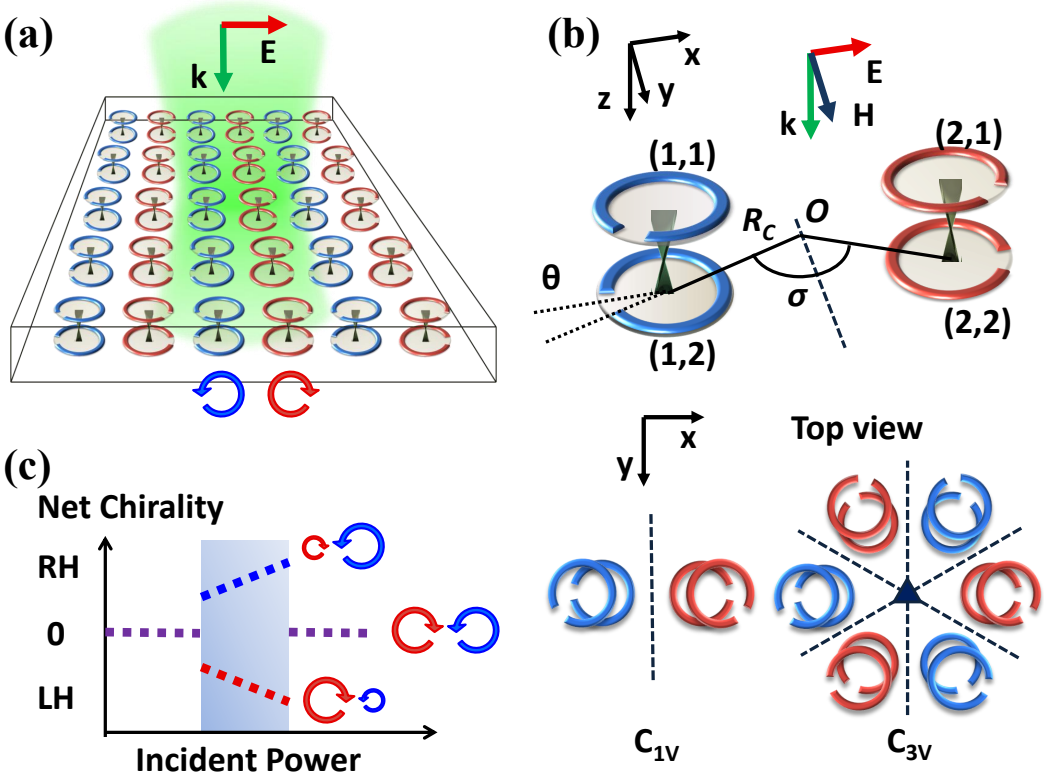

Figure 6.2: Schematics of torsional metamaterial enantiomers and spontaneous chiral symmetry breaking. (a) Conceptual layout of torsional metamaterials with chiral symmetry. Each meta-molecule consists of two coaxial twisted meta-atoms (SRRs) connected elastically, and meta-molecules with right and left handedness are plotted in blue and red colors, respectively. The green shaded region represents the incident EM waves, and the responses of enantiomers are denoted by circular arrows. (b) Configurations of enantiomeric meta-molecules with C_{Nv} symmetry. The displacement vector between a meta-molecule and the rotation center O is $\mathbf{R}_C$ and the rotation angle $\sigma = \pi/N$. $\theta_{l,j}$ is the twist angle of an SRR with respect to $\mathbf{R}_C$, where the first index reflects the number of SRR pair, and the second index distinguishes between the upper ($j = 1$) and lower ($j = 2$) SRRs in the pair. The dashed lines are the axes of mirror symmetry. (c) Schematic showing the phase-transition of net chirality of the system when the incident power changes. In the shaded regime, spontaneous chiral symmetry breaking occurs and the net chirality can fall into either the left handed (LH) or the right handed (RH) regime.

bility; in Chapter 5, we further predicted that novel nonlinear dynamic effects such as damping-immune self-oscillation and dynamic nonlinear optical activity would be feasible under moderate pump powers.

In this chapter, we will study the nonlinear behaviour when two or more torsional meta-molecules with opposite handedness (enantiomeric meta-molecules) are electromagnetically coupled, i.e. a coupled system with *chiral symmetry* (see Fig. 6.2). The term “chiral symmetry" used in this chapter follows the same definition as in previous studies of enantiomeric molecules [433,434] — for a given set of dynamic equations F that describe the interaction and evolution of the enantiomeric meta-molecules (x_L, x_R), they are covariant under parity transformation $\mathcal{P}$, i.e. $\mathcal{P}[F(x_L, x_R)] = F(x_R, x_L)$. Intuitively, under such a symmetry condition, torsional meta-molecules with opposite handedness should have identical magnitudes of EM response if they are equally

excited; the net chirality of the whole system should also vanish due to chiral symmetry. However, our study explicitly shows that when the interaction between meta-molecules becomes sufficiently strong, the system undergoes spontaneous symmetry breaking and becomes chiral.

In this chapter, we start with the simple case of a pair of enantiomeric meta-molecules, each composed of a pair of twisted split-ring resonators, the same as the one studied in Chapter 4, and we show that chiral symmetry breaking can exist due to intermolecular interaction. This process leads to the sudden occurrence of polarization rotation and localization, an analogy to phase-transition effects. To understand the underlying mechanism, we use the method introduced in Sec. 5.3 and analyze the evolution of local stability of the system, showing the critical role of intermolecular interaction in creating new stable states with broken chiral symmetry. Furthermore, we perform a proof-of-concept microwave experiment to study the nonlinear behaviour of a pair of enantiomeric meta-molecules, and the results provide a concrete verification of our theoretical prediction. Finally, we extend our study to meta-molecular necklaces with $C_{N\mathrm{v}}$ symmetry and periodic arrays that mimic the situation in bulk torsional metamaterials, and show how to use perturbation of the incident polarization to achieve uniform chiral symmetry breaking throughout the whole array.

6.2 Coupled Torsional Meta-molecules with Chiral Symmetry

The system studied is shown in Fig. 6.2, with each torsional meta-molecule consisting of two coaxial split ring resonators (SRRs) connected by an elastic thin wire. As in Chapter 5, we choose the radii of thin SRRs as $r_{\mathrm{a}} = 6\,\mathrm{mm}$, slit width 1 mm, and inter-ring distance 3 mm; we fix the upper rings and restrict the allowed movement of the bottom rings to azimuthal rotation; perfect electric conductor is used as the material for the SRRs so only the radiative component of the EM force/torque is taken into account. For clarity, we denote the upper and lower SRRs of meta-molecule number l as $(l,1)$ and $(l,2)$, respectively. To confirm the chiral symmetry of the system, $2N$ ($N \in \mathbb{N}$) torsional meta-molecules with opposite handedness are symmetrically coupled and uniformly excited with the same amplitude and phase. For a finite system, this can be done by arranging the $2N$ torsional meta-molecules in a way that the whole system satisfies $C_{N\mathrm{v}}$ symmetry, i.e. $\sigma = \pi/N$. The displacement vector pointing from the rotation center O to the center of a meta-molecule is $\mathbf{R}_{\mathrm{C}}$, and θ is the twist angle of an SRR, defined by the orientation of the slit with respect to $\mathbf{R}_{\mathrm{C}}$.

To provide the first insight of the physics, we employ the near-field interaction model in Appendix A to calculate the EM torque, and solve the following coupled equations to study the nonlinear response of the system

$$-\mathrm{i}\omega \sum_{m=1}^{N} \sum_{j=1}^{2} Z_{(l,i),(m,j)}(\theta_{l,i}\theta_{m,j}) Q_{m,j} = \mathcal{E}_{l,i}, \tag{6.1}$$

$$\ddot{\theta}_{l,2} + \Gamma\dot{\theta}_{l,2} = \frac{1}{I} M_l \tag{6.2}$$

The notations are the same as those used in Eq. (5.5) and Eq. (5.4). $M_l = M_l^{\mathrm{EM}} + M_l^{\mathrm{R}}$ is the total torque experienced by the lower SRR of meta-molecule l.

We start with the simplest case when two enantiomeric torsional meta-molecules are coupled. Without loss of generality, we choose the y-z plane as the plane of mirror

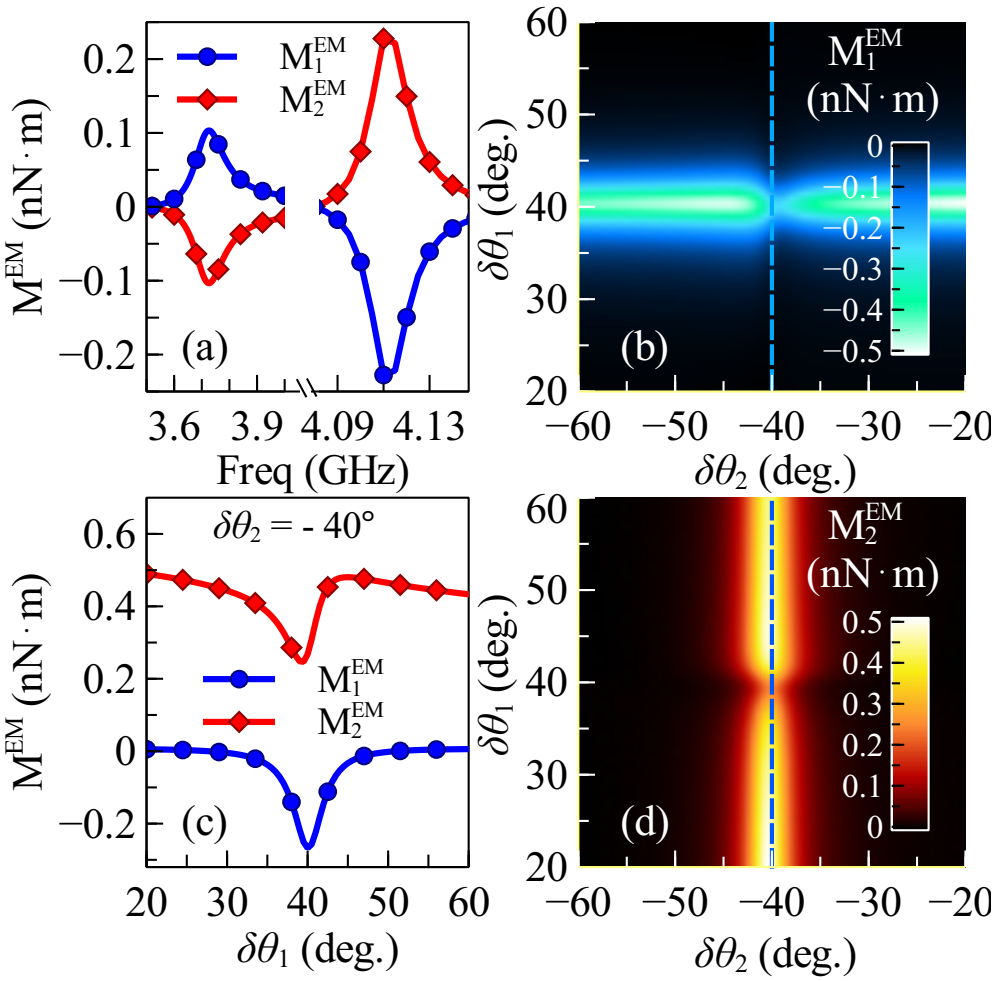

Figure 6.3: EM torque experienced by the rotatable SRRs. (a) Spectra of EM torque experienced by SRRs $(1,2)$ and $(2,2)$ [denoted as M_1^{EM} (blue circles) and M_2^{EM} (red diamonds)], with twist angles $\theta_{1,1} = -\theta_{2,1} = 90°$, $\theta_{1,2} = -\theta_{2,2} = 45°$, and $|\mathbf{R}_C| = 2.5$ r_a. (b) and (d) are the EM torque as functions of the two mutual twist angles $\delta\theta_1 = \theta_{1,2} - \theta_{1,1}$ and $\delta\theta_2 = \theta_{2,2} - \theta_{2,1}$, with pump frequency 4.1 GHz; the corresponding cross-sections along the blue dashed lines are shown in (c) (blue circles for M_1^{EM} and red diamonds for M_2^{EM}). The EM torque has been normalized to the power density of 1 mW mm^{-2}.

symmetry and the system is excited with an x-polarized plane wave propagating in the z direction, as shown in Fig. 6.2 (b). Since the Hamiltonian possesses chiral symmetry — the effective impedance Z has components $Z_{(1,1),(2,2)} = Z_{(2,1),(1,2)}$ — the resulting mode amplitudes and EM torques also possess the same symmetry, i.e. $|Q_{1,1}| = |Q_{2,1}|, |Q_{1,2}| = |Q_{2,2}|$, $M_1^{\text{EM}} = -M_2^{\text{EM}}$. As an example, we calculate the EM torque experienced by SRRs $(1,2)$ and $(2,2)$ (denoted as M_1^{EM} and M_2^{EM}), with twist angles $\theta_{1,1} = -\theta_{2,1} = 90°$ and $\theta_{1,2} = -\theta_{2,2} = 45°$, and $|\mathbf{R}_C| = 2.5r_a$. It should be noted that, in a system with $2N$ resonators, $2N$ hybrid resonances can be supported in general. However, the number of resonances excited can be reduced due to symmetry. If the system satisfies C_{Nv} symmetry and is excited uniformly, only two resonances can be observed. This property provides an important spectral reference to estimate the chiral symmetry of the system in experiments. Since the EM interaction is dominated by the intra-molecular coupling for such separation, the

overall lineshape is qualitatively similar to the single meta-molecule we studied in Chapter 4. As can be seen from Fig. 6.3(a), the directions of resonance-enhanced EM torques induced by the two hybrid modes are opposite due to the different mode symmetries.

However, even a relatively weak intermolecular interaction is sufficient to introduce modulation of the resonant amplitude and of the EM torque. This effect can be clearly observed in Figs. 6.3 (b) and (d), which show the EM torques experienced by SRRs $(1,2)$ and $(2,2)$ under pump frequency 4.1 GHz, as functions of the mutual twist angles ($\delta\theta_l = \theta_{l,2} - \theta_{l,1}$) in two meta-molecules. This modulation becomes the strongest when both meta-molecules are in resonance ($\delta\theta_1 \approx -\delta\theta_2$) [see Fig. 6.3(c) for the cross-sections along the blue dashed lines]. Note that although the EM torque experienced by a meta-molecule is still a Lorentz-like function of its own twist angle, it is also modulated by the twist angle from the other meta-molecule, which gives a more general Fano lineshape.

6.3 Spontaneous Chiral Symmetry Breaking in Dimers

As shown above, the interaction between two enantiomeric meta-molecules results in EM torque which depends on the configuration of both meta-molecules. It is this interaction that modifies the stability of the system and leads to the spontaneous chiral symmetry breaking, as will be shown below. Importantly, such chiral symmetry breaking can be found in the stationary response of the system, which means this is an effect independent of mechanical damping, and this is a desirable property for their future realization in optics.

By calculating the dynamics of the system in Fig. 6.3 under different pump frequencies and power densities P_I, we notice that such an effect can be found at frequencies just below resonance. For clarity, we focus on the resonance centred around 4.11 GHz, in which the currents of the two SRRs within each meta-molecule flow in opposite directions. For each frequency, the pump power density P_I is increased from 0 to 4 mW mm^{-2} and decreased back to 0 mW mm^{-2} in steps of 0.05 mW mm^{-2}. The damping coefficient $\Gamma = 1.42$ Hz is equivalent to the damping experienced in water, and the system can become stable after damped oscillations. The regime of broken symmetry can be found by summing the two stable twist angles $|\delta\theta_1 + \delta\theta_2|$, which would be non-zero if the symmetry is broken. The results clearly show that this symmetry breaking effect has hysteretic features [see Fig. 6.4 (a)].

As an example, Fig. 6.4 (b) depicts this process for a pump frequency of 4.1 GHz. The chiral symmetry of the system is preserved for low power. However, such symmetry can suddenly be broken ($\delta\theta_1 + \delta\theta_2 \neq 0$) when the pump power surpasses a certain threshold, and Fig. 6.4 (c) depicts the dynamics of the lower rings $(1,2)$ and $(2,2)$ at the threshold power of 0.7 mW mm^{-2}, during which the system evolves from a symmetric state to an asymmetric state. The threshold powers can be different for increasing (red solid circles) and decreasing (blue open circles) power levels, showing hysteresis. At the threshold power level where chiral symmetry is broken, the system can fall from the symmetric state into either of the two asymmetric states with opposite handedness, and the final “observed" state is random if there is no predefined bias in the initial state. This process is also known as “hidden" symmetry [402, 403], since the two asymmetric states are still mirror symmetric with respect to each other, although only one of them can be finally “observed" each time.

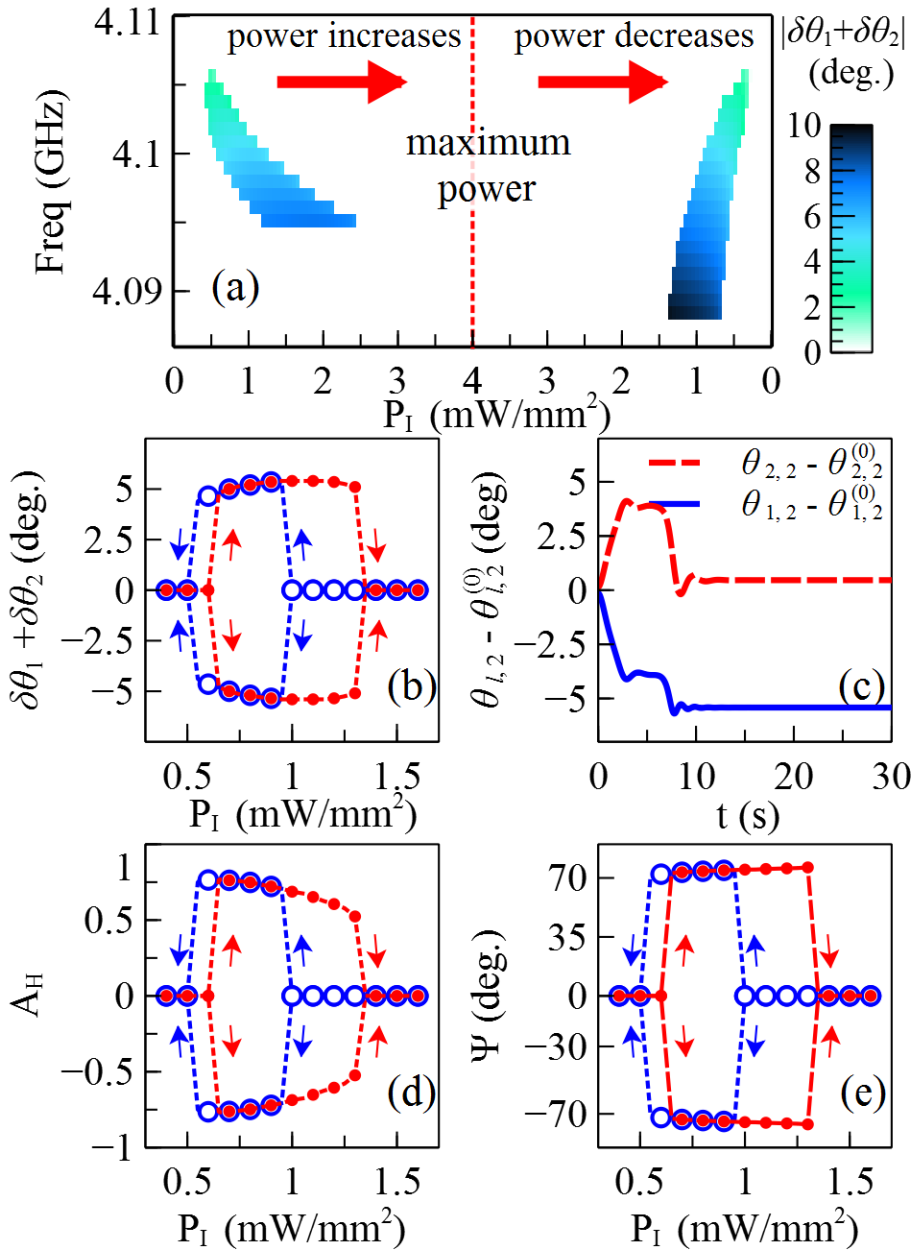

Figure 6.4: Chiral symmetry breaking of enantiomeric dimers. (a) Regime of spontaneous chiral symmetry breaking as a function of incident power density P_I and pump frequency. The initial twist angles are chosen to be the same as in Fig. 6.3. For pump frequency 4.10 GHz, (b) the asymmetry of twist angles, characterized by $\delta\theta_1 + \delta\theta_2$, and (c) the corresponding time dependent response of the symmetry breaking process under $P_I = 0.7$ mW mm^{-2}, where $\theta^{(0)}_{1,2} = -\theta^{(0)}_{2,2} = 45°$ are the initial twist angles; the blue solid curve and red dashed curve correspond to $\theta_{1,2} - \theta^{(0)}_{1,2}$ and $\theta_{2,2} - \theta^{(0)}_{2,2}$, respectively. (d) The asymmetry of EM energy stored within each meta-molecule, and (e) the corresponding polarization rotation Ψ of the forward scattered wave. The red solid and blue empty circles denote the states under increasing and decreasing power, respectively. In the broken chiral symmetry regime, the system could fall into either of the two states with opposite handedness.

In the near-field, such broken symmetry directly leads to asymmetry or even localization of the EM energy. Figure 6.4 (d) depicts such a change, where the asymme-

try factor is defined as $A_H = (H_1 - H_2)/(H_1 + H_2)$, with $H_l = \frac{1}{2}Re(\mathcal{E}_{l,1}Q^*_{l,1} + \mathcal{E}_{l,2}Q^*_{l,2})$ being the input energy from the incident field on each meta-molecule, which is equal to the energy scattered and stored by each meta-molecule. The most noticeable consequence of this symmetry breaking is the sudden occurrence of giant polarization rotation of forward/backward scattered waves [see Fig 6.4 (e)], and this phase transition process could provide a new mechanism to construct artificial phase-change metamaterials without introducing any naturally occurring phase-change materials [222], as will be further confirmed below.

6.4 Underlying Mechanism

The mechanism of the above process can be fully understood by analyzing the local stability of the system, using the approach introduced in Sec. 5.3 . Figures 6.5 (a) to (i) demonstrate how the total torque and equilibria evolve as pump power changes. The color scale and vectors show the amplitude and direction of the total torque experienced by the system, and it is defined as $\mathbf{M} = M_1\hat{\mathbf{e}}_{\theta_{1,2}} + M_2\hat{\mathbf{e}}_{\theta_{2,2}}$. The blue and red curves correspond to $M_1 = 0$ and $M_2 = 0$, respectively; their crossovers are the equilibria of the system $|\mathbf{M}| = 0$, which are pump power-dependent. Importantly, one can also evaluate the stability of the equilibria in Fig. 6.5 by identifying the direction of the vectors, which shows the direction of the total torque and tells whether an equilibrium is “attractive" (stable) or “repulsive" (unstable).

Under low power density, only one stable equilibrium exists around the initial configuration with chiral symmetry [Fig. 6.5 (a)]. As power further increases, two new stable equilibria with broken chiral symmetry exist [Fig. 6.5 (b)], and the stable equilibrium (black circle) of the symmetric state around $\delta\theta_1 = -\delta\theta_2 \approx 43.5^\circ$ starts to overlap with the two unstable ones nearby (yellow circles) [Fig. 6.5 (b) to (c)], and it finally turns into an unstable point (undergoes the *first* bifurcation) as power increases [Fig. 6.5 (c) to (d)]. Then the original symmetric state is no longer stable, and the system falls into either of the two nearby stable states by breaking the original chiral symmetry, as depicted in Figs. 6.4 (b) and (c). The unstable chiral symmetric state further evolves into a new stable state after the *second* bifurcation as power increases [Fig. 6.5 (e) to (f)]. The asymmetric state exists below the *third* bifurcation threshold [see Fig. 6.5(g) to (h), the stable points of asymmetric states overlap with the nearby unstable ones and disappear as power further increases], and the system hops back to the second stable symmetric state when the power density surpasses 1.3 mW mm^{-2} [Fig. 6.5(h) to (i)], as has been shown in Figs. 6.4 (b) to (e).

It has to be emphasized that the chiral symmetry breaking effect shown here is attributed to the EM interaction between meta-molecules. As shown in Fig. 6.3, such interaction leads to additional modulation of the EM torques, and it directly results in different threshold powers of bifurcation for symmetric and asymmetric states, which provides a necessary (but not sufficient) condition for symmetry breaking. For simplicity, we denote $P_1^{(s)}$ and $P_2^{(s)}$ the threshold powers of the two symmetric states under low and high pumping power density, and $P_1^{(a)}$ and $P_2^{(a)}$ are the threshold powers of the asymmetric state in the intermediate power regime.

Figure 6.6 (a) depicts the threshold powers of bifurcation for the symmetric and the asymmetric states as a function of $|\mathbf{R}_C|$ at a frequency of 4.1 GHz. The threshold powers of bifurcation exhibit interesting asymptotically oscillating features due to the influence of retardation on the EM coupling. Note that for a given $|\mathbf{R}_C|$, the

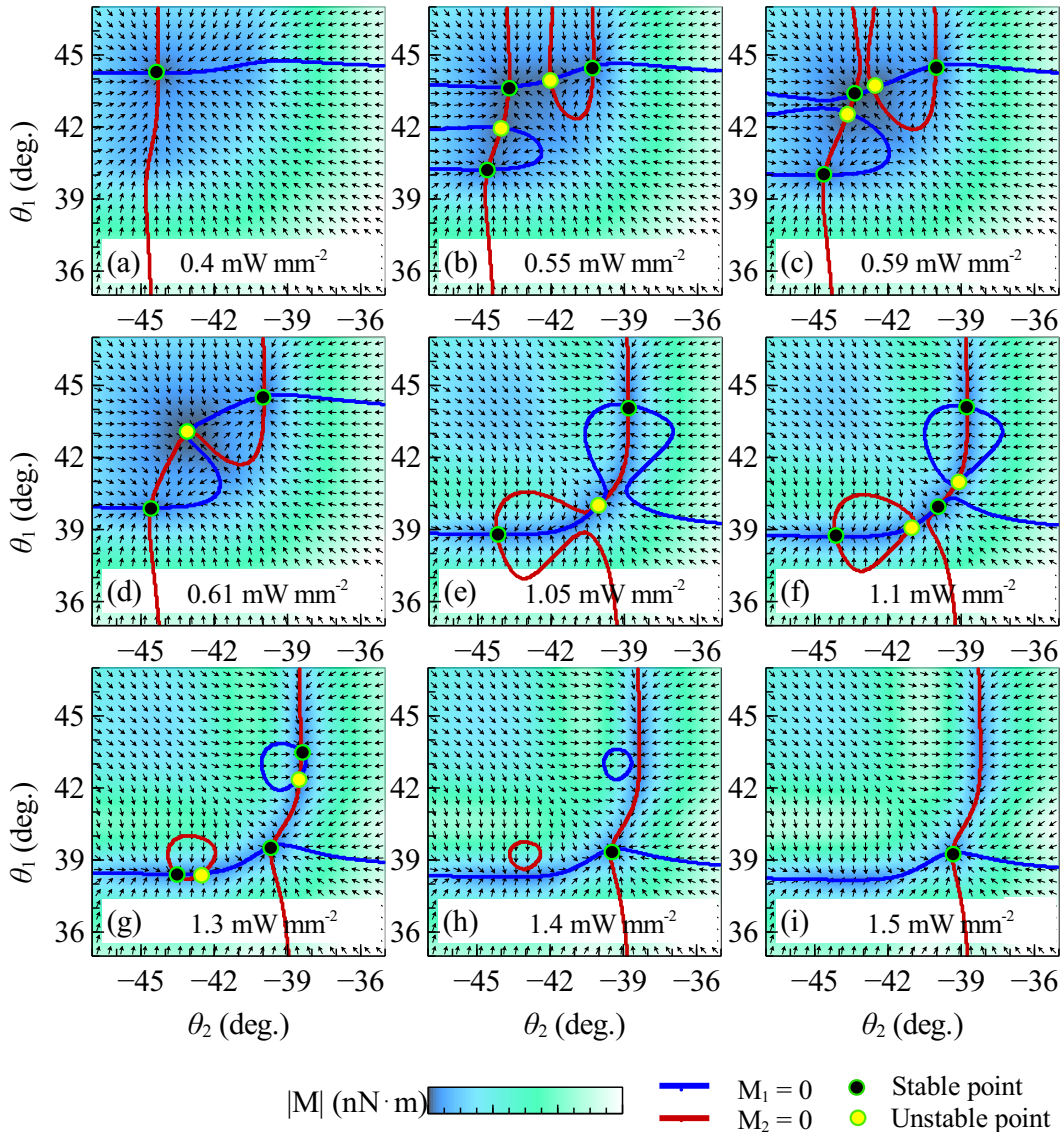

Figure 6.5: (a) to (i) Evolution of the total torque as a function of pump power density under inter-molecular distance $|\mathbf{R}_C| = 2.5r_a$. The total torque experienced by the system is defined as $\mathbf{M} = M_1\hat{\mathbf{e}}_{\theta_{1,2}} + M_2\hat{\mathbf{e}}_{\theta_{2,2}}$. The vectors and color scale indicate the direction and amplitude of total torque, respectively. The crossovers of $M_1 = 0$ (blue curves) and $M_2 = 0$ (red curves) are the equilibria of the system. Pump frequency is 4.1 GHz, the same as in Figs. 6.4 (b) to (e).

chiral symmetry breaking effects for increasing power and decreasing power only exist within the power regime of $P_1^{(s)} < P_I < P_1^{(a)}$ and $P_2^{(a)} < P_I < P_2^{(s)}$, respectively. Thus the regime of symmetry breaking also follows similar asymptotically oscillating behaviour as $|\mathbf{R}_C|$ increases. The oscillation period is the resonant wavelength in vacuum (for 4.1 GHz, the period is approximately $6r_a$), and the power regime of chiral symmetry breaking decreases dramatically as inter-molecular separation enters the far-field regime ($|\mathbf{R}_C| > 6r_a$).

Strictly speaking, the sufficient condition for chiral symmetry breaking is that when the bifurcation of one stable symmetric state happens, the only available state is the stable asymmetric state. The first situation that satisfies such sufficient condition is the case shown in Figs. 6.5 (c) to (d) — when the bifurcation of the first

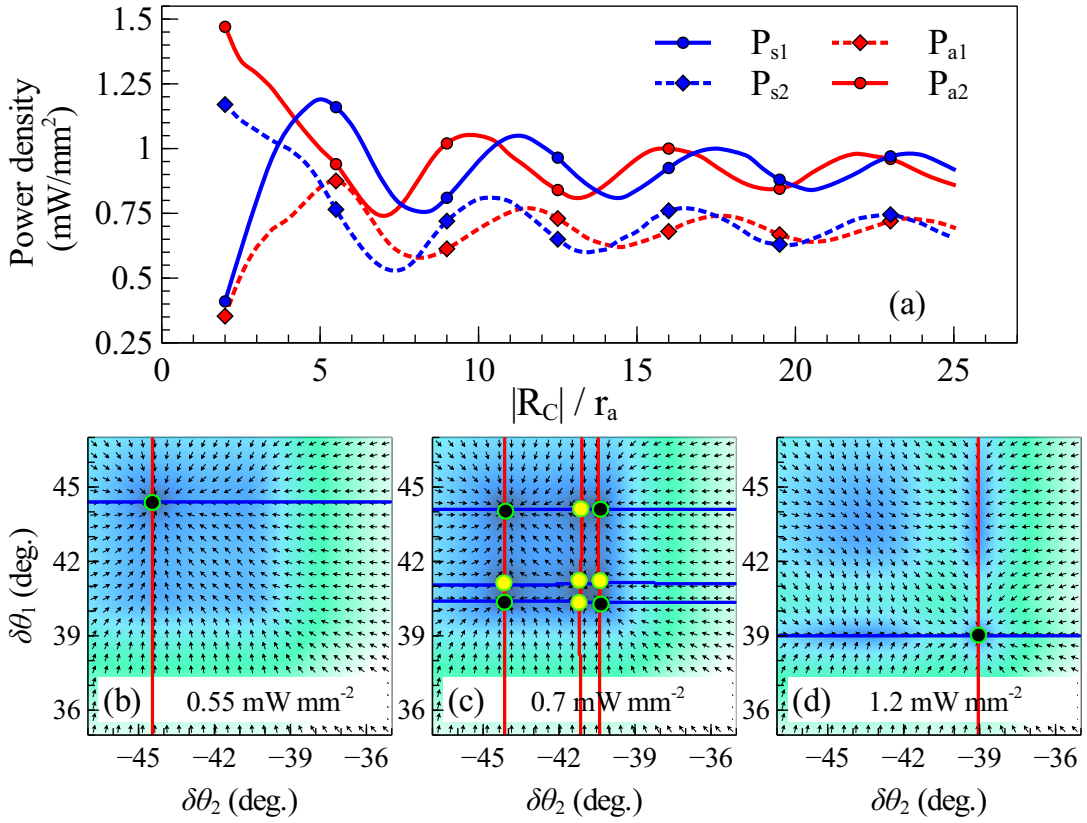

Figure 6.6: (a) Evolution of the threshold powers of bifurcation for the two symmetric states (denoted as $P_1^{(s)}, P_2^{(s)}$) and the asymmetric state (denoted as $P_1^{(a)}, P_2^{(a)}$), as a function of $|\mathbf{R}_C|$. (b) to (d) Evolution of the total torque as a function of pump power density under inter-molecular distance $|\mathbf{R}_C| = 250r_a$; pump frequency is chosen as 4.1 GHz.

symmetric state occurs, the second symmetric state has not emerged due to its higher threshold power of bifurcation ($P_1^{(s)} < P_2^{(s)}$), and the system can only fall into the existing asymmetric state. The second situation is such that when the bifurcation of the first symmetric state occurs, the second symmetric state already exists ($P_1^{(s)} > P_2^{(s)}$); however, due to an additional unstable point in-between the two symmetric states, the trajectory of the system will still be "pushed" away from the axis of $\delta\theta_1 = -\delta\theta_2$ and falls into the asymmetric state.

The powers of bifurcation for symmetric and asymmetric states become *degenerate* ($|P_1^{(a)} - P_1^{(s)}| \to 0, |P_2^{(a)} - P_2^{(s)}| \to 0$) eventually when the separation becomes very large. Figs. 6.6 (c), (d), (e) show the extreme situations under a very large distance $|\mathbf{R}_C| = 250r_a$, at which the intermolecular interaction becomes negligible. As a result, the curves for $M_1 = 0$ and $M_2 = 0$ reduce to straight lines, and the stable points of the symmetric and asymmetric states around $\delta\theta_1 \approx 44°$ and $\delta\theta_2 \approx -44°$ [Fig. 6.5 (c)] will disappear simultaneously when the power further increases, since they have the same threshold power of bifurcation. In this case, the system can only jump to the second stable symmetric state with smaller mutual twist angles [see Fig. 6.5 (d)]: this process is exactly the bistable hopping found in Chapter 4. In contrast, the hysteresis shown in Fig. 6.4 is actually a *multistable* process, during which three independent stable states (two symmetric states for low and high power density, and

one asymmetric state for intermediate power density) are accessed. Therefore, intermolecular interaction is indispensable for the existence of a *non-degenerate* state with broken chiral symmetry.

6.5 Experimental Verification

We confirm the theoretical prediction of spontaneous chiral symmetry breaking by performing a pump-probe experiment in the microwave regime, with a setup similar to one in Chapter 4. We have used four copper split-ring resonators printed on Rogers R4003 substrate (relative permittivity 3.5, loss tangent 0.0027, substrate thickness 0.5 mm) to construct two pairs of chiral meta-molecules. The outer radius, track width, slit width and thickness of each SRR are 4.2 mm, 1.0 mm, 0.2 mm and 0.035 mm, respectively. Two of the SRRs are fixed on a polystyrene (relative permittivity around 1) block and positioned at the centre of a circular waveguide (diameter $\sim$ 58.2 mm), with their slits oriented parallel with the wave propagation direction (see Fig. 6.7). The other two SRRs are suspended with thin rubber wires (radius $a = 50$ μm, length $d = 19.4$ mm, and shear modulus 0.6 MPa), and are well aligned coaxially with the two fixed SRRs, with a face to face distance around 1.2 mm and the initial twist angles $\delta\theta_1^{(0)} = -\delta\theta_2^{(0)} \approx 70^\circ$. The centre-centre distance of the two chiral meta-molecules is 12.7 mm. Due to experimental constraints, the orientation of the incident field relative to the meta-molecules differs from that in our theoretical analysis; however, by exciting the two meta-molecules with the same magnitude and phase, we preserve the symmetry required to demonstrate the effect. The two pairs of twisted split rings are positioned in a circular waveguide, and are excited with the TE_{11} waveguide mode, having its electric field parallel to the SRRs.

The transmission spectrum is measured by a vector network analyser (Rohde and Schwarz ZVB-20). In general, the four-SRR system can give rise to four resonances due to mutual coupling, and two of them can be observed within the frequency regime of interest ($<$ 4 GHz). These two modes can be understood as a further hybridization of the original symmetric modes (with currents flowing in the same direction) supported by the SRR pairs, as discussed in previous studies [152]. However, in the chiral symmetric configuration, one of these two modes will not be excited due to its zero overlap with the incident field. This property provides an accurate reference for tuning the initial positions of the two twisted SRR pairs – only when the two ring pairs are positioned almost perfectly symmetrically can we observe a single resonance with Lorentz lineshape. Our simulation further confirms that the “hidden" mode can be excited and becomes easily distinguishable once the difference of initial twist angles becomes larger than one degree. Thus, the horizontal positions, the longitudinal separations, and the initial twist angles can be carefully adjusted so that only one resonance is observed.

We choose a pump frequency at 3.53 GHz, which is just below the initial resonance of around 3.55 GHz. The CW pump signal is generated by a signal generator (HP 8673B) and is further amplified by a power amplifier (ZHL-16W-43-S+). The pump power is increased in 0.5 dB steps and the spectra are recorded once the system reaches a steady-state. The normalized transmission spectra $|S_{21}|$ as a function of pump power are plotted in Fig. 6.8 (a), where the black dots denote the positions of the resonances, and the blank regime is where the system undergoes self-oscillations, hence no steady-state signal can be recorded. It is clearly shown that the original

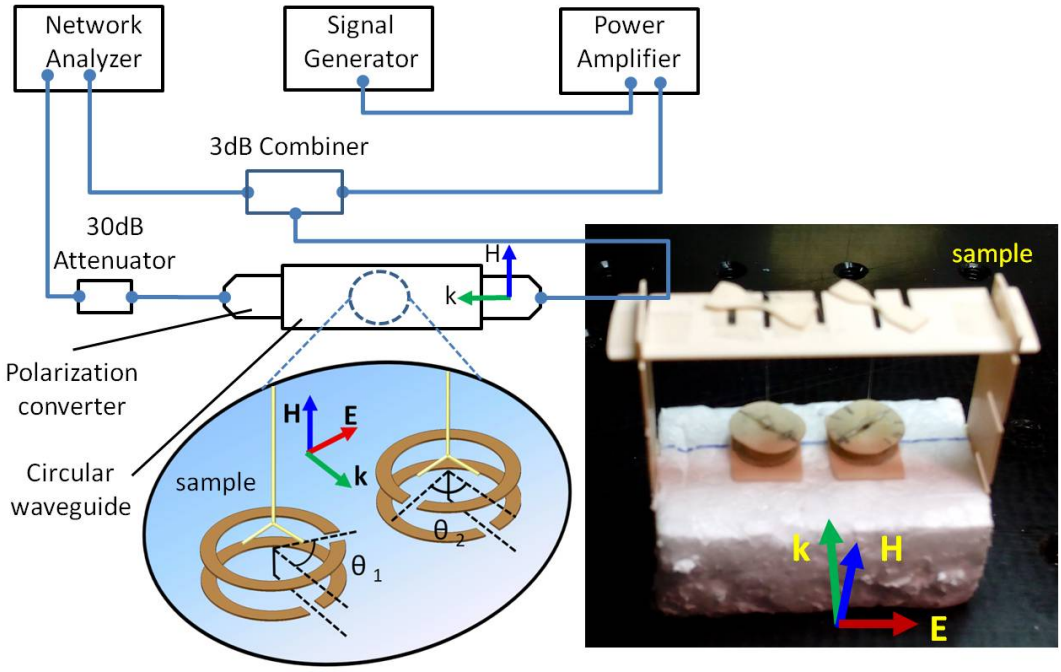

Figure 6.7: Experimental setup. Schematic of the experimental setup of the microwave pump-probe measurement. For clarity, the substrate of the sample in the schematic is omitted. The inset is the photograph of the sample. The fine rubber wires suspending the top SRRs are attached to two small wire winders (the bow-tie-shaped objects on the top of the shelf), so that the twist angles, the lateral and longitudinal positions of the SRRs can be tuned separately.

single resonance at around 3.55 GHz red shifts as pump power increases, and it suddenly splits into two new resonances when the power surpasses 24 dBm. This is clear evidence for the existence of spontaneous chiral symmetry breaking.

As the power further increases, the state with broken symmetry becomes unstable and the system exhibits self-oscillations. Recall that in Chapter 5, we already predicted the possible existence of self-oscillations in a single torsional meta-molecule with two mechanical degrees of freedom. The effect observed here is intrinsically the same as the situation studied in Sec. 5.3.2 – due to the absence of stable state in the system (which is confirmed with full wave simulation, see discussion below). In such a scenario, the system starts to "wander" in phase space (for the case of two degrees of freedom studied here, the phase space is four dimensional) and transforms EM energy into mechanical oscillation. We choose a probe frequency of 3.52 GHz to record the time evolution of the transmission coefficient. Some of the examples are shown in Fig. 6.8 (b), where the periodicity of the signals indicates that the system undergoes limit cycles. For other pump powers, more complicated behaviour such as aperiodic or even chaos-like dynamics are observed.

Remarkably, the system becomes stable again when the power exceeds 32 dBm. The two split resonances disappear and a new single resonance appears at around 3.5 GHz, which red shifts as power further increases. This is a clear verification of our theoretical prediction that the system will eventually hop back to the second symmetric state (the only stable state) when the pump power is sufficiently strong.

To confirm the observation, we perform a full wave simulation using CST Microwave Studio to reproduce the measured spectra by taking into account the influ-

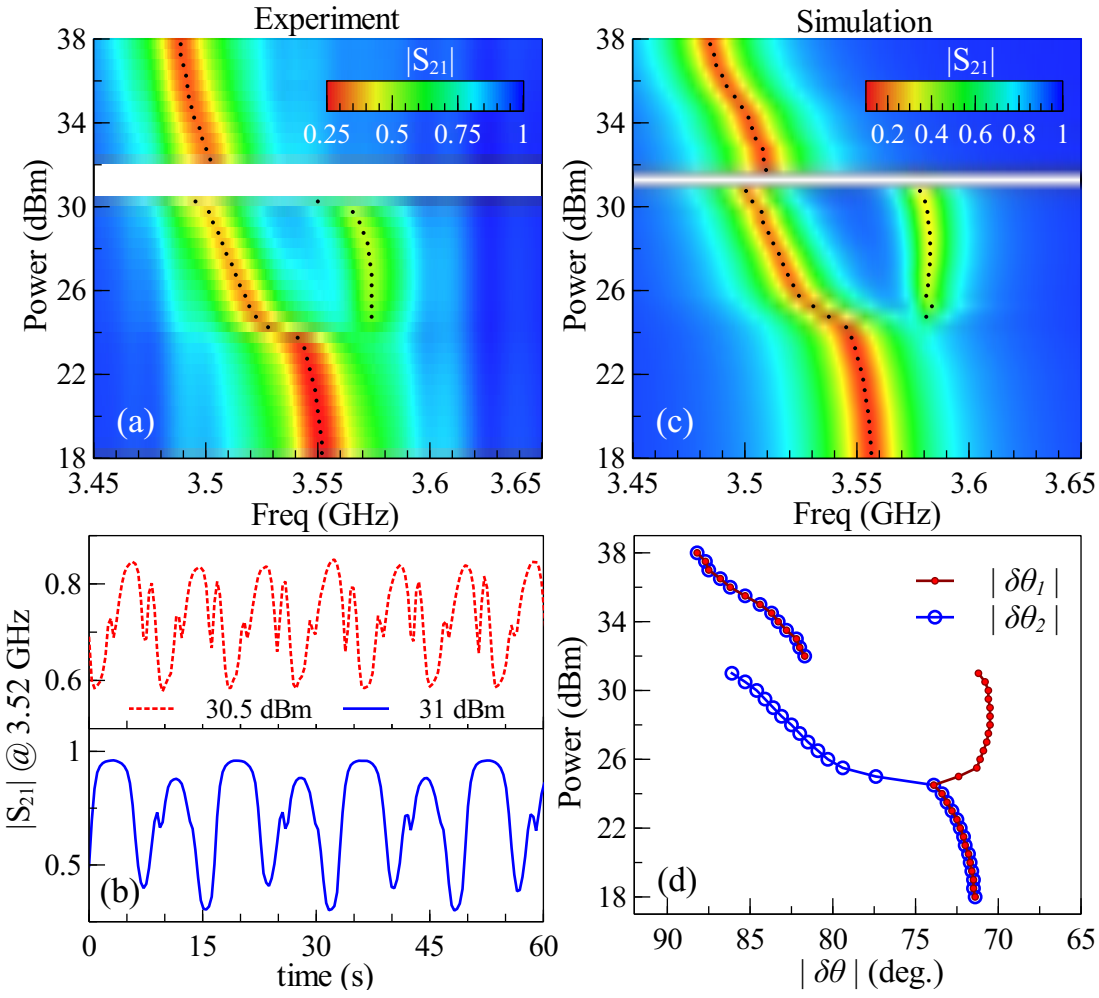

Figure 6.8: Observation of chiral symmetry breaking and self-oscillation. (a) Measured transmission spectra in stationary state as a function of pump power. The pump frequency is chosen at 3.53 GHz, and the power is swept from 18 dBm to 38 dBm in 0.5 dB steps. The black dots denote the position of the resonances, and the blank area shows region of parameters where self-oscillation occurs. (b) Time evolution of transmission coefficient at 3.52 GHz when the system exhibits self-oscillation. The red dashed curve and blue solid curve correspond to pump power 30.5 dBm and 31 dBm, respectively (c) Simulated transmission spectra and (d) the corresponding fitted mutual twist angles for different power levels, where red solid circles and blue open circles correspond to $|\delta\theta_1|$ and $|\delta\theta_2|$, respectively.

ence of substrate and waveguide (see Sec. A.4 for more details). We calculate the EM torque experienced by the two suspended SRRs with Maxwell-stress tensor, under different mutual twist angles $(\delta\theta_1, \delta\theta_2)$ when the structure is pumped at frequency 3.53 GHz, and the result gives a two dimensional map similar to Fig. 6.3 (b) and (d). Then the equilibria of the system and their stability under different pump powers can be found by following the procedure used in the Fig. 6.5, in which the initial twist angles are chosen as $\delta\theta_1 = -\delta\theta_2 = 71°$. These stable mutual twist angles can again be remapped to the transmission spectra with full wave calculation. The transmission coefficients under different pump powers, and the corresponding stable mutual twist angles are shown in Fig. 6.8 (c) and (d) (for clarity, we only plot one of the possible asymmetric states where $|\delta\theta_1| < |\delta\theta_2|$). Despite the complexity of the system, the

simulation spectra are in good agreement with the measured results. As can be seen, in the power regime where chiral symmetry breaking happens ($|\delta\theta_1| \neq |\delta\theta_2|$), the original single resonance splits into two; it is also confirmed by the stability analysis that the system does not possess any stable equilibrium in the blank regime, which leads to self-oscillations. Therefore, the evolution of chiral symmetry breaking predicted above – from the symmetric state at low pump power, to an asymmetric state in the intermediate power regime, and finally back to the symmetric state at high power, is fully verified by the experiment.

6.6 Enantiomeric Necklace Rings and Arrays

Having revealed the basic mechanism of chiral symmetry breaking in dimer enantiomers, it is desirable to show how this mechanism can influence the behaviour in larger scale systems where more than two enantiomers are coupled, and to determine whether this process can be applied to realize phase-change metamaterials. To do so, we extend our theoretical study of dimer enantiomers to more complex systems.

One very interesting configuration is a necklace ring composed of $2N$ enantiomeric meta-molecules with the configuration of the whole system satisfying $C_{N\mathrm{v}}$ symmetry, as shown in Fig. 6.2 (b). To excite all the meta-molecules uniformly, one can use azimuthally polarized waves. In the following calculation, we use the same initial twist angles $\theta_{l,1}^{(0)} = 180^\circ$ and $\theta_{l,2}^{(0)} = \pm 135^\circ$ for all the necklace rings, and the radius of necklace $|\mathbf{R}_\mathrm{C}|$ is chosen such that the center-center distance between nearest neighbouring meta-molecules is $5r_\mathrm{a}$.

By calculating the dynamic and stable states of the system, we notice that despite the complexity of nonlinear modes available, these modes still satisfy the same symmetry as the structure. Similar to the dimer enantiomers, the system always occupies the $C_{N\mathrm{v}}$ states under low or high power density, in which the system has only one stable point. In the intermediate power level where more than one stable point can exist, various states with reduced symmetry are available, including those with broken mirror symmetry (such as C_N states), reduced rotational symmetry ($C_{n\mathrm{V}}|_{n<N}$ states) and completely broken symmetry (C_1 states). Within these various types of nonlinear states, the $C_N|_{N>2}$ states are particularly interesting, since structures with such symmetry are intrinsically isotropic and their corresponding eigenstates of forward/backward radiation are circular polarized. Some examples of these modes are shown in Fig 6.9 (a), in which the direction of the rotation angle $\theta_{l,2} - \theta_{l,2}^{(0)}$ is indicated by red open circles and blue solid circles, and its magnitude is represented by the distance between the circle and the center of the polar plot.

Another exotic type of behaviour that the necklace ring can also exhibit is self-oscillations. The mechanism is the same as what we studied in Chapter 5 – when the system has no stable point, it enters a consistent oscillation state, corresponding to the limit cycle on the phase diagram; as has been discussed in Sec. 5.3.2 and thus the oscillations are damping-immune. Interestingly, some of these oscillation states still satisfy C_N symmetry, and an example of $N = 5$ is depicted in Fig. 6.9 (b), which shows the time evolution of the rotation angles of SRRs $(l, 2)$. Remarkably, due to the chiral symmetry of the system, the oscillation amplitudes of meta-molecules with $\theta_{l,2} - \theta_{l,2}^{(0)} > 0$ and $\theta_{l,2} - \theta_{l,2}^{(0)} < 0$ are exactly the same; this means the system actually oscillates back and forth between the unstable left-handed and right-handed C_N states — the “hidden" symmetry of the system is revealed via self-oscillations.

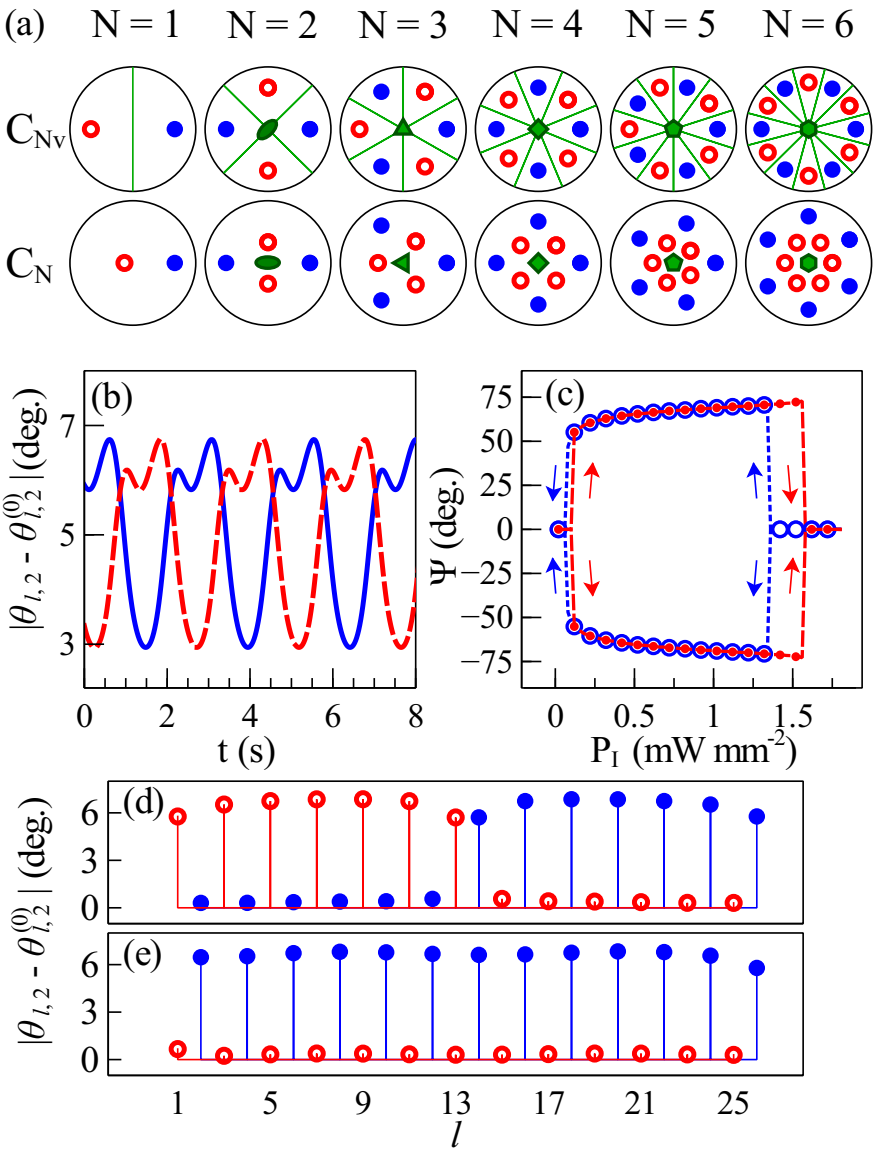

Figure 6.9: Chiral symmetry breaking in necklace rings and 1D arrays. (a) Examples of nonlinear modes with C_{Nv} and C_N symmetry accessed by the necklace rings with $2N$ enantiomeric meta-molecules. The direction of angle rotation of SRRs are denoted with red open circles ($\theta_{l,2} - \theta_{l,2}^{(0)} > 0$) and blue solid circles ($\theta_{l,2} - \theta_{l,2}^{(0)} < 0$), respectively; the distance between the circle and the center of polar plots denote the magnitudes of rotation. (b) Time evolution of self-oscillation states for necklace with C_5 symmetry. The pump frequency and power density are 4.105 GHz and 1.8 mW mm^{-2}, respectively. The blue solid curve and red dashed curve correspond to the dynamics of SRRs with $\theta_{l,2} - \theta_{l,2}^{(0)} < 0$ and $\theta_{l,2} - \theta_{l,2}^{(0)} > 0$, respectively. (c) Polarization rotation of forward scattered waves in an infinite array of enantiomeric meta-molecules, as a function of pump power density; pump frequency is chosen at 4.1 GHz for comparison with Fig. 6.4 (e). An example of chiral symmetry breaking in a finite 1D array (13 enantiomeric pairs) with (d) a symmetric excitation, and (e) a small perturbation in polarization (0.05 degree). The configuration of meta-molecules and the periodicity are the same as the infinite array. The frequency and power density are 4.1 GHz and 0.8 mW mm^{-2}, respectively.

Finally, we study the phase transition in an array of enantiomeric meta-molecules. We first calculate the response of a one dimensional infinite array to check the feasibility of the effect. We employ periodic boundary conditions to simplify the problem, assuming that the electromagnetic and mechanical responses in all the unit cells are identical, and the degrees of freedom of the whole system can be reduced to two. By taking into account the coupling of over 360 neighboring meta-molecules in the multipole expansion model (see Section A.3 of Appendix A), the results converge.

For convenience of comparison, we depict the polarization rotation of the forward scattered wave of an array in Fig. 6.9 (c). The unit cell of the array is a pair of enantiomeric dimers [Fig. 6.2(b)], with configuration the same as the one studied in Fig. 6.4; the pump frequency and the incident polarization (along the x direction) are also identical to the case shown in Fig. 6.4 (e). The array is periodic along the x direction, with a periodicity of $10r_a$. Despite the more complex and long-range coupling in an infinite array, the overall behaviour is still similar to that shown for dimers, since the origin of symmetry breaking in our system is inter-molecular interaction. As can be seen, the chiral symmetry is preserved for low and high power, and such symmetry is broken within some intermediate power regime, which leads to the existence of giant polarization rotation. The power regime of symmetry breaking becomes wider than the case of a dimer [see Fig. 6.4 (e)] due to the stronger inter-molecular interaction in the array system.

We note that the periodic boundary condition used above is a simplification which neglects many other possible solutions of symmetry breaking. In general, the nonlinear behaviour of an array system, either with finite or infinite size, can be very complicated if the number of degrees of freedom is large, and the spontaneous chiral symmetry breaking effect would occur in the form of domains, as in many natural materials. However, by properly engineering our artificial materials, it is technically possible to exclude the undesirable complexity and achieve uniform chiral response over the whole system. One simple concept is to mechanically connect all the meta-molecules of the same handedness, so that all the left-handed or right-handed meta-molecules can have identical deformation and the degrees of freedom of the whole system can be reduced to two (for conceptual layouts of 2D array, see Fig. 6.10).

Alternatively, it is also possible to access a uniform chiral response by introducing a small perturbation in the polarization state of incident waves, so that the left-handed and right-handed meta-molecules experience a slightly different EM torque. Such variation has little influence when the system is operated in the linear regime, but it can be used to control the symmetry breaking effect, since the system is highly sensitive to small perturbations around critical points. Fig. 6.9 (d) and (e) show an example of the chiral symmetry breaking response of a 1D finite array (13 enantiomeric pairs) under the same pump frequency and power density, but with slightly different polarization states. The configuration of meta-molecules, the periodicity and the pump frequency are the same as the infinite array. As can be seen, under the same pump power density, the original chiral domain response under symmetric excitation (polarization in x direction) turns into uniform chiral response when a small perturbation (0.05 degree) is introduced.

The chiral symmetry breaking effect for the necklace and array systems shown above can be considered as a chiral analogy of the phase transition from the antiferromagnetic state to the ferrimagnetic state found in iron selenide [435, 436]. We emphasize that this analogy is actually based on the similarity of the physical picture (the change of the effective potential of the system), rather than the actual physical

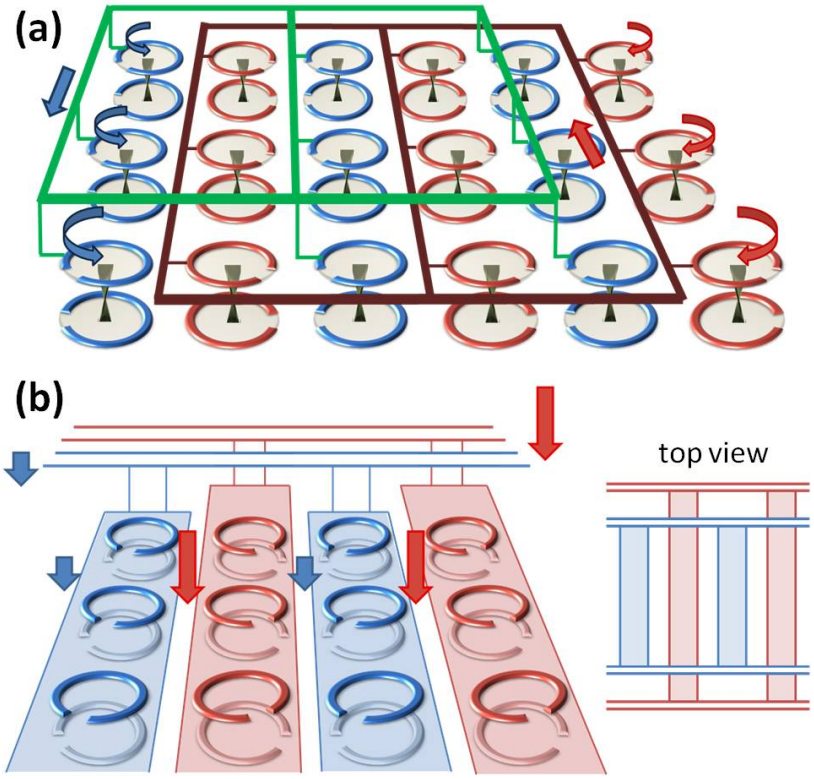

Figure 6.10: Conceptual layout of two dimensional arrays with mechanical connection. (a) Conceptual layout of the implementation of a two dimensional array of enantiomeric meta-molecules. Meta-molecules of the same handedness are mechanically connected with stiff parts so that they can deform uniformly. (b) A more practical design is based on cantilever arrays. Instead of torsion, longitudinal deformation due to EM forces can be utilized.

quantity (magnetic field or EM field) involved. In the picture of spontaneous magnetization, temperature is the tuning parameter; when the temperature is below Curie temperature, the effective potential evolves into a double well potential, and spontaneous magnetization occurs. Although in this situation external magnetic field is not required to achieve magnetization, low temperature is still indispensable to maintain the effect. Analogously, input field strength is the tuning parameter in our system, and only when the field strength surpasses a threshold value, the effective potential of the system (determined by the electromagnetic torque) can show instability for the symmetric state, and spontaneous chiral symmetry breaking occurs. In this situation, although circular polarization light or other types of chiral input is not required to induce chirality, input field is still indispensable to maintain the chirality, just as low temperature to spontaneous magnetization. Although there is some difference between the two systems, the physical picture is similar. Therefore, our study shows a new possibility to create and design artificial phase-transition effects on demand in metamaterials, without the need to introduce naturally existing phase-change materials.

6.7 Summary

To understand how the interaction among torsional meta-molecules will influence the system dynamics, in this chapter, we studied the nonlinear behaviour of a complex system with multiple enantiomeric torsional meta-molecules that are electromagnetically coupled. Specifically, we introduced and developed the concept of spontaneous chiral symmetry breaking in metamaterials, and revealed that such a system can lead to a variety of novel effects in the physics of metamaterials.

In particular, we predicted that when the intermolecular coupling becomes sufficiently strong, the system can exhibit a phase-transition by suddenly breaking the original chiral symmetry. By analyzing the evolution of the system stability of a pair of enantiomeric meta-molecules, we revealed that intermolecular interaction is indispensable for this effect – when the intermolecular interaction is sufficiently strong, the threshold powers of bifurcation of asymmetric states become different from those of symmetric states, and this allows the system to transit to asymmetric state when the symmetric state becomes unstable. By introducing a multipole approximation for far-field interaction in the model (Sec. A.3), we also explored such processes in large scale system such as enantiomeric necklace rings and long arrays of meta-molecules, showing that spontaneous chiral symmetry breaking is general in such type of system and the direction of bifurcation can be controlled with the perturbation in incident polarization.

To verify the feasibility of our concept, we performed a pump-probe microwave experiment with a pair of enantiomeric torsional meta-molecules. We successfully observed mode splitting due to chiral symmetry breaking in the intermediate pump power regime, and the results can be reproduced with full wave simulation; this provides a concrete verification of our theoretical predictions. We also observed self-oscillation effects due to the absence of stable equilibrium in the system; the underlying mechanism is identical to the one revealed in Chapter 5 for a single torsional meta-molecule. Thus, the self-oscillations observed here also verified our prediction in Chapter 5.

The study present in this chapter provides a novel and feasible mechanism for creating artificial phase-transitions in assemblies of meta-molecules without naturally occurring phase-change materials.

Statement

This chapter was written based on the work published in the journal paper:
Mingkai Liu, David A. Powell, Ilya V. Shadrivov, Mikhail Lapine, and Yuri S. Kivshar, "Spontaneous chiral symmetry breaking in metamaterials", *Nature Commun*. **5**, p 4441-9 (2014).
In this work, Y. S. Kivshar and I discussed and conceived the idea. I developed the theory, performed the simulation and experiment. D. A. Powell and I. V. Shadrivov helped with the experiment. M. Lapine and Y. S. Kivshar contributed to the discussion of the results and the writing of the manuscript.

Conclusion and Outlook

7.1 Conclusion

Over the past 15 years, the advances in metamaterials brought in many novel concepts, and most importantly, revolutionized our traditional ideas of how electromagnetic waves can be manipulated. As one of the important classes of metamaterials, chiral metamaterials offer new opportunities in manipulating the polarization of electromagnetic waves on the subwavelength scale, and novel effects such as giant optical activity and negative refractive index have been extensively studied.

While a lot of work has been done on using chiral metamaterials to control electromagnetic waves via strong light-matter interaction, the accompanying effects, such as the electromagnetic force and torque acting on the structure, as well as the nonlinear optomechanical effects are still largely unexplored. This thesis represents a study of the new effects of chiral meta-molecules and chiral metamaterials. In particular, it focuses on the optomechanical properties of such systems, covering several closely related topics, and a number of theoretical and experimental advances have been made.

(1) **The mechanism of near-field interaction, giant optical activity and the optimum configuration of polarization rotation were analyzed for a chiral meta-molecule based on twisted cut-wires, using a semi-analytical model.**

To understand the basic mechanism of chiral meta-molecules, we introduced a semi-analytical method based on the free-space Green's function under the eigenmode approximation. We employed the model to simulate the near-field coupling, far-field scattering and optical activity of chiral meta-molecules based on twisted coupled cut-wire pairs. Excellent agreement was found by comparing the results from our model and full wave calculation, indicating that the accuracy of our model is in the full wave regime. Our study also confirmed that spatial dispersion is the origin of chirality and strong near-field interaction is responsible for the giant enhancement of optical activity. Moreover, we found that the optimum twist angle for achieving the strongest polarization rotation, varies with frequency, and near the resonance is substantially lower than 45 degrees. The underlying reasons of this "counter-intuitive" effect are the strong phase variation near the resonance and the finite width of the cut-wires. These findings can provide useful insight for the design of chiral metamaterials.

(2) **The condition for achieving continuous rotation was determined for a chiral meta-molecule based on a pair of twisted split-ring resonators; this structure can generate strong rotation power and would be a good candidate for sub-wavelength light-driven actuators.**

We studied the electromagnetic torque of chiral meta-molecules based on a pair of twisted split-ring resonators, and showed that chiral meta-molecules themselves can experience strong scattering torque due to their strong interaction with electromagnetic waves. We found that the condition for achieving continuous rotation, and the roles played by chirality and anisotropy can be explained explicitly with a simple analytical model, and the rotation power of such a structure is comparable to a previously studied dielectric structure that is three orders of magnitude larger. This structure combines strong chirality and anisotropy, and therefore can support different optomechanical dynamics, working as an optical motor or an optical wrench under different frequencies of incident waves. Our study indicated that this type of chiral meta-molecules is a promising prototype for subwavelength light-driven actuators, and it would find new potential applications in nano-robotics and nano-fluidics.

(3) **A new design based on torsional chiral meta-molecules was proposed to achieve strong electromagnetic-elastic coupling; for the first time in such metamaterials, giant bistability was demonstrated experimentally.**

Much stronger electromagnetic torque can be found between the constituent meta-atoms within a chiral meta-molecule, and it can be exploited to deform meta-molecules and achieve strong nonlinear optomechanical effects. Previous studies in magnetoelastic metamaterials already demonstrated a nonlinear frequency shift, but achieving a giant nonlinear response such as bistability was still challenging. To enhance the effect based on electromagnetic-elastic coupling, we introduced torsional chiral meta-molecules based on coupled pairs of twisted split-ring resonators connected with elastic thin wires. Since the elastic feedback is very sensitive, this new design allows giant structural deformation under moderate incident power, and the elastic and electromagnetic properties can be independently designed to optimize the response. We performed a microwave experiment on a prototype structure, and successfully demonstrated a rich range of predicted nonlinear phenomena including self-tuning and bistability. This study indicates that torsional chiral meta-molecules provide an excellent platform to study various strong slow nonlinear effects in metamaterials.

(4) **Novel nonlinear dynamics, including damping-immune self-oscillations and nonlinear dynamic optical activity were revealed in torsional chiral meta-molecules with more than one mechanical degree of freedom; for the first time in metamaterials, self-oscillations were predicted and experimentally demonstrated.**

Apart from the giant stationary nonlinear response, we also demonstrated the nontrivial dynamic nonlinear response in torsional meta-molecules. Although the retardation of electromagnetic torque with respect to the mechanical motion is negligible in a pair of rings, we showed that it is still possible to achieve a dynamic nonlinear response if we introduce more than one mechanical degree of freedom. The system chosen is a torsional trimer meta-molecule with two mechanical degrees of freedom. The additional degree of freedom introduced allows the system to accumulate electromagnetic energy to compensate the damping loss and achieve nontrivial nonlinear dynamics such as self-oscillations and chaos. Contrary to many previously studied optomechanical systems, self-oscillations of torsional meta-molecules can become damping-immune when the system does not process any stable equilibrium.

As a result of the self-oscillations, the polarization rotation of chiral meta-molecules varies with time and incident power – an effect dubbed dynamic nonlinear optical activity. For the first time in metamaterials, self-oscillations were experimentally demonstrated in a system composed of two coupled torsional meta-molecules.

(5) **The concept of spontaneous chiral symmetry breaking was introduced in metamaterials, where intermolecular interaction was found to be indispensable. For the first time in metamaterials, this effect was predicted and experimentally demonstrated with coupled enantiomeric torsional meta-molecules.**

When torsional meta-molecules are assembled into large arrays, the intermolecular electromagnetic interaction could bring in qualitatively new effects. We studied a nonlinear system composed of two or more coupled enantiomeric torsional meta-molecules, i.e. torsional chiral meta-molecules with opposite handedness. It was found that intermolecular electromagnetic coupling can change the system stability and lead to spontaneous breaking of the original chiral symmetry. Such symmetry breaking can be found in both the dynamic and stationary responses of the system, and it leads to a giant nonlinear polarization change, energy localization and mode splitting. We also showed how to manipulate such symmetry breaking in a large scale array by introducing a perturbation in the polarization. For the first time in metamaterials, such an effect was predicted and demonstrated successfully in a microwave pump-probe experiment. This novel effect provides a new possibility for creating an artificial phase transition in metamaterials without requiring naturally occurring phase change materials.

7.2 Outlook

The studies presented in this thesis are of interest from both fundamental and applied points of view, and they could be extended in a number of new directions.

For the methodology part, the near-field interaction model introduced here can be applied to non-chiral structures and can become more sophisticated by taking into account fast nonlinearity, gain media and even quantum effects. It would be particularly useful when dealing with large scale and finite-sized coupled systems, as is often the case in practical devices; the introduction of randomness, special lattices such as quasi-crystalline structures, or gradients in structural geometries can also be taken into account. This would help us to predict and understand novel effects such as Anderson localization, topological states, random lasing, etc. in the context of metamaterials.

For the nonlinear optomechanical effects, although the experimental studies presented here are in the microwave regime, we expect that similar effects can also be found in high frequency regimes such as terahertz, infrared or even visible light. In these high frequency regimes, structures that are easier to fabricate with top-down approaches, such as cantilevers or nano-beams would be more favorable. It is exciting to see that recent advances in bottom-up fabrication techniques, such as DNA origami, already allowed programmable fabrication of complex structures from the molecular level; plasmonic structures similar to the designed torsional meta-molecules in our study have been realized recently [158]. Importantly, since most of the novel effects predicted and demonstrated in this thesis are independent of me-

chanical damping, the liquid environment required for DNA origami will not be a detrimental factor; this could provide a novel bottom-up platform to study various optomechanical effects at visible light frequencies.

The spontaneous chiral symmetry breaking of enantiomeric metamaterials provides a chiral analogy of the antiferromagnetic-ferrimagnetic transition found in magnetic materials. The critical phenomena around the bifurcation points may reveal yet further interesting physics, since unlike many condensed matter systems, the system studied here is non-conservative. The possibility of using such instability around the critical points for ultra-high sensitivity measurements is quite exciting. For example, one can utilize this property as an event counter by measuring the symmetry breaking triggered due to the perturbation of mechanical or electromagnetic environment. An event that can introduce mechanical vibration, or change the input electromagnetic signal could be measured. In addition, the excitation of self-oscillations around the bifurcation point could provide a further enhancement of the sensitivity due to the involvement of periodic oscillating signals – the tiny environmental perturbation can be characterized from the change of oscillating signals in either the time domain or the frequency domain. Furthermore, the achiral-chiral transition shown here is not the only one possible in metamaterials, there are also positive-negative index and elliptic-hyperbolic dispersion transitions which warrant exploration.

From the practical point of view, the coupling of electromagnetic and elastic properties also provides a novel route for *fully spatial control* of meta-surfaces. It is particularly useful for near infrared and optical frequencies where the introduction of electronic control to each individual meta-molecule becomes increasingly challenging or even undesirable due to the involvement of metals and semi-conductors that are absorptive at optical frequencies. Instead, one can use a spatial light modulator to control the spatial profile of the pump field to achieve active spatial tuning of meta-surfaces. While spatial light modulators widely used today focus on manipulation of far-field wave components, a metasurface with dynamic modulation property could do similar operation to the near-field components, and it would have great impact in a wide range of fields such as super-resolution imaging.

Appendix A

Theoretical Framework of Electromagnetic Interaction in Coupled Meta-atoms

In metamaterials, the electromagnetic (EM) interaction of meta-atoms, such as split rings and cut-wires, etc., can greatly alter the EM properties of the whole metamaterial system, for example, the frequencies and linewidths of resonances as well as the efficiencies and profiles of far-field scattering. When the separation between meta-atoms is much smaller than the operation wavelength, such interaction is in the near-field regime and is thus called *near-field interaction*. This is usually the case when two or more meta-atoms are closely packed and function as a meta-molecule. This appendix gives an overview of the background and the theoretical framework employed in this thesis. Particularly, the semi-analytical methods introduced here can be used to quantitatively describe the complex electromagnetic interaction of meta-atoms. Such interaction is related to both the energy and momentum aspects of electromagnetic waves.

Below, the first section will focus on the energy aspect of interaction of meta-atoms, a semi-analytical method based on free space Green's function will be introduced; the second section emphasizes the momentum aspect of interaction, i.e. the electromagnetic force and torque; the third section will introduce the multipole expansion of the model for far-field interaction.

A.1 Electromagnetic Coupling of Meta-atoms

The interaction, particularly the near-field interaction of meta-atoms provides additional degrees of freedom to control the properties of the composed meta-molecules. Such interaction can lead to hybridized modes with different resonant frequencies and bandwidths, and their properties are governed by the energy aspect of the interaction – for example, the amount of electric and magnetic energy that is mutually coupled among meta-atoms and the power lost as scattering and heat.

The calculation and interpretation of these hybridization effects generally rely on full wave simulation in conjunction with intuitive effective circuit models or coupled-oscillators description that require many fitted parameters [150, 357, 366, 437]. Apparently, these approaches are only useful for understanding the effects in relatively simple systems and would become impractical when the number of meta-atoms involved is large. Below, we will introduce the semi-analytical method used in this thesis from the basis of electromagnetic theory. This method can be considered as an

eigenmode approximation of the full wave methods such as Method of Moment and Integral Equation Method. Unlike previous approach based on the effective circuit model, our method can be used to calculate the electromagnetic response of a large scale coupled system with no fitted parameters. This method can provide reasonably good accuracy, while remaining physically insightful and computationally efficient.

A.1.1 Electric and Magnetic Energy

We start from the most basic theory of Lorentz force in harmonic field $\sim \exp(-\mathrm{i}\omega t)$. For a meta-atom with electric current and charge distribution $\mathbf{J}(\omega, \mathbf{r})$ and $\rho(\omega, \mathbf{r})$ in an electromagnetic field given by $\mathbf{E}(\omega, \mathbf{r})$ and $\mathbf{B}(\omega, \mathbf{r})$, the complex Lorentz force density experienced by the meta-atom is described as

$$\mathbf{f}^{\mathrm{EM}}(\omega, \mathbf{r}) = \rho^*(\omega, \mathbf{r})\mathbf{E}(\omega, \mathbf{r}) + \mathbf{J}^*(\omega, \mathbf{r}) \times \mathbf{B}(\omega, \mathbf{r}). \tag{A.1}$$

The time averaged force density can be obtained from $\frac{1}{2}\mathrm{Re}[\mathbf{f}^{\mathrm{EM}}(\omega, \mathbf{r})]$. Here, magnetic current and charge are not taken into account since only nonmagnetic materials are used in our study. For a meta-atom composed of homogeneous isotropic lossy material $\epsilon(\omega) = \epsilon^{'}(\omega) + \mathrm{i}\epsilon^{''}(\omega)$, the induced current is directly related to the real and imaginary parts of the induced polarization $\mathbf{P}(\omega, \mathbf{r}) = [\epsilon(\omega) - \epsilon_0]\mathbf{E}(\omega, \mathbf{r})$:

$$\begin{aligned} \mathbf{J}(\omega, \mathbf{r}) &= \frac{\partial}{\partial t}[\mathrm{Re}(\mathbf{P}) + \mathrm{i}\,\mathrm{Im}(\mathbf{P})] \\ &= -\mathrm{i}\omega[\epsilon^{'}(\omega) - \epsilon_0]\mathbf{E} + \mathrm{i}\omega\epsilon^{''}(\omega)\mathbf{E} \\ &= \mathbf{J}^{\mathrm{P}}(\omega, \mathbf{r}) + \mathbf{J}^{\mathrm{R}}(\omega, \mathbf{r}). \end{aligned} \tag{A.2}$$

The part corresponds to $\epsilon^{'}(\omega)$ is generally called polarization current $\mathbf{J}^{\mathrm{P}}(\omega, \mathbf{r})$; while $\mathbf{J}^{\mathrm{R}}(\omega, \mathbf{r})$ corresponds to $\epsilon^{''}(\omega)$, and it includes the effects of both conductive and dielectric losses, leading to Joule dissipation.

Since the magnetic field does not contribute to the work done, the complex work that is done on the meta-atom can be expressed as

$$\begin{aligned} \int_{\mathrm{V}} \mathbf{f}^{\mathrm{EM}}(\omega, \mathbf{r}) \cdot \dot{\mathbf{r}}\, \mathrm{d}\mathbf{r}^3 &= \int_{\mathrm{V}} [\rho^*(\omega, \mathbf{r})\mathbf{E}(\omega, \mathbf{r}) + \mathbf{J}^*(\omega, \mathbf{r}) \times \mathbf{B}(\omega, \mathbf{r})] \cdot \dot{\mathbf{r}}\, \mathrm{d}\mathbf{r}^3 \\ &= \int_{\mathrm{V}} \mathbf{J}^*(\omega, \mathbf{r}) \cdot \mathbf{E}(\omega, \mathbf{r}) \mathrm{d}\mathbf{r}^3. \end{aligned} \tag{A.3}$$

Note that the electric field $\mathbf{E}(\omega, \mathbf{r})$ is the total field including the incident field $\mathbf{E}^{\mathrm{i}}(\omega, \mathbf{r})$ and scattered field $\mathbf{E}^{\mathrm{s}}(\omega, \mathbf{r})$. Suppose there are N meta-atoms distributed in free space, then the complex work which is done on meta-atom m is expressed as

$$\int_{\mathrm{V}_m} \mathbf{J}_m^* \cdot \mathbf{E} \mathrm{d}\mathbf{r}^3 = \int_{\mathrm{V}_m} \mathbf{J}_m^* \cdot (\mathbf{E}^{\mathrm{i}} + \mathbf{E}^{\mathrm{s}}) \mathrm{d}\mathbf{r}^3 \tag{A.4}$$

with

$$\begin{aligned}
&\int \mathbf{J}_m^* \cdot \mathbf{E}^s \mathrm{d}\mathbf{r}^3 \\
=\ &\int_{\mathrm{V}_m} \mathbf{J}_m^* \cdot (-\nabla\phi - \frac{\partial}{\partial t}\mathbf{A})\mathrm{d}\mathbf{r}^3 \\
=\ &\int_{\mathrm{V}_m} -\nabla\cdot(\phi\mathbf{J}_m^*) + \phi\nabla\cdot\mathbf{J}_m^* + \mathrm{i}\omega\mathbf{J}_m^*\cdot\mathbf{A}\mathrm{d}\mathbf{r}^3 \\
=\ &\mathrm{i}\omega\int_{\mathrm{V}_m} \mathbf{J}_m^*\cdot\mathbf{A} - \rho_m^*\phi\mathrm{d}\mathbf{r}^3 \\
=\ &\mathrm{i}\omega\sum_n^N \left[\int_{\mathrm{V}_m}\int_{\mathrm{V}_n}\left(\frac{\mathbf{J}_m^*\cdot\mathbf{J}_n}{c^2} - \rho_m^*\rho_n\right)\frac{e^{\mathrm{i}k_0|\mathbf{r}_m-\mathbf{r}_n|}}{4\pi\epsilon_0|\mathbf{r}_m-\mathbf{r}_n|}\mathrm{d}\mathbf{r}_m^3\mathrm{d}\mathbf{r}_n^3\right],
\end{aligned} \tag{A.5}$$

where the free space Green's function $\exp(\mathrm{i}k_0|\mathbf{r}-\mathbf{r}'|)/|\mathbf{r}-\mathbf{r}'|$ is used for the vector potential $\mathbf{A}$ and the scalar potential ϕ generated by *all* the meta-atoms, under the Lorenz gauge condition [438]. The integral at the singular point can be evaluated separately with known analytical expressions [439].

The above integral equation is directly related to the electric and magnetic interaction energy between meta-atoms m and n, and is the foundation of full wave calculation methods such as the Method of Moments, Integral Equation Method and Boundary Element Method, in which the unknown current distribution $\mathbf{J}$ is further discretized into many small current elements [440–444].

A.1.2 Near-field Interaction Model with the Eigenmode Approximation

Although full wave methods such as the Method of Moments are accurate, they do not provide much physical insight and would become numerically expensive once the number of coupled elements increases. In fact, it is possible to build a simpler model with useful physical insight by sacrificing some accuracy.

In general, a meta-atom can support a series of resonant eigenmodes with different current and charge distributions [see example in Fig. A.1]; the *normalized* spatial distributions of current $\mathbf{j}(\omega,\mathbf{r})$ and charge $\mathrm{q}(\omega,\mathbf{r})$ for a specific eigenmode *vary with frequency*. However, such variation can be very small (but not always), particularly when the meta-atom is subwavelength in size (so that the retardation effect is small) and the constitutitive material has a very large permittivity (such as good conductors and high index dielectrics). Under such conditions, the current and charge response can usually be well-approximated by separating the frequency-dependent amplitude (mode amplitude) that captures the resonant behaviour, and the spatially-dependent distribution (mode profile, now becomes frequency-independent around the resonance) that can be used to calculate the interaction coefficients [152, 244, 445]:

$$\begin{aligned}
\rho(\omega,\mathbf{r}) &= Q(\omega)\mathrm{q}(\mathbf{r}), \\
\mathbf{J}(\omega,\mathbf{r}) &= -\mathrm{i}\omega Q(\omega)\mathbf{j}(\mathbf{r}),
\end{aligned} \tag{A.6}$$

where Q is the amplitude of oscillating charges, and $\mathrm{q}(\mathbf{r}) = -\nabla\cdot\mathbf{j}(\mathbf{r})$.

Based on the above approximation, Eq. (A.4) can be rewritten as

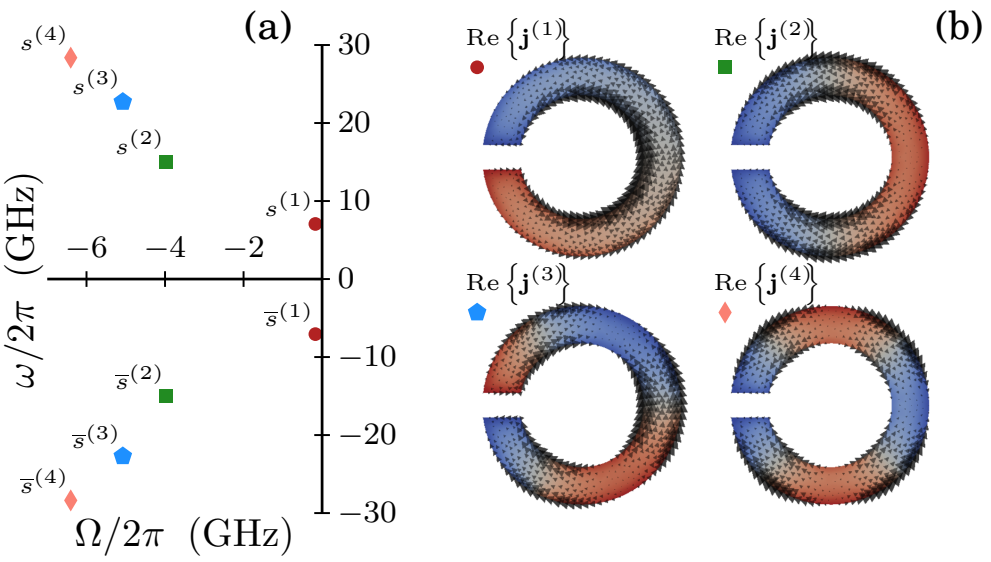

Figure A.1: (a) Resonant frequencies ω and decay rates Ω of the first four eigenmodes supported by a metallic split-ring resonator; (b) the normalized current distributions of the eigenmodes [445].

$$\int \mathbf{J}_m^* \cdot \mathbf{E} \mathrm{d}\mathbf{r}^3 = \mathrm{i}\omega Q_m^*(\omega) \left[-\mathcal{E}_m + \sum_n^N \left(\omega^2 L_{m,n} - \frac{1}{C_{m,n}} \right) Q_n(\omega) \right] \tag{A.7}$$

with

$$L_{m,n} = \iint \frac{\mathbf{j}_m \cdot \mathbf{j}_n}{4\pi c^2 \varepsilon_0} \frac{e^{\mathrm{i}k_0|\mathbf{r}_m - \mathbf{r}_n|}}{|\mathbf{r}_m - \mathbf{r}_n|} \, \mathrm{d}^3\mathbf{r}_m \, \mathrm{d}\mathbf{r}_n^3, \tag{A.8}$$

$$\frac{1}{C_{m,n}} = \iint \frac{\mathrm{q}_m \mathrm{q}_n}{4\pi\varepsilon_0} \frac{e^{\mathrm{i}k_0|\mathbf{r}_m - \mathbf{r}_n|}}{|\mathbf{r}_m - \mathbf{r}_n|} \, \mathrm{d}^3\mathbf{r}_m \, \mathrm{d}^3\mathbf{r}_n, \tag{A.9}$$

being the effective inductance and elastance (inverse of capacitance) between meta-atoms m and n, respectively. The real parts of these two quantities are related to the magnetic and electric energy exchanged between meta-atoms, while the imaginary parts are directly related to radiative loss [382]. The electromotive force induced by the incident EM fields $\mathbf{E}^{\mathrm{i}}$ can be found by overlapping the incident field with the mode profile:

$$\mathcal{E}_m = -\int \mathbf{j}_m \cdot \mathbf{E}^{\mathrm{i}} \mathrm{d}\mathbf{r}_m^3. \tag{A.10}$$

On the other hand, the complex work can also be separated into real and imaginary parts, corresponding to the contribution of polarization current $\mathbf{J}^{\mathrm{P}}$ and the dissipation part $\mathbf{J}^{\mathrm{R}}$:

$$\begin{aligned}\int \mathbf{J}_m^* \cdot \mathbf{E} \mathrm{d}\mathbf{r}_m^3 &= \int (\mathbf{J}_m^{\mathrm{P}*} + \mathbf{J}_m^{\mathrm{R}*}) \cdot \mathbf{E} \mathrm{d}\mathbf{r}_m^3 \\ &= \frac{1}{-\mathrm{i}\omega[\epsilon'(\omega) - \epsilon_0]} \int \mathbf{J}_m^{\mathrm{P}*} \cdot \mathbf{J}_m^{\mathrm{P}} \mathrm{d}\mathbf{r}_m^3 + \frac{1}{\omega \epsilon''(\omega)} \int \mathbf{J}_m^{\mathrm{R}*} \cdot \mathbf{J}_m^{\mathrm{R}} \mathrm{d}\mathbf{r}_m^3 \\ &= (\mathrm{i}\omega P_m + \omega R_m) Q_m^* Q_m \end{aligned} \tag{A.11}$$

with

$$P_m = \frac{1}{\epsilon'(\omega) - \epsilon_0} \int \mathbf{j}_m^{\mathrm{P}*} \cdot \mathbf{j}_m^{\mathrm{P}} \mathrm{d}\mathbf{r}_m^3, \tag{A.12}$$

$$R_m = \frac{1}{\epsilon''(\omega)} \int \mathbf{j}_m^{\mathrm{R}*} \cdot \mathbf{j}_m^{\mathrm{R}} \mathrm{d}\mathbf{r}_m^3, \tag{A.13}$$

being the "local" terms related to the power stored and dissipated by the meta-atom, respectively. For very low loss dielectric, $P_m \neq 0, R_m \to 0$; for good conductors, $P_m \to 0, R_m \neq 0$; for perfect electric conductors, since there is no volume current, and the surface current is perpendicular to the local electric field, $P_m = R_m = 0$.

Combining Eq. (A.4) and Eq. (A.11), the set of coupled equations can be written in a compact matrix form

$$-i\omega \sum_n^N Z_{m,n} Q_n(\omega) = \mathcal{E}_m \tag{A.14}$$

with the effective impedance

$$Z_{m,n} = \mathrm{i}\omega L_{m,n} + \frac{1}{\mathrm{i}\omega}\left(\frac{1}{C_{m,n}} + \delta_{m,n} P_m - \mathrm{i}\delta_{m,n} R_m\right), \tag{A.15}$$

$\delta_{m,n}$ is the delta function. According to reciprocity, the effective impedance matrix is complex symmetric, i.e. $Z_{m,n} = Z_{n,m}$. $Z_{m,m}$ is the self-impedance of a single meta-atom's eigenmode. To increase the accuracy of calculation, higher orders of eigenmodes can be taken into account. Equation (A.14) is used in the following chapters to calculate the electromagnetic responses of multiple coupled meta-atoms. In practice, the current and charge spatial distributions of the eigenmodes of a single meta-atom can be found numerically with full wave methods, which will be further utilized to calculate the coefficients in Eq. (A.15).

A.2 Electromagnetic Force and Torque in Coupled Meta-atoms

The momentum and angular momentum of electromagnetic waves can be transferred to meta-atoms via scattering or absorption. Such action is generally weak if only the interaction between the incident wave and a single meta-atom is taken into account (radiative force and torque). However, the EM force and torque can be significantly enhanced when multiple meta-atoms are strongly coupled, creating meta-molecules with properties beyond single meta-atoms; in such cases, the EM force and torque due to near-field interaction between meta-atoms becomes dominant (the so-called gradient force and torque).

A.2.1 Momentum Conservation and Maxwell Stress Tensor

Starting from the expression for Lorentz force density, it can be proved that, the momentum and angular momentum conservation of a system under EM wave illumination are given by

$$\frac{\mathrm{d}}{\mathrm{d}t}\mathbf{P}_{\text{mech}} + \frac{\mathrm{d}}{\mathrm{d}t}\mathbf{P}_{\text{field}} = \oint_{\mathrm{S}} \bar{\bar{\mathbf{T}}} \cdot \mathbf{n}\mathrm{d}\mathbf{r}^{\mathbf{2}}, \tag{A.16}$$

$$\frac{\mathrm{d}}{\mathrm{d}t}\mathbf{L}_{\text{mech}} + \frac{\mathrm{d}}{\mathrm{d}t}\mathbf{L}_{\text{field}} = \oint_{\mathrm{S}} \mathbf{r} \times (\bar{\bar{\mathbf{T}}} \cdot \mathbf{n})\mathrm{d}\mathbf{r}^{\mathbf{2}}, \tag{A.17}$$

where

$$\mathbf{P}_{\text{field}} = \frac{1}{c^2}\int_{\mathrm{V}} \mathbf{E} \times \mathbf{H}\mathrm{d}\mathbf{r}^3, \tag{A.18}$$

$$\mathbf{L}_{\text{field}} = \frac{1}{c^2}\int_{\mathrm{V}} \mathbf{r} \times (\mathbf{E} \times \mathbf{H})\mathrm{d}\mathbf{r}^3 \tag{A.19}$$

are the momentum and angular momentum of the EM field, respectively; $\bar{\bar{\mathbf{T}}}$ is the Maxwell stress tensor, $\mathbf{n}$ is the normal unit vector on the enclosed surface S surrounding the meta-atom volume V, and $\mathbf{r}$ is the displacement vector with respect to the *centre of rotation* [382].

The EM force and torque acting on a meta-atom are given by the time derivative of the mechanical momentum and angular momentum: $\mathbf{F}^{\text{EM}} = \frac{\mathrm{d}}{\mathrm{d}t}\mathbf{P}_{\text{mech}}$ and $\mathbf{M}^{\text{EM}} = \frac{\mathrm{d}}{\mathrm{d}t}\mathbf{L}_{\text{mech}}$, respectively. For a *mechanically stable* meta-atom under harmonic field illumination, $\frac{\mathrm{d}}{\mathrm{d}t}\mathbf{P}_{\text{field}} = 0$, $\frac{\mathrm{d}}{\mathrm{d}t}\mathbf{L}_{\text{field}} = 0$, and the time-averaged electromagnetic force and torque can be expressed as [382]

$$\mathbf{F}^{\text{EM}} = \oint_{\mathrm{S}} < \bar{\bar{\mathbf{T}}} > \cdot\mathbf{n}\,\mathrm{d}\mathbf{r}^{\mathbf{2}}, \tag{A.20}$$

$$\mathbf{M}^{\text{EM}} = \oint_{\mathrm{S}} \mathbf{r} \times (< \bar{\bar{\mathbf{T}}} > \cdot\mathbf{n})\,\mathrm{d}\mathbf{r}^{\mathbf{2}}. \tag{A.21}$$

For meta-atoms in vacuum, the time-averaged tensor component is given by

$$< T_{i,j} > = \frac{1}{2}\mathrm{Re}\left[\epsilon_0(E_i E_j^* - \frac{1}{2}\delta_{i,j}E^2) + \mu_0(H_i H_j^* - \frac{1}{2}\delta_{i,j}H^2)\right]. \tag{A.22}$$

A.2.2 Electromagnetic Force and Torque Calculation based on the Eigenmode Approximation

The Maxwell stress tensor provides a general approach to estimate the EM force and torque based on the EM field distribution, and would be particularly useful when accurate full-wave simulation is employed; however, it is also computationally expensive and could introduce undesirable numerical inaccuracy if the surface integral mesh is not dense enough to resolve the highly localized fields. The problem would become even more challenging if one needs to deal with dynamic multi-physics coupling – for example, the coupling between EM resonance and EM force induced mechanical deformation. In fact, after finding the electromagnetic response of the coupled system with the above near-field interaction model, it is much more straight forward and efficient to calculate the force and torque directly from the current and

charge. Importantly, it allows us to explicitly calculate the electromagnetic force and torque between any two meta-atoms, which becomes quite useful when analysing a complex system.

Back to Eq. (A.1), the time-averaged Lorentz force acting on meta-atom m is now expressed as

$$\begin{aligned}\mathbf{F}_m^{\mathrm{EM}}(\omega) &= \frac{1}{2}\mathrm{Re}\left[Q_m^*(\omega)\int_{\mathrm{V}_m} \mathrm{q}_m\mathbf{E}(\omega,\mathbf{r}_m)+\mathrm{i}\omega\mathbf{j}_m\times\mathbf{B}(\omega,\mathbf{r}_m)\mathrm{d}\mathbf{r}_m^3\right]\\ &= \mathbf{F}_m^{\mathrm{E}}(\omega)+\mathbf{F}_m^{\mathrm{M}}(\omega),\end{aligned} \tag{A.23}$$

where $\mathbf{F}^{\mathrm{E}}$ and $\mathbf{F}^{\mathrm{M}}$ are the contribution from electric and magnetic components, corresponding to Coulomb force and Laplace force, respectively.

For the Coulomb force, it can be further separated into the external part that comes from incident field $\mathbf{E}_{\mathrm{i}}$, and the internal part that comes from the scattered field $\mathbf{E}_{\mathrm{s}}$ from meta-atoms within the coupled system:

$$\mathbf{F}_m^{\mathrm{E}}(\omega)=\mathbf{F}_m^{\mathrm{E,int}}(\omega)+\mathbf{F}_m^{\mathrm{E,ext}}(\omega), \tag{A.24}$$

with the external part

$$\mathbf{F}_m^{\mathrm{E,ext}}(\omega)=\frac{1}{2}\mathrm{Re}\left[Q_m^*(\omega)\int_{\mathrm{V}_m}\mathrm{q}_m\mathbf{E}^{\mathrm{i}}(\omega,\mathbf{r}_m)\mathrm{d}\mathbf{r}_m^3\right], \tag{A.25}$$

and the internal part

$$\mathbf{F}_m^{\mathrm{E,int}}(\omega)=\frac{1}{2}\mathrm{Re}\left[Q_m^*(\omega)\int_{\mathrm{V}_m}\mathrm{q}_m\mathbf{E}^{\mathrm{s}}(\omega,\mathbf{r}_m)\mathrm{d}\mathbf{r}_m^3\right]. \tag{A.26}$$

From

$$\begin{aligned}\mathbf{E}^{\mathrm{s}}(\omega,\mathbf{r}_m) &= \sum_n^N\int_{\mathrm{V}_n}\nabla\phi(\mathbf{r}_m)-\frac{\partial}{\partial t}\mathbf{A}(\mathbf{r}_m)\mathrm{d}\mathbf{r}_n^3\\ &= \sum_n^N\int_{\mathrm{V}_n}\nabla\frac{e^{\mathrm{i}k_0|\mathbf{r}_m-\mathbf{r}_n|}}{4\pi\epsilon_0|\mathbf{r}_m-\mathbf{r}_n|}\rho_n-\frac{\partial}{\partial t}\frac{e^{\mathrm{i}k_0|\mathbf{r}_m-\mathbf{r}_n|}}{4\pi c^2\epsilon_0|\mathbf{r}_m-\mathbf{r}_n|}\mathbf{J}_n\mathrm{d}\mathbf{r}_n^3\\ &= \sum_n^N Q_n(\omega)\int_{\mathrm{V}_n}\frac{e^{\mathrm{i}k_0|\mathbf{r}_m-\mathbf{r}_n|}}{4\pi\epsilon_0|\mathbf{r}_m-\mathbf{r}_n|}\left[\left(\frac{1}{|\mathbf{r}_m-\mathbf{r}_n|}-\mathrm{i}k_0\right)\mathrm{q}_n\mathbf{e}_{\mathbf{R}}+k_0^2\mathbf{j}_n\right]\mathrm{d}\mathbf{r}_n^3,\end{aligned} \tag{A.27}$$

we have the final expression for the internal part

$$\begin{aligned}\mathbf{F}_m^{\mathrm{E,int}}(\omega)=\frac{1}{2}\mathrm{Re}\Bigg\{&\sum_n^N Q_n(\omega)Q_m^*(\omega)\int_{\mathrm{V}_m}\int_{\mathrm{V}_n}\frac{e^{\mathrm{i}k_0|\mathbf{r}_m-\mathbf{r}_n|}}{4\pi\epsilon_0|\mathbf{r}_m-\mathbf{r}_n|}\\ &\cdot\left[\left(\frac{1}{|\mathbf{r}_m-\mathbf{r}_n|}-\mathrm{i}k\right)\mathrm{q}_m\mathrm{q}_n\mathbf{e}_{\mathbf{R}}+k_0^2\mathrm{q}_m\mathbf{j}_n\right]\mathrm{d}\mathbf{r}_n^3\mathrm{d}\mathbf{r}_m^3\Bigg\},\end{aligned} \tag{A.28}$$

where $\mathbf{e_R} = (\mathbf{r}_m - \mathbf{r}_n)/|\mathbf{r}_m - \mathbf{r}_n|$. Similarly, for the Laplace force

$$\mathbf{F}_m^{\mathrm{M}}(\omega) = \mathbf{F}_m^{\mathrm{M,int}}(\omega) + \mathbf{F}_m^{\mathrm{M,ext}}(\omega). \tag{A.29}$$

with the external part

$$\mathbf{F}_m^{\mathrm{M,ext}}(\omega) = \frac{1}{2}\mathrm{Re}\left[\mathrm{i}\omega Q_m^*(\omega)\int_{\mathrm{V}_m}\mathbf{j}_m \times \mathbf{B}^{\mathrm{i}}(\omega,\mathbf{r}_m)\mathrm{d}\mathbf{r}_m^3\right], \tag{A.30}$$

and the internal part

$$\begin{aligned}\mathbf{F}_m^{\mathrm{M,int}}(\omega) &= \frac{1}{2}\mathrm{Re}\left[\mathrm{i}\omega Q_m^*(\omega)\int_{\mathrm{V}_m}\mathbf{j}_m \times \mathbf{B}^{\mathrm{s}}(\omega,\mathbf{r}_m)\mathrm{d}\mathbf{r}_m^3\right] \\ &= \frac{1}{2}\mathrm{Re}\Bigg\{\sum_n^N \omega^2 Q_n(\omega)Q_m^*(\omega)\int_{\mathrm{V}_m}\int_{\mathrm{V}_n}\frac{e^{\mathrm{i}k_0|\mathbf{r}_m-\mathbf{r}_n|}}{4\pi c^2\epsilon_0|\mathbf{r}_m-\mathbf{r}_n|} \\ &\cdot\left[\left(\mathrm{i}k_0 - \frac{1}{|\mathbf{r}_m-\mathbf{r}_n|}\right)\mathbf{j}_m \times (\mathbf{e_R}\times\mathbf{j}_n)\right]\mathrm{d}\mathbf{r}_n^3\mathrm{d}\mathbf{r}_m^3\Bigg\}.\end{aligned} \tag{A.31}$$

The time-averaged electromagnetic torque, with respect to the rotation center $\mathbf{r}_m^{(\mathrm{c})}$, can be expressed as

$$\mathbf{M}_m^{\mathrm{EM}}(\omega) = \mathbf{M}_m^{\mathrm{E,int}}(\omega) + \mathbf{M}_m^{\mathrm{E,ext}}(\omega) + \mathbf{M}_m^{\mathrm{M,int}}(\omega) + \mathbf{M}_m^{\mathrm{M,ext}}(\omega), \tag{A.32}$$

with the electric components

$$\mathbf{M}_m^{\mathrm{E,ext}}(\omega) = \frac{1}{2}\mathrm{Re}\left\{Q_m^*(\omega)\int_{\mathrm{V}_m}\mathrm{q}_m(\mathbf{r}_m - \mathbf{r}_m^{(\mathrm{c})})\times\mathbf{E}^{\mathrm{i}}(\omega,\mathbf{r}_m)\mathrm{d}\mathbf{r}_m^3\right\}, \tag{A.33}$$

$$\begin{aligned}\mathbf{M}_m^{\mathrm{E,int}}(\omega) &= \frac{1}{2}\mathrm{Re}\left\{Q_m^*(\omega)\int_{\mathrm{V}_m}\mathrm{q}_m(\mathbf{r}_m - \mathbf{r}_m^{(\mathrm{c})})\times\mathbf{E}^{\mathrm{s}}(\omega,\mathbf{r}_m)\mathrm{d}\mathbf{r}_m^3\right\} \\ &= \frac{1}{2}\mathrm{Re}\Bigg\{\sum_n^N Q_n(\omega)Q_m^*(\omega)\int_{\mathrm{V}_m}\int_{\mathrm{V}_n}\frac{\mathrm{q}_m e^{\mathrm{i}k_0|\mathbf{r}_m-\mathbf{r}_n|}}{4\pi\epsilon_0|\mathbf{r}_m-\mathbf{r}_n|} \\ &\cdot(\mathbf{r}_m - \mathbf{r}_m^{(\mathrm{c})})\times\left[\left(\frac{1}{|\mathbf{r}_m-\mathbf{r}_n|} - \mathrm{i}k\right)\mathrm{q}_n\mathbf{e_R} + k_0^2\mathbf{j}_n\right]\mathrm{d}\mathbf{r}_n^3\mathrm{d}\mathbf{r}_m^3\Bigg\};\end{aligned} \tag{A.34}$$

and the magnetic components

$$\mathbf{M}_m^{\mathrm{M,ext}}(\omega) = \frac{1}{2}\mathrm{Re}\left\{\mathrm{i}\omega Q_m^*(\omega)\int_{\mathrm{V}_m}(\mathbf{r}_m - \mathbf{r}_m^{(\mathrm{c})})\times\left[\mathbf{j}_m\times\mathbf{B}^{\mathrm{i}}(\omega,\mathbf{r}_m)\right]\mathrm{d}\mathbf{r}_m^3\right\}, \tag{A.35}$$

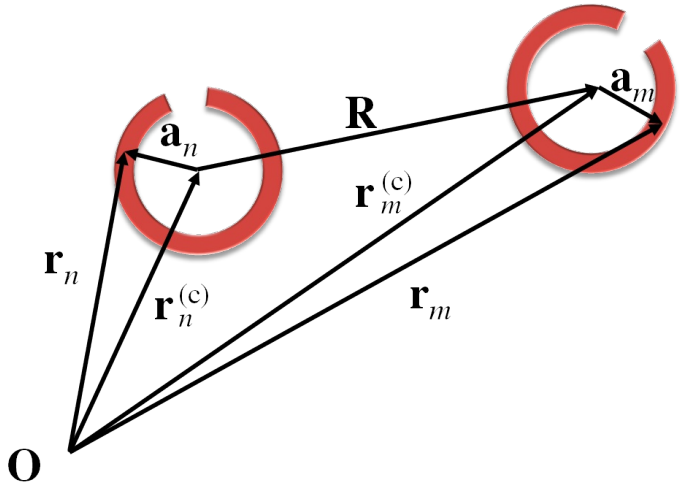

Figure A.2: Definition of displacement vectors.

$$\begin{aligned}\mathbf{M}_m^{\mathrm{M,int}}(\omega) &= \frac{1}{2}\mathrm{Re}\left\{\mathrm{s}\omega Q_m^*(\omega)\int_{\mathrm{V}_m}(\mathbf{r}_m-\mathbf{r}_m^{(\mathrm{c})})\times[\mathbf{j}_m\times\mathbf{B}^{\mathrm{s}}(\omega,\mathbf{r}_m)]\,\mathrm{d}\mathbf{r}_m^3\right\}\\ &= \frac{1}{2}\mathrm{Re}\left\{\sum_n^N\omega^2 Q_n(\omega)Q_m^*(\omega)\int_{\mathrm{V}_m}\int_{\mathrm{V}_n}\frac{e^{\mathrm{i}k_0|\mathbf{r}_m-\mathbf{r}_n|}}{4\pi c^2\epsilon_0|\mathbf{r}_m-\mathbf{r}_n|}\right.\\ &\left.\cdot(\mathbf{r}_m-\mathbf{r}_m^{(\mathrm{c})})\times\left[\left(\mathrm{i}k_0-\frac{1}{|\mathbf{r}_m-\mathbf{r}_n|}\right)\mathbf{j}_m\times(\mathbf{e}_{\mathbf{R}}\times\mathbf{j}_n)\right]\mathrm{d}\mathbf{r}_n^3\mathrm{d}\mathbf{r}_m^3\right\}.\end{aligned} \tag{A.36}$$

A.3 Multipole Approximation of the Interaction Model

The above near-field model based on the eigenmode approximation is much more efficient than full wave simulation and has comparable accuracy. However, since it requires a double volume integral, it is still not efficient enough to study the interaction and complex nonlinear dynamics when a large number of meta-atoms are coupled. For a large system where meta-atoms are coupled in both the near-field and far-field regimes, the effective impedance terms $Z_{m,n}$ can be calculated with different methods, depending on the separation of the interacting meta-atoms. For closely spaced meta-atoms, the near-field model is required; while for the situation where the separation is much larger than the scale of a meta-atom, a multipole approximation can be developed.

A.3.1 Taylor Expansion of the Green's Function

We rewrite the displacement vector of two meta-atoms as

$$\begin{aligned}\mathbf{r}_m &= \mathbf{r}_m^{(\mathrm{c})}+\mathbf{a}_m,\\ \mathbf{r}_n &= \mathbf{r}_n^{(\mathrm{c})}+\mathbf{a}_n.\end{aligned} \tag{A.37}$$

$\mathbf{r}_m^{(c)}$ is the displacement of meta-atoms' centres with respect to the coordinate origin, and $\mathbf{a}_m$ is the position vector with respect to the centre of the m-th meta-atom [Figure A.2].

Define $\mathbf{R} = R \cdot \mathbf{n} = \mathbf{r}_m^{(c)} - \mathbf{r}_n^{(c)}$ the displacement between the centres of meta-atoms, when $|\mathbf{a}| \ll R$,

$$\begin{aligned}
|\mathbf{r}_m - \mathbf{r}_n| &= |\mathbf{r}_m^{(c)} - \mathbf{r}_n^{(c)} + \mathbf{a}_m - \mathbf{a}_n| \\
&\approx |\mathbf{R} + \mathbf{a}_m| - \frac{(\mathbf{R} + \mathbf{a}_m) \cdot \mathbf{a}_n}{|\mathbf{R} + \mathbf{a}_m|} \\
&\approx R + \mathbf{n} \cdot \mathbf{a}_m - \frac{R\,\mathbf{n} \cdot \mathbf{a}_n + \mathbf{a}_m \cdot \mathbf{a}_n}{R + \mathbf{n} \cdot \mathbf{a}_m} \\
&= R + \frac{R\,(\mathbf{n} \cdot \mathbf{a}_m - \mathbf{n} \cdot \mathbf{a}_n) + (\mathbf{n} \cdot \mathbf{a}_m)^2 - \mathbf{a}_m \cdot \mathbf{a}_n}{R + \mathbf{n} \cdot \mathbf{a}_m} \\
&\approx R + \frac{1}{R}\left(1 - \frac{\mathbf{n} \cdot \mathbf{a}_m}{R}\right)\left[R\,\mathbf{n} \cdot (\mathbf{a}_m - \mathbf{a}_n) + (\mathbf{n} \cdot \mathbf{a}_m)^2 - \mathbf{a}_m \cdot \mathbf{a}_n\right] \\
&= R + \mathbf{n} \cdot (\mathbf{a}_m - \mathbf{a}_n) + \frac{1}{R}\left[(\mathbf{n} \cdot \mathbf{a}_m)(\mathbf{n} \cdot \mathbf{a}_n) - \mathbf{a}_m \cdot \mathbf{a}_n\right] \\
&+ \frac{1}{R^2}\left[(\mathbf{n} \cdot \mathbf{a}_m)(\mathbf{a}_m \cdot \mathbf{a}_n) - (\mathbf{n} \cdot \mathbf{a}_m)^3\right]. \qquad \text{(A.38)}
\end{aligned}$$

Note that the above expression for distance should be invariant when interchanging m and n (unit vector $\mathbf{n}$ reverses direction), so the third order term is modified as $\frac{1}{2R^2}\left[\mathbf{n} \cdot (\mathbf{a}_n - \mathbf{a}_m)\,(\mathbf{a}_m \cdot \mathbf{a}_n) - (\mathbf{n} \cdot \mathbf{a}_m)^3 + (\mathbf{n} \cdot \mathbf{a}_n)^3\right]$. Truncated by the third order term $1/R^2$, the displacement term is approximated as

$$\begin{aligned}
|\mathbf{r}_m - \mathbf{r}_n| \approx R + \mathbf{n} \cdot (\mathbf{a}_n - \mathbf{a}_m) + \frac{1}{R}\left[(\mathbf{n} \cdot \mathbf{a}_m)\,(\mathbf{n} \cdot \mathbf{a}_n) - \mathbf{a}_m \cdot \mathbf{a}_n\right] \\
+ \frac{1}{2R^2}\left[\mathbf{n} \cdot (\mathbf{a}_n - \mathbf{a}_m)\,(\mathbf{a}_m \cdot \mathbf{a}_n) + (\mathbf{n} \cdot \mathbf{a}_m)^3 - (\mathbf{n} \cdot \mathbf{a}_n)^3\right]. \qquad \text{(A.39)}
\end{aligned}$$

Substituting the approximation Eq. (A.39) into the Green's function $e^{\mathrm{i}k_0|\mathbf{r}_m - \mathbf{r}_n|} \Big/ |\mathbf{r}_m - \mathbf{r}_n|$, using Taylor expansion again and truncating it by the third order term,

$$\begin{aligned}
&\frac{e^{\mathrm{i}k_0|\mathbf{r}_m - \mathbf{r}_n|}}{|\mathbf{r}_m - \mathbf{r}_n|} \\
\approx &\frac{e^{\mathrm{i}k_0 R}}{R}\left\{1 + \left(\frac{1}{R} - \mathrm{i}k\right)(\mathbf{n} \cdot \mathbf{a}_m - \mathbf{n} \cdot \mathbf{a}_n)\right. \\
&+ \left(\frac{1}{R^2} - \frac{\mathrm{i}k}{R} - \frac{k^2}{2}\right)(\mathbf{n} \cdot \mathbf{a}_m - \mathbf{n} \cdot \mathbf{a}_n)^2 + \left(\frac{\mathrm{i}k}{R} - \frac{1}{R^2}\right)\left[(\mathbf{n} \cdot \mathbf{a}_m)(\mathbf{n} \cdot \mathbf{a}_n) - \mathbf{a}_m \cdot \mathbf{a}_n\right] \\
&+ \left(\frac{1}{R^3} - \frac{\mathrm{i}k}{R^2} - \frac{k^2}{2R} + \frac{\mathrm{i}k^3}{6}\right)(\mathbf{n} \cdot \mathbf{a}_m - \mathbf{n} \cdot \mathbf{a}_n)^3 \\
&+ \left(\frac{2}{R^3} - \frac{k^2}{R} - \frac{\mathrm{i}2k}{R^2}\right)\mathbf{n} \cdot (\mathbf{a}_n - \mathbf{a}_m)\left[(\mathbf{n} \cdot \mathbf{a}_m)(\mathbf{n} \cdot \mathbf{a}_n) - \mathbf{a}_m \cdot \mathbf{a}_n\right] \\
&\left. + \left(\frac{\mathrm{i}k}{2R^2} - \frac{1}{2R^3}\right)\left[\mathbf{n} \cdot (\mathbf{a}_n - \mathbf{a}_m)(\mathbf{a}_m \cdot \mathbf{a}_n) - (\mathbf{n} \cdot \mathbf{a}_n)^3 + (\mathbf{n} \cdot \mathbf{a}_m)^3\right] + \cdots\right\}. \qquad \text{(A.40)}
\end{aligned}$$

This expression is the basis of the following multipole expansion of the effective

impedance. As will be shown, the expansion terms with displacement vector $\mathbf{a}$ are directly related to the multipole moments of the system.

A.3.2 Multipole Approximation of the Effective Inductance

Substituting Eq. (A.40) in to Eq. (A.8), we have the Taylor expansion of the effective inductance,

$$\begin{aligned} L_{m,n} &= \frac{1}{4\pi\varepsilon_0 c^2} \iint \mathbf{j}(\mathbf{r}_m)\cdot\mathbf{j}(\mathbf{r}_n)\frac{e^{\mathrm{i}k_0|\mathbf{r}_m-\mathbf{r}_n|}}{|\mathbf{r}_m-\mathbf{r}_n|}\,\mathrm{d}\mathbf{r}_m^3\,\mathrm{d}\mathbf{r}_n^3 \\ &\approx \frac{e^{\mathrm{i}k_0 R}}{4\pi\varepsilon_0 c^2 R}\iint \mathbf{j}(\mathbf{a}_m)\cdot\mathbf{j}(\mathbf{a}_n)\left[1+\left(\frac{1}{R}-\mathrm{i}k\right)(\mathbf{n}\cdot\mathbf{a}_m-\mathbf{n}\cdot\mathbf{a}_n)+\cdots\right]\mathrm{d}\mathbf{a}_m^3\,\mathrm{d}\mathbf{a}_n^3. \end{aligned} \tag{A.41}$$

The zeroth order term in the integral gives

$$\begin{aligned} L^{(0)} &= \iint \mathbf{j}_m\cdot\mathbf{j}_n\,\mathrm{d}\mathbf{a}_m^3\,\mathrm{d}\mathbf{a}_n^3 \\ &= \frac{1}{-\omega^2 Q_m Q_n}\iint \mathbf{J}(\mathbf{a}_m,t)\cdot\mathbf{J}(\mathbf{a}_n,t)\,\mathrm{d}\mathbf{a}_m^3\,\mathrm{d}\mathbf{a}_n^3 \\ &= \frac{1}{-\omega^2 Q_m Q_n}\iint (\rho_m\dot{\mathbf{a}}_m)\cdot(æ_n\dot{\mathbf{a}}_n)\,\mathrm{d}\mathbf{a}_m^3\,\mathrm{d}\mathbf{a}_n^3 \\ &= \frac{1}{-\omega^2 Q_m Q_n}\int(-\mathrm{i}\omega Q_m \mathrm{q}_m\mathbf{a}_m)\,\mathrm{d}\mathbf{a}_m^3\cdot\int(-\mathrm{i}\omega Q_n\mathrm{q}_n\mathbf{a}_n)\,\mathrm{d}\mathbf{a}_n^3 \\ &= \mathbf{l}_m\cdot\mathbf{l}_n, \end{aligned} \tag{A.42}$$

where $\mathbf{l}=\int \mathrm{q}\mathbf{a}\,\mathrm{d}\mathbf{a}^3$ is the normalized electric dipole moment of an eigen mode. So the above term corresponds to the contribution of electric dipole-dipole interaction.

The first order term

$$\begin{aligned} L^{(1)} &= \left(\frac{1}{R}-\mathrm{i}k\right)\iint \mathbf{j}_m\cdot\mathbf{j}_n(\mathbf{n}\cdot\mathbf{a}_m-\mathbf{n}\cdot\mathbf{a}_n)\,\mathrm{d}\mathbf{a}_m^3\,\mathrm{d}\mathbf{a}_n^3 \\ &= \left(\frac{1}{R}-\mathrm{i}k\right)\left\{\iint \mathbf{j}_m\cdot\mathbf{j}_n(\mathbf{n}\cdot\mathbf{a}_m)\,\mathrm{d}\mathbf{a}_m^3\,\mathrm{d}\mathbf{a}_n^3-\iint \mathbf{j}_m\cdot\mathbf{j}_n(\mathbf{n}\cdot\mathbf{a}_n)\,\mathrm{d}\mathbf{a}_m^3\,\mathrm{d}\mathbf{a}_n^3\right\}, \end{aligned} \tag{A.43}$$

with

$$\begin{aligned} &\iint \mathbf{j}_m\cdot\mathbf{j}_n(\mathbf{n}\cdot\mathbf{a}_m)\,\mathrm{d}\mathbf{a}_m^3\,\mathrm{d}\mathbf{a}_n^3 \\ &= \mathbf{l}_n\cdot\int \mathbf{j}_m\cdot(\mathbf{n}\cdot\mathbf{a}_m)\,\mathrm{d}\mathbf{a}_m^3 \\ &= \mathbf{l}_n\cdot\left\{\int \frac{1}{2}\left[\mathbf{j}_m\cdot(\mathbf{n}\cdot\mathbf{a}_m)-\mathbf{a}_m\cdot(\mathbf{j}_m\cdot\mathbf{n})\right]+\frac{1}{2}\left[\mathbf{j}_m\cdot(\mathbf{n}\cdot\mathbf{a}_m)+\mathbf{a}_m\cdot(\mathbf{j}_m\cdot\mathbf{n})\right]\mathrm{d}\mathbf{a}_m^3\right\} \\ &= \mathbf{l}_n\cdot\left(-\mathbf{n}\times\mathbf{u}_m+\frac{1}{2}\mathbf{n}\cdot\bar{\bar{\mathbf{l}}}_m\right). \end{aligned} \tag{A.44}$$

Finally,

$$L^{(1)} = \left(\frac{1}{R}-\mathrm{i}k\right)\left[\mathbf{l}_n\cdot\left(-\mathbf{n}\times\mathbf{u}_m+\frac{1}{2}\mathbf{n}\cdot\bar{\bar{\mathbf{l}}}_m\right)+\mathbf{l}_m\cdot\left(-\mathbf{n}\times\mathbf{u}_n+\frac{1}{2}\mathbf{n}\cdot\bar{\bar{\mathbf{l}}}_n\right)\right], \tag{A.45}$$

where $\mathbf{u} = \frac{1}{2}\int(\mathbf{a}\times\mathbf{j})\,\mathrm{d}^3\mathbf{a}$ and $\bar{\bar{\mathbf{l}}} = \int \mathrm{q}\mathbf{a}\mathbf{a}\,\mathrm{d}^3\mathbf{a}$ are the normalized magnetic dipole and electric quadrupole moments. This term corresponds to the interaction between electric dipole and magnetic dipole as well as electric quadrupole.

The second order terms include two parts: $L^{(2)} = L_1^{(2)} + L_2^{(2)}$.

$$L_1^{(2)} = \left(\frac{1}{R^2} - \frac{\mathrm{i}k}{R} - \frac{k^2}{2}\right)\iint \mathbf{j}_m\cdot\mathbf{j}_n(\mathbf{n}\cdot\mathbf{a}_m - \mathbf{n}\cdot\mathbf{a}_n)^2\,\mathrm{d}^3\mathbf{a}_m\,\mathrm{d}\mathbf{a}_n^3, \tag{A.46}$$

The integral is evaluated as

$$\begin{aligned}
&\iint \mathbf{j}_m\cdot\mathbf{j}_n\Big[(\mathbf{n}\cdot\mathbf{a}_m)^2 + (\mathbf{n}\cdot\mathbf{a}_n)^2 - 2(\mathbf{n}\cdot\mathbf{a}_m)(\mathbf{n}\cdot\mathbf{a}_n)\Big]\,\mathrm{d}\mathbf{a}_m^3\,\mathrm{d}\mathbf{a}_n^3\\
= \;& \mathbf{l}_n\cdot\int \mathbf{j}_m(\mathbf{n}\cdot\mathbf{a}_m)^2\,\mathrm{d}\mathbf{a}_m^3 + \mathbf{l}_m\cdot\int \mathbf{j}_n(\mathbf{n}\cdot\mathbf{a}_n)^2\,\mathrm{d}\mathbf{a}_n^3\\
& -2\int \mathbf{j}_m\cdot\mathbf{j}_n(\mathbf{n}\cdot\mathbf{a}_m)(\mathbf{n}\cdot\mathbf{a}_n)\,\mathrm{d}\mathbf{a}_m^3\,\mathrm{d}\mathbf{a}_n^3,
\end{aligned} \tag{A.47}$$

where

$$\int \mathbf{j}_m(\mathbf{n}\cdot\mathbf{a}_m)^2\,\mathrm{d}\mathbf{a}_m^3 = \frac{1}{-\mathrm{i}\omega}\int \mathrm{q}_m\underbrace{(\mathbf{a}_m\cdot\mathbf{n})^2\,\dot{\mathbf{a}}_m}_{A}\,\mathrm{d}\mathbf{a}_m^3. \tag{A.48}$$

From

$$\begin{aligned}
&\mathbf{n}\cdot\frac{\mathrm{d}}{\mathrm{d}t}(\mathrm{q}_m\mathbf{a}_m\mathbf{a}_m\mathbf{a}_m)\cdot\mathbf{n}\\
=\;& \mathrm{q}_m\left[\mathbf{n}\cdot(\dot{\mathbf{a}}_m\mathbf{a}_m\mathbf{a}_m + \mathbf{a}_m\dot{\mathbf{a}}_m\mathbf{a}_m + \mathbf{a}_m\mathbf{a}_m\dot{\mathbf{a}}_m)\cdot\mathbf{n}\right]\\
=\;& \mathrm{q}_m\left[(\dot{\mathbf{a}}_m\cdot\mathbf{n})\,\mathbf{a}_m(\mathbf{a}_m\cdot\mathbf{n}) + (\mathbf{a}_m\cdot\mathbf{n})\,\dot{\mathbf{a}}_m(\mathbf{a}_m\cdot\mathbf{n}) + (\mathbf{a}_m\cdot\mathbf{n})\,\mathbf{a}_m(\dot{\mathbf{a}}_m\cdot\mathbf{n})\right]\\
=\;& \mathrm{q}_m\Big[\underbrace{2(\dot{\mathbf{a}}_m\cdot\mathbf{n})(\mathbf{a}_m\cdot\mathbf{n})\,\mathbf{a}_m + (\mathbf{a}_m\cdot\mathbf{n})^2\,\dot{\mathbf{a}}_m}_{2B+A}\Big],
\end{aligned} \tag{A.49}$$

and

$$\begin{aligned}
&-\mathbf{n}\times\left[(\mathbf{a}_m\times\mathbf{j}_m)\,\mathbf{a}_m\right]\cdot\mathbf{n}\\
=\;& \left[-\mathbf{n}\times(\mathbf{a}_m\times\mathbf{j}_m)\right]\mathbf{a}_m\cdot\mathbf{n}\\
=\;& \left[-\mathbf{n}\times(\mathbf{a}_m\times\mathbf{j}_m)\right](\mathbf{a}_m\cdot\mathbf{n})\\
=\;& \left[\mathbf{j}_m\cdot(\mathbf{n}\cdot\mathbf{a}_m) - \mathbf{a}_m\cdot(\mathbf{j}_m\cdot\mathbf{n})\right](\mathbf{a}_m\cdot\mathbf{n})\\
=\;& \mathrm{q}_m\Big[\underbrace{(\mathbf{a}_m\cdot\mathbf{n})^2\,\dot{\mathbf{a}}_m - (\dot{\mathbf{a}}_m\cdot\mathbf{n})(\mathbf{a}_m\cdot\mathbf{n})\,\mathbf{a}_m}_{A-B}\Big],
\end{aligned} \tag{A.50}$$

Eq. (A.48) can be expressed as

$$\begin{aligned}
&\int \mathbf{j}_m(\mathbf{n}\cdot\mathbf{a}_m)^2\,\mathrm{d}\mathbf{a}_m^3\\
=\;& -\frac{2}{3}\mathbf{n}\times\int\left[(\mathbf{a}_m\times\mathbf{j}_m)\mathbf{a}_m\right]\cdot\mathbf{n}\,\mathrm{d}\mathbf{a}_m^3 + \frac{1}{3}\mathbf{n}\cdot\int\frac{\mathrm{d}}{\mathrm{d}t}(\mathrm{q}_m\mathbf{a}_m\mathbf{a}_m\mathbf{a}_m)\cdot\mathbf{n}\,\mathrm{d}\mathbf{a}_m^3\\
=\;& -\mathbf{n}\times(\bar{\bar{\mathbf{u}}}\cdot\mathbf{n}) + \frac{1}{3}\mathbf{n}\cdot(\hat{\mathbf{l}}\cdot\mathbf{n}),
\end{aligned} \tag{A.51}$$

where $\overline{\overline{\mathbf{u}}} = \frac{2}{3}\int(\mathbf{a}\times\mathbf{j})\,\mathbf{a}\,\mathrm{d}^3\mathbf{a}$ and $\widehat{\mathbf{l}} = \int \mathrm{q}\,\mathbf{a}\,\mathbf{a}\,\mathbf{a}\,\mathrm{d}^3\mathbf{a}$ are the normalized magnetic quadrupole and electric sextupole moments, respectively. In addition, it can be proved that

$$\begin{aligned}
&\int \mathbf{j}_m\cdot\mathbf{j}_n(\mathbf{n}\cdot\mathbf{a}_m)(\mathbf{n}\cdot\mathbf{a}_n)\,\mathrm{d}\mathbf{a}_m^3\,\mathrm{d}\mathbf{a}_n^3\\
=&\int \mathbf{j}_m(\mathbf{n}\cdot\mathbf{a}_m)\,\mathrm{d}\mathbf{a}_m^3\cdot\int \mathbf{j}_n(\mathbf{n}\cdot\mathbf{a}_n)\,\mathrm{d}\mathbf{a}_n^3\\
=&\left(-\mathbf{n}\times\mathbf{u}_m+\frac{1}{2}\mathbf{n}\cdot\overline{\overline{\mathbf{l}}}_m\right)\cdot\left(-\mathbf{n}\times\mathbf{u}_n+\frac{1}{2}\mathbf{n}\cdot\overline{\overline{\mathbf{l}}}_n\right),
\end{aligned}\tag{A.52}$$

and

$$\int \mathbf{j}_m\cdot\mathbf{j}_n(\mathbf{a}_m\cdot\mathbf{a}_n)\,\mathrm{d}\mathbf{a}_m^3\,\mathrm{d}\mathbf{a}_n^3 = 2\mathbf{u}_m\cdot\mathbf{u}_n+\frac{1}{4}\overline{\overline{\mathbf{l}}}_m:\overline{\overline{\mathbf{l}}}_n,\tag{A.53}$$

where " : " is the double dot product operation [446]. So we have

$$\begin{aligned}
L_2^{(2)} \;=\;& \left(\frac{\mathrm{i}k}{R}-\frac{1}{R^2}\right)\left[\left(-\mathbf{n}\times\mathbf{u}_m+\frac{1}{2}\mathbf{n}\cdot\overline{\overline{\mathbf{l}}}_m\right)\right.\\
&\left.\cdot\left(-\mathbf{n}\times\mathbf{u}_n+\frac{1}{2}\mathbf{n}\cdot\overline{\overline{\mathbf{l}}}_n\right)-\left(2\mathbf{u}_m\cdot\mathbf{u}_n+\frac{1}{4}\overline{\overline{\mathbf{l}}}_m:\overline{\overline{\mathbf{l}}}_n\right)\right].
\end{aligned}\tag{A.54}$$

Finally, the effective inductance up to second order terms can be expressed as

$$\begin{aligned}
L_{mn} &\approx \frac{\mu_0 e^{\mathrm{i}k_0R}}{4\pi R}\left(L^{(0)}+L^{(1)}+L_1^{(2)}+L_2^{(2)}\right)\\
&= \frac{\mu_0 e^{\mathrm{i}k_0R}}{4\pi R}\left\{\mathbf{l}_m\cdot\mathbf{l}_n+\left(\frac{1}{R}-\mathrm{i}k\right)\left[\mathbf{l}_n\cdot\left(-\mathbf{n}\times\mathbf{u}_m+\frac{1}{2}\mathbf{n}\cdot\overline{\overline{\mathbf{l}}}_m\right)\right.\right.\\
&\quad\left.-\mathbf{l}_m\cdot\left(-\mathbf{n}\times\mathbf{u}_n+\frac{1}{2}\mathbf{n}\cdot\overline{\overline{\mathbf{l}}}_n\right)\right]\\
&\quad+\left(\frac{1}{R^2}-\frac{\mathrm{i}k}{R}-\frac{k^2}{2}\right)\left\{\mathbf{l}_m\cdot\left[(\mathbf{u}_n\cdot\mathbf{n})\times\mathbf{n}+\frac{1}{3}\mathbf{n}\cdot(\widehat{\mathbf{l}}_n\cdot\mathbf{n})\right]\right.\\
&\quad\left.+\mathbf{l}_n\cdot\left[(\mathbf{u}_m\cdot\mathbf{n})\times\mathbf{n}+\frac{1}{3}\mathbf{n}\cdot(\widehat{\mathbf{l}}_m\cdot\mathbf{n})\right]\right\}\\
&\quad+\left(-\frac{3}{R^2}+\frac{\mathrm{i}3k}{R}+k^2\right)\left(-\mathbf{n}\times\mathbf{u}_m+\frac{1}{2}\mathbf{n}\cdot\overline{\overline{\mathbf{l}}}_m\right)\cdot\left(-\mathbf{n}\times\mathbf{u}_n+\frac{1}{2}\mathbf{n}\cdot\overline{\overline{\mathbf{l}}}_n\right)\\
&\quad+\left(-\frac{\mathrm{i}k}{R}+\frac{1}{R^2}\right)\left(2\mathbf{u}_m\cdot\mathbf{u}_n+\frac{1}{4}\overline{\overline{\mathbf{l}}}_m:\overline{\overline{\mathbf{l}}}_n\right)\Bigg\}.
\end{aligned}\tag{A.55}$$

A.3.3 Multipole Approximation of the Effective Elastance

A similar procedure can be applied to the effective elastance

$$\begin{aligned}1/C_{mn} =& \frac{1}{4\pi\varepsilon_0}\iint \mathrm{q}(\mathbf{a}_m)\mathrm{q}(\mathbf{a}_n)\frac{e^{\mathrm{i}k_0|\mathbf{a}_m-\mathbf{a}_n|}}{|\mathbf{a}_m-\mathbf{a}_n|}\,\mathrm{d}\mathbf{a}_m^3\,\mathrm{d}\mathbf{a}_n^3\\ \approx& \frac{e^{\mathrm{i}k_0R}}{4\pi\varepsilon_0 R}\iint \mathrm{q}_m\mathrm{q}_n\left[1+\left(\frac{1}{R}-\mathrm{i}k\right)(\mathbf{n}\cdot\mathbf{a}_m-\mathbf{n}\cdot\mathbf{a}_n)+\cdots\right]\mathrm{d}\mathbf{a}_m^3\,\mathrm{d}\mathbf{a}_n^3\\ =& \frac{e^{\mathrm{i}k_0R}}{4\pi\varepsilon_0 R}\Big(1/C^{(0)}+1/C^{(1)}+1/C_1^{(2)}+1/C_2^{(2)}+1/C_1^{(3)}+1/C_2^{(3)}\\ &+1/C_3^{(3)}+\cdots\Big).\end{aligned} \tag{A.56}$$

Since the net charge of the resonators $\mathcal{Q}$ is zero,

$$1/C^{(0)} = \iint \mathrm{q}_m\mathrm{q}(\mathbf{a}_n)\,\mathrm{d}\mathbf{a}_m^3\,\mathrm{d}\mathbf{a}_n^3 = \mathcal{Q}_m\mathcal{Q}_n = 0, \tag{A.57}$$

Similarly, for the first order term

$$1/C^{(1)} = \left(\frac{1}{R}-\mathrm{i}k\right)\iint \mathrm{q}_m\mathrm{q}_n(\mathbf{n}\cdot\mathbf{a}_m-\mathbf{n}\cdot\mathbf{a}_n)\,\mathrm{d}\mathbf{a}_m^3\,\mathrm{d}\mathbf{a}_n^3 = \mathcal{Q}_n\mathbf{n}\cdot\mathbf{l}_m-\mathcal{Q}_m\mathbf{n}\cdot\mathbf{l}_n = 0. \tag{A.58}$$

For the second order terms

$$\begin{aligned}1/C_1^{(2)} =& \left(\frac{1}{R^2}-\frac{\mathrm{i}k}{R}-\frac{k^2}{2}\right)\iint \mathrm{q}_m\mathrm{q}_n(\mathbf{n}\cdot\mathbf{a}_m-\mathbf{n}\cdot\mathbf{a}_n)^2\,\mathrm{d}\mathbf{a}_m^3\,\mathrm{d}\mathbf{a}_n^3\\ =& \left(-\frac{2}{R^2}+\frac{\mathrm{i}2k}{R}+k^2\right)(\mathbf{n}\cdot\mathbf{l}_m)(\mathbf{n}\cdot\mathbf{l}_n),\end{aligned} \tag{A.59}$$

$$\begin{aligned}1/C_2^{(2)} =& \left(\frac{\mathrm{i}k}{R}-\frac{1}{R^2}\right)\iint \mathrm{q}_m\mathrm{q}_n\left[(\mathbf{n}\cdot\mathbf{a}_m)(\mathbf{n}\cdot\mathbf{a}_n)-\mathbf{a}_m\cdot\mathbf{a}_n\right]\mathrm{d}\mathbf{a}_m^3\,\mathrm{d}\mathbf{a}_n^3\\ =& \left(\frac{\mathrm{i}k}{R}-\frac{1}{R^2}\right)\left[(\mathbf{n}\cdot\mathbf{l}_m)(\mathbf{n}\cdot\mathbf{l}_n)-\mathbf{l}_m\cdot\mathbf{l}_n\right].\end{aligned} \tag{A.60}$$

For the third order terms

$$\begin{aligned}1/C_1^{(3)} =& \left(\frac{1}{R^3}-\frac{\mathrm{i}k}{R^2}-\frac{k^2}{2R}+\frac{\mathrm{i}k^3}{6}\right)\iint \mathrm{q}_m\mathrm{q}_n(\mathbf{n}\cdot\mathbf{a}_m-\mathbf{n}\cdot\mathbf{a}_n)^3\,\mathrm{d}\mathbf{a}_m^3\,\mathrm{d}\mathbf{a}_n^3\\ =& \left(\frac{3}{R^3}-\frac{\mathrm{i}3k}{R^2}-\frac{3k^2}{2R}+\frac{\mathrm{i}k^3}{2}\right)\left[(\mathbf{n}\cdot\mathbf{l}_m)(\mathbf{n}\cdot\bar{\bar{\mathbf{l}}}_n\cdot\mathbf{n})-(\mathbf{n}\cdot\mathbf{l}_n)(\mathbf{n}\cdot\bar{\bar{\mathbf{l}}}_m\cdot\mathbf{n})\right],\end{aligned} \tag{A.61}$$

$$\begin{aligned}1/C_2^{(3)} =& \left(\frac{2}{R^3}-\frac{k^2}{R}-\frac{\mathrm{i}2k}{R^2}\right)\iint \mathrm{q}_m\mathrm{q}_n\mathbf{n}\cdot(\mathbf{a}_n-\mathbf{a}_m)\left[(\mathbf{n}\cdot\mathbf{a}_m)(\mathbf{n}\cdot\mathbf{a}_n)-\mathbf{a}_m\cdot\mathbf{a}_n\right]\mathrm{d}\mathbf{a}_m^3\,\mathrm{d}\mathbf{a}_n^3\\ =& \left(\frac{2}{R^3}-\frac{k^2}{R}-\frac{\mathrm{i}2k}{R^2}\right)\Big[(\mathbf{n}\cdot\mathbf{l}_m)(\mathbf{n}\cdot\bar{\bar{\mathbf{l}}}_n\cdot\mathbf{n})-(\mathbf{n}\cdot\mathbf{l}_n)(\mathbf{n}\cdot\bar{\bar{\mathbf{l}}}_m\cdot\mathbf{n})\\ &+\mathbf{l}_n\cdot(\bar{\bar{\mathbf{l}}}_m\cdot\mathbf{n})-\mathbf{l}_m\cdot(\bar{\bar{\mathbf{l}}}_n\cdot\mathbf{n})\Big],\end{aligned} \tag{A.62}$$

$$
\begin{aligned}
1/C_3^{(3)} =& \left(\frac{\mathrm{i}k}{2R^2} - \frac{1}{2R^3}\right) \iint \mathrm{q}_m \mathrm{q}_n \left[\mathbf{n}\cdot(\mathbf{a}_n - \mathbf{a}_m)(\mathbf{a}_m\cdot\mathbf{a}_n) - (\mathbf{n}\cdot\mathbf{a}_n)^3 + (\mathbf{n}\cdot\mathbf{a}_m)^3\right] \mathrm{d}\mathbf{a}_m^3\, \mathrm{d}\mathbf{a}_n^3 \\
=& \left(\frac{\mathrm{i}k}{2R^2} - \frac{1}{2R^3}\right) \left[\mathbf{l}_n\cdot(\bar{\bar{\mathbf{l}}}_m\cdot\mathbf{n}) - \mathbf{l}_m\cdot(\bar{\bar{\mathbf{l}}}_n\cdot\mathbf{n})\right]. \qquad \text{(A.63)}
\end{aligned}
$$

Finally, the effective capacitance up to third order terms gives

$$
\begin{aligned}
1/C_{m,n} \approx& \frac{e^{\mathrm{i}k_0 R}}{4\pi\varepsilon_0 R}\left(1/C^{(0)} + 1/C^{(1)} + 1/C^{(2)} + 1/C^{(3)} + \cdots\right) \\
=& \frac{e^{\mathrm{i}k_0 R}}{4\pi\varepsilon_0 R}\left\{\left(-\frac{3}{R^2} + \frac{\mathrm{i}3k}{R} + k^2\right)(\mathbf{n}\cdot\mathbf{l}_m)(\mathbf{n}\cdot\mathbf{l}_n) + \left(-\frac{\mathrm{i}k}{R} + \frac{1}{R^2}\right)\mathbf{l}_m\cdot\mathbf{l}_n\right. \\
&+ \left(\frac{5}{R^3} - \frac{\mathrm{i}5k}{R^2} - \frac{5k^2}{2R} + \frac{\mathrm{i}k^3}{2}\right)\left[(\mathbf{n}\cdot\mathbf{l}_m)(\mathbf{n}\cdot\bar{\bar{\mathbf{l}}}_n\cdot\mathbf{n}) - (\mathbf{n}\cdot\mathbf{l}_n)(\mathbf{n}\cdot\bar{\bar{\mathbf{l}}}_m\cdot\mathbf{n})\right] \\
&\left.+ \left(\frac{3}{2R^3} - \frac{k^2}{R} - \frac{\mathrm{i}3k}{2R^2}\right)\left[\mathbf{l}_n\cdot(\bar{\bar{\mathbf{l}}}_m\cdot\mathbf{n}) - \mathbf{l}_m\cdot(\bar{\bar{\mathbf{l}}}_n\cdot\mathbf{n})\right]\right\}. \qquad \text{(A.64)}
\end{aligned}
$$

By combining the near-field model and multipole approximation for in the effective impedance matrix of the system, we can find the EM response $Q_m(\omega)$ much more efficiently compared to full wave numerical simulation.

A.3.4 Multipole Approximation of the Electromagnetic Force and Torque

The EM force and torque between closely spaced meta-atoms need to be calculated with the full model shown above. For large separation, they can be approximated by considering the effect of multipole moments. Once the mode amplitude of EM resonance Q_m is found, the corresponding multipole moments can be expressed explicitly: $\mathbf{p} = Q_m\mathbf{l}_m$, $\mathbf{m} = -\mathrm{i}\omega Q_m\mathbf{u}_m$, $\bar{\bar{\mathbf{q}}}_m = Q_m\bar{\bar{\mathbf{l}}}_m$.

The vector potential under the multipole approximation is

$$
\mathbf{A}(R) \approx \frac{\mu_0 e^{\mathrm{i}kR}}{4\pi R}\left[\dot{\mathbf{p}} + \left(\frac{1}{R} - \mathrm{i}k\right)\left(\mathbf{n}\times\mathbf{m} + \frac{1}{2}\mathbf{n}\cdot\dot{\bar{\bar{\mathbf{q}}}}\right) + \cdots\right]. \qquad \text{(A.65)}
$$

The corresponding magnetic and electric fields of the electric dipole moment are

$$
\mathbf{B}_\mathbf{p} = \nabla\times\mathbf{A}_\mathbf{p} = \frac{\mu_0}{4\pi}\nabla\times\left(\frac{e^{\mathrm{i}kR}}{R}\dot{\mathbf{p}}\right) = \frac{e^{\mathrm{i}kR}}{4\pi\varepsilon_0 c}k^2\left(\frac{1}{R} - \frac{1}{\mathrm{i}kR^2}\right)\mathbf{n}\times\mathbf{p} \qquad \text{(A.66)}
$$

$$
\begin{aligned}
\mathbf{E}_\mathbf{p} =& \frac{\mathrm{i}c}{k}\nabla\times\mathbf{B}_\mathbf{p} \\
=& \nabla\times\frac{e^{\mathrm{i}kR}}{4\pi R\varepsilon_0}\left[\left(\mathrm{i}k - \frac{1}{R}\right)\mathbf{n}\times\mathbf{p}\right] \\
=& \frac{e^{\mathrm{i}kR}}{4\pi\varepsilon_0 R}\left\{k^2(\mathbf{n}\times\mathbf{p})\times\mathbf{n} + \left(\frac{1}{R^2} - \frac{\mathrm{i}k}{R}\right)\left[3(\mathbf{p}\cdot\mathbf{n})\mathbf{n} - \mathbf{p}\right]\right\}.
\end{aligned} \qquad \text{(A.67)}
$$

For the magnetic dipole

$$\begin{aligned}
\mathbf{B_m} =& \nabla \times \mathbf{A_m} \\
=& \frac{\mu_0}{4\pi} \nabla \times \left[\frac{e^{\mathrm{i}kR}}{R} \left(\frac{1}{R} - \mathrm{i}k \right) \mathbf{n} \times \mathbf{m} \right] \\
=& \frac{\mu_0 e^{\mathrm{i}kR}}{4\pi R} \left\{ k^2 (\mathbf{n} \times \mathbf{m}) \times \mathbf{n} + \left(\frac{1}{R^2} - \frac{\mathrm{i}k}{R} \right) \left[3(\mathbf{m} \cdot \mathbf{n})\mathbf{n} - \mathbf{m} \right] \right\} \\
\mathbf{E_m} =& \frac{\mathrm{i}c}{k} \nabla \times \mathbf{B_m} = \frac{e^{\mathrm{i}kR}}{4\pi\varepsilon_0 c} k^2 \left(\frac{1}{R} - \frac{1}{\mathrm{i}kR^2} \right) \mathbf{m} \times \mathbf{n}.
\end{aligned} \tag{A.68}$$

For the electric quadrupole

$$\begin{aligned}
\mathbf{B}_{\bar{\bar{\mathbf{q}}}} =& \nabla \times \mathbf{A}_{\bar{\bar{\mathbf{q}}}} \\
=& \frac{-\mathrm{i}\omega\mu_0}{8\pi} \nabla \times \left[\frac{e^{\mathrm{i}kR}}{R} \left(\frac{1}{R} - \mathrm{i}k \right) (\mathbf{n} \cdot \dot{\bar{\bar{\mathbf{q}}}}) \right] \\
=& \frac{-\mathrm{i}\omega\mu_0}{8\pi} \frac{e^{\mathrm{i}kR}}{R} \left(k^2 + \frac{\mathrm{i}3k}{R} - \frac{3}{R^2} \right) \mathbf{n} \times (\mathbf{n} \cdot \bar{\bar{\mathbf{q}}})
\end{aligned} \tag{A.69}$$

$$\begin{aligned}
\mathbf{E}_{\bar{\bar{\mathbf{q}}}} =& \frac{\mathrm{i}c}{k} \nabla \times \mathbf{B}_{\bar{\bar{\mathbf{q}}}} \\
=& \frac{1}{8\pi\varepsilon_0} \left\{ \frac{e^{\mathrm{i}kR}}{R} \left(k^2 + \frac{\mathrm{i}3k}{R} - \frac{3}{R^2} \right) \nabla \times \left[\mathbf{n} \times (\mathbf{n} \cdot \bar{\bar{\mathbf{q}}}) \right] \right. \\
& \left. + \nabla \left[\frac{e^{\mathrm{i}kR}}{R} \left(k^2 + \frac{\mathrm{i}3k}{R} - \frac{3}{R^2} \right) \right] \times \left[\mathbf{n} \times (\mathbf{n} \cdot \bar{\bar{\mathbf{q}}}) \right] \right\}.
\end{aligned} \tag{A.70}$$

The term

$$\begin{aligned}
& \nabla \times \left[\mathbf{n} \times (\mathbf{n} \cdot \bar{\bar{\mathbf{q}}}) \right] \\
=& \left[\nabla \cdot (\mathbf{n} \cdot \bar{\bar{\mathbf{q}}}) \right] \mathbf{n} + \left[(\mathbf{n} \cdot \bar{\bar{\mathbf{q}}}) \cdot \nabla \right] \mathbf{n} - (\nabla \cdot \mathbf{n})(\mathbf{n} \cdot \bar{\bar{\mathbf{q}}}) - (\mathbf{n} \cdot \nabla)(\mathbf{n} \cdot \bar{\bar{\mathbf{q}}}) \\
=& \frac{1}{R} \left[\mathrm{tr}(\bar{\bar{\mathbf{q}}}) - 2(\mathbf{n} \cdot \bar{\bar{\mathbf{q}}}) \cdot \mathbf{n} \right] \mathbf{n} - \frac{1}{R} (\mathbf{n} \cdot \bar{\bar{\mathbf{q}}}),
\end{aligned} \tag{A.71}$$

where $\mathrm{tr}(\bar{\bar{\mathbf{q}}})$ is the trace of the quadrupole tensor.

And

$$\begin{aligned}
& \nabla \left[\frac{e^{\mathrm{i}kR}}{R} \left(k^2 + \frac{\mathrm{i}3k}{R} - \frac{3}{R^2} \right) \right] \\
=& \frac{e^{\mathrm{i}kR}}{R} \left[k^2 \left(\mathrm{i}k - \frac{1}{R} \right) + \frac{\mathrm{i}3k}{R} \left(\mathrm{i}k - \frac{2}{R} \right) + \frac{3}{R^2} \left(\mathrm{i}k + \frac{2}{R} \right) \right] \mathbf{n} \\
=& \frac{e^{\mathrm{i}kR}}{R} \left(\mathrm{i}k^3 - \frac{4k^2}{R} - \frac{\mathrm{i}3k}{R^2} + \frac{6}{R^3} \right) \mathbf{n}.
\end{aligned} \tag{A.72}$$

Finally, we have

$$\begin{aligned}\mathbf{E}_{\bar{\bar{\mathbf{q}}}} =& \frac{e^{\mathrm{i}kR}}{8\pi\varepsilon_0 R}\left\{\left(\frac{k^2}{R}+\frac{\mathrm{i}3k}{R^2}-\frac{3}{R^3}\right)\left[\left[\mathrm{tr}(\bar{\bar{\mathbf{q}}})-2(\mathbf{n}\cdot\bar{\bar{\mathbf{q}}})\cdot\mathbf{n}\right]\mathbf{n}-(\mathbf{n}\cdot\bar{\bar{\mathbf{q}}})\right]\right.\\ &\left.+\left(\mathrm{i}k^3-\frac{4k^2}{R}-\frac{\mathrm{i}3k}{R^2}+\frac{6}{R^3}\right)\mathbf{n}\times\left[\mathbf{n}\times(\mathbf{n}\cdot\bar{\bar{\mathbf{q}}})\right]\right\}. \end{aligned} \tag{A.73}$$

The field generated by meta-atom n at meta-atom m is approximated as

$$\mathbf{E}(\mathbf{r}_m) \approx \mathbf{E}_{\mathbf{p}}(\mathbf{p}_n,\mathbf{r}_m)+\mathbf{E}_{\mathbf{m}}(\mathbf{m}_n,\mathbf{r}_m)+\mathbf{E}_{\bar{\bar{\mathbf{q}}}}(\bar{\bar{\mathbf{q}}}_n,\mathbf{r}_m). \tag{A.74}$$

The corresponding EM force and torque acting on meta-atom m by meta-atom n, expanded up to electric quadrupole terms give

$$\begin{aligned}\mathbf{F}_m^{\mathrm{EM}} =& \frac{1}{2}\mathrm{Re}\left\{\int \rho_m^*\mathbf{E}(\mathbf{r}_m)+\mathbf{J}_m^*\times\mathbf{B}(\mathbf{r}_m)\mathrm{d}\mathbf{r}_m^3\right\}\\ \approx& \frac{1}{2}\mathrm{Re}\left\{\int \rho_m^*\left[\mathbf{E}(\mathbf{r}_m^{(\mathrm{c})})+\mathbf{a}_m\cdot\nabla\mathbf{E}(\mathbf{r}_m^{(\mathrm{c})})+\frac{1}{2}\mathbf{a}_m\mathbf{a}_m:\nabla\nabla\mathbf{E}(\mathbf{r}_m^{(\mathrm{c})})\right]\right.\\ &\left.+\mathbf{J}_m^*\times\left[\mathbf{B}(\mathbf{r}_m^{(\mathrm{c})})+\mathbf{a}_m\cdot\nabla\mathbf{B}(\mathbf{r}_m^{(\mathrm{c})})+\frac{1}{2}\mathbf{a}_m\mathbf{a}_m:\nabla\nabla\mathbf{B}(\mathbf{r}_m^{(\mathrm{c})})\right]\mathrm{d}\mathbf{r}_m^3\right\}\\ \approx& \frac{1}{2}\mathrm{Re}\left\{\nabla\mathbf{E}(\mathbf{r}_m^{(\mathrm{c})})\cdot\mathbf{p}_m^*+\frac{1}{2}\nabla\nabla\mathbf{E}(\mathbf{r}_m^{(\mathrm{c})}):\bar{\bar{\mathbf{q}}}_m^*+\nabla\mathbf{B}(\mathbf{r}_m^{(\mathrm{c})})\cdot\mathbf{m}_m^*\right\}, \end{aligned} \tag{A.75}$$

$$\begin{aligned}\mathbf{M}_m^{\mathrm{EM}} =& \frac{1}{2}\mathrm{Re}\left\{\int(\mathbf{r}_m-\mathbf{r}_m^{(\mathrm{c})})\times[\rho_m^*\mathbf{E}(\mathbf{r}_m)+\mathbf{J}_m^*\times\mathbf{B}(\mathbf{r}_m)]\,\mathrm{d}\mathbf{r}_m^3\right\}\\ \approx& \frac{1}{2}\mathrm{Re}\left\{\int\rho_m^*\mathbf{a}_m\times\left[\mathbf{E}(\mathbf{r}_m^{(\mathrm{c})})+\mathbf{a}_m\cdot\nabla\mathbf{E}(\mathbf{r}_m^{(\mathrm{c})})\right]\right.\\ &\left.+\mathbf{a}_m\times\left[\mathbf{J}_m^*\times\left[\mathbf{B}(\mathbf{r}_m^{(\mathrm{c})})+\mathbf{a}_m\cdot\nabla\mathbf{B}(\mathbf{r}_m^{(\mathrm{c})})\right]\right]\mathrm{d}\mathbf{a}_m^3\right\}\\ \approx& \frac{1}{2}\mathrm{Re}\left\{\mathbf{p}_m^*\times\mathbf{E}(\mathbf{r}_m^{(\mathrm{c})})+\bar{\bar{\mathbf{q}}}_m^*\dot{\times}\left[\nabla\mathbf{E}(\mathbf{r}_m^{(\mathrm{c})})\right]\right.\\ &\left.-2\mathbf{B}(\mathbf{r}_m^{(\mathrm{c})})\times\mathbf{m}_m^*-\frac{\mathrm{i}\omega}{2}\mathbf{B}(\mathbf{r}_m^{(\mathrm{c})})\cdot\left[\bar{\bar{\mathbf{q}}}_m^*-2\mathrm{tr}(\bar{\bar{\mathbf{q}}}_m^*)\right]\right\}, \end{aligned} \tag{A.76}$$

where $\nabla\mathbf{E}(\mathbf{r}_m^{(\mathrm{c})})$ is the gradient of electric field around the centre, which is a tensor, and $\dot{\times}$ is the dot-cross product operator [446].

As an example, we compare the EM torques presented in Fig. 6.3 (c), in which intermolecular interaction is calculated based on multipole approximation introduced above, and the ones using complete near-field interaction model presented in Sec. A.2.2, very nice agreement can be found (see Fig. A.3).

A.4 Numerical Simulation

All the full wave simulation in this thesis were performed with the commercial software CST Microwave Studio. Several different types of boundary conditions were utilized in this research.

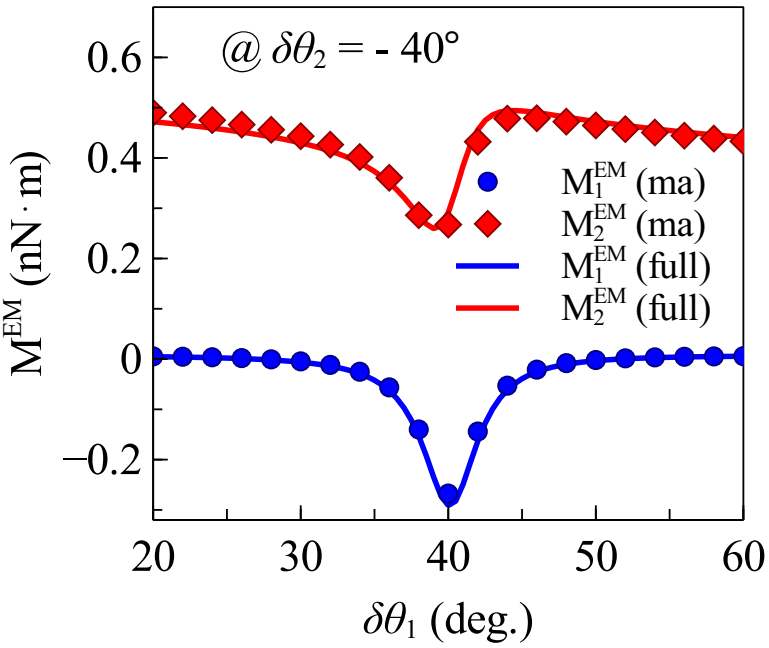

Figure A.3: Comparison of EM torques calculated with complete near-field interaction model (full) and multipole approximation (ma) for intermolecular interaction. The configuration is the same as the one studied in Fig. 6.3 (c) of Chapter. 6.

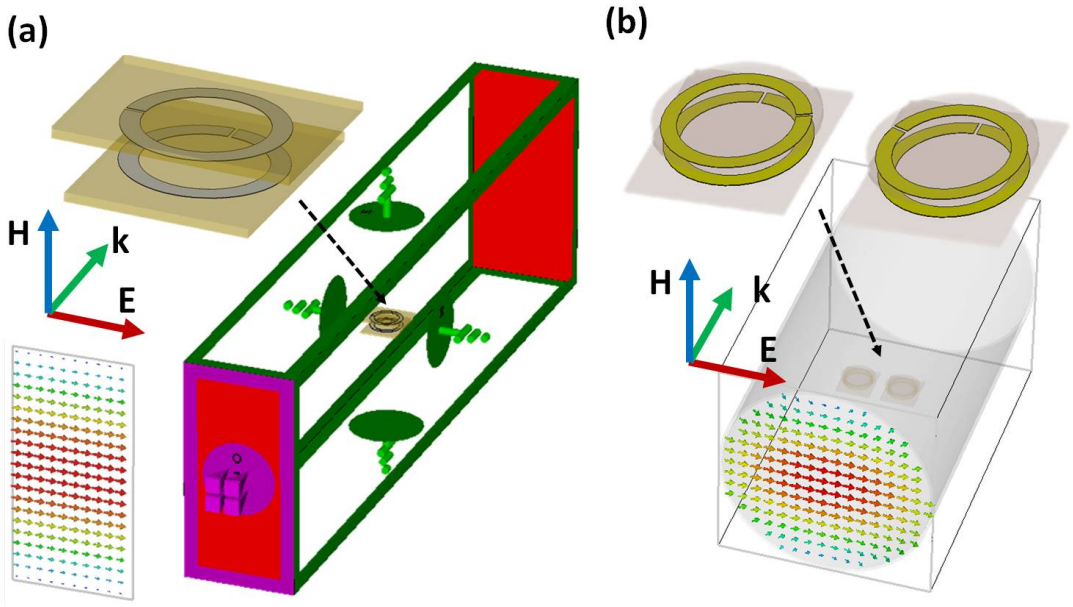

Figure A.4: (a) The model used to calculate the electromagnetic response of a pair of twisted split-ring resonators within a rectangular waveguide [2.29 inches (∼ 58.2 mm) × 1.145 inches (∼ 29.1 mm)]. (b) The model used to calculate the electromagnetic response of two pairs of enantiomeric twisted split-ring resonators within a circular waveguide (diameter ∼58.2 mm). Perfect electric conductor boundary conditions are employed in the transverse directions, and the system is excited with the lowest order waveguide mode.

For the simulation of free space scattering, as in Chapter. 2 and 3, we use a plane wave to excite the structure and open boundaries are employed in all six directions.

For the modeling of experimental systems measured in a waveguide, as in Chapter. 4 and 6, we use perfect electric conductors for the waveguides. The system is excited with the lowest order waveguide mode (as shown in Fig. A.4), and perfect electric conductor boundaries are employed in the transverse directions. For the simulation of periodic arrays, unit-cell boundaries and open boundaries are employed in the transverse and propagating directions, respectively.

The electric and magnetic fields are recorded with field monitors, and the time averaged torque is calculated with the Maxwell stress tensor, as discussed in Sec. A.2.1.

A.5 Summary

This appendix introduced the semi-analytical model and the numerical simulation methods employed in the thesis. The model can be considered as an eigenmode approximation of the full wave approaches such as Methods of Moments. The parameters introduced are physically meaningful, representing the stored electric and magnetic power, as well as power loss due to scattering and ohmic heat. The matrix form of the model allows one to find out the resonant behaviour and electromagnetic force/torque in a complex coupled system very efficiently. The method is quite general and can be applied to different types of meta-atoms.

References

1. G. Eleftheriades and K. Balmain, *Negative-refraction metamaterials: fundamental principles and applications*. Wiley-IEEE Press, 2005. (cited on page 2)

2. N. Engheta and R. W. Ziolkowski, *Metamaterials: Physics and Engineering Explorations*. John Wiley & Sons, 2006. (cited on page 2)

3. D. Smith, W. Padilla, D. Vier, S. Nemat-Nasser, and S. Schultz, "Composite medium with simultaneously negative permeability and permittivity," *Phys. Rev. Lett.*, vol. 84, no. 18, pp. 4184–4187, 2000. (cited on pages 2 and 3)

4. R. Shelby, D. Smith, and S. Schultz, "Experimental verification of a negative index of refraction," *Science*, vol. 292, no. 5514, pp. 77–79, 2001. (cited on page 2)

5. M. Silveirinha and N. Engheta, "Tunneling of electromagnetic energy through subwavelength channels and bends using ε-near-zero materials," *Phys. Rev. Lett.*, vol. 97, no. 15, p. 157403, 2006. (cited on page 2)

6. D. Smith and D. Schurig, "Electromagnetic wave propagation in media with indefinite permittivity and permeability tensors," *Phys. Rev. Lett.*, vol. 90, no. 7, p. 77405, 2003. (cited on page 2)

7. M. Choi, S. Lee, Y. Kim, S. Kang, J. Shin, M. Kwak, K. Kang, Y. Lee, N. Park, and B. Min, "A terahertz metamaterial with unnaturally high refractive index," *Nature*, vol. 470, no. 7334, pp. 369–373, 2011. (cited on page 2)

8. D. Smith, S. Schultz, P. Markoš, and C. Soukoulis, "Determination of effective permittivity and permeability of metamaterials from reflection and transmission coefficients," *Phys. Rev. B*, vol. 65, no. 19, p. 195104, 2002. (cited on page 2)

9. D. R. Smith and J. B. Pendry, "Homogenization of metamaterials by field averaging," *J Opt. Soc. Am. B*, vol. 23, no. 3, pp. 391–403, 2006. (cited on page 2)

10. M. G. Silveirinha, "Metamaterial homogenization approach with application to the characterization of microstructured composites with negative parameters," *Phys. Rev. B*, vol. 75, no. 11, p. 115104, 2007. (cited on pages 2 and 8)

11. A. Alù, "First-principles homogenization theory for periodic metamaterials," *Phys. Rev. B*, vol. 84, no. 7, p. 075153, 2011. (cited on pages 2 and 8)

12. V. M. Shalaev, W. Cai, U. K. Chettiar, H.-K. Yuan, A. K. Sarychev, V. P. Drachev, and A. V. Kildishev, "Negative index of refraction in optical metamaterials," *Opt. Lett.*, vol. 30, no. 24, pp. 3356–3358, 2005. (cited on pages 2, 3, 6, and 31)

13. N. Fang, H. Lee, C. Sun, and X. Zhang, "Sub–diffraction-limited optical imaging with a silver superlens," *Science*, vol. 308, no. 5721, pp. 534–537, 2005. (cited on pages 2 and 3)

14. Z. Liu, H. Lee, Y. Xiong, C. Sun, and X. Zhang, "Far-field optical hyperlens magnifying sub-diffraction-limited objects," *Science*, vol. 315, no. 5819, pp. 1686–1686, 2007. (cited on pages 2 and 3)

15. A. Poddubny, I. Iorsh, P. Belov, and Y. Kivshar, "Hyperbolic metamaterials," *Nature Photon.*, vol. 7, no. 12, pp. 948–957, 2013. (cited on pages 2 and 3)

16. M. Noginov, H. Li, Y. Barnakov, D. Dryden, G. Nataraj, G. Zhu, C. Bonner, M. Mayy, Z. Jacob, and E. Narimanov, "Controlling spontaneous emission with metamaterials," *Opt. Lett.*, vol. 35, no. 11, pp. 1863–1865, 2010. (cited on pages 2 and 3)

17. J. Bose, "On the rotation of plane of polarisation of electric waves by a twisted structure," *Proc. Roy. Soc. Lond.*, vol. 63, no. 389-400, pp. 146–152, 1898. (cited on pages 2 and 11)

18. T. Wu, *Frequency selective surface and grid array*, vol. 40. Wiley-Interscience, 1995. (cited on page 2)

19. B. Munk, *Frequency selective surfaces*. John Wiley & Sons, 2000. (cited on page 2)

20. J. Pendry, A. Holden, W. Stewart, and I. Youngs, "Extremely low frequency plasmons in metallic mesostructures," *Phys. Rev. Lett.*, vol. 76, no. 25, pp. 4773–4776, 1996. (cited on page 2)

21. J. Pendry, A. Holden, D. Robbins, and W. Stewart, "Magnetism from conductors and enhanced nonlinear phenomena," *IEEE Trans. Microw. Theory Tech.*, vol. 47, no. 11, pp. 2075–2084, 1999. (cited on pages 2, 6, and 15)

22. V. Veselago *et al.*, "The electrodynamics of substances with simultaneously negative values of ε and μ," *Physics-Uspekhi*, vol. 10, no. 4, pp. 509–514, 1968. (cited on pages 2 and 21)

23. J. Pendry, D. Schurig, and D. Smith, "Controlling electromagnetic fields," *Science*, vol. 312, no. 5781, pp. 1780–1782, 2006. (cited on pages 3 and 4)

24. D. Schurig, J. Mock, B. Justice, S. Cummer, J. Pendry, A. Starr, and D. Smith, "Metamaterial electromagnetic cloak at microwave frequencies," *Science*, vol. 314, no. 5801, pp. 977–980, 2006. (cited on pages 3 and 4)

25. J. Valentine, J. Li, T. Zentgraf, G. Bartal, and X. Zhang, "An optical cloak made of dielectrics," *Nature Mater.*, vol. 8, no. 7, pp. 568–571, 2009. (cited on pages 3 and 4)

26. Y. Lai, H. Chen, Z.-Q. Zhang, and C. Chan, "Complementary media invisibility cloak that cloaks objects at a distance outside the cloaking shell," *Phys. Rev. Lett.*, vol. 102, no. 9, p. 093901, 2009. (cited on pages 3 and 4)

27. A. Aubry, D. Lei, A. Fernández-Domínguez, Y. Sonnefraud, S. Maier, and J. Pendry, "Plasmonic light-harvesting devices over the whole visible spectrum," *Nano Lett.*, vol. 10, no. 7, pp. 2574–2579, 2010. (cited on pages 3 and 4)

28. S. Zhang, C. Xia, and N. Fang, "Broadband acoustic cloak for ultrasound waves," *Phys. Rev. Lett.*, vol. 106, no. 2, p. 024301, 2011. (cited on pages 3 and 4)

29. S. Narayana and Y. Sato, "Heat flux manipulation with engineered thermal materials," *Phys. Rev. Lett.*, vol. 108, no. 21, p. 214303, 2012. (cited on pages 3 and 4)

30. V. V. Cheianov, V. Fal'ko, and B. Altshuler, "The focusing of electron flow and a veselago lens in graphene pn junctions," *Science*, vol. 315, no. 5816, pp. 1252–1255, 2007. (cited on pages 3 and 4)

31. S. Zhang, W. Fan, N. Panoiu, K. Malloy, R. Osgood, and S. Brueck, "Experimental demonstration of near-infrared negative-index metamaterials," *Phys. Rev. Lett.*, vol. 95, no. 13, p. 137404, 2005. (cited on pages 2 and 7)

32. G. Dolling, C. Enkrich, M. Wegener, C. M. Soukoulis, and S. Linden, "Low-loss negative-index metamaterial at telecommunication wavelengths," *Opt. Lett.*, vol. 31, no. 12, pp. 1800–1802, 2006. (cited on pages 2 and 7)

33. S. Xiao, U. K. Chettiar, A. V. Kildishev, V. P. Drachev, and V. M. Shalaev, "Yellow-light negative-index metamaterials," *Opt. Llett.*, vol. 34, no. 22, pp. 3478–3480, 2009. (cited on pages 2 and 7)

34. S. P. Burgos, R. de Waele, A. Polman, and H. A. Atwater, "A single-layer wide-angle negative-index metamaterial at visible frequencies," *Nature Mater.*, vol. 9, no. 5, pp. 407–412, 2010. (cited on page 2)

35. J. Pendry, "Negative refraction makes a perfect lens," *Phys. Rev. Lett.*, vol. 85, no. 18, pp. 3966–3969, 2000. (cited on page 2)

36. I. I. Smolyaninov, Y.-J. Hung, and C. C. Davis, "Magnifying superlens in the visible frequency range," *Science*, vol. 315, no. 5819, pp. 1699–1701, 2007. (cited on page 2)

37. X. Zhang and Z. Liu, "Superlenses to overcome the diffraction limit," *Nature Mater.*, vol. 7, no. 6, pp. 435–441, 2008. (cited on page 2)

38. Z. Jacob, L. V. Alekseyev, and E. Narimanov, "Optical hyperlens: far-field imaging beyond the diffraction limit," *Opt. Express*, vol. 14, no. 18, pp. 8247–8256, 2006. (cited on page 2)

39. H. N. Krishnamoorthy, Z. Jacob, E. Narimanov, I. Kretzschmar, and V. M. Menon, "Topological transitions in metamaterials," *Science*, vol. 336, no. 6078, pp. 205–209, 2012. (cited on page 2)

40. C. Cortes, W. Newman, S. Molesky, and Z. Jacob, "Quantum nanophotonics using hyperbolic metamaterials," *J. Opt.*, vol. 14, no. 6, p. 063001, 2012. (cited on page 2)

41. G. A. Wurtz, R. Pollard, W. Hendren, G. Wiederrecht, D. Gosztola, V. Podolskiy, and A. V. Zayats, "Designed ultrafast optical nonlinearity in a plasmonic nanorod metamaterial enhanced by nonlocality," *Nature Nanotech.*, vol. 6, no. 2, pp. 107–111, 2011. (cited on pages 2 and 15)

42. A. Kabashin, P. Evans, S. Pastkovsky, W. Hendren, G. Wurtz, R. Atkinson, R. Pollard, V. Podolskiy, and A. Zayats, "Plasmonic nanorod metamaterials for biosensing," *Nature Mater.*, vol. 8, no. 11, pp. 867–871, 2009. (cited on page 2)

43. J. Joannopoulos, S. Johnson, J. Winn, and R. Meade, *Photonic crystals: molding the flow of light*. Princeton university press, 2008. (cited on page 2)

44. U. Leonhardt, "Optical conformal mapping," *Science*, vol. 312, no. 5781, pp. 1777–1780, 2006. (cited on page 3)

45. H. Chen, C. Chan, and P. Sheng, "Transformation optics and metamaterials," *Nature Mater.*, vol. 9, no. 5, pp. 387–396, 2010. (cited on page 3)

46. W. Cai, U. Chettiar, A. Kildishev, and V. Shalaev, "Optical cloaking with metamaterials," *Nature Photon.*, vol. 1, no. 4, pp. 224–227, 2007. (cited on page 3)

47. J. Li and J. Pendry, "Hiding under the carpet: a new strategy for cloaking," *Phy. Rev. Lett.*, vol. 101, no. 20, p. 203901, 2008. (cited on page 3)

48. T. Ergin, N. Stenger, P. Brenner, J. Pendry, and M. Wegener, "Three-dimensional invisibility cloak at optical wavelengths," *Science*, vol. 328, no. 5976, pp. 337–339, 2010. (cited on page 3)

49. D. Kwon and D. Werner, "Transformation optical designs for wave collimators, flat lenses and right-angle bends," *New J. Phys.*, vol. 10, no. 11, p. 115023, 2008. (cited on page 3)

50. N. Kundtz and D. Smith, "Extreme-angle broadband metamaterial lens," *Nature Mater.*, vol. 9, no. 2, pp. 129–132, 2009. (cited on page 3)

51. A. Aubry, D. Lei, S. Maier, and J. Pendry, "Interaction between plasmonic nanoparticles revisited with transformation optics," *Phys. Rev. Lett.*, vol. 105, no. 23, p. 233901, 2010. (cited on page 3)

52. A. Fernández-Domínguez, A. Wiener, F. García-Vidal, S. Maier, and J. Pendry, "Transformation-optics description of nonlocal effects in plasmonic nanostructures," *Phys. Rev. Lett.*, vol. 108, no. 10, p. 106802, 2012. (cited on page 3)

53. J. Li and C. Chan, "Double-negative acoustic metamaterial," *Phys. Rev. E*, vol. 70, no. 5, p. 055602, 2004. (cited on page 3)

54. H. Chen and C. Chan, "Acoustic cloaking in three dimensions using acoustic metamaterials," *Appl. Phys. Lett.*, vol. 91, no. 18, pp. 183518–183518, 2007. (cited on page 3)

55. M. Farhat, S. Enoch, S. Guenneau, and A. Movchan, "Broadband cylindrical acoustic cloak for linear surface waves in a fluid," *Phys. Rev. Lett.*, vol. 101, no. 13, p. 134501, 2008. (cited on page 3)

56. M. Farhat, S. Guenneau, and S. Enoch, "Ultrabroadband elastic cloaking in thin plates," *Phys. Rev. Lett.*, vol. 103, no. 2, p. 24301, 2009. (cited on page 3)

57. C. Fan, Y. Gao, and J. Huang, "Shaped graded materials with an apparent negative thermal conductivity," *Appl. Phys. Lett.*, vol. 92, no. 25, p. 251907, 2008. (cited on page 3)

58. S. Guenneau, C. Amra, and D. Veynante, "Transformation thermodynamics: cloaking and concentrating heat flux," *Opt. Express*, vol. 20, no. 7, pp. 8207–8218, 2012. (cited on page 3)

59. M. Maldovan, "Sound and heat revolutions in phononics," *Nature*, vol. 503, no. 7475, pp. 209–217, 2013. (cited on page 3)

60. S. Zhang, D. Genov, C. Sun, and X. Zhang, "Cloaking of matter waves," *Phys. Rev. Lett.*, vol. 100, no. 12, p. 123002, 2008. (cited on page 3)

61. M. G. Silveirinha and N. Engheta, "Effective medium approach to electron waves: graphene superlattices," *Phys. Rev. B*, vol. 85, no. 19, p. 195413, 2012. (cited on page 3)

62. N. Yu and F. Capasso, "Flat optics with designer metasurfaces," *Nature Mater.*, vol. 13, no. 2, pp. 139–150, 2014. (cited on pages 4 and 5)

63. N. Yu, P. Genevet, M. A. Kats, F. Aieta, J.-P. Tetienne, F. Capasso, and Z. Gaburro, "Light propagation with phase discontinuities: generalized laws of reflection and refraction," *Science*, vol. 334, no. 6054, pp. 333–337, 2011. (cited on pages 4 and 5)

64. S. Sun, Q. He, S. Xiao, Q. Xu, X. Li, and L. Zhou, "Gradient-index meta-surfaces as a bridge linking propagating waves and surface waves," *Nature Mater.*, vol. 11, no. 5, pp. 426–431, 2012. (cited on pages 4 and 5)

65. C. Pfeiffer and A. Grbic, "Metamaterial huygens' surfaces: Tailoring wave fronts with reflectionless sheets," *Phys. Rev. Lett.*, vol. 110, no. 19, p. 197401, 2013. (cited on pages 4 and 5)

66. N. Yu, F. Aieta, P. Genevet, M. A. Kats, Z. Gaburro, and F. Capasso, "A broadband, background-free quarter-wave plate based on plasmonic metasurfaces," *Nano Lett.*, vol. 12, no. 12, pp. 6328–6333, 2012. (cited on pages 4, 5, and 12)

67. B. Walther, C. Helgert, C. Rockstuhl, F. Setzpfandt, F. Eilenberger, E.-B. Kley, F. Lederer, A. Tünnermann, and T. Pertsch, "Spatial and spectral light shaping with metamaterials," *Adv. Mater.*, vol. 24, no. 47, pp. 6300–6304, 2012. (cited on page 5)

68. L. Huang, X. Chen, H. Mühlenbernd, G. Li, B. Bai, Q. Tan, G. Jin, T. Zentgraf, and S. Zhang, "Dispersionless phase discontinuities for controlling light propagation," *Nano Lett.*, vol. 12, no. 11, pp. 5750–5755, 2012. (cited on page 5)

69. C. M. Soukoulis and M. Wegener, "Past achievements and future challenges in the development of three-dimensional photonic metamaterials," *Nature Photon.*, vol. 5, no. 9, pp. 523–530, 2011. (cited on page 3)

70. C. L. Holloway, E. F. Kuester, J. A. Gordon, J. O'Hara, J. Booth, and D. R. Smith, "An overview of the theory and applications of metasurfaces: The two-dimensional equivalents of metamaterials," *IEEE, Antennas Prop. Mag.*, vol. 54, no. 2, pp. 10–35, 2012. (cited on page 4)

71. A. V. Kildishev, A. Boltasseva, and V. M. Shalaev, "Planar photonics with metasurfaces," *Science*, vol. 339, no. 6125, p. 1232009, 2013. (cited on page 4)

72. Y. Zhao and A. Alù, "Manipulating light polarization with ultrathin plasmonic metasurfaces," *Phys. Rev. B*, vol. 84, no. 20, p. 205428, 2011. (cited on page 4)

73. F. Aieta, P. Genevet, M. A. Kats, N. Yu, R. Blanchard, Z. Gaburro, and F. Capasso, "Aberration-free ultrathin flat lenses and axicons at telecom wavelengths based on plasmonic metasurfaces," *Nano Lett.*, vol. 12, no. 9, pp. 4932–4936, 2012. (cited on page 4)

74. X. Yin, Z. Ye, J. Rho, Y. Wang, and X. Zhang, "Photonic spin hall effect at metasurfaces," *Science*, vol. 339, no. 6126, pp. 1405–1407, 2013. (cited on page 4)

75. W. Hardy and L. Whitehead, "Split-ring resonator for use in magnetic resonance from 200–2000 MHz," *Rev. Scient. Instr.*, vol. 52, no. 2, pp. 213–216, 1981. (cited on page 6)

76. T.-J. Yen, W. Padilla, N. Fang, D. Vier, D. Smith, J. Pendry, D. Basov, and X. Zhang, "Terahertz magnetic response from artificial materials," *Science*, vol. 303, no. 5663, pp. 1494–1496, 2004. (cited on page 6)

77. S. Linden, C. Enkrich, M. Wegener, J. Zhou, T. Koschny, and C. M. Soukoulis, "Magnetic response of metamaterials at 100 terahertz," *Science*, vol. 306, no. 5700, pp. 1351–1353, 2004. (cited on page 6)

78. S. Zhang, W. Fan, B. Minhas, A. Frauenglass, K. Malloy, and S. Brueck, "Mid-infrared resonant magnetic nanostructures exhibiting a negative permeability," *Phys. Rev. Lett.*, vol. 94, no. 3, p. 037402, 2005. (cited on page 6)

79. N. Liu, H. Guo, L. Fu, S. Kaiser, H. Schweizer, and H. Giessen, "Three-dimensional photonic metamaterials at optical frequencies," *Nature Mater.*, vol. 7, no. 1, pp. 31–37, 2007. (cited on pages 6 and 11)

80. J. Valentine, S. Zhang, T. Zentgraf, E. Ulin-Avila, D. Genov, G. Bartal, and X. Zhang, "Three-dimensional optical metamaterial with a negative refractive index," *Nature*, vol. 455, no. 7211, pp. 376–379, 2008. (cited on pages 6 and 7)

81. J. C. Ginn, I. Brener, D. W. Peters, J. R. Wendt, J. O. Stevens, P. F. Hines, L. I. Basilio, L. K. Warne, J. F. Ihlefeld, P. G. Clem, and M. B. Sinclair, "Realizing optical magnetism from dielectric metamaterials," *Phys. Rev. Lett.*, vol. 108, p. 097402, Feb 2012. (cited on pages 6 and 7)

82. J. Zhou, T. Koschny, M. Kafesaki, E. Economou, J. Pendry, and C. Soukoulis, "Saturation of the magnetic response of split-ring resonators at optical frequencies," *Phys. Rev. Lett.*, vol. 95, no. 22, p. 223902, 2005. (cited on page 6)

83. V. A. Podolskiy, A. K. Sarychev, and V. M. Shalaev, "Plasmon modes in metal nanowires and left-handed materials," *J. Nonl. Opt. Phys. Mater.*, vol. 11, no. 01, pp. 65–74, 2002. (cited on page 6)

84. L. Panina, A. Grigorenko, and D. Makhnovskiy, "Optomagnetic composite medium with conducting nanoelements," *Phys. Rev. B*, vol. 66, no. 15, p. 155411, 2002. (cited on page 6)

85. S. O'Brien and J. B. Pendry, "Photonic band-gap effects and magnetic activity in dielectric composites," *J Phys.: Cond. Matter.*, vol. 14, no. 15, p. 4035, 2002. (cited on page 7)

86. C. L. Holloway, E. F. Kuester, J. Baker-Jarvis, and P. Kabos, "A double negative (DNG) composite medium composed of magnetodielectric spherical particles embedded in a matrix," *IEEE Trans. Antennas Prop.*, vol. 51, no. 10, pp. 2596–2603, 2003. (cited on page 7)

87. L. Peng, L. Ran, H. Chen, H. Zhang, J. A. Kong, and T. M. Grzegorczyk, "Experimental observation of left-handed behavior in an array of standard dielectric resonators," *Phys. Rev. Lett.*, vol. 98, p. 157403, Apr 2007. (cited on page 7)

88. U. Levy, M. Abashin, K. Ikeda, A. Krishnamoorthy, J. Cunningham, and Y. Fainman, "Inhomogenous dielectric metamaterials with space-variant polarizability," *Phys. Rev. Lett.*, vol. 98, p. 243901, Jun 2007. (cited on page 7)

89. B.-I. Popa and S. A. Cummer, "Compact dielectric particles as a building block for low-loss magnetic metamaterials," *Phys. Rev. Lett.*, vol. 100, p. 207401, May 2008. (cited on page 7)

90. P. Moitra, Y. Yang, Z. Anderson, I. I. Kravchenko, D. P. Briggs, and J. Valentine, "Realization of an all-dielectric zero-index optical metamaterial," *Nature Photon.*, vol. 7, no. 10, pp. 791–795, 2013. (cited on page 7)

91. L. Lewin, "The electrical constants of a material loaded with spherical particles," *J. Instit. Elec. Eng. Part III: Radio Comm. Eng.*, vol. 94, no. 27, pp. 65–68, 1947. (cited on page 7)

92. Q. Zhao, J. Zhou, F. Zhang, and D. Lippens, "Mie resonance-based dielectric metamaterials," *Mater. Today*, vol. 12, no. 12, pp. 60–69, 2009. (cited on page 7)

93. A. I. Kuznetsov, A. E. Miroshnichenko, Y. H. Fu, J. Zhang, and B. Luk'yanchuk, "Magnetic light," *Sci. Rep.*, vol. 2, p. 492, 2012. (cited on page 7)

94. A. E. Krasnok, A. E. Miroshnichenko, P. A. Belov, and Y. S. Kivshar, "All-dielectric optical nanoantennas," *Opt. Express*, vol. 20, no. 18, pp. 20599–20604, 2012. (cited on page 7)

95. A. B. Evlyukhin, S. M. Novikov, U. Zywietz, R. L. Eriksen, C. Reinhardt, S. I. Bozhevolnyi, and B. N. Chichkov, "Demonstration of magnetic dipole resonances of dielectric nanospheres in the visible region," *Nano Lett.*, vol. 12, no. 7, pp. 3749–3755, 2012. (cited on page 7)

96. Y. H. Fu, A. I. Kuznetsov, A. E. Miroshnichenko, Y. F. Yu, and B. Luk'yanchuk, "Directional visible light scattering by silicon nanoparticles," *Nature Comm.*, vol. 4, p. 1527, 2013. (cited on page 7)

97. I. Staude, A. E. Miroshnichenko, M. Decker, N. T. Fofang, S. Liu, E. Gonzales, J. Dominguez, T. S. Luk, D. N. Neshev, I. Brener, *et al.*, "Tailoring directional scattering through magnetic and electric resonances in subwavelength silicon nanodisks," *ACS nano*, vol. 7, no. 9, pp. 7824–7832, 2013. (cited on page 7)

98. Y. Yang, W. Wang, P. Moitra, I. I. Kravchenko, D. P. Briggs, and J. Valentine, "Dielectric meta-reflectarray for broadband linear polarization conversion and optical vortex generation," *Nano Lett.*, vol. 14, no. 3, pp. 1394–1399, 2014. (cited on page 7)

99. C. Wu, N. Arju, G. Kelp, J. A. Fan, J. Dominguez, E. Gonzales, E. Tutuc, I. Brener, and G. Shvets, "Spectrally selective chiral silicon metasurfaces based on infrared fano resonances," *Nature Comm.*, vol. 5, p. 3892, 2014. (cited on page 7)

100. D. Lin, P. Fan, E. Hasman, and M. L. Brongersma, "Dielectric gradient metasurface optical elements," *Science*, vol. 345, no. 6194, pp. 298–302, 2014. (cited on page 7)

101. M. Decker, I. Staude, M. Falkner, J. Dominguez, D. N. Neshev, I. Brener, T. Pertsch, and Y. S. Kivshar, "High-efficiency light-wave control with all-dielectric optical huygens' metasurfaces," *Adv. Opt. Mater. (Accepted), arXiv preprint arXiv:1405.5038*, 2014. (cited on page 7)

102. J. Hopfield and D. Thomas, "Theoretical and experimental effects of spatial dispersion on the optical properties of crystals," *Phys. Rev.*, vol. 132, no. 2, p. 563, 1963. (cited on page 7)

103. V. M. Agranovich, V. L. Ginzburg, and V. L. Ginzburg, *Spatial dispersion in crystal optics and the theory of excitons*, vol. 18. Interscience Publishers New Delhi, 1966. (cited on page 7)

104. A. Serdyukov, I. Semchenko, S. Tretyakov, and A. Sihvola, *Electromagnetics of bi-anisotropic materials: Theory and applications*. Gordon and Breach, 2001. (cited on pages 8 and 9)

105. C. Simovski and S. Tretyakov, "On effective electromagnetic parameters of artificial nanostructured magnetic materials," *Photon. Nanostr. Fundam. Appl.*, vol. 8, no. 4, pp. 254–263, 2010. (cited on pages 8, 35, and 36)

106. I. Sersic, C. Tuambilangana, T. Kampfrath, and A. F. Koenderink, "Magnetoelectric point scattering theory for metamaterial scatterers," *Phys. Rev. B*, vol. 83, no. 24, p. 245102, 2011. (cited on pages 9 and 31)

107. I. Sersic, M. A. van de Haar, F. B. Arango, and A. F. Koenderink, "Ubiquity of optical activity in planar metamaterial scatterers," *Phys. Rev. Lett.*, vol. 108, no. 22, p. 223903, 2012. (cited on pages 9 and 13)

108. P. Lunnemann, I. Sersic, and A. F. Koenderink, "Optical properties of two-dimensional magnetoelectric point scattering lattices," *Phys. Rev. B*, vol. 88, no. 24, p. 245109, 2013. (cited on page 9)

109. W. T. B. Kelvin, *Baltimore lectures on molecular dynamics and the wave theory of light*. CJ Clay and Sons, 1904. (cited on page 9)

110. S. C. Nanita and R. G. Cooks, "Serine octamers: cluster formation, reactions, and implications for biomolecule homochirality," *Angewandte Chemie International Edition*, vol. 45, no. 4, pp. 554–569, 2006. (cited on page 9)

111. M. Mauksch and S. B. Tsogoeva, "Life's single chirality: Origin of symmetry breaking in biomolecules," *Biom. Organ. Synth.*, pp. 823–845, 2011. (cited on page 9)

112. V. Sharma, M. Crne, J. O. Park, and M. Srinivasarao, "Structural origin of circularly polarized iridescence in jeweled beetles," *Science*, vol. 325, no. 5939, pp. 449–451, 2009. (cited on page 10)

113. D. Emerson, "The work of Jagadis Chandra Bose: 100 years of mm-wave research," *IEEE Trans. Microw. Theory Tech.*, vol. 45, no. 12, p. 2267, 1997. (cited on page 10)

114. Wikipedia, "Louis Pasteur — Wikipedia, The Free Encyclopedia," 2014. (cited on page 10)

115. M. Weisberg, P. Needham, and R. Hendry, "Philosophy of chemistry," in *The Stanford Encyclopedia of Philosophy* (E. N. Zalta, ed.), ch. 2.2, winter 2011 ed., 2011. (cited on page 10)

116. I. Barba, A. Cabeceira, A. García-Collado, G. Molina-Cuberos, J. Margineda, and J. Represa, *Quasi-planar Chiral Materials for Microwave Frequencies*. InTech, 2011. (cited on page 10)

117. I. Dierking, *Textures of liquid crystals*. John Wiley & Sons, 2006. (cited on page 10)

118. Wikipedia, "Liquid Crystal — Wikipedia, The Free Encyclopedia," 2014. (cited on page 10)

119. M. Debije, "Solar & alternative energy: Solar power from plastics?," *SPIE Newsroom*, p. DOI: 10.1117/2.1201009.003251, 2010. (cited on page 10)

120. L. D. Barron, *Molecular light scattering and optical activity*, vol. 2. Cambridge University Press Cambridge, 2004. (cited on page 10)

121. L. Pasteur, "On the relations that can exist between crystalline form, chemical composition, and the sense of rotary polarization (original in french)," in *Annales de Chimie Physique*, vol. 24, pp. 442–459, 1848. (cited on page 11)

122. R. M. Walser, "Electromagnetic metamaterials," in *International Symposium on Optical Science and Technology*, pp. 1–15, International Society for Optics and Photonics, 2001. (cited on page 11)

123. K. F. Lindman, "Über eine durch ein isotropes system von spiralförmigen resonatoren erzeugte rotationspolarisation der elektromagnetischen wellen," *Annalen der Physik*, vol. 368, no. 23, pp. 621–644, 1920. (cited on page 11)

124. I. Tinoco Jr and M. P. Freeman, "The optical activity of oriented copper helices. I. Experimental," *J Phys. Chem.*, vol. 61, no. 9, pp. 1196–1200, 1957. (cited on page 11)

125. R. Hollinger, V. Varadan, D. Ghodgaonkar, and V. Varadan, "Experimental characterization of isotropic chiral composites in circular waveguides," *Rad. Sci.*, vol. 27, no. 2, pp. 161–168, 1992. (cited on page 11)

126. D. Jaggard, A. Mickelson, and C. Papas, "On electromagnetic waves in chiral media," *Appl. Phys. A: Mater. Sci. Proc.*, vol. 18, no. 2, pp. 211–216, 1979. (cited on page 11)

127. A. Lakhtakia, V. Varadan, and V. Varadan, "Time-harmonic electromagnetic fields in chiral media," in *Time-Harmonic Electromagnetic Fields in Chiral Media*, vol. 335, 1989. (cited on page 11)

128. C. Eftimiu and L. Pearson, "Guided electromagnetic waves in chiral media," *Radio Sci.*, vol. 24, no. 3, pp. 351–359, 1989. (cited on page 11)

129. P. Pelet and N. Engheta, "The theory of chirowaveguides," *IEEE Trans. Antennas Prop.*, vol. 38, no. 1, pp. 90–98, 1990. (cited on page 11)

130. S. Chandrasekhar, H. Kitzerow, and C. Bahr, *Chirality in liquid crystals*. Springer, 2000. (cited on page 11)

131. J. B. Pendry, "A chiral route to negative refraction," *Science*, vol. 306, no. 5700, p. 1353, 2004. (cited on pages 11 and 12)

132. J. K. Gansel, M. Thiel, M. S. Rill, M. Decker, K. Bade, V. Saile, G. von Freymann, S. Linden, and M. Wegener, "Gold helix photonic metamaterial as broadband circular polarizer," *Science*, vol. 325, no. 5947, pp. 1513–1515, 2009. (cited on pages 12 and 79)

133. S. Zhang, Y. Park, J. Li, X. Lu, W. Zhang, and X. Zhang, "Negative refractive index in chiral metamaterials," *Phys. Rev. Lett.*, vol. 102, no. 2, p. 23901, 2009. (cited on pages 11 and 12)

134. Y. Zhao, M. Belkin, and A. Alù, "Twisted optical metamaterials for planarized ultrathin broadband circular polarizers," *Nature Comm.*, vol. 3, p. 870, 2012. (cited on page 12)

135. C. Wu, H. Li, X. Yu, F. Li, H. Chen, and C. Chan, "Metallic helix array as a broadband wave plate," *Phys. Rev. Lett.*, vol. 107, no. 17, p. 177401, 2011. (cited on page 12)

136. A. Kuzyk, R. Schreiber, Z. Fan, G. Pardatscher, E.-M. Roller, A. Högele, F. C. Simmel, A. O. Govorov, and T. Liedl, "DNA-based self-assembly of chiral plasmonic nanostructures with tailored optical response," *Nature*, vol. 483, no. 7389, pp. 311–314, 2012. (cited on pages 12, 20, 63, and 77)

137. S. Tretyakov, A. Sihvola, and L. Jylhä, "Backward-wave regime and negative refraction in chiral composites," *Photon. Nanostr. Fund. Appl.*, vol. 3, no. 2, pp. 107–115, 2005. (cited on page 11)

138. B. Bokut', V. Gvozdev, and A. Serdyukov, "Peculiar waves in naturally gyrotropic media," *J. Appl. Spec.*, vol. 34, no. 4, pp. 460–465, 1981. (cited on page 11)

139. E. Plum, J. Zhou, J. Dong, V. Fedotov, T. Koschny, C. Soukoulis, and N. Zheludev, "Metamaterial with negative index due to chirality," *Phys. Rev. B*, vol. 79, no. 3, p. 035407, 2009. (cited on page 11)

140. J. Zhou, J. Dong, B. Wang, T. Koschny, M. Kafesaki, and C. M. Soukoulis, "Negative refractive index due to chirality," *Phys. Rev. B*, vol. 79, no. 12, p. 121104, 2009. (cited on pages 11 and 31)

141. B. Wang, J. Zhou, T. Koschny, and C. M. Soukoulis, "Nonplanar chiral metamaterials with negative index," *Appl. Phys. Lett.*, vol. 94, no. 15, p. 151112, 2009. (cited on page 11)

142. C. Wu, H. Li, Z. Wei, X. Yu, and C. Chan, "Theory and experimental realization of negative refraction in a metallic helix array," *Phys. Rev. Lett.*, vol. 105, no. 24, p. 247401, 2010. (cited on page 11)

143. J. Pierce and P. K. Tien, "Coupling of modes in helixes," *Proc. IRE*, vol. 42, no. 9, pp. 1389–1396, 1954. (cited on page 11)

144. S. Sensiper, "Electromagnetic wave propagation on helical structures (a review and survey of recent progress)," *Proc. IRE*, vol. 43, no. 2, pp. 149–161, 1955. (cited on page 11)

145. N. Kalyanasundaram and G. N. Babu, "Dispersion of electromagnetic waves guided by an open tape helix I," *Prog. Electrom. Res. B*, vol. 16, pp. 311–331, 2009. (cited on page 11)

146. N. Kalyanasundaram and G. N. Babu, "Dispersion of electromagnetic waves guided by an open tape helix II," *Prog. Electrom. Res. B*, vol. 19, pp. 133–150, 2010. (cited on page 11)

147. M. Decker, M. Klein, M. Wegener, and S. Linden, "Circular dichroism of planar chiral magnetic metamaterials," *Opt. Lett.*, vol. 32, no. 7, pp. 856–858, 2007. (cited on pages 11 and 79)

148. M. Decker, M. Ruther, C. E. Kriegler, J. Zhou, C. Soukoulis, S. Linden, and M. Wegener, "Strong optical activity from twisted-cross photonic metamaterials," *Opt. Lett.*, vol. 34, no. 16, pp. 2501–2503, 2009. (cited on pages 11, 32, and 79)

149. H. Liu, D. Genov, D. Wu, Y. Liu, Z. Liu, C. Sun, S. Zhu, and X. Zhang, "Magnetic plasmon hybridization and optical activity at optical frequencies in metallic nanostructures," *Phys. Rev. B*, vol. 76, no. 7, p. 073101, 2007. (cited on pages 11, 31, 56, and 79)

150. N. Liu, H. Liu, S. Zhu, and H. Giessen, "Stereometamaterials," *Nature Photon.*, vol. 3, no. 3, pp. 157–162, 2009. (cited on pages 11, 31, 32, 56, and 101)

151. M. Decker, R. Zhao, C. M. Soukoulis, S. Linden, and M. Wegener, "Twisted split-ring-resonator photonic metamaterial with huge optical activity," *Opt. Lett.*, vol. 35, no. 10, pp. 1593–1595, 2010. (cited on pages 11 and 31)

152. D. Powell, K. Hannam, I. Shadrivov, and Y. Kivshar, "Near-field interaction of twisted split-ring resonators," *Phys. Rev. B*, vol. 83, no. 23, p. 235420, 2011. (cited on pages 11, 31, 47, 51, 56, 89, and 103)

153. Z. Wei, Y. Cao, Y. Fan, X. Yu, and H. Li, "Broadband polarization transformation via enhanced asymmetric transmission through arrays of twisted complementary split-ring resonators," *Appl. Phys. Lett.*, vol. 99, no. 22, pp. 221907–221907, 2011. (cited on page 12)

154. K. Hannam, D. A. Powell, I. V. Shadrivov, and Y. S. Kivshar, "Dispersionless optical activity in metamaterials," *Appl. Phys. Lett.*, vol. 102, no. 20, p. 201121, 2013. (cited on page 12)

155. M. Hentschel, M. Schäferling, T. Weiss, N. Liu, and H. Giessen, "Three-dimensional chiral plasmonic oligomers," *Nano Lett.*, vol. 12, no. 5, pp. 2542–2547, 2012. (cited on page 12)

156. G. Shemer, O. Krichevski, G. Markovich, T. Molotsky, I. Lubitz, and A. B. Kotlyar, "Chirality of silver nanoparticles synthesized on DNA," *J. Am. Chem. Soc.*, vol. 128, no. 34, pp. 11006–11007, 2006. (cited on page 12)

157. W. Ma, H. Kuang, L. Wang, L. Xu, W.-S. Chang, H. Zhang, M. Sun, Y. Zhu, Y. Zhao, L. Liu, *et al.*, "Chiral plasmonics of self-assembled nanorod dimers," *Sci. Rep.*, vol. 3, p. 1934, 2013. (cited on pages 12, 20, and 63)

158. A. Kuzyk, R. Schreiber, H. Zhang, A. O. Govorov, T. Liedl, and N. Liu, "Reconfigurable 3d plasmonic metamolecules," *Nature materials*, vol. 13, no. 9, pp. 862–866, 2014. (cited on pages 12, 19, 20, 63, and 99)

159. B. Bai, Y. Svirko, J. Turunen, and T. Vallius, "Optical activity in planar chiral metamaterials: Theoretical study," *Phys. Rev. A*, vol. 76, no. 2, p. 023811, 2007. (cited on page 13)

160. E. Plum, *Chirality and metamaterials*. PhD thesis, University of Southampton, 2010. (cited on page 13)

161. E. Plum, V. Fedotov, and N. Zheludev, "Optical activity in extrinsically chiral metamaterial," *Appl. Phys. Lett.*, vol. 93, no. 19, p. 191911, 2008. (cited on page 13)

162. E. Plum, X.-X. Liu, V. Fedotov, Y. Chen, D. Tsai, and N. Zheludev, "Metamaterials: optical activity without chirality," *Phys. Rev. Lett.*, vol. 102, no. 11, p. 113902, 2009. (cited on page 13)

163. E. Plum, V. Fedotov, and N. Zheludev, "Extrinsic electromagnetic chirality in metamaterials," *J. Opt. A: Pure Appl. Opt.*, vol. 11, no. 7, p. 074009, 2009. (cited on page 13)

164. E. Plum, V. Fedotov, and N. Zheludev, "Asymmetric transmission: a generic property of two-dimensional periodic patterns," *J. Opt.*, vol. 13, no. 2, p. 024006, 2011. (cited on page 13)

165. V. Fedotov, P. Mladyonov, S. Prosvirnin, A. Rogacheva, Y. Chen, and N. Zheludev, "Asymmetric propagation of electromagnetic waves through a planar chiral structure," *Phys. Rev. Lett.*, vol. 97, no. 16, p. 167401, 2006. (cited on pages 13 and 79)

166. V. Fedotov, A. Schwanecke, N. Zheludev, V. Khardikov, and S. Prosvirnin, "Asymmetric transmission of light and enantiomerically sensitive plasmon resonance in planar chiral nanostructures," *Nano Lett.*, vol. 7, no. 7, pp. 1996–1999, 2007. (cited on page 13)

167. S. V. Zhukovsky, A. V. Novitsky, and V. M. Galynsky, "Elliptical dichroism: operating principle of planar chiral metamaterials," *Opt. Lett.*, vol. 34, no. 13, pp. 1988–1990, 2009. (cited on page 14)

168. S. V. Zhukovsky, C. Kremers, and D. N. Chigrin, "Plasmonic rod dimers as elementary planar chiral meta-atoms," *Opt. Lett.*, vol. 36, no. 12, pp. 2278–2280, 2011. (cited on page 14)

169. A. G. Curto, G. Volpe, T. H. Taminiau, M. P. Kreuzer, R. Quidant, and N. F. van Hulst, "Unidirectional emission of a quantum dot coupled to a nanoantenna," *Science*, vol. 329, no. 5994, pp. 930–933, 2010. (cited on pages 14 and 79)

170. T. Kosako, Y. Kadoya, and H. F. Hofmann, "Directional control of light by a nano-optical Yagi–Uda antenna," *Nature Photon.*, vol. 4, no. 5, pp. 312–315, 2010. (cited on pages 14 and 79)

171. V. Fedotov, M. Rose, S. Prosvirnin, N. Papasimakis, and N. Zheludev, "Sharp trapped-mode resonances in planar metamaterials with a broken structural symmetry," *Phys. Rev. Lett.*, vol. 99, no. 14, p. 147401, 2007. (cited on page 14)

172. N. Zheludev, S. Prosvirnin, N. Papasimakis, and V. Fedotov, "Lasing spaser," *Nature Photon.*, vol. 2, no. 6, pp. 351–354, 2008. (cited on page 14)

173. A. E. Nikolaenko, F. De Angelis, S. A. Boden, N. Papasimakis, P. Ashburn, E. Di Fabrizio, and N. I. Zheludev, "Carbon nanotubes in a photonic metamaterial," *Phys. Rev. Lett.*, vol. 104, no. 15, p. 153902, 2010. (cited on pages 14, 15, and 16)

174. N. Papasimakis, Z. Luo, Z. Shen, F. De Angelis, E. Di Fabrizio, A. Nikolaenko, and N. Zheludev, "Graphene in a photonic metamaterial," *Opt. Express*, vol. 18, no. 8, pp. 8353–8359, 2010. (cited on page 14)

175. C. Wu, A. Khanikaev, and G. Shvets, "Broadband slow light metamaterial based on a double-continuum fano resonance," *Phys. Rev. Lett.*, vol. 106, no. 10, p. 107403, 2011. (cited on page 14)

176. C. Wu, A. Khanikaev, R. Adato, N. Arju, A. Yanik, H. Altug, and G. Shvets, "Fano-resonant asymmetric metamaterials for ultrasensitive spectroscopy and identification of molecular monolayers," *Nature Mater.*, vol. 11, no. 1, pp. 69–75, 2012. (cited on page 14)

177. M. C. Rechtsman, J. M. Zeuner, Y. Plotnik, Y. Lumer, D. Podolsky, F. Dreisow, S. Nolte, M. Segev, and A. Szameit, "Photonic Floquet topological insulators," *Nature*, vol. 496, no. 7444, pp. 196–200, 2013. (cited on page 14)

178. A. B. Khanikaev, S. H. Mousavi, W.-K. Tse, M. Kargarian, A. H. MacDonald, and G. Shvets, "Photonic topological insulators," *Nature Mater.*, vol. 12, no. 3, pp. 233–239, 2013. (cited on page 14)

179. N. I. Zheludev and Y. S. Kivshar, "From metamaterials to metadevices," *Nature Mater.*, vol. 11, no. 11, pp. 917–924, 2012. (cited on page 14)

180. C. Denz, S. Flach, and Y. Kivshar, *Nonlinearities in Periodic Structures and Metamaterials*. Springer Series in Optical Sciences, 2009. (cited on page 15)

181. M. Lapine, I. V. Shadrivov, and Y. S. Kivshar, "Colloquium: Nonlinear metamaterials," *Rev. Mod. Phys.*, vol. 86, no. 3, p. 1093, 2014. (cited on page 15)

182. A. Zharov, I. Shadrivov, and Y. Kivshar, "Nonlinear properties of left-handed metamaterials," *Phys. Rev. Lett.*, vol. 91, no. 3, p. 37401, 2003. (cited on pages 15 and 80)

183. M. Lapine, M. Gorkunov, and K. Ringhofer, "Nonlinearity of a metamaterial arising from diode insertions into resonant conductive elements," *Phys. Rev. E*, vol. 67, no. 6, p. 065601, 2003. (cited on pages 15 and 80)

184. I. V. Shadrivov, S. K. Morrison, and Y. S. Kivshar, "Tunable split-ring resonators for nonlinear negative-index metamaterials," *Opt. Express*, vol. 14, no. 20, pp. 9344–9349, 2006. (cited on page 15)

185. I. V. Shadrivov, A. B. Kozyrev, D. W. van der Weide, and Y. S. Kivshar, "Nonlinear magnetic metamaterials," *Opt. Express*, vol. 16, no. 25, pp. 20266–20271, 2008. (cited on pages 15 and 16)

186. D. Powell, I. Shadrivov, Y. Kivshar, and M. Gorkunov, "Self-tuning mechanisms of nonlinear split-ring resonators," *Appl. Phys. Lett.*, vol. 91, no. 14, p. 144107, 2007. (cited on page 15)

187. D. A. Powell, I. V. Shadrivov, and Y. S. Kivshar, "Nonlinear electric metamaterials," *Appl. Phys. Lett.*, vol. 95, no. 8, p. 084102, 2009. (cited on page 15)

188. K. M. Dani, Z. Ku, P. C. Upadhya, R. P. Prasankumar, S. Brueck, and A. J. Taylor, "Subpicosecond optical switching with a negative index metamaterial," *Nano Lett.*, vol. 9, no. 10, pp. 3565–3569, 2009. (cited on pages 15, 16, and 17)

189. I. Shadrivov, V. Fedotov, D. Powell, Y. Kivshar, and N. Zheludev, "Electromagnetic wave analogue of an electronic diode," *New J. Phys.*, vol. 13, no. 3, p. 033025, 2011. (cited on pages 16, 31, 63, and 74)

190. A. Minovich, J. Farnell, D. N. Neshev, I. McKerracher, F. Karouta, J. Tian, D. A. Powell, I. V. Shadrivov, H. H. Tan, C. Jagadish, *et al.*, "Liquid crystal based nonlinear fishnet metamaterials," *Appl. Phys. Lett.*, vol. 100, no. 12, p. 121113, 2012. (cited on pages 16 and 17)

191. T. Driscoll, S. Palit, M. M. Qazilbash, M. Brehm, F. Keilmann, B.-G. Chae, S.-J. Yun, H.-T. Kim, S. Cho, N. M. Jokerst, *et al.*, "Dynamic tuning of an infrared hybrid-metamaterial resonance using vanadium dioxide," *Appl. Phys. Lett.*, vol. 93, no. 2, p. 024101, 2008. (cited on pages 16 and 17)

192. H.-T. Chen, W. J. Padilla, J. M. Zide, A. C. Gossard, A. J. Taylor, and R. D. Averitt, "Active terahertz metamaterial devices," *Nature*, vol. 444, no. 7119, pp. 597–600, 2006. (cited on pages 16 and 17)

193. S. Zhang, J. Zhou, Y.-S. Park, J. Rho, R. Singh, S. Nam, A. K. Azad, H.-T. Chen, X. Yin, A. J. Taylor, *et al.*, "Photoinduced handedness switching in terahertz chiral metamolecules," *Nature Comm.*, vol. 3, p. 942, 2012. (cited on pages 16 and 17)

194. D. Huang, E. Poutrina, and D. R. Smith, "Analysis of the power dependent tuning of a varactor-loaded metamaterial at microwave frequencies," *Appl. Phys. Lett.*, vol. 96, no. 10, p. 104104, 2010. (cited on page 15)

195. B. Wang, J. Zhou, T. Koschny, and C. M. Soukoulis, "Nonlinear properties of split-ring resonators," *Opt. Express*, vol. 16, no. 20, pp. 16058–16063, 2008. (cited on page 15)

196. A. Degiron, J. J. Mock, and D. R. Smith, "Modulating and tuning the response of metamaterials at the unit cell level," *Opt. Express*, vol. 15, no. 3, pp. 1115–1127, 2007. (cited on pages 15 and 17)

197. P. V. Kapitanova, S. I. Maslovski, I. V. Shadrivov, P. M. Voroshilov, D. S. Filonov, P. A. Belov, and Y. S. Kivshar, "Controlling split-ring resonators with light," *Appl. Phys. Lett.*, vol. 99, no. 25, p. 251914, 2011. (cited on page 15)

198. I. V. Shadrivov, P. V. Kapitanova, S. I. Maslovski, and Y. S. Kivshar, "Metamaterials controlled with light," *Phys Rev. Lett.*, vol. 109, no. 8, p. 083902, 2012. (cited on page 15)

199. N. Lazarides and G. Tsironis, "RF superconducting quantum interference device metamaterials," *Appl. Phys. Lett.*, vol. 90, no. 16, p. 163501, 2007. (cited on page 15)

200. C. Kurter, A. Zhuravel, J. Abrahams, C. Bennett, A. Ustinov, and S. M. Anlage, "Superconducting RF metamaterials made with magnetically active planar spirals," *IEEE Trans. Appl. Supercond.*, vol. 21, no. 3, pp. 709–712, 2011. (cited on page 15)

201. M. Trepanier, D. Zhang, O. Mukhanov, and S. M. Anlage, "Realization and modeling of metamaterials made of RF superconducting quantum-interference devices," *Phys. Rev. X*, vol. 3, p. 041029, Dec 2013. (cited on page 15)

202. K. Fan, H. Y. Hwang, M. Liu, A. C. Strikwerda, A. Sternbach, J. Zhang, X. Zhao, X. Zhang, K. A. Nelson, and R. D. Averitt, "Nonlinear terahertz metamaterials via field-enhanced carrier dynamics in GaAs," *Phys. Rev. Lett.*, vol. 110, no. 21, p. 217404, 2013. (cited on page 15)

203. D. J. Cho, W. Wu, E. Ponizovskaya, P. Chaturvedi, A. M. Bratkovsky, S.-Y. Wang, X. Zhang, F. Wang, and Y. R. Shen, "Ultrafast modulation of optical metamaterials," *Opt. Express*, vol. 17, no. 20, pp. 17652–17657, 2009. (cited on pages 15 and 17)

204. A. E. Nikolaenko, N. Papasimakis, E. Atmatzakis, Z. Luo, Z. X. Shen, F. De Angelis, S. A. Boden, E. Di Fabrizio, and N. I. Zheludev, "Nonlinear graphene metamaterial," *Appl. Phys. Lett.*, vol. 100, no. 18, p. 181109, 2012. (cited on page 15)

205. M. Ren, B. Jia, J.-Y. Ou, E. Plum, J. Zhang, K. F. MacDonald, A. E. Nikolaenko, J. Xu, M. Gu, and N. I. Zheludev, "Nanostructured plasmonic medium for terahertz bandwidth all-optical switching," *Adv. Mater.*, vol. 23, no. 46, pp. 5540–5544, 2011. (cited on page 15)

206. I. V. Shadrivov, "Pure nonlinear optical activity in metamaterials," *Appl. Phys. Lett.*, vol. 101, no. 4, p. 041911, 2012. (cited on page 16)

207. M. Ren, E. Plum, J. Xu, and N. I. Zheludev, "Giant nonlinear optical activity in a plasmonic metamaterial," *Nature Comm.*, vol. 3, p. 833, 2012. (cited on pages 16 and 74)

208. Q. Zhao, L. Kang, B. Du, B. Li, J. Zhou, H. Tang, X. Liang, and B. Zhang, "Electrically tunable negative permeability metamaterials based on nematic liquid crystals," *Appl. Phys. Lett.*, vol. 90, no. 1, p. 011112, 2007. (cited on page 17)

209. F. Zhang, Q. Zhao, L. Kang, D. P. Gaillot, X. Zhao, J. Zhou, and D. Lippens, "Magnetic control of negative permeability metamaterials based on liquid crystals," *Appl. Phys. Lett.*, vol. 92, no. 19, p. 193104, 2008. (cited on page 17)

210. F. Zhang, Q. Zhao, W. Zhang, J. Sun, J. Zhou, and D. Lippens, "Voltage tunable short wire-pair type of metamaterial infiltrated by nematic liquid crystal," *Appl. Phys. Lett.*, vol. 97, no. 13, p. 134103, 2010. (cited on page 17)

211. F. Zhang, W. Zhang, Q. Zhao, J. Sun, K. Qiu, J. Zhou, and D. Lippens, "Electrically controllable fishnet metamaterial based on nematic liquid crystal," *Opt. Express*, vol. 19, no. 2, pp. 1563–1568, 2011. (cited on page 17)

212. Z. Liu, C.-Y. Huang, H. Liu, X. Zhang, and C. Lee, "Resonance enhancement of terahertz metamaterials by liquid crystals/indium tin oxide interfaces," *Opt. Express*, vol. 21, no. 5, pp. 6519–6525, 2013. (cited on page 17)

213. D. Shrekenhamer, W.-C. Chen, and W. J. Padilla, "Liquid crystal tunable metamaterial absorber," *Phys. Rev. Lett.*, vol. 110, no. 17, p. 177403, 2013. (cited on page 17)

214. S. Savo, D. Shrekenhamer, and W. J. Padilla, "Liquid crystal metamaterial absorber spatial light modulator for thz applications," *Adv. Opt. Mater.*, vol. 2, no. 3, pp. 275–279, 2014. (cited on page 17)

215. L. Liu, I. V. Shadrivov, D. A. Powell, M. R. Raihan, H. T. Hattori, M. Decker, E. Mironov, and D. N. Neshev, "Temperature control of terahertz metamaterials with liquid crystals," *IEEE Trans. THz Sci. Tech.*, vol. 3, pp. 827 – 831, 2013. (cited on page 17)

216. X. Wang, D.-H. Kwon, D. H. Werner, I.-C. Khoo, A. V. Kildishev, and V. M. Shalaev, "Tunable optical negative-index metamaterials employing anisotropic liquid crystals," *Appl. Phys. Lett.*, vol. 91, no. 14, p. 143122, 2007. (cited on page 17)

217. S. Xiao, U. K. Chettiar, A. V. Kildishev, V. Drachev, I. Khoo, and V. M. Shalaev, "Tunable magnetic response of metamaterials," *Appl. Phys. Lett.*, vol. 95, no. 3, p. 033115, 2009. (cited on page 17)

218. B. Kang, J. Woo, E. Choi, H.-H. Lee, E. Kim, J. Kim, T.-J. Hwang, Y.-S. Park, D. Kim, and J. Wu, "Optical switching of near infrared light transmission in metamaterial-liquid crystal cell structure," *Opt. Express*, vol. 18, no. 16, pp. 16492–16498, 2010. (cited on page 17)

219. O. Buchnev, J. Ou, M. Kaczmarek, N. Zheludev, and V. Fedotov, "Electro-optical control in a plasmonic metamaterial hybridised with a liquid-crystal cell," *Opt. Express*, vol. 21, no. 2, pp. 1633–1638, 2013. (cited on page 17)

220. M. Decker, C. Kremers, A. Minovich, I. Staude, A. E. Miroshnichenko, D. Chigrin, D. N. Neshev, C. Jagadish, and Y. S. Kivshar, "Electro-optical switching by liquid-crystal controlled metasurfaces," *Opt. Express*, vol. 21, no. 7, pp. 8879–8885, 2013. (cited on page 17)

221. H.-T. Kim, Y. W. Lee, B.-J. Kim, B.-G. Chae, S. J. Yun, K.-Y. Kang, K.-J. Han, K.-J. Yee, and Y.-S. Lim, "Monoclinic and correlated metal phase in VO_2 as evidence of the mott transition: coherent phonon analysis," *Phys. Rev. Lett.*, vol. 97, no. 26, p. 266401, 2006. (cited on page 17)

222. T. Driscoll, H.-T. Kim, B.-G. Chae, B.-J. Kim, Y.-W. Lee, N. M. Jokerst, S. Palit, D. R. Smith, M. Di Ventra, and D. N. Basov, "Memory metamaterials," *Science*, vol. 325, no. 5947, pp. 1518–1521, 2009. (cited on pages 17 and 86)

223. Q.-Y. Wen, H.-W. Zhang, Q.-H. Yang, Y.-S. Xie, K. Chen, and Y.-L. Liu, "Terahertz metamaterials with VO_2 cut-wires for thermal tunability," *Appl. Phys. Lett.*, vol. 97, no. 2, pp. 021111–021111, 2010. (cited on page 17)

224. M. Seo, J. Kyoung, H. Park, S. Koo, H.-s. Kim, H. Bernien, B. J. Kim, J. H. Choe, Y. H. Ahn, H.-T. Kim, *et al.*, "Active terahertz nanoantennas based on VO_2 phase transition," *Nano Lett.*, vol. 10, no. 6, pp. 2064–2068, 2010. (cited on page 17)

225. M. Goldflam, T. Driscoll, B. Chapler, O. Khatib, N. M. Jokerst, S. Palit, D. Smith, B.-J. Kim, G. Seo, H.-T. Kim, *et al.*, "Reconfigurable gradient index using VO_2 memory metamaterials," *Appl. Phys. Lett.*, vol. 99, no. 4, p. 044103, 2011. (cited on page 17)

226. Z. Samson, K. MacDonald, F. De Angelis, B. Gholipour, K. Knight, C. Huang, E. Di Fabrizio, D. Hewak, and N. Zheludev, "Metamaterial electro-optic switch of nanoscale thickness," *Appl. Phys. Lett.*, vol. 96, no. 14, p. 143105, 2010. (cited on page 17)

227. A.-K. U. Michel, D. N. Chigrin, T. W. Maß, K. Schönauer, M. Salinga, M. Wuttig, and T. Taubner, "Using low-loss phase-change materials for mid-infrared antenna resonance tuning," *Nano Lett.*, vol. 13, no. 8, pp. 3470–3475, 2013. (cited on page 17)

228. B. Gholipour, J. Zhang, K. F. MacDonald, D. W. Hewak, and N. I. Zheludev, "An all-optical, non-volatile, bidirectional, phase-change meta-switch," *Adv. Mater.*, vol. 25, no. 22, pp. 3050–3054, 2013. (cited on page 17)

229. O. Reynet and O. Acher, "Voltage controlled metamaterial," *Appl. Phys. Lett.*, vol. 84, no. 7, pp. 1198–1200, 2004. (cited on page 17)

230. S. Lim, C. Caloz, and T. Itoh, "Metamaterial-based electronically controlled transmission-line structure as a novel leaky-wave antenna with tunable radiation angle and beamwidth," *IEEE Trans. Microw. Theory Tech.*, vol. 52, no. 12, pp. 2678–2690, 2004. (cited on page 17)

231. W. J. Padilla, A. J. Taylor, C. Highstrete, M. Lee, and R. D. Averitt, "Dynamical electric and magnetic metamaterial response at terahertz frequencies," *Phys. Rev. Lett.*, vol. 96, no. 10, p. 107401, 2006. (cited on page 17)

232. H.-T. Chen, J. F. O'Hara, A. K. Azad, A. J. Taylor, R. D. Averitt, D. B. Shrekenhamer, and W. J. Padilla, "Experimental demonstration of frequency-agile terahertz metamaterials," *Nature Photon.*, vol. 2, no. 5, pp. 295–298, 2008. (cited on page 17)

233. H.-T. Chen, W. J. Padilla, M. J. Cich, A. K. Azad, R. D. Averitt, and A. J. Taylor, "A metamaterial solid-state terahertz phase modulator," *Nature Photon.*, vol. 3, no. 3, pp. 148–151, 2009. (cited on page 17)

234. D. Shrekenhamer, S. Rout, A. C. Strikwerda, C. Bingham, R. D. Averitt, S. Sonkusale, and W. J. Padilla, "High speed terahertz modulation from metamaterials with embedded high electron mobility transistors," *Opt. Express*, vol. 19, no. 10, pp. 9968–9975, 2011. (cited on page 17)

235. H.-T. Chen, W. J. Padilla, J. M. Zide, S. R. Bank, A. C. Gossard, A. J. Taylor, and R. D. Averitt, "Ultrafast optical switching of terahertz metamaterials fabricated on ErAs/GaAs nanoisland superlattices," *Opt. Lett.*, vol. 32, no. 12, pp. 1620–1622, 2007. (cited on page 17)

236. J. Zhou, D. R. Chowdhury, R. Zhao, A. K. Azad, H.-T. Chen, C. M. Soukoulis, A. J. Taylor, and J. F. O'Hara, "Terahertz chiral metamaterials with giant and dynamically tunable optical activity," *Phys. Rev. B*, vol. 86, no. 3, p. 035448, 2012. (cited on page 17)

237. N. Kanda, K. Konishi, and M. Kuwata-Gonokami, "Dynamics of photo-induced terahertz optical activity in metal chiral gratings," *Opt. Lett.*, vol. 37, no. 17, pp. 3510–3512, 2012. (cited on page 17)

238. N. Kanda, K. Konishi, and M. Kuwata-Gonokami, "All-photoinduced terahertz optical activity," *Opt. Lett.*, vol. 39, no. 11, pp. 3274–3277, 2014. (cited on page 17)

239. L. Ju, B. Geng, J. Horng, C. Girit, M. Martin, Z. Hao, H. A. Bechtel, X. Liang, A. Zettl, Y. R. Shen, *et al.*, "Graphene plasmonics for tunable terahertz metamaterials," *Nature Nanotech.*, vol. 6, no. 10, pp. 630–634, 2011. (cited on page 17)

240. S. H. Lee, M. Choi, T.-T. Kim, S. Lee, M. Liu, X. Yin, H. K. Choi, S. S. Lee, C.-G. Choi, S.-Y. Choi, *et al.*, "Switching terahertz waves with gate-controlled active graphene metamaterials," *Nature Mater.*, vol. 11, no. 11, pp. 936–941, 2012. (cited on page 17)

241. H. Yan, X. Li, B. Chandra, G. Tulevski, Y. Wu, M. Freitag, W. Zhu, P. Avouris, and F. Xia, "Tunable infrared plasmonic devices using graphene/insulator stacks," *Nature Nanotech.*, vol. 7, no. 5, pp. 330–334, 2012. (cited on page 17)

242. M. Tamagnone, A. Fallahi, J. R. Mosig, and J. Perruisseau-Carrier, "Fundamental limits and near-optimal design of graphene modulators and non-reciprocal devices," *Nature Photon.*, vol. 8, pp. 556–563, 2014. (cited on page 18)

243. M. Lapine, D. Powell, M. Gorkunov, I. Shadrivov, R. Marqués, and Y. Kivshar, "Structural tunability in metamaterials," *Appl. Phys. Lett.*, vol. 95, no. 8, p. 084105, 2009. (cited on pages 18 and 51)

244. D. A. Powell, M. Lapine, M. V. Gorkunov, I. V. Shadrivov, and Y. S. Kivshar, "Metamaterial tuning by manipulation of near-field interaction," *Phys. Rev. B*, vol. 82, no. 15, p. 155128, 2010. (cited on pages 18, 31, 51, and 103)

245. H. Tao, A. Strikwerda, K. Fan, W. Padilla, X. Zhang, and R. Averitt, "Reconfigurable terahertz metamaterials," *Phys. Rev. Lett.*, vol. 103, no. 14, p. 147401, 2009. (cited on pages 18 and 19)

246. Y. H. Fu, A. Q. Liu, W. M. Zhu, X. M. Zhang, D. P. Tsai, J. B. Zhang, T. Mei, J. F. Tao, H. C. Guo, X. H. Zhang, *et al.*, "A micromachined reconfigurable metamaterial via reconfiguration of asymmetric split-ring resonators," *Adv. Func. Mater.*, vol. 21, no. 18, pp. 3589–3594, 2011. (cited on pages 18 and 19)

247. T. Kan, A. Isozaki, N. Kanda, N. Nemoto, K. Konishi, M. Kuwata-Gonokami, K. Matsumoto, and I. Shimoyama, "Spiral metamaterial for active tuning of optical activity," *Appl. Phys. Lett.*, vol. 102, no. 22, p. 221906, 2013. (cited on pages 18 and 19)

248. X. Liu and W. J. Padilla, "Dynamic manipulation of infrared radiation with mems metamaterials," *Adv. Opt. Mater.*, vol. 1, no. 8, pp. 559–562, 2013. (cited on pages 18 and 19)

249. T. S. Kasirga, Y. N. Ertas, and M. Bayindir, "Microfluidics for reconfigurable electromagnetic metamaterials," *Appl. Phys. Lett.*, vol. 95, no. 21, p. 214102, 2009. (cited on pages 19 and 20)

250. W. Zhu, Q. Song, A. Liu, D. Tsai, H. Cai, Z. Shen, R. Huang, S. Ting, Q. Liang, H. Liu, *et al.*, "A random access reconfigurable metamaterial and a tunable flat lens," *arXiv preprint arXiv:1406.2757*, 2014. (cited on pages 19 and 20)

251. J.-Y. Ou, E. Plum, J. Zhang, and N. I. Zheludev, "An electromechanically reconfigurable plasmonic metamaterial operating in the near-infrared," *Nature Nanotech.*, vol. 8, no. 4, pp. 252–255, 2013. (cited on pages 18 and 19)

252. T. Hand and S. Cummer, "Characterization of tunable metamaterial elements using mems switches," *IEEE, Antennas Wireless Prop. Lett.*, vol. 6, pp. 401–404, 2007. (cited on page 18)

253. W. M. Zhu, A. Q. Liu, X. M. Zhang, D. P. Tsai, T. Bourouina, J. H. Teng, X. H. Zhang, H. C. Guo, H. Tanoto, T. Mei, *et al.*, "Switchable magnetic metamaterials using micromachining processes," *Adv. Mater.*, vol. 23, no. 15, pp. 1792–1796, 2011. (cited on page 18)

254. W. Zhu, A. Liu, T. Bourouina, D. Tsai, J. Teng, X. Zhang, G. Lo, D. Kwong, and N. Zheludev, "Microelectromechanical maltese-cross metamaterial with tunable terahertz anisotropy," *Nature Comm.*, vol. 3, p. 1274, 2012. (cited on page 18)

255. J.-Y. Ou, E. Plum, L. Jiang, and N. I. Zheludev, "Reconfigurable photonic metamaterials," *Nano Lett.*, vol. 11, no. 5, pp. 2142–2144, 2011. (cited on page 18)

256. D. Shin, Y. Urzhumov, Y. Jung, G. Kang, S. Baek, M. Choi, H. Park, K. Kim, and D. R. Smith, "Broadband electromagnetic cloaking with smart metamaterials," *Nature Comm.*, vol. 3, p. 1213, 2012. (cited on page 19)

257. D. Shin, Y. Urzhumov, D. Lim, K. Kim, and D. R. Smith, "A versatile smart transformation optics device with auxetic elasto-electromagnetic metamaterials," *Sci. Rep.*, vol. 4, p. 4084, 2014. (cited on page 19)

258. J. Wang, S. Liu, Z. V. Vardeny, and A. Nahata, "Liquid metal-based plasmonics," *Opt. Express*, vol. 20, no. 3, pp. 2346–2353, 2012. (cited on page 20)

259. J. Wang, S. Liu, S. Guruswamy, and A. Nahata, "Reconfigurable liquid metal based terahertz metamaterials via selective erasure and refilling to the unit cell level," *Appl. Phys. Lett.*, vol. 103, no. 22, p. 221116, 2013. (cited on page 20)

260. F. Casadei and K. Bertoldi, "Harnessing fluid-structure interactions to design self-regulating acoustic metamaterials," *J. Appl. Phys.*, vol. 115, no. 3, p. 034907, 2014. (cited on page 20)

261. G. Bahl, K. H. Kim, W. Lee, J. Liu, X. Fan, and T. Carmon, "Brillouin cavity optomechanics with microfluidic devices," *Nature Comm.*, vol. 4, p. 1994, 2013. (cited on page 20)

262. B. Yurke, A. J. Turberfield, A. P. Mills, F. C. Simmel, and J. L. Neumann, "A DNA-fuelled molecular machine made of DNA," *Nature*, vol. 406, no. 6796, pp. 605–608, 2000. (cited on page 20)

263. N. C. Seeman, "DNA in a material world," *Nature*, vol. 421, no. 6921, pp. 427–431, 2003. (cited on page 20)

264. P. W. Rothemund, "Folding DNA to create nanoscale shapes and patterns," *Nature*, vol. 440, no. 7082, pp. 297–302, 2006. (cited on page 20)

265. J. Zhang, Y. Liu, Y. Ke, and H. Yan, "Periodic square-like gold nanoparticle arrays templated by self-assembled 2D DNA nanogrids on a surface," *Nano Lett.*, vol. 6, no. 2, pp. 248–251, 2006. (cited on page 20)

266. J. Sharma, R. Chhabra, A. Cheng, J. Brownell, Y. Liu, and H. Yan, "Control of self-assembly of DNA tubules through integration of gold nanoparticles," *Science*, vol. 323, no. 5910, pp. 112–116, 2009. (cited on page 20)

267. B. Ding, Z. Deng, H. Yan, S. Cabrini, R. N. Zuckermann, and J. Bokor, "Gold nanoparticle self-similar chain structure organized by DNA origami," *J. Am. Chem. Soc.*, vol. 132, no. 10, pp. 3248–3249, 2010. (cited on page 20)

268. S. J. Tan, M. J. Campolongo, D. Luo, and W. Cheng, "Building plasmonic nanostructures with DNA," *Nature Nanotech.*, vol. 6, no. 5, pp. 268–276, 2011. (cited on pages 20 and 77)

269. X. Shen, A. Asenjo-Garcia, Q. Liu, Q. Jiang, F. J. García de Abajo, N. Liu, and B. Ding, "Three-dimensional plasmonic chiral tetramers assembled by DNA origami," *Nano Lett.*, vol. 13, no. 5, pp. 2128–2133, 2013. (cited on pages 20 and 63)

270. X. Lan, Z. Chen, G. Dai, X. Lu, W. Ni, and Q. Wang, "Bifacial DNA origami-directed discrete, three-dimensional, anisotropic plasmonic nanoarchitectures with tailored optical chirality," *J. Am. Chem. Soc.*, vol. 135, no. 31, pp. 11441–11444, 2013. (cited on pages 20 and 63)

271. R. Schreiber, N. Luong, Z. Fan, A. Kuzyk, P. C. Nickels, T. Zhang, D. M. Smith, B. Yurke, W. Kuang, A. O. Govorov, *et al.*, "Chiral plasmonic DNA nanostructures with switchable circular dichroism," *Nature Comm.*, vol. 4, p. 2948, 2013. (cited on page 20)

272. D. G. Grier, "A revolution in optical manipulation," *Nature*, vol. 424, no. 6950, pp. 810–816, 2003. (cited on pages 21, 23, and 41)

273. J. R. Moffitt, Y. R. Chemla, S. B. Smith, and C. Bustamante, "Recent advances in optical tweezers," *Annu. Rev. Biochem.*, vol. 77, pp. 205–228, 2008. (cited on pages 21 and 41)

274. A. La Porta and M. D. Wang, "Optical torque wrench: angular trapping, rotation, and torque detection of quartz microparticles," *Phys. Rev. Lett.*, vol. 92, no. 19, p. 190801, 2004. (cited on pages 21, 41, and 42)

275. F. Pedaci, Z. Huang, M. van Oene, S. Barland, and N. Dekker, "Excitable particles in an optical torque wrench," *Nature Phys.*, vol. 7, no. 3, pp. 259–264, 2010. (cited on pages 21 and 41)

276. P. Galajda and P. Ormos, "Complex micromachines produced and driven by light," *Appl. Phys. Lett.*, vol. 78, p. 249, 2001. (cited on pages 21, 41, and 42)

277. L. Kelemen, S. Valkai, and P. Ormos, "Integrated optical motor," *Appl. Opt.*, vol. 45, no. 12, pp. 2777–2780, 2006. (cited on pages 21 and 41)

278. P. Lebedew, "Untersuchungen über die druckkräfte des lichtes," *Annalen der Physik*, vol. 311, no. 11, pp. 433–458, 1901. (cited on pages 21 and 52)

279. B. A. Kemp, J. A. Kong, and T. M. Grzegorczyk, "Reversal of wave momentum in isotropic left-handed media," *Phys. Rev. A*, vol. 75, no. 5, p. 053810, 2007. (cited on page 21)

280. V. Yannopapas and P. G. Galiatsatos, "Electromagnetic forces in negative-refractive-index metamaterials: a first-principles study," *Phys. Rev. A*, vol. 77, no. 4, p. 043819, 2008. (cited on pages 21 and 23)

281. V. G. Veselago, "Energy, linear momentum and mass transfer by an electromagnetic wave in a negative-refraction medium," *Physics-Uspekhi*, vol. 52, no. 6, p. 649, 2009. (cited on page 21)

282. M. Gorkunov and A. Kondratov, "Macroscopic view of light pressure on a continuous medium," *Phys. Rev. A*, vol. 88, no. 1, p. 011804, 2013. (cited on page 21)

283. K. J. Webb *et al.*, "Negative electromagnetic plane-wave force in gain media," *Phys. Rev. E*, vol. 84, no. 5, p. 057602, 2011. (cited on page 21)

284. M. Mansuripur and A. R. Zakharian, "Radiation pressure and photon momentum in negative-index media," in *SPIE NanoScience+ Engineering*, pp. 845511–845511, International Society for Optics and Photonics, 2012. (cited on page 21)

285. A. Dogariu, S. Sukhov, and J. Sáenz, "Optically induced 'negative forces'," *Nature Photon.*, vol. 7, no. 1, pp. 24–27, 2013. (cited on page 21)

286. J. Chen, J. Ng, Z. Lin, and C. Chan, "Optical pulling force," *Nature Photon.*, vol. 5, no. 9, pp. 531–534, 2011. (cited on page 21)

287. H. Chen, B. Zhang, Y. Luo, B. A. Kemp, J. Zhang, L. Ran, and B.-I. Wu, "Lorentz force and radiation pressure on a spherical cloak," *Phys. Rev. A*, vol. 80, p. 011808, Jul 2009. (cited on page 21)

288. P. C. Chaumet, A. Rahmani, F. Zolla, and A. Nicolet, "Electromagnetic forces on a discrete spherical invisibility cloak under time-harmonic illumination," *Phys. Rev. E*, vol. 85, no. 5, p. 056602, 2012. (cited on page 21)

289. K. Ding, J. Ng, L. Zhou, and C. Chan, "Realization of optical pulling forces using chirality," *Phys. Rev. A*, vol. 89, no. 6, p. 063825, 2014. (cited on page 22)

290. S. Wang and C. Chan, "Lateral optical force on chiral particles near a surface," *Nature Comm.*, vol. 5, p. 3307, 2014. (cited on page 22)

291. M. Liu, T. Zentgraf, Y. Liu, G. Bartal, and X. Zhang, "Light-driven nanoscale plasmonic motors," *Nature Nanotech.*, vol. 5, no. 8, pp. 570–573, 2010. (cited on pages 22, 41, 42, and 43)

292. Y. Urzhumov, W. Chen, C. Bingham, W. Padilla, and D. R. Smith, "Magnetic levitation of metamaterial bodies enhanced with magnetostatic surface resonances," *Phys. Rev. B*, vol. 85, no. 5, p. 054430, 2012. (cited on page 22)

293. F. J. Rodríguez-Fortuño, A. Vakil, and N. Engheta, "Electric levitation using ϵ-near-zero metamaterials," *Phys. Rev. Lett.*, vol. 112, no. 3, p. 033902, 2014. (cited on pages 22 and 23)

294. U. Leonhardt and T. G. Philbin, "Quantum levitation by left-handed metamaterials," *New J. Phys.*, vol. 9, no. 8, p. 254, 2007. (cited on page 22)

295. F. Rosa, D. Dalvit, and P. Milonni, "Casimir-lifshitz theory and metamaterials," *Phys. Rev. Lett.*, vol. 100, no. 18, p. 183602, 2008. (cited on page 22)

296. A. Grigorenko, N. Roberts, M. Dickinson, and Y. Zhang, "Nanometric optical tweezers based on nanostructured substrates," *Nature Photon.*, vol. 2, no. 6, pp. 365–370, 2008. (cited on pages 23 and 24)

297. R. Zhao, P. Tassin, T. Koschny, and C. M. Soukoulis, "Optical forces in nanowire pairs and metamaterials," *Opt. Express*, vol. 18, no. 25, pp. 25665–25676, 2010. (cited on pages 22 and 23)

298. V. Ginis, P. Tassin, C. M. Soukoulis, and I. Veretennicoff, "Enhancing optical gradient forces with metamaterials," *Phys. Rev. Lett.*, vol. 110, no. 5, p. 057401, 2013. (cited on page 23)

299. Y. Zheng, J. Ryan, P. Hansen, Y.-T. Cheng, T.-J. Lu, and L. Hesselink, "Nanooptical conveyor belt, part II: Demonstration of handoff between near-field optical traps," *Nano Lett.*, vol. 14, pp. 2971–2976, 2014. (cited on pages 23 and 24)

300. H. Liu, J. Ng, S. Wang, Z. Lin, Z. Hang, C. Chan, and S. Zhu, "Strong light-induced negative optical pressure arising from kinetic energy of conduction electrons in plasmon-type cavities," *Phys. Rev. Lett.*, vol. 106, no. 8, p. 87401, 2011. (cited on page 22)

301. S. Wang, J. Ng, H. Liu, H. Zheng, Z. Hang, and C. Chan, "Sizable electromagnetic forces in parallel-plate metallic cavity," *Phys. Rev. B*, vol. 84, no. 7, p. 075114, 2011. (cited on page 22)

302. J. Zhang, K. F. MacDonald, and N. I. Zheludev, "Giant optical forces in planar dielectric photonic metamaterials," *Opt. lett.*, vol. 39, no. 16, pp. 4883–4886, 2014. (cited on page 22)

303. J. Zhang, K. MacDonald, and N. Zheludev, "Optical gecko toe: Optically controlled attractive near-field forces between plasmonic metamaterials and dielectric or metal surfaces," *Phys. Rev. B*, vol. 85, no. 20, p. 205123, 2012. (cited on page 22)

304. Y. He, S. He, J. Gao, and X. Yang, "Giant transverse optical forces in nanoscale slot waveguides of hyperbolic metamaterials," *Opt. Express*, vol. 20, no. 20, pp. 22372–22382, 2012. (cited on page 22)

305. A. Ashkin, *Optical trapping and manipulation of neutral particles using lasers*. World Scientific, 2006. (cited on page 23)

306. M. L. Juan, M. Righini, and R. Quidant, "Plasmon nano-optical tweezers," *Nature Photon.*, vol. 5, no. 6, pp. 349–356, 2011. (cited on page 23)

307. O. M. Maragò, P. H. Jones, P. G. Gucciardi, G. Volpe, and A. C. Ferrari, "Optical trapping and manipulation of nanostructures," *Nature nanotechnology*, vol. 8, no. 11, pp. 807–819, 2013. (cited on page 23)

308. M. Righini, A. S. Zelenina, C. Girard, and R. Quidant, "Parallel and selective trapping in a patterned plasmonic landscape," *Nature Phys.*, vol. 3, no. 7, pp. 477–480, 2007. (cited on page 23)

309. R. Quidant, D. Petrov, and G. Badenes, "Radiation forces on a Rayleigh dielectric sphere in a patterned optical near field," *Opt. Lett.*, vol. 30, no. 9, pp. 1009–1011, 2005. (cited on page 23)

310. K. Wang, E. Schonbrun, P. Steinvurzel, and K. B. Crozier, "Trapping and rotating nanoparticles using a plasmonic nano-tweezer with an integrated heat sink," *Nature Comm.*, vol. 2, p. 469, 2011. (cited on page 24)

311. M. Righini, P. Ghenuche, S. Cherukulappurath, V. Myroshnychenko, F. J. García de Abajo, and R. Quidant, "Nano-optical trapping of Rayleigh particles and Escherichia coli bacteria with resonant optical antennas," *Nano Lett.*, vol. 9, no. 10, pp. 3387–3391, 2009. (cited on page 24)

312. W. Zhang, L. Huang, C. Santschi, and O. J. Martin, "Trapping and sensing 10 nm metal nanoparticles using plasmonic dipole antennas," *Nano Lett.*, vol. 10, no. 3, pp. 1006–1011, 2010. (cited on page 24)

313. E.-S. Kwak, T.-D. Onuta, D. Amarie, R. Potyrailo, B. Stein, S. C. Jacobson, W. Schaich, and B. Dragnea, "Optical trapping with integrated near-field apertures," *J. Phys. Chem. B*, vol. 108, no. 36, pp. 13607–13612, 2004. (cited on page 24)

314. Y. Pang and R. Gordon, "Optical trapping of a single protein," *Nano Lett.*, vol. 12, no. 1, pp. 402–406, 2011. (cited on page 24)

315. A. Kotnala and R. Gordon, "Quantification of high-efficiency trapping of nanoparticles in a double nanohole optical tweezer," *Nano Lett.*, vol. 14, no. 2, pp. 853–856, 2014. (cited on page 24)

316. M. L. Juan, R. Gordon, Y. Pang, F. Eftekhari, and R. Quidant, "Self-induced back-action optical trapping of dielectric nanoparticles," *Nature Phys.*, vol. 5, no. 12, pp. 915–919, 2009. (cited on page 24)

317. P. Hansen, Y. Zheng, J. Ryan, and L. Hesselink, "Nano-optical conveyor belt, part I: Theory," *Nano Lett.*, vol. 14, pp. 2965–2970, 2014. (cited on page 24)

318. T. J. Kippenberg and K. J. Vahala, "Cavity opto-mechanics," *Opt. Express*, vol. 15, no. 25, pp. 17172–17205, 2007. (cited on pages 25 and 65)

319. M. Aspelmeyer, T. J. Kippenberg, and F. Marquardt, "Cavity optomechanics," *Rev. Mod. Phys.*, vol. 86, pp. 1391–1452, Dec 2014. (cited on pages 24, 25, 26, 51, 52, and 66)

320. M. Poggio, C. Degen, H. Mamin, and D. Rugar, "Feedback cooling of a cantilever's fundamental mode below 5 mK," *Phys. Rev. Lett.*, vol. 99, no. 1, p. 017201, 2007. (cited on pages 25 and 65)

321. T. Carmon, M. Cross, and K. J. Vahala, "Chaotic quivering of micron-scaled on-chip resonators excited by centrifugal optical pressure," *Phys. Rev. Lett.*, vol. 98, no. 16, p. 167203, 2007. (cited on page 25)

322. E. Verhagen, S. Deléglise, S. Weis, A. Schliesser, and T. J. Kippenberg, "Quantum-coherent coupling of a mechanical oscillator to an optical cavity mode," *Nature*, vol. 482, no. 7383, pp. 63–67, 2012. (cited on page 25)

323. A. H. Safavi-Naeini, T. M. Alegre, J. Chan, M. Eichenfield, M. Winger, Q. Lin, J. T. Hill, D. Chang, and O. Painter, "Electromagnetically induced transparency and slow light with optomechanics," *Nature*, vol. 472, no. 7341, pp. 69–73, 2011. (cited on pages 25 and 65)

324. M. Lapine, I. V. Shadrivov, D. A. Powell, and Y. S. Kivshar, "Magnetoelastic metamaterials," *Nature Mater.*, vol. 11, no. 1, pp. 30–33, 2012. (cited on pages 25, 26, 51, and 52)

325. A. Abramovici, W. E. Althouse, R. W. Drever, Y. Gürsel, S. Kawamura, F. J. Raab, D. Shoemaker, L. Sievers, R. E. Spero, K. S. Thorne, *et al.*, "LIGO: The laser interferometer gravitational-wave observatory," *Science*, vol. 256, no. 5055, pp. 325–333, 1992. (cited on page 24)

326. A. Dorsel, J. McCullen, P. Meystre, E. Vignes, and H. Walther, "Optical bistability and mirror confinement induced by radiation pressure," *Phys. Rev. Lett.*, vol. 51, no. 17, p. 1550, 1983. (cited on pages 24 and 51)

327. P. Meystre, E. Wright, J. McCullen, and E. Vignes, "Theory of radiation-pressure-driven interferometers," *J Opt. Soc. Am. B*, vol. 2, no. 11, pp. 1830–1840, 1985. (cited on page 24)

328. A. Gozzini, F. Maccarrone, F. Mango, I. Longo, and S. Barbarino, "Light-pressure bistability at microwave frequencies," *J. Opt. Soc. Am. B*, vol. 2, no. 11, pp. 1841–1845, 1985. (cited on pages 24 and 51)

329. B. S. Sheard, M. B. Gray, C. M. Mow-Lowry, D. E. McClelland, and S. E. Whitcomb, "Observation and characterization of an optical spring," *Phys. Rev. A*, vol. 69, no. 5, p. 051801, 2004. (cited on page 25)

330. T. Corbitt, Y. Chen, E. Innerhofer, H. Müller-Ebhardt, D. Ottaway, H. Rehbein, D. Sigg, S. Whitcomb, C. Wipf, and N. Mavalvala, "An all-optical trap for a gram-scale mirror," *Phys. Rev. Lett.*, vol. 98, no. 15, p. 150802, 2007. (cited on page 25)

331. P.-F. Cohadon, A. Heidmann, and M. Pinard, "Cooling of a mirror by radiation pressure," *Phys. Rev. Lett.*, vol. 83, no. 16, p. 3174, 1999. (cited on page 25)

332. C. H. Metzger and K. Karrai, "Cavity cooling of a microlever," *Nature*, vol. 432, no. 7020, pp. 1002–1005, 2004. (cited on pages 25 and 65)

333. S. Gigan, H. Böhm, M. Paternostro, F. Blaser, G. Langer, J. Hertzberg, K. Schwab, D. Bäuerle, M. Aspelmeyer, and A. Zeilinger, "Self-cooling of a micromirror by radiation pressure," *Nature*, vol. 444, no. 7115, pp. 67–70, 2006. (cited on pages 25 and 65)

334. M. Li, W. H. P. Pernice, and H. X. Tang, "Reactive cavity optical force on microdisk-coupled nanomechanical beam waveguides," *Phys. Rev. Lett.*, vol. 103, p. 223901, Nov 2009. (cited on page 25)

335. J. Chan, T. M. Alegre, A. H. Safavi-Naeini, J. T. Hill, A. Krause, S. Gröblacher, M. Aspelmeyer, and O. Painter, "Laser cooling of a nanomechanical oscillator into its quantum ground state," *Nature*, vol. 478, no. 7367, pp. 89–92, 2011. (cited on page 25)

336. F. Marquardt, J. Harris, and S. Girvin, "Dynamical multistability induced by radiation pressure in high-finesse micromechanical optical cavities," *Phys. Rev. Lett.*, vol. 96, no. 10, p. 103901, 2006. (cited on pages 25, 65, and 66)

337. C. Metzger, M. Ludwig, C. Neuenhahn, A. Ortlieb, I. Favero, K. Karrai, and F. Marquardt, "Self-induced oscillations in an optomechanical system driven by bolometric backaction," *Phys Rev. Lett.*, vol. 101, no. 13, p. 133903, 2008. (cited on pages 25 and 65)

338. Q. Lin, J. Rosenberg, X. Jiang, K. J. Vahala, and O. Painter, "Mechanical oscillation and cooling actuated by the optical gradient force," *Phys. Rev. Lett.*, vol. 103, no. 10, p. 103601, 2009. (cited on page 25)

339. F. Marquardt, J. P. Chen, A. A. Clerk, and S. M. Girvin, "Quantum theory of cavity-assisted sideband cooling of mechanical motion," *Phys. Rev. Lett.*, vol. 99, p. 093902, Aug 2007. (cited on page 25)

340. A. Schliesser, R. Rivière, G. Anetsberger, O. Arcizet, and T. J. Kippenberg, "Resolved-sideband cooling of a micromechanical oscillator," *Nature Phys.*, vol. 4, no. 5, pp. 415–419, 2008. (cited on page 25)

341. Y.-S. Park and H. Wang, "Resolved-sideband and cryogenic cooling of an optomechanical resonator," *Nature Phys.*, vol. 5, no. 7, pp. 489–493, 2009. (cited on page 25)

342. J. Teufel, T. Donner, D. Li, J. Harlow, M. Allman, K. Cicak, A. Sirois, J. Whittaker, K. Lehnert, and R. Simmonds, "Sideband cooling of micromechanical motion to the quantum ground state," *Nature*, vol. 475, no. 7356, pp. 359–363, 2011. (cited on page 25)

343. S. Gröblacher, K. Hammerer, M. R. Vanner, and M. Aspelmeyer, "Observation of strong coupling between a micromechanical resonator and an optical cavity field," *Nature*, vol. 460, no. 7256, pp. 724–727, 2009. (cited on page 25)

344. J. D. Teufel, D. Li, M. Allman, K. Cicak, A. Sirois, J. Whittaker, and R. Simmonds, "Circuit cavity electromechanics in the strong-coupling regime," *Nature*, vol. 471, no. 7337, pp. 204–208, 2011. (cited on page 25)

345. G. Agarwal and S. Huang, "Electromagnetically induced transparency in mechanical effects of light," *Phys. Rev. A*, vol. 81, no. 4, p. 041803, 2010. (cited on page 25)

346. S. Weis, R. Rivière, S. Deléglise, E. Gavartin, O. Arcizet, A. Schliesser, and T. J. Kippenberg, "Optomechanically induced transparency," *Science*, vol. 330, no. 6010, pp. 1520–1523, 2010. (cited on page 25)

347. M. Aspelmeyer, S. Gröblacher, K. Hammerer, and N. Kiesel, "Quantum optomechanics: throwing a glance [invited]," *J. Opt. Soc. Am. B*, vol. 27, no. 6, pp. A189–A197, 2010. (cited on page 26)

348. M. Aspelmeyer, P. Meystre, and K. Schwab, "Quantum optomechanics," *Phys. Today*, vol. 65, no. 7, pp. 29–35, 2012. (cited on page 26)

349. M. Lapine, I. V. Shadrivov, D. A. Powell, and Y. S. Kivshar, "Metamaterials with conformational nonlinearity," *Sci. Rep.*, vol. 1, p. 138, 2011. (cited on pages 26 and 51)

350. A. P. Slobozhanyuk, M. Lapine, D. A. Powell, I. V. Shadrivov, Y. S. Kivshar, R. C. McPhedran, and P. A. Belov, "Flexible helices for nonlinear metamaterials," *Adv. Mater.*, vol. 25, no. 25, pp. 3409–3412, 2013. (cited on pages 26, 51, and 52)

351. J. Zhang, K. F. MacDonald, and N. I. Zheludev, "Nonlinear dielectric optomechanical metamaterials," *Light: Sci. Appl.*, vol. 2, no. 8, p. e96, 2013. (cited on pages 26 and 52)

352. J.-Y. Ou, E. Plum, J. Zhang, and N. I. Zheludev, "Controlling light with light in a plasmonic nanooptomechanical metamaterial," in *CLEO: Sci. Inn.*, pp. SF1M–1, Optical Society of America, 2014. (cited on page 26)

353. A. Ourir, A. de Lustrac, and J. M. Lourtioz, "All-metamaterial-based subwavelength cavities ($\lambda/60$) for ultrathin directive antennas," *Appl. Phys. Lett.*, vol. 88, p. 084103, 2006. (cited on page 31)

354. J. Anker, W. Hall, O. Lyandres, N. Shah, J. Zhao, and R. Van Duyne, "Biosensing with plasmonic nanosensors," *Nature Mater.*, vol. 7, no. 6, pp. 442–453, 2008. (cited on page 31)

355. D. R. Smith, J. B. Pendry, and M. C. K. Wiltshire, "Metamaterials and negative refractive index," *Science*, vol. 305, no. 5685, p. 788, 2004. (cited on page 31)

356. N. Liu, L. Langguth, T. Weiss, J. Kästel, M. Fleischhauer, T. Pfau, and H. Giessen, "Plasmonic analogue of electromagnetically induced transparency at the Drude damping limit," *Nature Mater.*, vol. 8, no. 9, pp. 758–762, 2009. (cited on page 31)

357. H. Liu, Y. Liu, T. Li, S. Wang, S. Zhu, and X. Zhang, "Coupled magnetic plasmons in metamaterials," *Phys. Stat. Sol. (b)*, vol. 246, no. 7, pp. 1397–1406, 2009. (cited on pages 31, 51, and 101)

358. M. Hentschel, M. Saliba, R. Vogelgesang, H. Giessen, A. P. Alivisatos, and N. Liu, "Transition from isolated to collective modes in plasmonic oligomers," *Nano Lett.*, vol. 10, pp. 2721–2726, 2010. (cited on page 31)

359. A. Miroshnichenko, S. Flach, and Y. Kivshar, "Fano resonances in nanoscale structures," *Rev. Mod. Phys.*, vol. 82, no. 3, p. 2257, 2010. (cited on pages 31 and 79)

360. B. Luk'yanchuk, N. I. Zheludev, S. A. Maier, N. J. Halas, P. Nordlander, H. Giessen, and C. T. Chong, "The Fano resonance in plasmonic nanostructures and metamaterials," *Nature Mater.*, vol. 9, no. 9, pp. 707–715, 2010. (cited on pages 31, 41, and 79)

361. A. Christ, S. Tikhodeev, N. Gippius, J. Kuhl, and H. Giessen, "Waveguide-plasmon polaritons: strong coupling of photonic and electronic resonances in a metallic photonic crystal slab," *Phys. Rev. Lett.*, vol. 91, no. 18, p. 183901, 2003. (cited on page 31)

362. A. V. Rogacheva, V. A. Fedotov, A. S. Schwanecke, and N. I. Zheludev, "Giant gyrotropy due to electromagnetic-field coupling in a bilayered chiral structure," *Phys. Rev. Lett.*, vol. 97, no. 17, p. 177401, 2006. (cited on pages 31, 32, and 79)

363. Y. Svirko, N. Zheludev, and M. Osipov, "Layered chiral metallic microstructures with inductive coupling," *Appl. Phys. Lett.*, vol. 78, p. 498, 2001. (cited on pages 31, 32, 38, and 39)

364. E. Plum, V. Fedotov, A. Schwanecke, N. Zheludev, and Y. Chen, "Giant optical gyrotropy due to electromagnetic coupling," *Appl. Phys. Lett.*, vol. 90, no. 22, p. 223113, 2007. (cited on page 31)

365. J. Dong, J. Zhou, T. Koschny, and C. Soukoulis, "Bi-layer cross chiral structure with strong optical activity and negative refractive index," *Opt. Express*, vol. 17, no. 16, pp. 14172–14179, 2009. (cited on page 31)

366. H. Liu, J. X. Cao, S. N. Zhu, N. Liu, R. Ameling, and H. Giessen, "Lagrange model for the chiral optical properties of stereometamaterials," *Phys. Rev. B*, vol. 81, no. 24, p. 241403, 2010. (cited on pages 31 and 101)

367. Z. Ruan and S. Fan, "Superscattering of light from subwavelength nanostructures," *Phys. Rev. Lett.*, vol. 105, no. 1, p. 013901, 2010. (cited on page 37)

368. L. Verslegers, Z. Yu, Z. Ruan, P. B. Catrysse, and S. Fan, "From electromagnetically induced transparency to superscattering with a single structure: a coupled-mode theory for doubly resonant structures," *Phys. Rev. Lett.*, vol. 108, no. 8, p. 083902, 2012. (cited on page 37)

369. W. Liu, A. E. Miroshnichenko, D. N. Neshev, and Y. S. Kivshar, "Broadband unidirectional scattering by magneto-electric core–shell nanoparticles," *ACS nano*, vol. 6, no. 6, pp. 5489–5497, 2012. (cited on page 37)

370. M. Osipov, B. Pickup, and D. Dunmur, "A new twist to molecular chirality: intrinsic chirality indices," *Molec. Phys.*, vol. 84, no. 6, pp. 1193–1206, 1995. (cited on page 38)

371. P. Allen, "A radiation torque experiment," *Am. J. Phys*, vol. 74, pp. 1185–1192, 1966. (cited on pages 41 and 42)

372. M. Barbic, J. J. Mock, A. P. Gray, and S. Schultz, "Electromagnetic micromotor for microfluidics applications," *Appl. Phys. Lett.*, vol. 79, p. 1399, 2001. (cited on page 41)

373. F. M. Fazal and S. M. Block, "Optical tweezers study life under tension," *Nature Photon.*, vol. 5, no. 6, pp. 318–321, 2011. (cited on page 41)

374. M. E. J. Friese, J. Enger, H. Rubinsztein-Dunlop, and N. R. Heckenberg, "Optical angular-momentum transfer to trapped absorbing particles," *Phys. Rev. A*, vol. 54, pp. 1593–1596, Aug 1996. (cited on page 41)

375. S. Franke-Arnold, L. Allen, and M. Padgett, "Advances in optical angular momentum," *Laser Photon. Rev.*, vol. 2, no. 4, pp. 299–313, 2008. (cited on page 41)

376. P. Galajda and P. Ormos, "Rotors produced and driven in laser tweezers with reversed direction of rotation," *Appl. Phys. Lett.*, vol. 80, p. 4653, 2002. (cited on page 41)

377. T. Nieminen, S. Parkin, N. Heckenberg, and H. Rubinsztein-Dunlop, "Optical torque and symmetry," in *Optical Trapping and Optical Micromanipulation*, vol. 5514, pp. 254–263, SPIE, 2011. (cited on page 41)

378. W. L. Collett, C. A. Ventrice, and S. M. Mahajan, "Electromagnetic wave technique to determine radiation torque on micromachines driven by light," *Appl. Phys. lett.*, vol. 82, p. 2730, 2003. (cited on pages 41 and 46)

379. N. Halas, S. Lal, W. Chang, S. Link, and P. Nordlander, "Plasmons in strongly coupled metallic nanostructures," *Chem. Rev.*, vol. 111, no. 6, pp. 3913–3961, 2011. (cited on page 41)

380. S. Parkin, G. Knöner, W. Singer, T. A. Nieminen, N. R. Heckenberg, and H. Rubinsztein-Dunlop, "Optical torque on microscopic objects," *Meth. Cell Biol.*, vol. 82, pp. 525–561, 2007. (cited on page 42)

381. J. E. Curtis and D. G. Grier, "Structure of optical vortices," *Phys. Rev. Lett.*, vol. 90, no. 13, p. 133901, 2003. (cited on page 42)

382. J. Jackson and R. Fox, *Classical electrodynamics*. John Wiley & Sons, Inc, 1999. (cited on pages 46, 56, 104, and 106)

383. T. J. Kippenberg and K. J. Vahala, "Cavity optomechanics: back-action at the mesoscale," *Science*, vol. 321, no. 5893, pp. 1172–1176, 2008. (cited on pages 51 and 65)

384. M. Aspelmeyer, T. J. Kippenberg, and F. Marquardt, *Cavity Optomechanics: Nano- and Micromechanical Resonators Interacting with Light*. Springer, 2014. (cited on page 51)

385. M. Lapine, I. Shadrivov, and Y. Kivshar, "Wide-band negative permeability of nonlinear metamaterials.," *Sci. Rep.*, vol. 2, p. 412, 2012. (cited on page 51)

386. A. N. Gent, *Engineering with rubber: how to design rubber components*. Carl Hanser Verlag GmbH Co KG, 2012. (cited on page 58)

387. S. Kielich, "Natural and magneto-optical rotation in the presence of an intense light beam," *Phys. Lett. A*, vol. 25, no. 7, pp. 517–518, 1967. (cited on page 63)

388. S. Strogatz, *Nonlinear Dynamics and Chaos: with applications to physics, biology, chemistry and engineering*. Perseus Books Group, 2001. (cited on page 65)

389. S. Wiggins, *Introduction to applied nonlinear dynamical systems and chaos*, vol. 2. Springer, 2003. (cited on pages 65 and 71)

390. A. Jenkins, "Self-oscillation," *Phys. Rep.*, vol. 525, no. 2, pp. 167–222, 2013. (cited on page 65)

391. D. Smith, "Eddington's valve and cepheid pulsations," *Sky Telesc.*, vol. 68, p. 519, 1984. (cited on page 66)

392. F. Smith and G. Vincent, "Aerodynamic stability of suspension bridges: with special reference to the tacoma narrows bridge," 1950. (cited on page 66)

393. H. Rokhsari, T. Kippenberg, T. Carmon, and K. J. Vahala, "Radiation-pressure-driven micro-mechanical oscillator," *Opt. Express*, vol. 13, no. 14, pp. 5293–5301, 2005. (cited on page 65)

394. A. M. Jayich, J. C. Sankey, B. M. Zwickl, C. Yang, J. D. Thompson, S. M. Girvin, A. A. Clerk, F. Marquardt, and J. G. E. Harris, "Dispersive optomechanics: a membrane inside a cavity," *New J. Phys.*, vol. 10, no. 9, p. 095008, 2008. (cited on page 65)

395. S. Zaitsev, A. K. Pandey, O. Shtempluck, and E. Buks, "Forced and self-excited oscillations of an optomechanical cavity," *Phys. Rev. E*, vol. 84, no. 4, p. 046605, 2011. (cited on page 65)

396. M. Gorkunov, M. Lapine, E. Shamonina, and K. H. Ringhofer, "Effective magnetic properties of a composite material with circular conductive elements," *Eur. Phys. J. B*, vol. 28, pp. 263–269, 2002. (cited on page 75)

397. R. R. A. Syms, E. Shamonina, V. Kalinin, and L. Solymar, "A theory of metamaterials based on periodically loaded transmission lines: Interaction between magnetoinductive and electromagnetic waves," *J Appl. Phys.*, vol. 97, p. 064909, 2005. (cited on page 75)

398. J. D. Baena, L. Jelinek, R. Marqués, and M. Silveirinha, "Unified homogenization theory for magnetoinductive and electromagnetic waves in split-ring metamaterials," *Phys. Rev. A*, vol. 78, p. 013842, 2008. (cited on page 75)

399. C. R. Simovski, "Material parameters of metamaterials (a review)," *Opt. Spect.*, vol. 107, no. 5, pp. 726–753, 2009. (cited on page 75)

400. R. Marqués, L. Jelinek, M. Freire, J. Baena, and M. Lapine, "Bulk metamaterials made of resonant rings," *Proc. IEEE*, vol. 99, pp. 1660–1668, 2011. (cited on page 75)

401. M. Lapine, L. Jelinek, and R. Marqués, "Surface mesoscopic effects in finite metamaterials," *Opt. Express*, vol. 20, no. 16, pp. 18297–18302, 2012. (cited on page 75)

402. F. Strocchi, *Symmetry breaking*, vol. 643. Springer Verlag, 2005. (cited on pages 79 and 84)

403. K. Brading and E. Castellani, "Symmetry and symmetry breaking," in *The Stanford Encyclopedia of Philosophy* (E. N. Zalta, ed.), spring 2013 ed., 2013. (cited on pages 79 and 84)

404. C.N.Yang, "The spontaneous magnetization of a two-dimensional Ising model," *Phys. Rev.*, vol. 85, no. 5, p. 808, 1952. (cited on page 79)

405. Y. Nambu and G. Jona-Lasinio, "Dynamical model of elementary particles based on an analogy with superconductivity. I," *Phys. Rev.*, vol. 122, no. 1, p. 345, 1961. (cited on page 79)

406. Y. Nambu and G. Jona-Lasinio, "Dynamical model of elementary particles based on an analogy with superconductivity. II," *Phys. Rev.*, vol. 124, no. 1, p. 246, 1961. (cited on page 79)

407. P. W. Higgs, "Broken symmetries and the masses of gauge bosons," *Phys. Rev. Lett.*, vol. 13, no. 16, p. 508, 1964. (cited on page 79)

408. F. Englert and R. Brout, "Broken symmetry and the mass of gauge vector mesons," *Phys. Rev. Lett.*, vol. 13, pp. 321–323, Aug 1964. (cited on page 79)

409. G. S. Guralnik, C. R. Hagen, and T. W. B. Kibble, "Global conservation laws and massless particles," *Phys. Rev. Lett.*, vol. 13, pp. 585–587, Nov 1964. (cited on page 79)

410. G. Aad, T. Abajyan, B. Abbott, J. Abdallah, S. Abdel Khalek, A. Abdelalim, O. Abdinov, R. Aben, B. Abi, M. Abolins, *et al.*, "Observation of a new particle in the search for the standard model higgs boson with the ATLAS detector at the LHC," *Phys. Lett. B*, vol. 716, no. 1, pp. 1–29, 2012. (cited on page 79)

411. S. Chatrchyan, V. Khachatryan, A. M. Sirunyan, A. Tumasyan, W. Adam, E. Aguilo, T. Bergauer, M. Dragicevic, J. Erö, C. Fabjan, *et al.*, "Observation of a new boson at a mass of 125 GeV with the CMS experiment at the LHC," *Phys. Lett. B*, vol. 716, no. 1, pp. 30–61, 2012. (cited on page 79)

412. R. Viswanathan, J. Zasadzinski, and D. Schwartz, "Spontaneous chiral symmetry breaking by achiral molecules in a Langmuir-Blodgett film," *Nature*, vol. 368, no. 6470, pp. 440–443, 1994. (cited on page 79)

413. V. Avetisov and V. Goldanskii, "Mirror symmetry breaking at the molecular level," *Proc. Nation. Acad. Sci.*, vol. 93, no. 21, pp. 11435–11442, 1996. (cited on page 79)

414. Y. Saito and H. Hyuga, "Colloquium: Homochirality: Symmetry breaking in systems driven far from equilibrium," *Rev. Mod. Phys.*, vol. 85, no. 2, p. 603, 2013. (cited on page 79)

415. T. Heil, I. Fischer, W. Elsässer, J. Mulet, and C. R. Mirasso, "Chaos synchronization and spontaneous symmetry-breaking in symmetrically delay-coupled semiconductor lasers," *Phys. Rev. Lett.*, vol. 86, no. 5, p. 795, 2001. (cited on page 79)

416. P. Kevrekidis, Z. Chen, B. Malomed, D. Frantzeskakis, and M. Weinstein, "Spontaneous symmetry breaking in photonic lattices: Theory and experiment," *Phys. Lett. A*, vol. 340, no. 1, pp. 275–280, 2005. (cited on page 79)

417. G. Herring, P. Kevrekidis, B. Malomed, R. Carretero-González, and D. Frantzeskakis, "Symmetry breaking in linearly coupled dynamical lattices," *Phys. Rev. E*, vol. 76, no. 6, p. 066606, 2007. (cited on page 79)

418. L. Sadler, J. Higbie, S. Leslie, M. Vengalattore, and D. Stamper-Kurn, "Spontaneous symmetry breaking in a quenched ferromagnetic spinor Bose–Einstein condensate," *Nature*, vol. 443, no. 7109, pp. 312–315, 2006. (cited on pages 79 and 80)

419. T. Mayteevarunyoo, B. A. Malomed, and G. Dong, "Spontaneous symmetry breaking in a nonlinear double-well structure," *Phys. Rev. A*, vol. 78, no. 5, p. 053601, 2008. (cited on page 79)

420. T. Shegai, S. Chen, V. D. Miljković, G. Zengin, P. Johansson, and M. Käll, "A bimetallic nanoantenna for directional colour routing," *Nature Comm.*, vol. 2, p. 481, 2011. (cited on page 79)

421. L. Huang, X. Chen, B. Bai, Q. Tan, G. Jin, T. Zentgraf, and S. Zhang, "Helicity dependent directional surface plasmon polariton excitation using a metasurface with interfacial phase discontinuity," *Light: Sci. Appl.*, vol. 2, no. 3, p. e70, 2013. (cited on page 79)

422. J. Lin, J. B. Mueller, Q. Wang, G. Yuan, N. Antoniou, X.-C. Yuan, and F. Capasso, "Polarization-controlled tunable directional coupling of surface plasmon polaritons," *Science*, vol. 340, no. 6130, pp. 331–334, 2013. (cited on page 79)

423. R. Singh, E. Plum, C. Menzel, C. Rockstuhl, A. Azad, R. Cheville, F. Lederer, W. Zhang, and N. Zheludev, "Terahertz metamaterial with asymmetric transmission," *Phys. Rev. B*, vol. 80, no. 15, p. 153104, 2009. (cited on page 79)

424. L. Alvarez-Gaumé and J. Ellis, "Eyes on a prize particle," *Nature Phys.*, vol. 7, no. 1, pp. 2–3, 2010. (cited on page 80)

425. A. Kostelecky, "The search for relativity violations," *Sci. Am.*, vol. 15, pp. 12–21, 2006. (cited on page 80)

426. Y. Saito and H. Hyuga, "Grinding-induced homochirality in crystal growth," *J. Cryst. Growth*, vol. 318, no. 1, pp. 93–98, 2011. (cited on page 80)

427. C. Denz, S. Flach, and Y. S. Kivshar, *Nonlinearities in periodic structures and metamaterials*, vol. 150. Springer, 2010. (cited on page 80)

428. N. Lazarides, M. Eleftheriou, and G. Tsironis, "Discrete breathers in nonlinear magnetic metamaterials," *Phys. Rev. Lett.*, vol. 97, no. 15, p. 157406, 2006. (cited on page 80)

429. Y. Liu, G. Bartal, D. A. Genov, and X. Zhang, "Subwavelength discrete solitons in nonlinear metamaterials," *Phys. Rev. Lett.*, vol. 99, no. 15, p. 153901, 2007. (cited on page 80)

430. N. N. Rosanov, N. V. Vysotina, A. N. Shatsev, A. S. Desyatnikov, and Y. S. Kivshar, "Knotted solitons in nonlinear magnetic metamaterials," *Phys. Rev. Lett.*, vol. 108, no. 13, p. 133902, 2012. (cited on page 80)

431. I. V. Shadrivov, A. A. Zharov, N. A. Zharova, and Y. S. Kivshar, "Nonlinear magnetoinductive waves and domain walls in composite metamaterials," *Photon. Nanostr. Fundam. Appl.*, vol. 4, no. 2, pp. 69–74, 2006. (cited on page 80)

432. N. N. Rosanov, N. V. Vysotina, A. N. Shatsev, I. V. Shadrivov, D. A. Powell, and Y. S. Kivshar, "Discrete dissipative localized modes in nonlinear magnetic metamaterials," *Opt. Express*, vol. 19, no. 27, pp. 26500–26506, 2011. (cited on page 80)

433. D. Kondepudi and G.-W. Nelson, "Chiral symmetry breaking in nonequilibrium systems," *Phys. Rev. Lett.*, vol. 50, no. 14, p. 1023, 1983. (cited on page 81)

434. C. Viedma, "Chiral symmetry breaking during crystallization: complete chiral purity induced by nonlinear autocatalysis and recycling," *Phys. Rev. Lett.*, vol. 94, no. 6, p. 065504, 2005. (cited on page 81)

435. M. Mekata, "Antiferro-ferrimagnetic transition in triangular Ising lattice," *J. Phys. Soc. Jap.*, vol. 42, no. 1, pp. 76–82, 1977. (cited on page 94)

436. P. Terzieff and K. L. Komarek, "The antiferromagnetic and ferrimagnetic properties of iron selenides with NiAs-type structure," *Monatshefte für Chemie/Chem. Monthly*, vol. 109, no. 5, pp. 1037–1047, 1978. (cited on page 94)

437. J. Petschulat, A. Chipouline, A. Tünnermann, T. Pertsch, C. Menzel, C. Rockstuhl, T. Paul, and F. Lederer, "Simple and versatile analytical approach for planar metamaterials," *Phys. Rev. B*, vol. 82, no. 7, p. 075102, 2010. (cited on page 101)

438. C.-T. Tai, *Dyadic Green functions in electromagnetic theory*, vol. 272. IEEE press New York, 1994. (cited on page 103)

439. D. J. Taylor, "Accurate and efficient numerical integration of weakly singular integrals in galerkin EFIE solutions," *IEEE Trans. Antennas Prop.*, vol. 51, no. 7, pp. 1630–1637, 2003. (cited on page 103)

440. W. J. J. Hwa, *Generalized moment methods in electromagnetics*. Wiley, 1991. (cited on page 103)

441. W. C. Chew, *Waves and fields in inhomogeneous media*, vol. 522. IEEE press New York, 1995. (cited on page 103)

442. R. F. Harrington and J. L. Harrington, *Field computation by moment methods*. Oxford University Press, 1996. (cited on page 103)

443. H. Ammari, G. Bao, and A. W. Wood, "An integral equation method for the electromagnetic scattering from cavities," *Math. Meth. Appl. Sci.*, vol. 23, no. 12, pp. 1057–1072, 2000. (cited on page 103)

444. J. Jin, *The finite element method in electromagnetics*. John Wiley & Sons, 2014. (cited on page 103)

445. D. A. Powell, "Resonant dynamics of arbitrarily shaped meta-atoms," *Phys. Rev. B*, vol. 90, p. 075108, Aug 2014. (cited on pages 103 and 104)

446. I. V. Lindell, *Methods for electromagnetic field analysis*. New York, NY (United States); Oxford Univ. Press, 1992. (cited on pages 113 and 117)